Structural and Stratigraphic Setting of the Rey de Plata Volcanogenic Massive Sulfide Deposit in the Guerrero Composite Terrane, Mexico

By

Ahiram Monter Ramírez B.Sc.

A Thesis submitted in partial fulfillment of the requirements for the degree of Master of Science in Geology (M.Sc.)

School of Graduate Studies
Laurentian University
Sudbury, Ontario
Canada, P3E 2C6

THESIS DEFENCE COMMITTEE/COMITÉ DE SOUTENANCE DE THÈSE
Laurentian Université/Université Laurentienne
School of Graduate Studies/École des études supérieures

Title of Thesis
Titre de la thèse STRUCTURAL AND STRATIGRAPHIC SETTING OF THE REY DE PLATA VOLCANOGENIC MASSIVE SULFIDE DEPOSIT IN THE GUERRERO COMPOSITE TERRANE, MEXICO

Name of Candidate
Nom du candidat Monter Ramirez, Ahiram

Degree
Diplôme Master of Science

Department/Program
Département/Programme Geology

Date of Defence
Date de la soutenance July 14, 2014

APPROVED/APPROUVÉ

Thesis Examiners/Examinateurs de thèse:

Dr. Bruno Lafrance
(Supervisor/Directeur(trice) de thèse)

Dr. Harold Gibson
(Co-supervisor/Co-directeur(trice) de these)

Mr. Juan Figueroa
(Committee member/Membre du comité)

Dr. Réal Daigneault Director, School of Graduate Studies
(External Examiner/Examinateur externe)

Approved for the School of Graduate Studies
Approuvé pour l'École des études supérieures
Dr. David Lesbarrères
M. David Lesbarrères
Directeur, École des études supérieures

ACCESSIBILITY CLAUSE AND PERMISSION TO USE

Abstract

The Rey de Plata volcanogenic massive sulfide (VMS) deposit is located in southern Mexico and within the Teloloapan subterrane of the Guerrero Composite Terrane. It is hosted by the Middle to Late Cretaceous Villa Ayala Formation, which is itself subdivided into three informal members. The lower Ahuehuetla member consists of basaltic flows, sills, and volcaniclastic rocks. The middle Rey de Plata member, which hosts the Rey de Plata deposit, consists of rhyolitic to rhyodacitic flows, sills, and volcaniclastic rocks. The timing of felsic volcanism and the formation of the Rey de Plata deposit is constrained between 139.1 ± 0.4 Ma to 129.4 ± 0.7 Ma by U/Pb dating of zircons from an aphyric flow. The upper Villa Ayala member consists of basaltic amygdaloidal sills and volcaniclastic rocks. The slightly LREE enrichment, negative Nb and positive Zr anomalies of the mafic rocks suggest that they formed either in a primitive to slightly evolved arc to back-arc setting with minor contamination by older arc (or continental) crust. The slight LREE enrichment, flat HREE pattern, and pronounced negative Nb anomaly of the felsic volcanic rocks are consistent with FII rhyolites, which indicate their formation and emplacement during rifting within an arc or nascent back-arc environment; an interpretation consistent with the geochemical signature of the associated basaltic rocks.

The Rey de Plata and Villa Ayala members are unconformably overlain by argillite of the Acapetlahuaya and turbiditic sandstone of the Miahuatepec Formations, which are capped by Eocene conglomerates of the Balsas Group. Detrital zircons from the Acapetlahuaya Formation have U/Pb ages ranging from 115 ± 4 Ma to 152 ± 4 Ma, similar to the age of volcanic rocks of the Villa Ayala Formation. This suggests that the Acapetlahuaya sedimentary rocks were deposited in an intra-arc basin or in a back-arc basin, which separated the Villa Ayala arc from continental Mexico. This basin was closed during deposition of the younger Miahuatepec Formation sedimentary rocks as these strata yielded older, 800 Ma to 1200 Ma, zircon populations derived from the erosion of older terranes previously accreted to continental Mexico.

D_1 at Rey de Plata corresponds to the Upper Cretaceous to Lower Tertiary Sievier-Laramide Orogeny. A shallowly SW-dipping S_1 cleavage, L_1 stretching lineation, and NE-verging F_1 folds formed in altered volcanic rocks, argillite and turbiditic sandstone during NE-directed D_1 thrusting. D_2 extensional collapse of the orogen occurred either during or shortly after D_1. It produced asymmetrical W-verging folds folding S_1, and an S_2 shear band cleavage (C'), indicating normal, west-directed slip down the dip of the S_1 foliation. During D_2, gold- and silver-rich epithermal veins were emplaced. These veins may have contributed to the high grade gold and silver zones of Rey de Plata deposit. Deformation of the Teloloapan subterrane resumed in the Eocene with the formation of D_3 normal brittle faults

linked by strike-slip brittle faults. W-verging F_3 drag folds are associated with the normal faults. Extensional basins formed during D_3 and were filled by fluvial conglomerate and ignimbrites of the Balsas Group. Late, NW-SE-directed, D_4 compression produced upright to inclined, NE- and SW-verging F_4 folds that overprint S_1 and S_2.

Rey de Plata is a bimodal-felsic type VMS deposit. It formed during rifting of an arc or backarc and consists of stratigraphically stacked Zn-Cu-Pb massive sulfide ore lenses with high Ag-Au grades. The lenses range in thickness from 3m to 60m, in length from 300m to 1500m, and in width from 100m to 500m. They consist of massive, semi-massive, and disseminated pyrite ± sphalerite ± galena ± chalcopyrite ± silver sulphosalts ± gold, together with gangue minerals of quartz ± barite. Extensive quartz-sericite-pyrite alteration surrounds the ore lenses. Graphitic argillite units up to 40m in thickness typically occur at the top and bottom contacts of the ore lenses. The ore lenses underwent the same deformation history as their host rocks. During D_1, they developed a strong S_1 foliation, they were stretched parallel to L_1, and their base metal zonation reflects clockwise rotation of the lenses (looking NW). Thereafter, during D_2 and D_3, the ore lenses were displaced southwestward by 200 meters along normal faults and shears and then openly folded by F_4 during D_4.

Acknowledgements

First and foremost I would like to express my sincere gratitude to the people at Servicios Administrativos Peñoles S. A de C.V. Inc. Company for allowing me the opportunity to undertake this study and for providing the logistical and financial support along the way.

Special thanks go out to Juan I. Figueroa Soto and Javier García Fons, without whom this study would not have been possible.

For their extraordinary patience, constant guidance and invaluable wisdom in the field, classroom, and walk of life, I am indebted to my supervisors Dr. Bruno Lafrance and Dr. Harold L. Gibson. Thank you Bruno and Harold for being such incredible supervisors, friends and human beings.

Thank you also to R. Ivan Zenón Gama, Antonio Vázquez Avendaño and Edras Fernán Bravo Cardona for all their invaluable technical support and their ability to solve my computer problems from afar.

I would like to express thanks to the entire faculty in the Department of Earth Sciences at Laurentian University for their input during the length of this study.

To all my good friends in Sudbury, thank you for your input and your support, and for making for me and my family the last two years an unforgettable experience, especially in winter time.

Very special thanks to my beloved daughters and wife for their unconditional support, patience and teachings.

Finally, thank you to all my family and friends in Mexico for their constant encouragement.

Dedication

To my daughters.

“Que mis enseñanzas sean los cimientos donde ellas construyan una vida mejor”

Contents

List of Figures

Chapter 1

Chapter 2

Chapter 3

Chapter 4

Chapter 5

Appendix 3

Appendix 5

Appendix 6

List of Tables

Chapter 3

Appendix 1

Appendix 2

Appendix 3

Appendix 4

Field data

Core data

Chapter 1: Introduction

The principal outcome of this research is a better understanding of the geological processes that controlled the shape and distribution of ore lenses at the Rey de Plata deposit, Mexico. Rey de Plata is a very important mining project for Servicios Administrativos Peñoles S. A de C.V. Inc. and for the Mexican mining industry. The study was supported by the Mexican Servicios Administrativos Peñoles S. A de C.V. Inc. and by the Natural Sciences and Engineering Research Council of Canada (NSERC).

Chapter 2 summarizes previous work that focused on the geology of western Mexico, and in particular the Guerrero Composite Terrane, and its five subterranes. These subterranes consist of arc-backarc successions that range in age from upper Jurassic (Tithonian) to Middle-Late Cretaceous (Cenomanian) (Centeno-García et al. 2008) and include numerous volcanogenic massive sulfide (VMS) deposits, such as the Rey de Plata and the well-known San Nicolás and Tizapa deposits.

Chapter 3 presents new data obtained during this study and provides the first stratigraphic subdivision and description of each lithological unit in the Rey de Plata deposit area, as well as their correlation with regional formations. Also, new geochronological and geochemical data are presented which constrain the age of volcanic and sedimentary units and define their lithogeochemical characteristics and geodynamic setting.

In chapter 4, the deformational history of the Rey de Plata deposit is presented, which includes early tilting of the volcanic sequence followed by four deformational events. Previous regional studies have only recognized the first three deformational events identified at Rey de Plata camp.

Chapter 5 contains the first description of base metal zonation within ore lenses at Rey de Plata and their deformational history. The former is used to define the paleo-upflow zones and to reconstruct fault offsets.

Chapter 6, contains the discussion and conclusions.

1.1 Problem statement

A more thorough understanding of the geology of southern Mexico would help define the processes that formed and later modified the Rey de Plata deposit which, in turn, would aid Servicios Administrativos Peñoles S. A. De C.V. Inc. geologists in their search for volcanogenic massive sulfide (VMS) deposits in other tectonic terranes of southern Mexico. Although these terranes contain several polymetallic deposits, they are poorly exposed. They share common geological features with the Rey de Plata deposit area so further understanding of the structural history and volcanic stratigraphy of the Rey de Plata area will benefit exploration for new deposits in southern Mexico.

In particular, it is of paramount importance to understand the current geometry of the VMS deposits and their host strata so a thorough documentation and understanding of the deposit's deformational history is the focus of this study.

1.2 Exploration history

Historical exploration work in the Rey de Plata deposit area began in the early 1900's with surface prospecting, trenching, and the development of shallow mine shafts and adits. Exploration continued between 1925 and 1929, but was abandoned due to operational problems. The first major mineralized zone was found by La Campaña Company immediately after the Second World War between 1946 and 1949. The company explored an area of 200m x 500m and delimited the

Rey Viejo deposit, which had silver values of up to 6 kg/ton. From the end of 1975 until 1980, Servicios Administrativos Peñoles S. A de C. V. Inc. conducted a 11,300 m drill program over a wider area, which culminated with the discovery of the Rey de Plata and Tehuixtla orebodies and the Cu-Zn lens (García-Fons et al. 1981; Giles and García-Fons 2000). In 1986, the Minera Antares Company, which stemmed from a partnership between Peñoles and Outokumpu Group Inc., sank a shaft and drove a ramp to the 865 mine level to intersect the Tehuixtla body. This provided an underground platform to further explore and delimit the ore body through a systematic diamond drilling program.

In 2000 and 2001, Servicios Administrativos Peñoles S. A de C.V. Inc., in partnership with Dowa Holdings Co., Ltd. and Sumitomo Corporation, operating under the name of the Minera Rey de Plata Company, constructed a 1,100 tons per day flotation beneficiation plant, which processed a total of 386,823 tons of ore at grades of 1.91 g/ton Au, 237.01 g/ton Ag, 2.32% Pb, 9.90% Zn, 0.33% Cu and 14.61% Fe (J. Figueroa, personal communication, 2012).

From 2007 to 2012, an aggressive exploration program by Peñoles, which included surface geology, systematic sampling and more than 400 deep diamond drill holes, resulted in the discovery and delineation of the Rey de Plata Superior, Medio and Inferior orebodies. The orebodies are estimated to contain more than 20 million of tons of ore. A ramp is being developed and a deep shaft is being sunk to mine these orebodies.

1.3 Localization of the Rey de Plata deposit

The Rey de Plata deposit is located within the Sierra del Sur Range in southern Mexico. It is one of several polymetallic VMS deposits in a belt that extends from the state of Guerrero, in southern Mexico, to the eastern part of the state of Zacatecas, in north-central Mexico. The largest deposits include Campo Morado

and Rey de Plata in Guerrero State, Tizapa in the Estado de Mexico State, and San Nicolas in Zacatecas State. (Figure 1.1).

Figure 1.1. Major VMS deposits in Mexico.

The Rey de Plata deposit is 262 kilometers by road from Mexico City. It is located next (or within the town limit) to the village of Tehuixtla, which is part of the greater Teloloapan Municipality in the state of Guerrero. It lies 1680 meters above sea level at latitude 18°22’04”N and longitude 99°52’26”W (Figure 1.2).

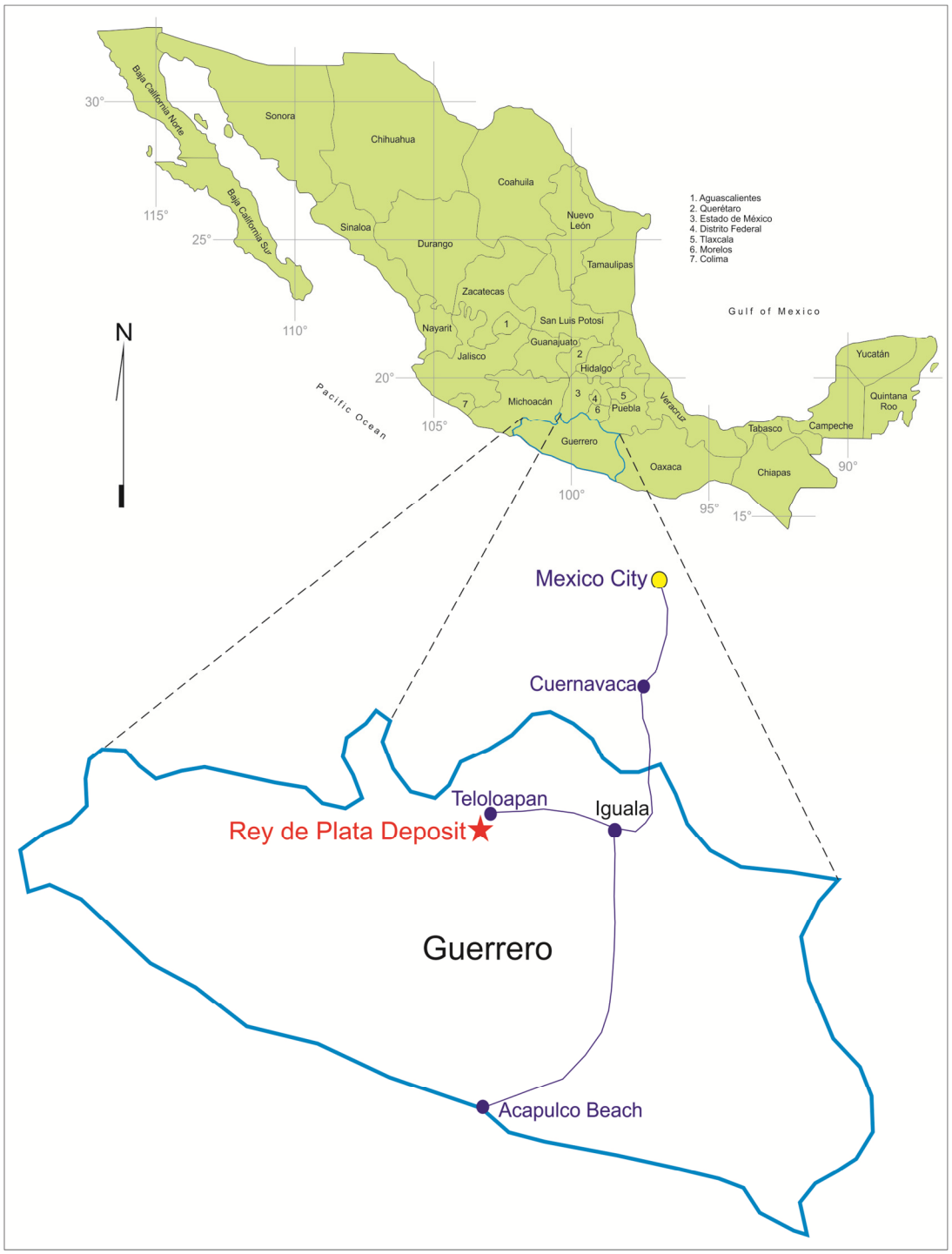

Figure 1.2. Location of the Rey de Plata deposit.

1.4 Objectives

The main objective of the thesis is to determine stratigraphic and structural controls on the massive sulfide ore lenses at the Rey de Plata deposit. The specific objectives are to define a lithostratigraphy for the Rey de Plata deposit, constrain the absolute age of the lithostratigraphic units, and determine the sequence of deformation events that affected the Rey de Plata deposit area and, more specifically, the ore lenses.

1.5 Methodology

Detailed mapping of road cuts was conducted along seven, roughly east-west and north-south traverses. Prior to mapping, the roads were surveyed by the mine surveyor using a differential GPS and distances were marked along the road cuts. UTM coordinates are in the 14Q region of the NAD 27 datum as defined for North America.

Samples were collected for whole rock, trace and rare earth element (REE) geochemistry to help correlation of units between traverses.

The analyses were done by the ALS Chemex lab in Vancouver, Canada. Samples were also collected for thin sections and these were examined to determine mineralogy, textures and to characterize structural kinematic indicators and microstructures. Additional structural data was measured in core from six oriented drill holes using the Ezy Logger goniometer, which was purchased from 2iC Australia Pty Ltd Company.

Three samples were collected for U-Pb zircon dating. A rhyolite sample from the footwall to massive sulfide at the Rey de Plata deposit was submitted to the Jack Satterly Geochronology Laboratory, Department of Earth Sciences, University of Toronto to constrain the age of volcanism and two samples of sedimentary rocks

from the Acapetlahuaya and Miahuatepec Formations were submitted to the ICPMS facility at Laurentian University, Sudbury for detrital U-Pb zircon geochronology.

Chapter 2: Introduction and Tectonic Setting of the Guerrero Composite Terrane

2.1 Introduction

This chapter provides a regional perspective of the geology which hosts the Rey de Plata VMS deposit and of the geology of Western Mexico. The regional information presented in this chapter was compiled from previous work.

Mexico was constructed by the accretion of basement crustal fragments and oceanic terranes. During the Mesozoic, accreted Proterozoic and Paleozoic terranes formed a relatively narrow neck of land that was linked to the North American craton. This land consisted of the Oaxaquia, Mixteca, Parral, and Cortes terranes (Figure 2.1). It was bordered to the east by a rifted continental margin and to the west by an active subduction zone (Centeno-García et al. 2008). Other terranes, including the Guerrero Composite Terrane and the Central Terrane, formed seaward of the subduction zone and were later accreted to Mexico during the Mesozoic (Figure 2.1).

2.2 Tectonic Setting of the Guerrero Composite Terrane

The Guerrero Composite Terrane is one-third of the size of Mexico and makes up most of the western margin of Mexico. It is the largest of all the Mexican terranes, and it is probably the second largest terrane in the North America Cordillera. It is dominated by submarine and locally subaerial volcanic and sedimentary successions that range in age from upper Jurassic (Tithonian) to Middle-Late Cretaceous (Cenomanian) (Centeno-García et al. 2008).

The Guerrero Composite Terrane is divided in two halves by the Cenozoic Trans-Mexican Volcanic Belt. The northern half is largely covered by mid-Tertiary volcanic deposits of the Sierra Madre Occidental Range and is exposed in only a few places along the Pacific coast in Sinaloa State and part of Guanajuato and Zacatecas States. In contrast, the southern half is well exposed, and stratigraphic relationships between units can generally be determined (Mendoza and Suastegui 2000). The Guerrero Composite Terrane is truncated to the East by Late Cretaceous to Early Paleocene low-angle thrust faults, which juxtaposed the Guerrero Terrane against the Oaxaquia and Mixteca terranes (Figure 2.1).

Numerous models have been proposed to explain the formation of the Guerrero Composite Terrane formed. Some authors suggested that it represents one or more peripheral arcs that were located relatively close to the Proterozoic Oaxaquia Terrane, which had been previously accreted to the continent during the Late Paleozoic (Ortega-Gutiérrez et al. 1995). Westward-dipping subduction under these arcs consumed the ocean between the arcs and the Oaxaquia Terrane, accreting the arcs to the continent in the Late Cretaceous (Campa and Ramirez 1979, Tardy et al. 1994, Mendoza and Suastegui 2000). Another model proposed that the terrane is autochtonous, and was built on Proterozoic continental crust of the Oaxaquia Terrane (Elías-Herrera and Sanchez-Zavala 1992). Centeno-García et al. (2008) suggested a more complex model or interpretation, involving cycles of multiple accretion to the continent followed by rifting. The basement to the Guerrero Composite Terrane is not well characterized because of poor exposure, but may be represented by metamorphic rocks of the Late Triassic-Early Jurassic Arteaga Complex (Centeno-García 1994), which is exposed in the western part of the terrane. The Arteaga Complex is composed mostly of terrigenous sediments with minor basaltic pillow lavas, chert, tuff and limestone (Centeno-García et al. 1993).

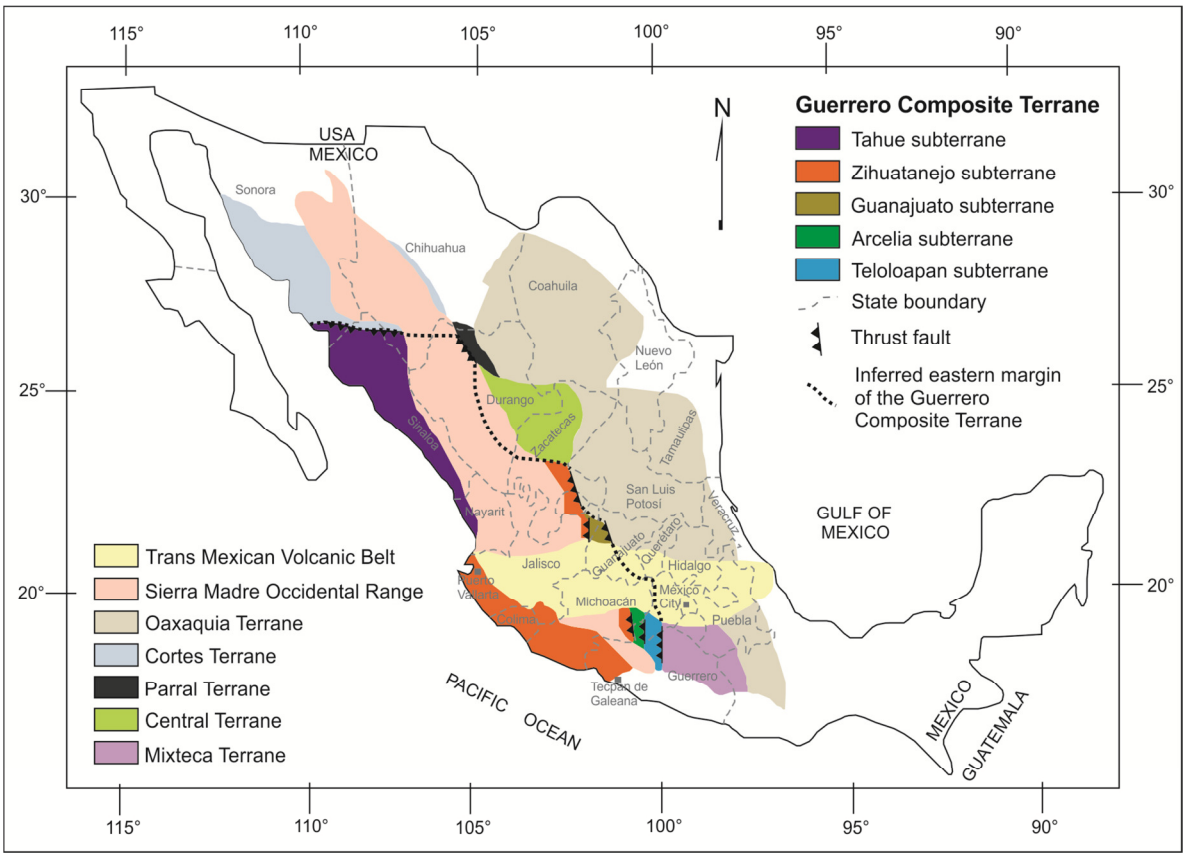

Figure 2.1. The Guerrero Composite Terrane in western Mexico (modified from Centeno-García et al. 2008).

Thus, the geodynamic setting of the Guerrero Composite Terrane is still under debate, but all the volcanic and volcaniclastic rocks within this terrane are interpreted to represent former arcs and back arc basins that were accreted to the continent during the Late Cretaceous (Campa and Ramirez 1979, Elías-Herrera and Sanchez-Zavala 1992, Mendoza and Suastegui 2000, Centeno-García et al. 2008).

2.3 Subdivision of the Guerrero Composite Terrane

Based on the work of Centeno-García (1993, 2008), Talavera-Mendoza (1995) and Mendoza et al. (2000) the Guerrero Composite Terrane is divided into five

subterranes that form parallel north-south trending belts bounded by regional structures. These subterranes are, from west to east: Tahue, Zihuatanejo, Guanajuato, Arcelia and Teloloapan (Figure 2.2).

2.3.1 Tahue subterrane

The Tahue subterrane consists of the oldest rocks within the Guerrero Composite Terrane. The subterrane is mainly exposed in the Sinaloa de Leyva-Porohui region. It consists of subaqueous rhyolitic-andesitic flows, epiclastic rocks and calcareous rocks of the Ordovician El Fuerte Complex (Centeno-García 2005, Centeno-García et al. 2008). A thin marbleized limestone bed yielded Middle to Late Ordovician conodonts (Poole et al. 2005), which have been also found in similar Paleozoic arc rocks in the Klamath Mountains of Northern California (Lapierre et al. 1987). The El Fuerte Complex is unconformably overlain by Cretaceous arc volcanic rocks and is cut by mafic and ultramafic intrusions that belong to the same Cretaceous arc magmatic system (Figure 2.2).

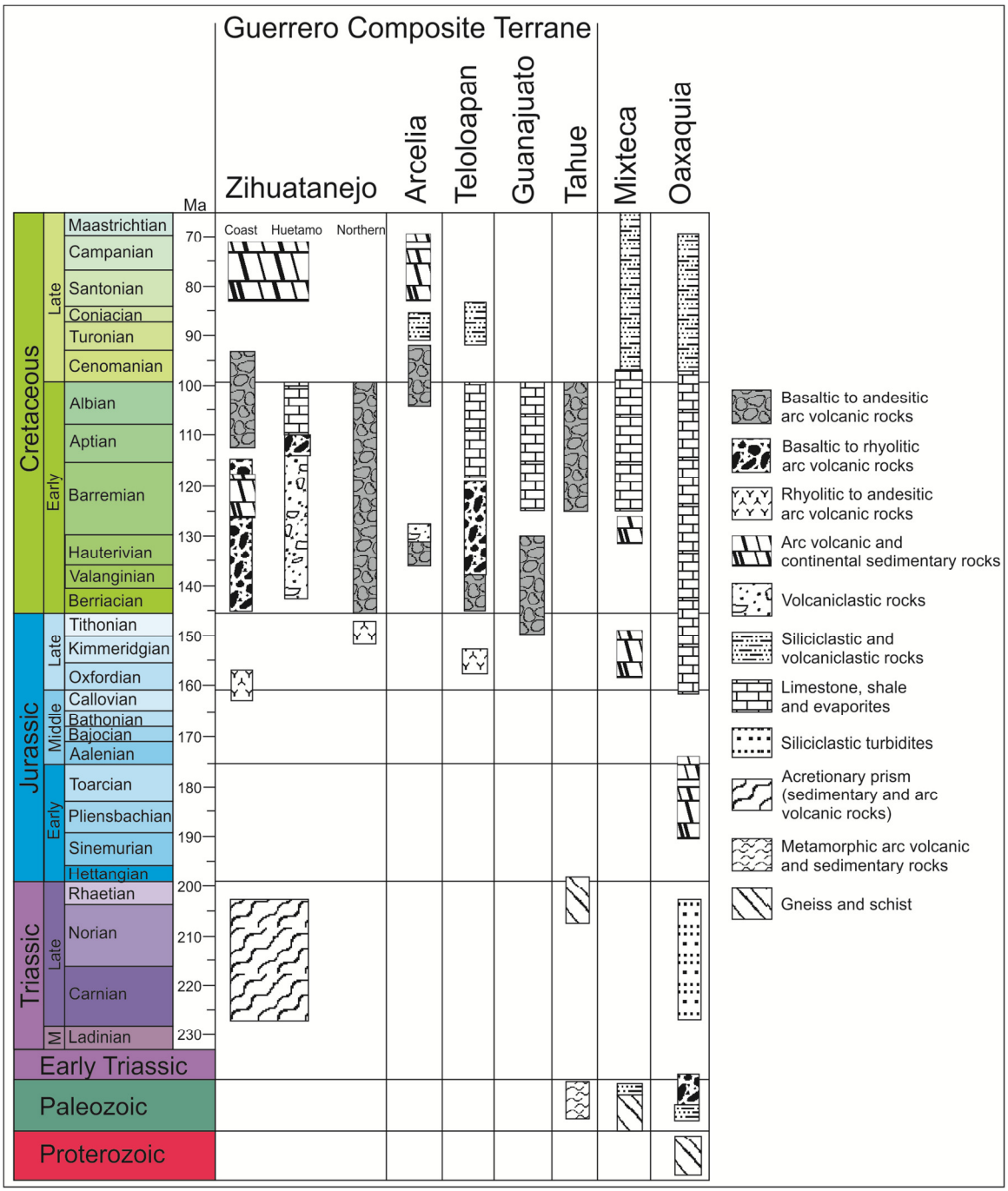

Figure 2.2. Simplified stratigraphic columns for subterranes of the Guerrero Composite Terrane and for Oaxaquia and Mixteco terranes. They show the age range of sedimentation and magmatism for western and central Mexico (modified from Centeno-García et al. 2008).

2.3.2 Zihuatanejo subterrane

The Zihuatanejo subterrane is exposed along the Pacific coast from the town of Tecpan de Galeana to the town of Puerto Vallarta, north of the Mexican Volcanic Belt (Figure 2.1). It is the largest of all the subterranes (Mendoza and Suastegui 2000, Centeno-García 2005, Centeno-García et al. 2008). It consists of Triassic (Norian) quartz-rich turbidites (sandstone and shale) that were tectonically imbricated (Campa and Ramirez 1979) with pillowed flows, diabase, banded gabbro, chert and limestone. Based on a block-in-matrix structure, these rocks constitute an Upper Triassic accretionary prism, which is interpreted as the basement to younger rocks of the Zihuatanejo subterrane (Centeno-García et al. 1993; Talavera-Mendoza 2000; Centeno-García et al. 2008. Martini et al. 2010, Figure 2.2). Depending on geographic location, these rocks have been named the Zacatecas Formation, Arteaga Complex, and Las Ollas Complex (Mendoza and Suastegui 2000, Centeno-García et al. 2008). The younger rocks of the Zihuatanejo subterrane are exposed along the Pacific coast. They comprise Middle to Late Jurassic, evolved arc volcanic rocks, including subaqueous rhyolitic lavas and volcaniclastic rocks, and granitoids that were emplaced in rocks of the accretionary prism (Bissig et al. 2003, Centeno-García et al. 2003). Younger Cretaceous arc successions, which range in age from Berriasian to Cenomanian, are exposed in the Huetamo region. They comprise basaltic to rhyolitic volcanic and volcaniclastic rocks, interbedded with limestones, evaporites, and lesser conglomeratic beds (Mendoza and Suastegui 2000, Centeno-García et al. 2008). These younger arcs were possibly constructed on an older, Late Jurassic arc because they overlie older volcanic rocks with Tithonian U/Pb zircon ages of 150 Ma to 148 Ma (Danielson 2000, Mortensen et al. 2003). These Jurassic-Cretaceous arc successions host several important volcanogenic massive sulfide (VMS) deposits, including the large San Nicolás deposit (Centeno-García et al. 2008).

The contact between the Zihuatanejo subterrane and the Oaxaquia Terrane is exposed at its northern limit, where Cretaceous arc rocks of the Zihuatanejo subterrane are thrust over shallow-marine, Oaxaquia limestone. Its contacts to the east with the Arcelia and Guanajuato subterranes are covered by uppermost Cretaceous and Cenozoic sedimentary and volcanic rocks, and is inferred to be an east-verging Late Cretaceous thrust, similar to other terrane bounding faults (Centeno-García 2005, Centeno-García et al. 2008, Figure 2.1).

2.3.3 Guanajuato subterrane

The Guanajuato subterrane is exposed mostly in the northern part of the state of Guanajuato (Figure 2.1). It is interpreted either as a primitive island arc that appears to lack an older basement (Ortiz-Hernandez et al. 1991, Ortiz-Hernandez 1992), or as the remnant of an oceanic basin that originally separated the Guerrero Composite Terrane from the continental Oaxaquia Terrane (Centeno-García 2005, Centeno-García et al. 2008). It consists of upper mantle and lower crustal gabbro, tonalite, serpentinite, wehrlite and gabbroic dike swarms that were thrust over pillow basalts, black detrital limestone, volcanic turbidites, chert, and rhyolitic tuffs (Centeno-García et al. 2008). The rhyolitic tuffs, which host the El Gordo VMS deposit, yielded a U/Pb zircon age of 146.1 ± 1.1 Ma (Tithonian to Berriasian) (Mortensen et al. 2008). Nanofossils of similar Tithonian-Hauterivian ages were reported by Ortiz-Hernandez et al. (2003). Thus, the Guanajuato subterrane is Upper Jurassic to Lower Cretaceous in age (Figure 2.2) and it was thrust over the continental Oaxaquia Terrane during the Upper Cretaceous (Centeno-García et al. 2008). The contact between the Guanajuato and Zihuatanejo subterranes is not exposed, but the tectonic and/or stratigraphic relationship between the two subterranes is thought to be an east-verging, Upper Cretaceous thrust fault.

2.3.4 Arcelia subterrane

The Arcelia subterrane forms a 40 km wide by 250 km long belt in northwestern areas of the Guerrero State. It is characterized by Early Cretaceous, deep-marine, primitive arc rocks, including basaltic pillow lavas and breccias, ultramafic rocks, black shale and chert, which are overlain by volcaniclastic turbidites. The volcanic rocks are amongst the least-evolved volcanic rocks within the Guerrero Composite Terrane (Talavera-Mendoza et al. 1995, Mendoza and Suastegui 2000). The Arcelia subterrane is thrust over the Teloloapan subterrane along an east-directed Laramide thrust and, in turn, is overthrusted by rocks of the Zihuatanejo subterrane along its western margin (Mendoza and Suastegui 2000, Figure 2.1).

2.3.5 Teloloapan subterrane

The Teloloapan subterrane hosts several polymetallic VMS deposits, including the Rey de Plata deposit (Figure 2.3). It is 300 km in length and 100 km in width and it extends from the state of Guerrero in southern Mexico to the eastern part of the state of Zacatecas and some parts of the state of Guanajuato in central Mexico (Figure 2.3).

The eastern half of the Teloloapan subterrane, where the Rey de Plata VMS deposit is located, is characterized by shallow marine, andesitic to basaltic massive flows, volcanic breccias and pyroclastic to volcaniclastic deposits of the Villa Ayala Formation (Talavera-Mendoza et al. 1995, Mendoza and Suastegui 2000, Centeno-García et al. 2008). These shallow marine rocks grade upward into massive, reefal limestone of the Teloloapan Formation, which at its base is intercalated with volcaniclastic rocks that contain upper Early Cretaceous (Aptian-Albian) rudists and nerineas. The Teloloapan Formation in turn grades upward into

turbiditic shales and sandstones of the early Late Cretaceous (Turonian), Pachivia Formation (Figure 2.2).

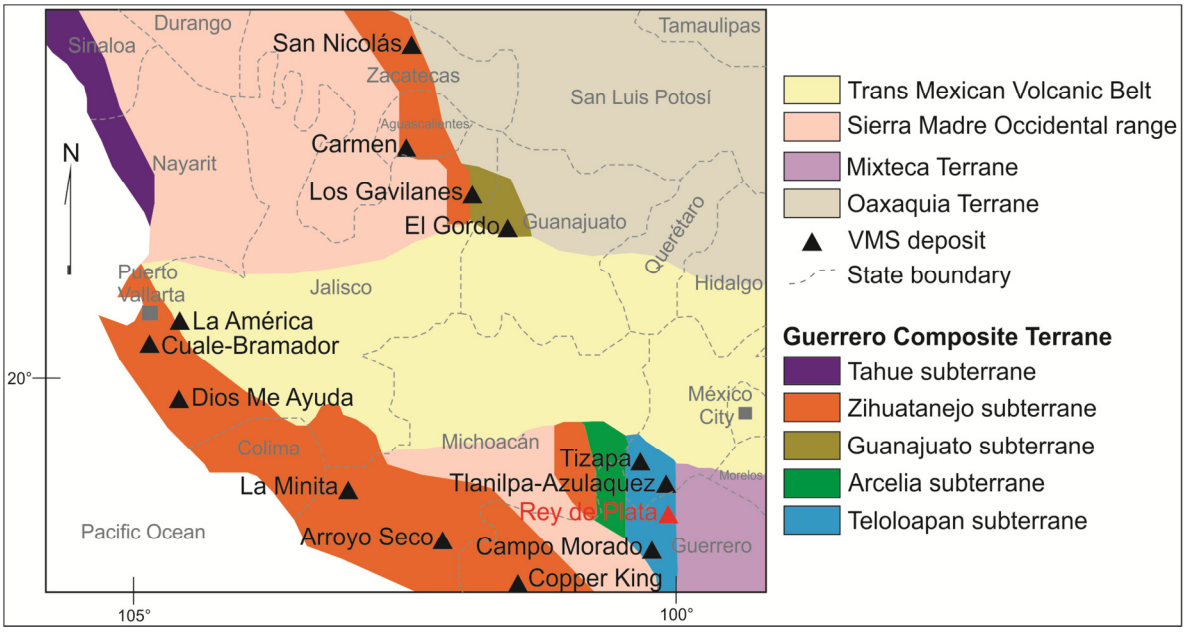

Figure 2.3. VMS deposits into the Guerrero Composite Terrane (Modified from Suastegui, et al., 2000).

In the western half of the Teloloapan subterrane, the Villa Ayala Formation formed in a deeper marine environment and consists of basaltic, andesitic and rhyolitic flows and volcaniclastic rocks. The latter contains Early Cretaceous fossil gastropods and bivalves that range in age from Hauterivian to Aptian (Guerrero-Suastegui et al. 1991, Ramirez-Espinoza et al. 1991, Talavera-Mendoza et al. 1995). Older, Late Jurassic to Early Cretaceous, U/Pb zircon ages of 139.7 ± 2.5 Ma to 157.4 ± 4.1 Ma (Oxfordian-Valanginian) were obtained from felsic rocks of the Campo Morado VMS district, which is located less than 50 km southwest of Rey de Plata (Mortensen et al. 2008). The Villa Ayala Formation is in transitional contact with the overlying late Early Cretaceous (Aptian) Acapetlahuaya Formation. The latter consists of thinly bedded greywacke, tuffaceous shale and volcaniclastic rocks (Talavera-Mendoza et al. 1995). It is in turn overlain by the Early to Late

Cretaceous (Albian-Cenomanian) Amatepec Formation, which is composed of thin-bedded, detrital, black limestone that noticeably lacks a volcanic component. The Amatepec Formation has been interpreted as a strongly deformed, deep basin succession that unconformably overlies both the Acapetlahuaya and the Villa Ayala formations. It is stratigraphically overlain by Late Cretaceous (Cenomanian) turbiditic sandstone and shale of the Miahuatepec Formation, which has been interpreted as a shallow marine sedimentary sequence that was deposited during the amalgamation of the Zihuatanejo, Arcelia and Teloloapan subterranes (Talavera-Mendoza et al. 1995, Mendoza and Suastegui 2000). The Miahuatepec Formation is correlated with the Pachivia Formation in the eastern half of the subterrane (Talavera-Mendoza et al. 1995, Mendoza and Suastegui 2000, Figure 2.2).

The Teloloapan subterrane is interpreted as an arc-backarc system (Talavera-Mendoza et al. 1995, Mendoza and Suastegui 2000, Centeno-García et al. 2008), which was constructed on older basement rocks represented by the Late Paleozoic-Early Jurassic, Tejupilco metamorphic complex. The complex consists of carbonaceous phyllite, quartzite, sericite schist, rhyolitic metatuff and mylonitic augen gneiss of granitic composition (Fries 1960, de Cserna and Fries 1981, Elías-Herrera and Sanchez-Zavala 1992). The Teloloapan subterrane is in thrust contact with metamorphosed sedimentary and arc-related volcanic and volcaniclastic rocks of the Lower Paleozoic to Middle Jurassic Mixteca Terrane to the east (Ortega-Gutiérrez 1981, de Cserna and Fries 1981, Ruíz et al. 1988, Yañez et al. 1991, Talavera-Mendoza 1993, Campa and Iriondo 2004, Figure 2.1).

Chapter 3: Stratigraphy, Geochronology and Geochemistry

3.1 Stratigraphy

This chapter presents the first stratigraphic subdivision of strata hosting the Rey de Plata deposit, as well as the first ages for the ore host rocks and younger sedimentary successions.

In the Rey de Plata deposit area, some of the Cretaceous units recognized during mapping and drilling correspond to previously recognized units that have regional correlation, but others are informal and have been defined because of their local significance within the mine area (Table 3.1). The oldest and most important regionally extensive unit is the Villa Ayala Formation, which is host to the Rey de Plata VMS deposit and the nearby Campo Morado VMS district. It has a U-Pb zircon age of 139.7 ± 2.5 Ma to 157.4 ± 4.1 Ma (Mortensen et al. 2008). Regionally, this formation comprises basaltic to andesitic and sometimes rhyolitic lava flows, and volcaniclastic rocks (Talavera-Mendoza et al. 1995, Mendoza and Suastegui 2000). However, at Rey De Plata, the Villa Ayala Formation is subdivided into three informal members, the Ahuehuetla, Rey de Plata and Villa Ayala members (Table 3.1). The Villa Ayala Formation, in the northern part of the map area is unconformably overlain by the Aptian Acapetlahuaya Formation (based on ammonoids and radiolarians, Campa et al. 1974), which had not been identified in previous work. It consists of thinly bedded greywacke, tuffaceous shale and volcaniclastics (Campa and Ramirez 1979, Talavera-Mendoza et al. 1995), whereas in the southern and west parts of the map area, it is unconformably overlain by the Cenomanian Miahuatepec Formation, which is a regionally extensive shallow marine, turbiditic succession of sandstones and shales (Guerrero-Suastegui 2004). The regionally extensive Amatepec and Teloloapan Formations, which conformably overly the Villa Ayala Formation, are absent at Rey de Plata and feldspar-phyric mafic intrusions locally occur at the unconformable contact between the Villa Ayala and Miahuatepec Formations (Figure 3.1; Table

3.1). The Miahuatepec Formation is overlain by conglomerates of the Balsas Group (Table 3.1). In the rock type descriptions that follow, the terms tuff, lapilli tuff, lapillistone and tuff breccia are use in a non-genetic sense to indicate the size of and percentage of components according to the original granulometric classification of volcaniclastic rocks as proposed by Fisher (1961) and as modified by Gibson et al. (1999) and White and Houghton (2006).

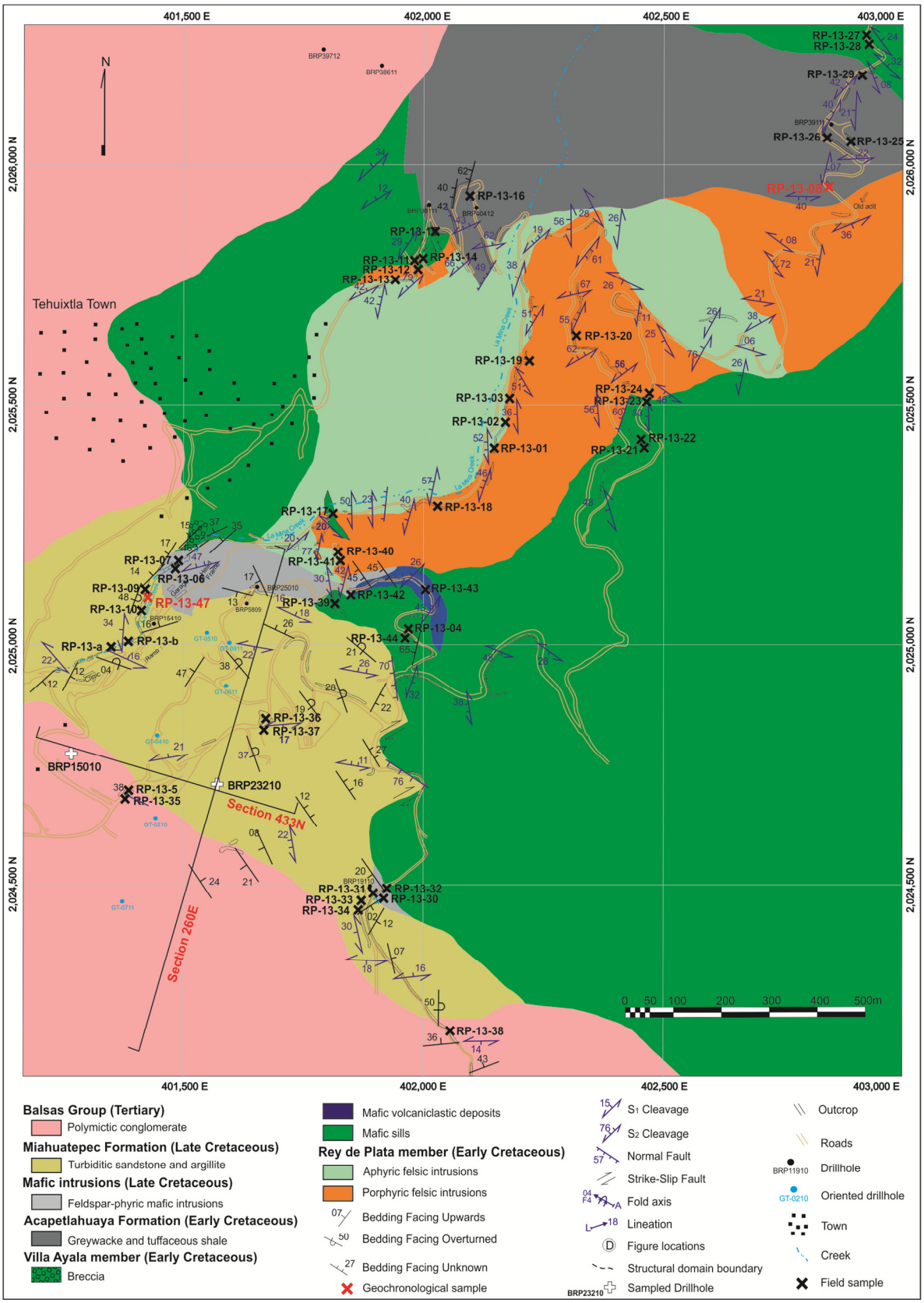

Figure 3.1. Geological map of the Rey de Plata Deposit (from this work).

Table 3.1. Comparison between regional formal and local informal stratigraphic units.

Regional Formal Stratigraphic Units	General Description	Local Informal Stratigraphic Units	General Description
Balsas Group (38.5 ± 1 Ma, K-Ar dating in biotite, Monter-Ramírez 2004).	Clast and matrix supported polymictic conglomerate, with layers of ignimbrite intercalated	Balsas Group	Clast and matrix supported polymictic conglomerate, with layers of ignimbrite intercalated. Its lower contact is erosional but sheared
Miahuatepec Formation (at least post-early Cenomanian because of its stratigraphic position, Talavera-Mendoza et al. 1995)	Composed of a turbiditic succession of sandstone and shale deposited in an erosional contact either over the Teloloapan Formation or the Amatepec Formation	Miahuatepec Formation (younger than 229 ± 5 Ma, this work)	Turbiditic succession of sandstone and shale. Contact with Villa Ayala member by an unconformity
Teloloapan Formation (Aptian to early Albian based on rudists and nerineas Guerrero-Suastegui et al. 1991)	Massive, reefal limestone, whose base consists of limestones intercalated with volcaniclastic rocks defining a transitional contact with the Villa Ayala Formation	Not present	
Amatepec Formation (late Albian to early Cenomanian, based on calcispherulids, planktonic foraminifers and radiolarians, Campa and Ramirez 1979)	Composed of thin bedded, detrital, black limestone that noticeably lacks a volcanic component. Tectonic contact at the base	Not present	
Acapetlahuaya Formation (Aptian based on ammonoids and radiolarians, Campa et al. 1974)	Composed of thinly bedded shale and volcanic sandstone. Conformable contact with the Villa Ayala Formation	Acapetlahuaya Formation (post 115 ± 4 Ma, this work)	Thinly bedded greywacke, tuffaceous shale and volcaniclastic rocks. In unconformable contact overlying both the Villa Ayala member and the Rey de Plata member
Villa Ayala Formation (139.7 ± 2.5 Ma to 157.4 ± 4.1 Ma, Mortensen et al. 2008)	Basaltic to andesitic and lesser rhyolitic lava flows, and volcaniclastic rocks.	Villa Ayala Member	Lithofacies of basaltic sills, and volcaniclastic deposits in conformable contact with the Rey de Plata member
		Rey de Plata Member. (129.4 ± 0.67 Ma to 139.1 ± 0.4 Ma, this work)	Felsic lithofacies including flows, associated breccias, volcaniclastic deposits, sills and graphitic argillites. Its contact with the Ahuehuetla member is conformable
		Ahuehuetla Member	Mafic lithofacies, including volcaniclastic deposits, basalt sills and graphitic argillite

3.2 Geochronology

3.2.1 Rey De Plata Rhyolite

Mortensen et al. (2008) determined an age for felsic volcanics and diorite at the nearby Campo Morado VMS deposit and in the Tlanilpa-Azulaquez districts of 139.7 ± 2.5 Ma to 157.4 ± 4.1 Ma. The Campo Morado VMS deposit occurs within the Villa Ayala Formation and the age of the Rey de Plata VMS deposit had been interpreted as similar (Centeno-García et al. 1993, Talavera-Mendoza et al. 1995, Mendoza and Suastegui 2000, Elías-Herrera et al. 2000). In order to determine the age of the Rey de Plata deposit a sample (RP-13-45) collected from drill core that intersected an aphyric rhyolitic flow located in the immediate footwall to massive sulfide mineralization. The sample was sent to the Jack Satterly Geochronology Laboratory at the Department of Geology, University of Toronto, for high-precision U-Pb zircon dating using thermal-ionization mass spectroscopy (TIMS).

Initial results, as those of Mortensen et al. (2008), are a little scattered as shown in a preliminary concordia plot (Figure 3.2) and the $^{206}Pb/^{238}U$ ages (which are the more accurate ones to cite in this age range) span 139.1 to 129.4 Ma. Although more zircon grains will need to be analyzed to determine a magmatic age for the rhyolite and, therefore, the Rey de Plata VMS deposit the data can be interpreted in three ways.

First, an interpretation would be to assume that some or all the results reflect inheritance, as Mortensen et al. (2008) reported significantly older xenocrystic zircons in their work. Given that all the analysis of the Rey de Plata rhyolite represent single grain fractions it may be that the 129 Ma fraction is magmatic, and that the two older ages, which are concordant within error, are zircons that may be inherited from underlying, but only slightly older volcanic rocks.

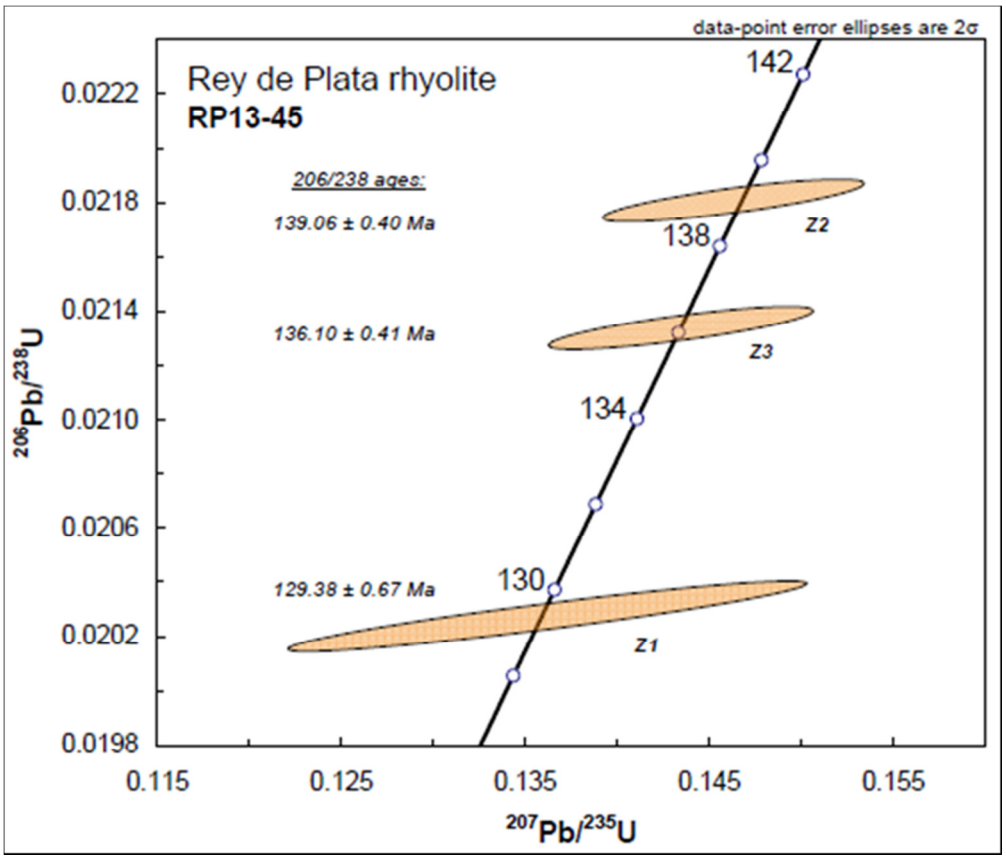

Figure 3.2. Preliminary Concordia plot of $^{206}Pb/^{238}U$ zircon ages for an aphyric rhyolitic flow within the Rey de Plata member.

Second, all of the analyses have undergone Pb-loss. However, because all fractions appear to be close to concordant a Pb-loss event would not be much younger than 129 Ma (short-track secondary Pb-loss track that is subparallel to the Concordia curve); however, a zero-aged, modern day Pb-loss path may look similar. In any case, if all the fractions show Pb-loss, even the oldest must be regarded as representing a minimum age. Thus, the true age could be older than 139 Ma, though presumably not by much.

Third, the oldest zircon fraction is magmatic and the two younger fractions could be interpreted as showing Pb-loss. If this is the case then the magmatic age for the rhyolite may be 139.1 Ma. In this regard it is important to note that Mortensen et al. (2008) reported U-Pb zircon lower intercepts or interpreted concordant magmatic ages between ca. 139-145 Ma for felsic volcanics at Campo Morado and the

Tlanilpa-Azulaquez districts, and they did not interpret any igneous ages younger than 138 Ma. The ages reported by Mortensen et al. (2008) and the occurrence of Hauterivian to Aptian (133-112 Ma) gastropods and bivalves in uppermost strata of the Villa Ayala Formation (Guerrero-Suastegui et al. 1991, Ramirez-Espinoza et al. 1991, Talavera-Mendoza et al. 1995), support this interpretation and a 139.1 Ma age for the Rey de Plata rhyolite and VMS deposit. Additional zircon fractions will be analyzed to test these interpretations.

3.2.2 LA-ICP-MA Zircon Geochronology of Sedimentary Units

Previous interpretations have grouped tuffaceous shale and volcaniclastics that appear to conformably overly the Rey de Plata member with Cenomanian (93.9-100 Ma; Talavera-Mendoza et al. 1995) turbiditic sedimentary rocks of the Miahuatepec Formation. In order to determine if these two sedimentary units represent facies variations within the Miahuatepec Formation, or if they are separate units of different age and provenance, a sample of each unit (RP-13-8, and RP-13-47 in Figure 3.1) were analyzed at the Department of Earth Sciences, Laurentian University, LA-ICP-MS facility to determine the U-Pb ages for zircons from each sample. LA-ICP-MS data (and ages) for individual zircons analyzed from each sample are contained in Tables 3.2 and 3.3, and in concordia and age distribution diagrams as illustrated in Figures 3.3 and 3.4. A $^{206}Pb/^{238}$ U age was used, as it is more precise for young zircons; however, the ages may not be accurate if significant Pb loss has occurred. A multi-gaussian peak fitting routine was performed on the younger ages to distinguish the most meaningful populations (Petrus, 2012, Figures 3.5 and 3.6).

An age distribution diagram for zircon ages from argillaceous sediments that overly the Rey de Plata member (RP-13-8) is shown in Figure 3.3, which show the entire zircon population analyzed and in Figure 3.5, which focuses on the youngest ages. From Figure 3.3, it apparent that only a few zircons yielded ages greater than 500 Ma, and the most significant age populations range from 115 ± 4 Ma to 152 ± 4

Ma, with the majority <140 Ma. In contrast, zircons from the Miahuatepec Formation (RP-13-47) yielded ages from 200 Ma to 1200 Ma, with the most significant populations occurring between 800-1200 Ma, and a smaller population from 200 to 300 Ma; there are no zircon ages < 200 Ma (Figures 3.4, 3.6).

The results suggest that volcanic rocks of the Villa Ayala formation (139.1 Ma) were the main source of zircons (115 – 152 Ma) for the fine argillaceous sediments that appear to unconformably overly the Rey de Plata and the Villa Ayala members. A dominantly local, volcanic provenance for the argillaceous sediments is consistent with the fine, euhedral morphology of the zircons (Figure 3.7). The age distribution of zircons from the argillaceous sediments at Rey de Plata is consistent with sediments of the Acapetlahuaya Formation (Aptian age based on ammonoids and radiolarians, Campa et al. 1974) with which, herein, they are tentatively correlated. Although the age distribution for zircons of the Miahuatepec Formation indicates a large provenance area, consistent with the variable size and high degree of rounding displayed by the zircons (Figure 3.8), two main populations can be distinguished. The largest zircon population spans an age interval between 800 to 1200 Ma, which is consistent with their derivation from Proterozoic rocks of the microcontinent Oaxaquia (Ortega-Gutiérrez et al. 1995) located about 300km north-northeast from the Rey de Plata deposit. The second zircon population spans an age interval between 200 to 300 Ma and may have been derived from the Mixteca Terrane located about 50km to the East, which contains rock sequences that range from Lower Paleozoic to Middle Jurassic in age (Elías-Herrera and Ortega-Gutiérrez 2002, Keppie et al. 2006, Centeno-García et al. 2011). Both sources suggest the presence of a pre-Cretaceous basin on the east side of the arc-volcanic sequence of the Villa Ayala Formation, which received sediments from continent and from volcanic arcs, and constitutes the easternmost sedimentary sequence of the Teloloapan Terrane.

Table 3.2. LA-ICP-MS data (and ages) for individual zircons analyzed from sample RP-13-8.

Identifier	Compositional Data [ppm]				Ratios							Ages [Ma]					
	Pb	U	Th	U/Th	$^{207}Pb/^{235}U$	2σ	$^{206}Pb/^{235}U$	2σ	rho	$^{207}Pb/^{206}Pb$	2σ	$^{207}Pb/^{235}U$	2σ	$^{206}Pb/^{235}U$	2σ	$^{207}Pb/^{206}Pb$	2σ
RP_13_8/1	3.4	114.7	52.5	2.2	0.162	0.017	0.0206	0.00074	0.07	0.0571	0.0069	153	15	132	5	495	247
RP_13_8/2	25.8	662.3	392.0	1.7	0.177	0.010	0.0242	0.00075	0.51	0.0531	0.0023	166	8	154	5	332	94
RP_13_8/3	12.4	530.0	185.6	2.9	0.153	0.008	0.0229	0.00043	0.40	0.0483	0.0023	144	7	146	3	114	108
RP_13_8/4	14.2	251.7	61.3	4.1	0.642	0.029	0.0851	0.00147	0.04	0.0547	0.0026	504	18	526	9	401	103
RP 13 8/5	7.2	350.5	120.1	2.9	0.153	0.011	0.0227	0.00046	0.23	0.0487	0.0038	144	10	145	3	136	176
RP_13_8/6	26.8	585.9	299.5	2.0	0.157	0.010	0.0238	0.00060	0.21	0.0479	0.0031	148	9	152	4	92	147
RP 13 8/7	13.3	707.3	237.2	3.0	0.143	0.008	0.0209	0.00034	0.35	0.0494	0.0024	135	7	134	2	168	111
RP 13 8/8	8.6	416.2	120.5	3.5	0.160	0.011	0.0231	0.00062	0.22	0.0504	0.0032	151	10	147	4	215	143
RP 13 8/9	24.5	740.2	419.6	1.8	0.136	0.009	0.0207	0.00042	0.39	0.0477	0.0031	130	8	132	3	85	148
RP_13_8/10	18.5	457.7	360.5	1.3	0.127	0.010	0.0191	0.00041	0.00	0.0483	0.0042	122	9	122	3	112	194
RP 13 8/11	4.6	164.1	70.1	2.3	0.149	0.019	0.0211	0.00066	0.07	0.0512	0.0079	141	17	135	4	248	321
RP 13 8/12	16.8	680.9	305.3	2.2	0.139	0.009	0.0206	0.00031	0.18	0.0490	0.0028	132	8	132	2	146	128
RP_13_8/13	8.1	360.2	85.0	4.2	0.239	0.026	0.0318	0.00136	-0.03	0.0545	0.0057	217	21	202	8	391	220
RP 13 8/14	8.1	230.1	141.4	1.6	0.132	0.014	0.0202	0.00043	0.26	0.0475	0.0054	126	13	129	3	72	252
RP 13 8/15	2.6	123.0	56.4	2.2	0.153	0.036	0.0192	0.00118	-0.13	0.0580	0.0181	145	31	122	7	529	567
RP_13_8/16	6.7	203.3	107.2	1.9	0.160	0.025	0.0228	0.00095	0.12	0.0509	0.0077	151	22	145	6	237	315
RP_13_8/17	26.7	1421.1	504.3	2.8	0.126	0.005	0.0193	0.00026	0.44	0.0476	0.0018	121	5	123	2	77	90
RP_13_8/18	41.9	278.6	86.3	3.2	1.839	0.068	0.1740	0.00272	-0.02	0.0766	0.0030	1059	24	1034	15	1112	77
RP_13_8/19	9.2	239.6	132.6	1.8	0.190	0.023	0.0284	0.00110	0.29	0.0485	0.0062	176	20	180	7	125	278
RP_13_8/20	4.0	136.9	63.4	2.2	0.133	0.019	0.0191	0.00065	-0.07	0.0503	0.0075	127	17	122	4	209	315
RP_13_8/21	20.7	614.4	348.7	1.8	0.136	0.007	0.0212	0.00043	0.27	0.0467	0.0022	130	6	135	3	33	110
RP 13 8/22	3.8	251.9	49.2	5.1	0.206	0.023	0.0315	0.00180	0.52	0.0473	0.0051	190	20	200	11	65	236
RP 13 8/23	23.9	750.7	450.6	1.7	0.141	0.008	0.0195	0.00034	0.27	0.0526	0.0026	134	7	124	2	312	110
RP 13 8/24	34.7	1650.9	637.7	2.6	0.128	0.005	0.0206	0.00030	0.50	0.0451	0.0019	122	5	131	2	175	81
RP 13 8/25	29.3	1172.4	441.9	2.7	0.147	0.007	0.0207	0.00050	0.42	0.0516	0.0022	139	6	132	3	266	97
RP_13_8/26	6.6	208.9	121.2	1.7	0.184	0.030	0.0179	0.00076	-0.05	0.0743	0.0152	171	25	115	5	1050	366
RP 13 8/27	10.0	522.4	173.8	3.0	0.159	0.020	0.0211	0.00042	-0.05	0.0544	0.0062	149	17	135	3	389	239
RP_13_8/28	6.9	229.2	110.2	2.1	0.140	0.017	0.0212	0.00071	0.31	0.0477	0.0062	133	15	135	4	87	282
RP 13 8/29	10.6	379.8	195.4	1.9	0.120	0.009	0.0183	0.00047	0.06	0.0475	0.0041	115	8	117	3	74	191
RP 13 8/30	10.1	373.4	156.3	2.4	0.136	0.011	0.0205	0.00055	0.29	0.0480	0.0043	129	10	131	4	97	198
RP 13 8/31	8.9	232.1	150.7	1.5	0.170	0.031	0.0213	0.00077	0.23	0.0578	0.0106	159	27	136	5	524	359
RP_13_8/32	33.1	106.6	106.4	1.0	0.930	0.107	0.1008	0.00337	0.10	0.0669	0.0056	668	55	619	20	835	164
RP_13_8/33	20.6	1035.2	311.3	3.3	0.144	0.006	0.0209	0.00055	-0.03	0.0500	0.0021	136	6	133	3	196	97
RP 13 8/34	6.9	234.4	114.7	2.0	0.147	0.015	0.0206	0.00062	0.04	0.0517	0.0051	139	13	131	4	273	213
RP_13_8/35	12.1	69.4	36.6	1.9	1.024	0.073	0.1204	0.00379	0.33	0.0617	0.0041	716	36	733	22	663	137
RP_13_8/36	13.4	475.0	200.1	2.4	0.157	0.010	0.0210	0.00039	-0.03	0.0540	0.0042	148	9	134	2	372	166
RP 13 8/37	20.3	637.1	358.8	1.8	0.142	0.008	0.0206	0.00035	0.25	0.0499	0.0029	135	7	132	2	192	130
RP_13_8/38	14.1	345.5	251.5	1.4	0.141	0.011	0.0212	0.00049	0.14	0.0485	0.0037	134	10	135	3	122	169
RP 13 8/39	35.1	1293.1	602.7	2.1	0.148	0.006	0.0200	0.00039	0.21	0.0536	0.0027	140	6	128	2	356	109
RP_13_8/40	41.5	812.3	771.3	1.1	0.137	0.007	0.0198	0.00042	0.39	0.0501	0.0023	130	6	126	3	198	105
RP_13_8/41	41.9	1278.5	645.6	2.0	0.142	0.018	0.0203	0.00095	0.34	0.0507	0.0060	134	16	129	6	227	253
RP_13_8/42	10.4	489.1	144.2	3.4	0.138	0.011	0.0195	0.00054	0.11	0.0512	0.0052	131	10	125	3	251	217
RP_13_8/43	10.5	469.4	180.9	2.6	0.132	0.009	0.0206	0.00056	0.03	0.0463	0.0036	126	8	132	4	15	178

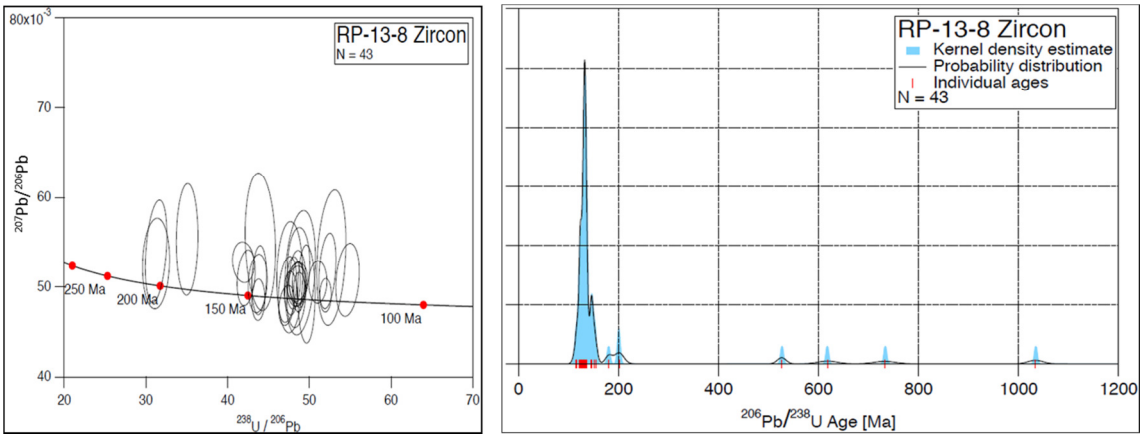

Figure 3.3. Concordia and age distribution diagrams for sample RP-13-8.

Table 3.3. LA-ICP-MS data (and ages) for individual zircons analyzed from sample RP-13-47.

	Compositional Data [ppm]				Ratios							Ages [Ma]					
Identifier	Pb	U	Th	U/Th	$^{207}Pb/^{235}U$	2σ	$^{206}Pb/^{235}U$	2σ	rho	$^{207}Pb/^{206}Pb$	2σ	$^{207}Pb/^{235}U$	2σ	$^{206}Pb/^{235}U$	2σ	$^{207}Pb/^{206}Pb$	2σ
RP_13_47/1	42.9	257.7	95.9	2.7	1.562	0.056	0.1586	0.0031	0.36	0.0714	0.0024	955	22	949	17	969	68
RP_13_47/2	14.6	75.5	33.5	2.3	1.581	0.068	0.1588	0.0032	0.06	0.0722	0.0032	963	27	950	18	992	89
RP_13_47/3	14.6	146.8	121.1	1.2	0.282	0.026	0.0390	0.0008	0.03	0.0524	0.0048	252	21	247	5	304	197
RP_13_47/4	42.9	176.0	109.4	1.6	1.577	0.038	0.1565	0.0015	0.03	0.0731	0.0018	961	15	937	8	1017	49
RP_13_47/5	42.9	244.4	153.2	1.6	0.975	0.029	0.1042	0.0019	0.14	0.0679	0.0018	691	15	639	11	866	55
RP_13_47/6	11.4	128.2	26.6	4.8	1.682	0.048	0.1625	0.0016	0.00	0.0751	0.0022	1002	18	971	9	1071	58
RP_13_47/7	36.0	206.5	91.2	2.3	1.583	0.059	0.1598	0.0026	0.12	0.0718	0.0028	963	23	956	14	981	77
RP_13_47/8	48.9	481.8	470.3	1.0	0.284	0.014	0.0404	0.0012	0.59	0.0510	0.0021	254	11	255	7	241	91
RP_13_47/9	58.2	239.8	130.6	1.8	1.614	0.054	0.1579	0.0027	0.13	0.0741	0.0029	976	21	945	15	1045	76
RP_13_47/10	54.7	481.5	159.6	3.0	1.495	0.031	0.1435	0.0023	0.37	0.0755	0.0015	928	13	865	13	1083	38
RP_13_47/11	61.4	372.8	300.8	1.2	0.613	0.019	0.0762	0.0009	0.19	0.0583	0.0018	485	12	473	5	541	65
RP_13_47/12	11.6	207.4	115.1	1.8	0.259	0.014	0.0364	0.0007	0.17	0.0516	0.0028	234	11	231	5	269	119
RP_13_47/13	10.6	133.6	109.2	1.2	0.255	0.017	0.0367	0.0007	0.03	0.0504	0.0035	231	14	232	5	213	155
RP_13_47/14	128.2	779.2	283.2	2.8	1.689	0.025	0.1688	0.0016	0.57	0.0726	0.0009	1004	9	1006	9	1002	24
RP_13_47/15	2.8	49.2	20.3	2.4	0.955	0.059	0.0930	0.0037	0.66	0.0745	0.0033	681	30	573	22	1054	87
RP_13_47/16	12.9	110.8	40.8	2.7	1.330	0.045	0.1346	0.0017	0.23	0.0717	0.0023	859	19	814	10	977	64
RP_13_47/17	33.4	152.0	100.9	1.5	1.503	0.068	0.1391	0.0025	0.48	0.0784	0.0034	932	27	840	14	1156	84
RP_13_47/18	17.2	216.3	57.1	3.8	1.187	0.028	0.1220	0.0015	0.31	0.0705	0.0017	795	13	742	9	944	49
RP_13_47/19	22.5	117.8	55.0	2.1	1.728	0.048	0.1571	0.0018	0.19	0.0798	0.0020	1019	18	940	10	1192	48
RP_13_47/20	33.6	182.0	62.5	2.9	2.016	0.067	0.1860	0.0032	0.01	0.0786	0.0028	1121	22	1099	18	1162	70
RP_13_47/21	111.0	255.4	190.0	1.3	1.980	0.051	0.1883	0.0027	0.33	0.0763	0.0021	1109	17	1112	15	1103	53
RP_13_47/22	59.9	669.6	574.8	1.2	0.245	0.011	0.0357	0.0005	0.16	0.0498	0.0022	223	9	226	3	186	102
RP_13_47/23	64.3	309.6	159.6	1.9	1.547	0.031	0.1502	0.0014	0.31	0.0747	0.0014	949	12	902	8	1061	38
RP_13_47/24	36.8	188.9	74.7	2.5	2.411	0.091	0.2053	0.0039	0.64	0.0852	0.0024	1246	27	1204	21	1320	54
RP_13_47/25	16.3	84.2	52.9	1.6	1.409	0.049	0.1292	0.0023	0.43	0.0791	0.0025	893	21	783	13	1174	60
RP_13_47/26	26.7	228.4	85.5	2.7	1.234	0.029	0.1196	0.0016	0.31	0.0748	0.0017	816	13	728	9	1064	46
RP_13_47/27	6.9	190.7	48.5	3.9	0.345	0.021	0.0475	0.0008	0.21	0.0526	0.0031	301	16	299	5	310	129
RP_13_47/28	15.1	102.5	41.5	2.5	1.370	0.046	0.1405	0.0017	0.10	0.0707	0.0023	876	19	847	9	950	67
RP_13_47/29	16.7	66.8	55.8	1.2	1.170	0.057	0.1162	0.0033	0.47	0.0730	0.0031	786	26	708	19	1015	83
RP_13_47/30	12.1	54.4	28.3	1.9	1.557	0.079	0.1597	0.0023	0.22	0.0707	0.0036	953	31	955	13	949	101
RP_13_47/31	18.8	224.4	183.9	1.2	0.248	0.013	0.0361	0.0006	-0.09	0.0497	0.0028	225	10	229	3	181	127
RP_13_47/32	16.2	215.5	143.8	1.5	0.289	0.019	0.0388	0.0009	0.15	0.0541	0.0037	258	15	245	6	373	148
RP_13_47/33	77.1	164.0	189.8	0.9	1.605	0.046	0.1559	0.0026	0.34	0.0747	0.0020	972	18	934	14	1060	53
RP_13_47/34	15.1	60.9	36.7	1.7	1.613	0.080	0.1489	0.0032	0.06	0.0786	0.0037	975	31	895	18	1162	91
RP_13_47/35	24.9	42.6	55.5	0.8	1.871	0.071	0.1735	0.0027	0.12	0.0782	0.0031	1071	25	1032	15	1152	76
RP_13_47/36	12.5	88.2	27.7	3.2	1.552	0.059	0.1556	0.0026	0.57	0.0724	0.0023	951	23	932	14	996	63
RP_13_47/37	11.2	166.6	103.5	1.6	0.281	0.017	0.0390	0.0008	-0.04	0.0523	0.0029	252	13	246	5	300	123
RP_13_47/38	37.8	249.8	84.0	3.0	1.590	0.039	0.1584	0.0024	0.49	0.0728	0.0016	966	15	948	13	1009	44
RP_13_47/39	57.2	278.7	109.8	2.5	1.993	0.047	0.1885	0.0030	0.30	0.0767	0.0017	1113	16	1113	16	1114	44
RP_13_47/40	40.5	237.7	95.5	2.5	1.475	0.060	0.1468	0.0019	0.40	0.0729	0.0029	920	24	883	10	1011	79
RP_13_47/41	47.4	281.0	102.8	2.7	1.588	0.044	0.1587	0.0023	0.08	0.0726	0.0021	966	17	949	13	1002	58
RP_13_47/42	6.2	151.9	53.1	2.9	0.315	0.017	0.0418	0.0007	0.37	0.0547	0.0031	278	13	264	5	398	121
RP_13_47/43	58.8	315.8	148.8	2.1	1.628	0.034	0.1569	0.0018	0.55	0.0752	0.0012	981	13	940	10	1074	33
RP_13_47/44	2.2	33.6	16.3	2.1	0.297	0.052	0.0395	0.0017	-0.08	0.0546	0.0111	264	40	250	11	395	402
RP_13_47/45	18.8	114.2	36.2	3.2	1.815	0.063	0.1750	0.0023	0.21	0.0752	0.0028	1051	23	1040	13	1074	74
RP_13_47/46	14.9	153.9	36.0	4.3	1.255	0.050	0.1381	0.0022	0.42	0.0660	0.0022	826	22	834	12	805	69
RP_13_47/47	46.6	206.6	112.7	1.8	1.596	0.041	0.1581	0.0019	0.35	0.0732	0.0018	969	16	946	10	1020	50
RP_13_47/48	54.2	251.9	167.7	1.5	1.342	0.035	0.1388	0.0015	0.33	0.0702	0.0018	864	15	838	8	933	51

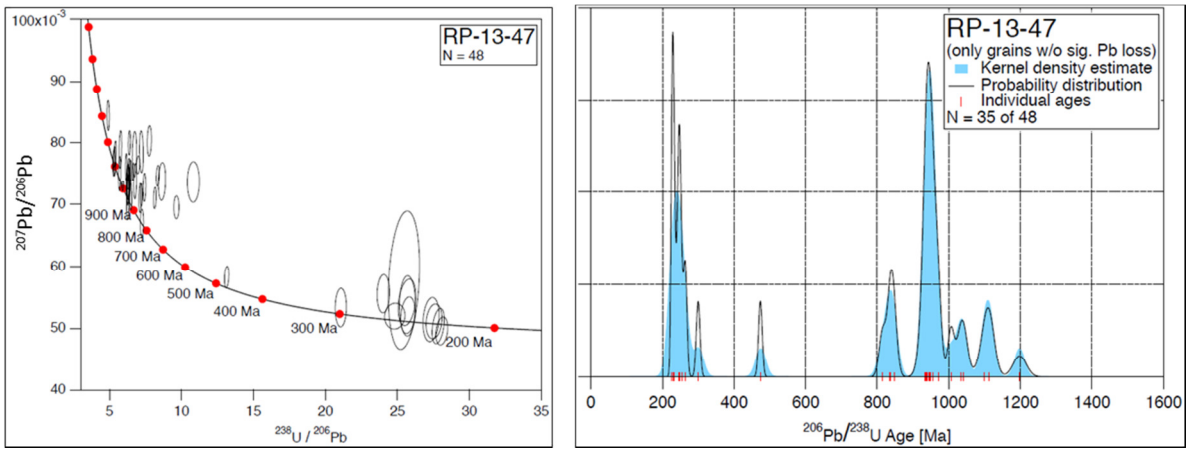

Figure 3.4. Concordia and age distribution diagrams for sample RP-13-47.

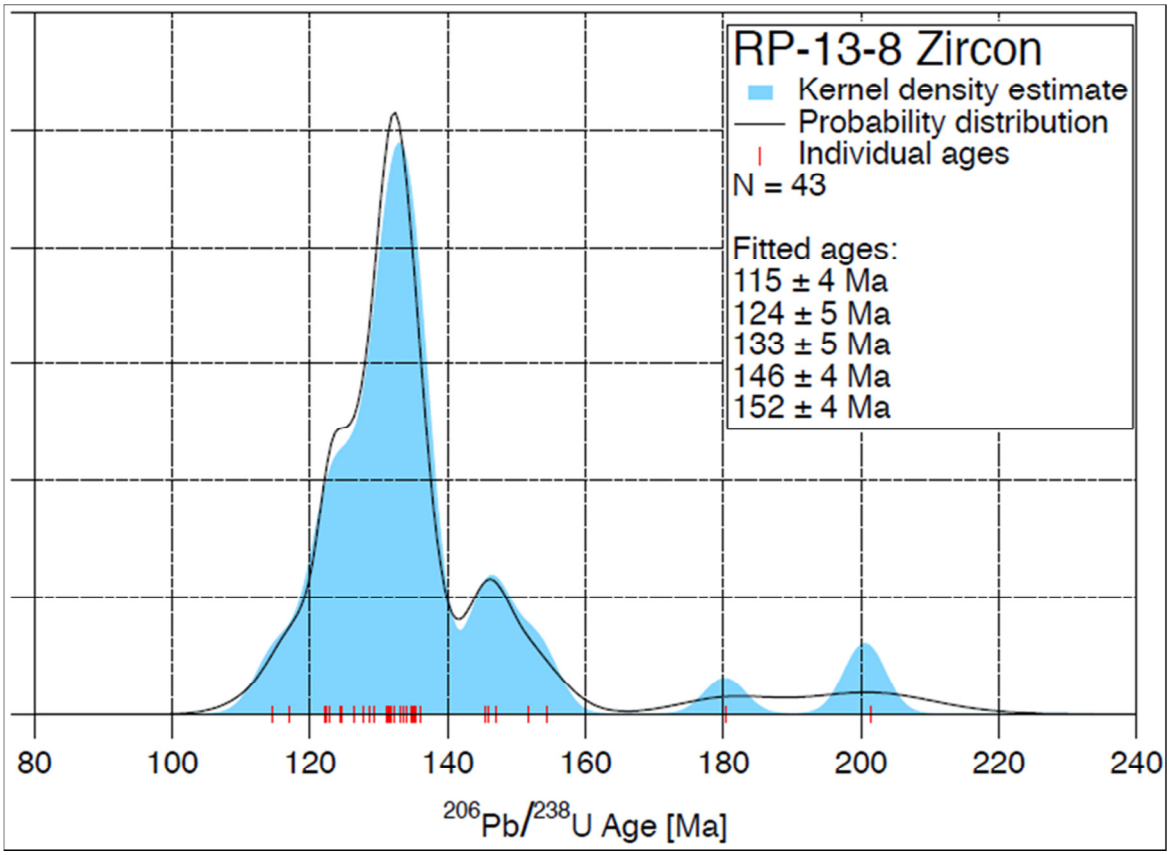

Figure 3.5. Multi-gaussian peak fitting for younger zircon ages in sample RP-13-8.

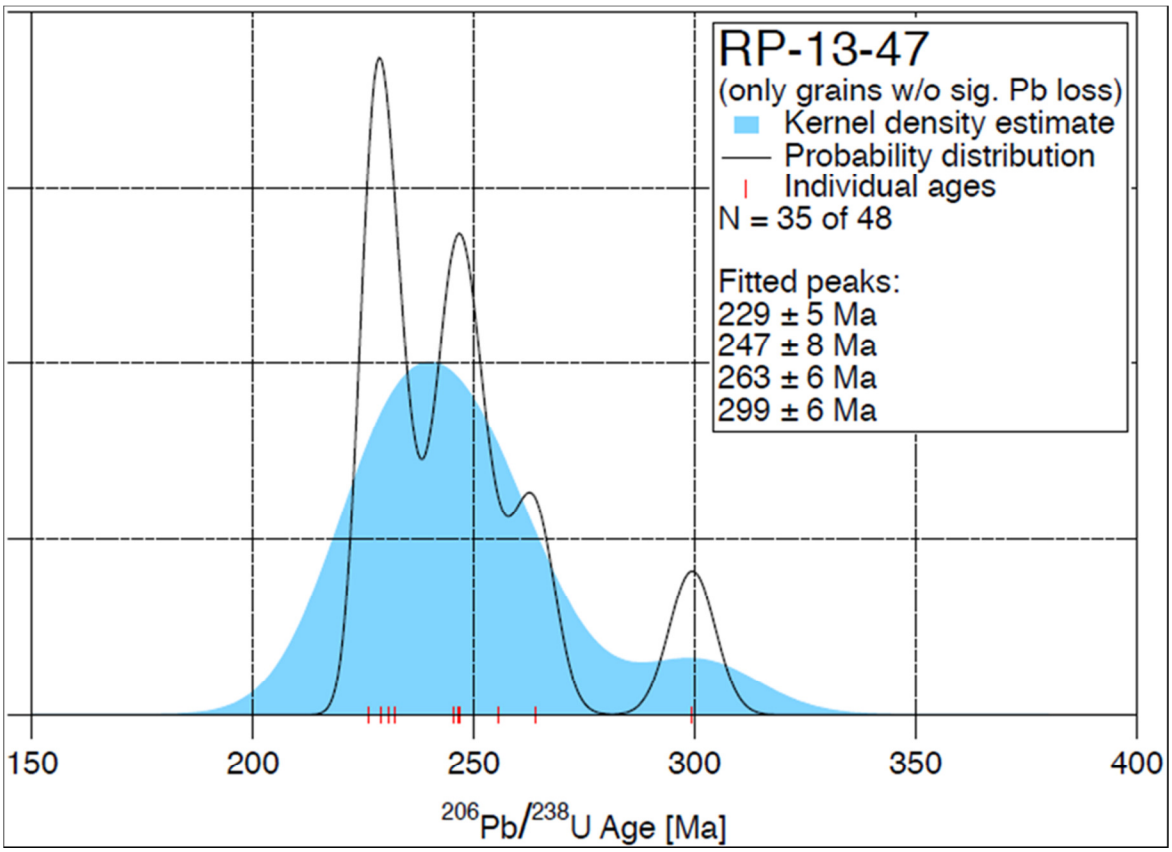

Figure 3.6. Multi-gaussian peak fitting for younger zircon ages in sample RP-13-47.

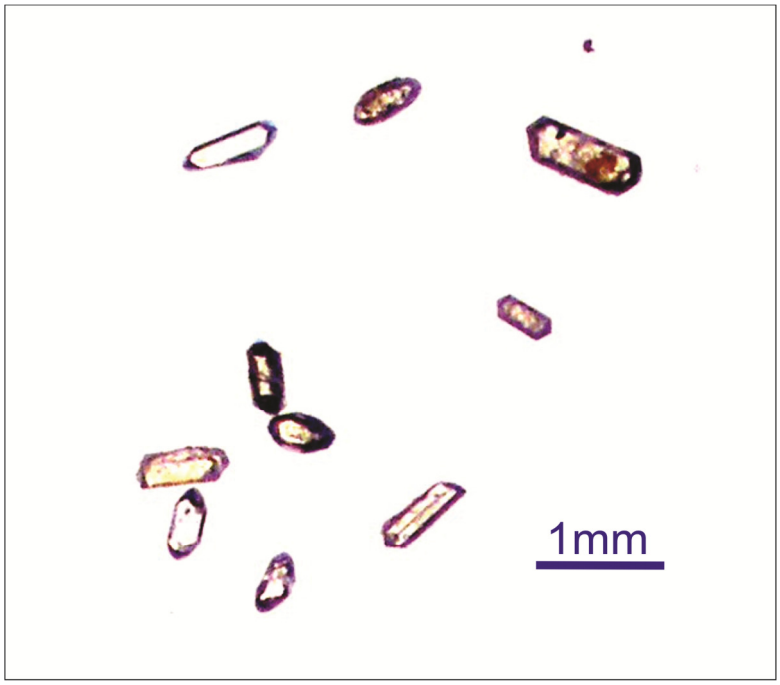

Figure 3.7. Euhedral zircons from sample RP-13-8.

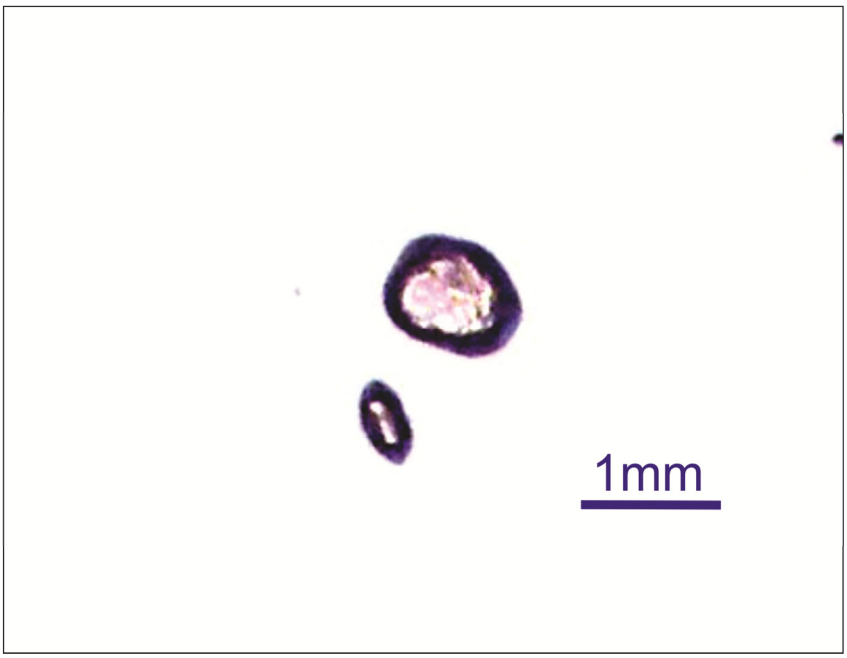

Figure 3.8. Rounded zircons from sample RP-13-47.

3.3 Villa Ayala Formation

The Villa Ayala Formation, at Rey de Plata, is divided into a basal mafic Ahuehuetla member that does not out crop and is of unknown thickness, which is conformably overlain by the felsic Rey de Plata member (30m to 250m in thickness), which in turn is conformably overlain by the mafic Villa Ayala member (200m to 250m in thickness; Figure 3.1 and Table 3.1). The volcano-sedimentary succession plunges shallowly towards the southwest at 11° to 19°. The Rey de Plata member hosts the VMS ore bodies.

3.3.1 Ahuehuetla member

The Ahuehuetla member consists of mafic volcaniclastic, intrusive and sedimentary lithofacies. It differs from the younger mafic Villa Ayala member in that the mafic volcaniclastic lithofacies are coarser volcanic breccias. This member does not outcrop, and it is defined solely on the basis of drill core. The basal contact of this unit is not observed so its total thickness is unknown. The contact with the

overlying Rey de Plata member although conformable, is locally sheared and tectonic.

3.3.1.1 Volcaniclastic Lithofacies

Volcanic breccias consist of up to 85% angular to rounded mafic, graphitic argillite, and scoria fragments and fragments of plagioclase phenocrysts within a finer (<2mm), mafic tuff matrix. Clast size ranges from 0.5cm to 10cm and beds commonly show normal gradating. The contacts with other volcaniclastic lithofacies are transitional, especially where are in contact with lapilli tuffs and graphitic argillites. Moderate to intense chlorite ± epidote alteration is the most common alteration type, although there are intervals that display weak argillic alteration. Veinlets of quartz, calcite and ankerite are common (Figure 3.9).

3.3.1.2 Lapilli Tuffs

Lapilli tuffs contain up to 30% lapilli sized fragments of scoria and subangular fragments of graphitic argillite, amygdular basalt, and plagioclase phenocrysts within a mafic, tuff-sized (<2mm) matrix. Lapilli and occasional blocks range in size from 2mm to 60mm. The volcaniclastic deposits are commonly intercalated with graphitic argillite beds up to 1m thick, especially close to the upper contact with the Rey de Plata member and the occurrence of either quartz or calcite veinlets is common. Contacts with mafic sills are sharp, but are transitional where peperite occurs at the contact (Figure 3.10).

Figure 3.9. Heterolitic mafic volcanic breccia, moderately sized sorted and poorly bedded.

3.3.1.3 Graphitic Argillites

Intervals of black graphitic argillite are thinly laminated and occur as thin units (1 to 5mm thick), but can attain thicknesses of up to 3 meters where interlayered with lapilli tuff near the contact with the overlying Rey de Plata member. The contact with lapilli tuff is typically transitional (Figure 3.11).

3.3.1.4 Mafic Sills

Mafic sills are massive, aphanitic, aphyric or plagioclase porphyritic and contain amygdules filled by quartz, calcite or epidote. Thicknesses range from 10cm up to few meters and they intrude lapilli tuffs and breccias. Moderate to intense chlorite ± epidote alteration is characteristic of these rocks. Contacts with volcaniclastic lithofacies are typically sharp, but are transitional where peperite occurs at the

contact. Veins and veinlets of quartz, calcite and ankerite are common and usually range from 0.5cm to 20cm in width (Figure 3.12).

Figure 3.10. Well bedded mafic lapilli tuffs intercalated with black argillite.

3.3.2 Rey de Plata member

The Rey de Plata member is, economically, the most important member because it contains VMS deposits that were mined, or that are currently under development for mining. The member comprises felsic flows/domes, sills and volcaniclastic lithofacies, the latter intercalated with lesser intervals of black graphitic argillite. Contacts with the underlying and overlying Ahuehuetla and Villa Ayala members appear to be conformable, but are locally defined by shear zones.

Intense to moderate quartz ± sericite ± pyrite alteration affects all felsic lithofacies, which commonly display a strong penetrative foliation. Outcrops of this member are well exposed in the north-central and northeast portion of the map (Figure 3.1),

and drilling indicates that the member extends to the south below the Villa Ayala member and Miahuatepec Formation. Drilling indicates that the thickness of the Rey de Plata member is variable and that significant variations in thickness occur over a limited strike length. For example, the member averages about 30m in thickness to the east and northeast, but is up to 250m thick to the west and southwest (Figures 3.13, 3.14). Quartz ± calcite veins and veinlets that crosscut the foliation and whose thickness range from 5mm to 15cm commonly occur in this member. These veins contain coarse euhedral pyrite ± sphalerite ± galena, and are often anomalous in their precious metal content (Figure 3.15).

Figure 3.11. Thinly bedded to laminated black graphitic argillite intercalated with mafic lapilli tuff of the Ahuehuetla member.

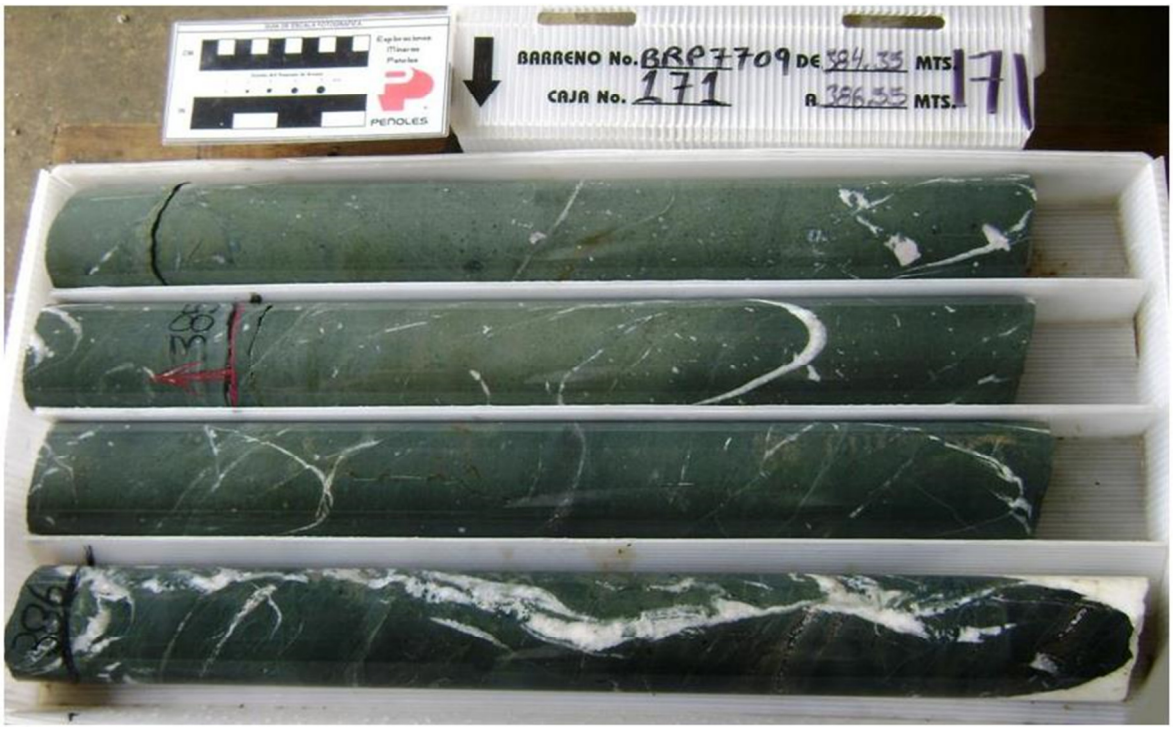

Figure 3.12. Massive, aphanitic mafic sill.

3.3.2.1 Felsic flows/domes

Felsic flows or domes up to 25m in thickness are aphanitic or contain quartz phenocrystals up to 4mm in size with occasional devitrified spherulitic intervals. This lithofacies is typically altered to a sericite ± quartz ± pyrite assemblage. Veins and veinlets which range in width from 3mm to 10cm and are typically banded with quartz ± pyrite ± honey sphalerite cross-cut the pervasive foliation developed in this lithofacies. Contacts are commonly sharp, but are gradational where in contact with in situ breccia and poorly sorted, non-bedded, monolithic breccia (Figure 3.15). A core sample (RP-13-45) located in the immediate footwall to massive sulfide mineralization from the drill hole BRP15010 drillhole yielded a U-Pb zircon age of 139 Ma +/-0.4 Ma, which is within the age range of zircons from felsic volcanic rocks at the Campo Morado VMS district, located 60km to the southwest, which yielded U-Pb zircon ages ranging from 139.7 ± 2.5 Ma to 157.4 ± 4.1 Ma (Mortensen et. al, 2008).

3.3.2.2 Felsic Sills

The felsic sills are quartz porphyritic or aphyric massive intrusions. The porphyritic sills contain sporadic quartz phenocrysts (up to 6mm). However, due to intense weathering and alteration, it was not possible to distinguish if these lithofacies constituted sills or flows (see Figure 3.1 where light green corresponds to aphyric intrusions and orange represents porphyritic intrusions). The intensity of quartz + sericite ± pyrite alteration increases with proximity to the ore bodies. Contacts with other rocks are commonly sharp, although sometimes peperite occurs where in contact with volcaniclastic or argillaceous sedimentary rocks. Contacts are commonly sheared due to the regional deformation that is manifest by a penetrative foliation (Figure 3.16).

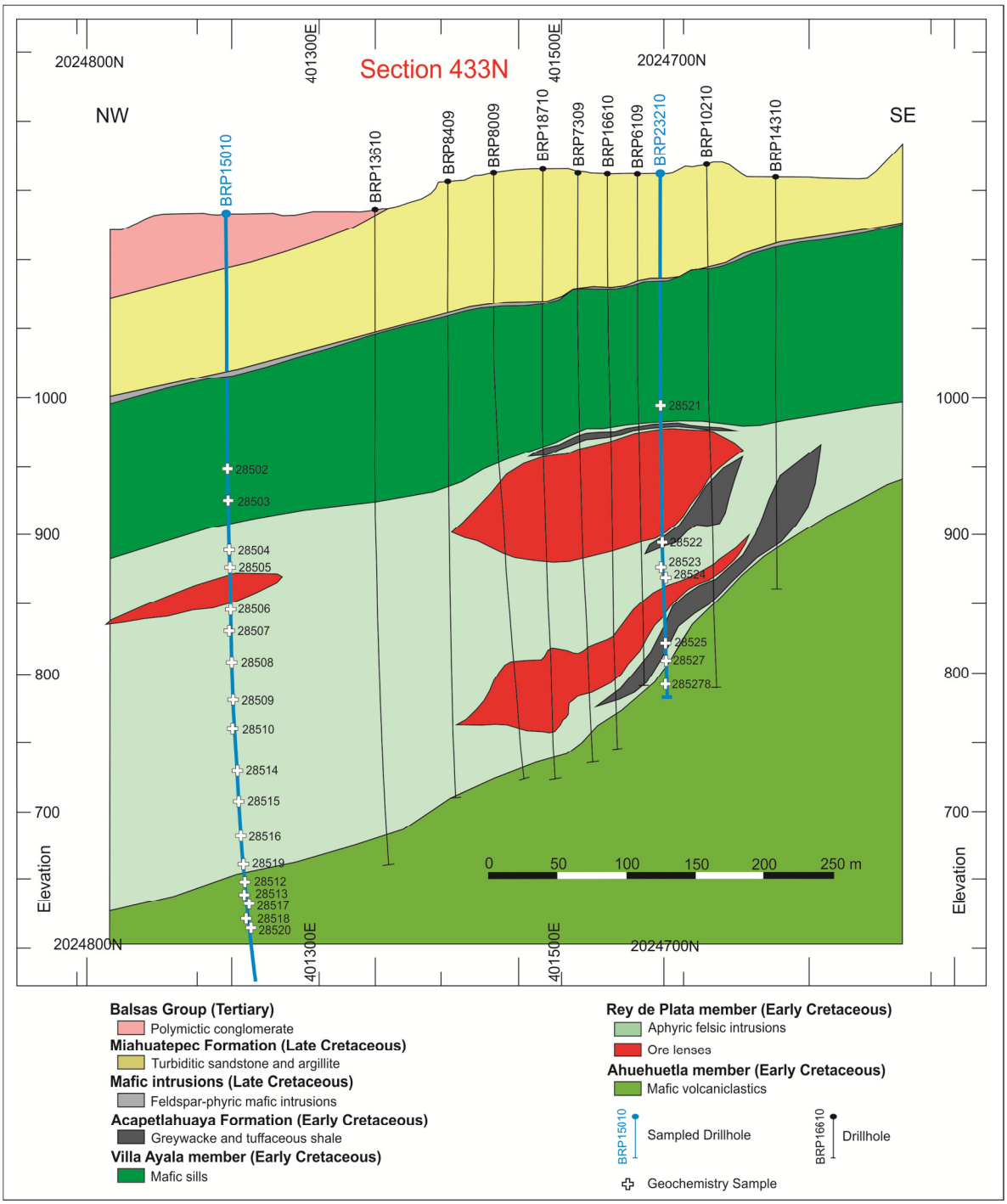

Figure 3.13. Section 433 illustrates an increase in thickness of the Rey de Plata member towards the West.

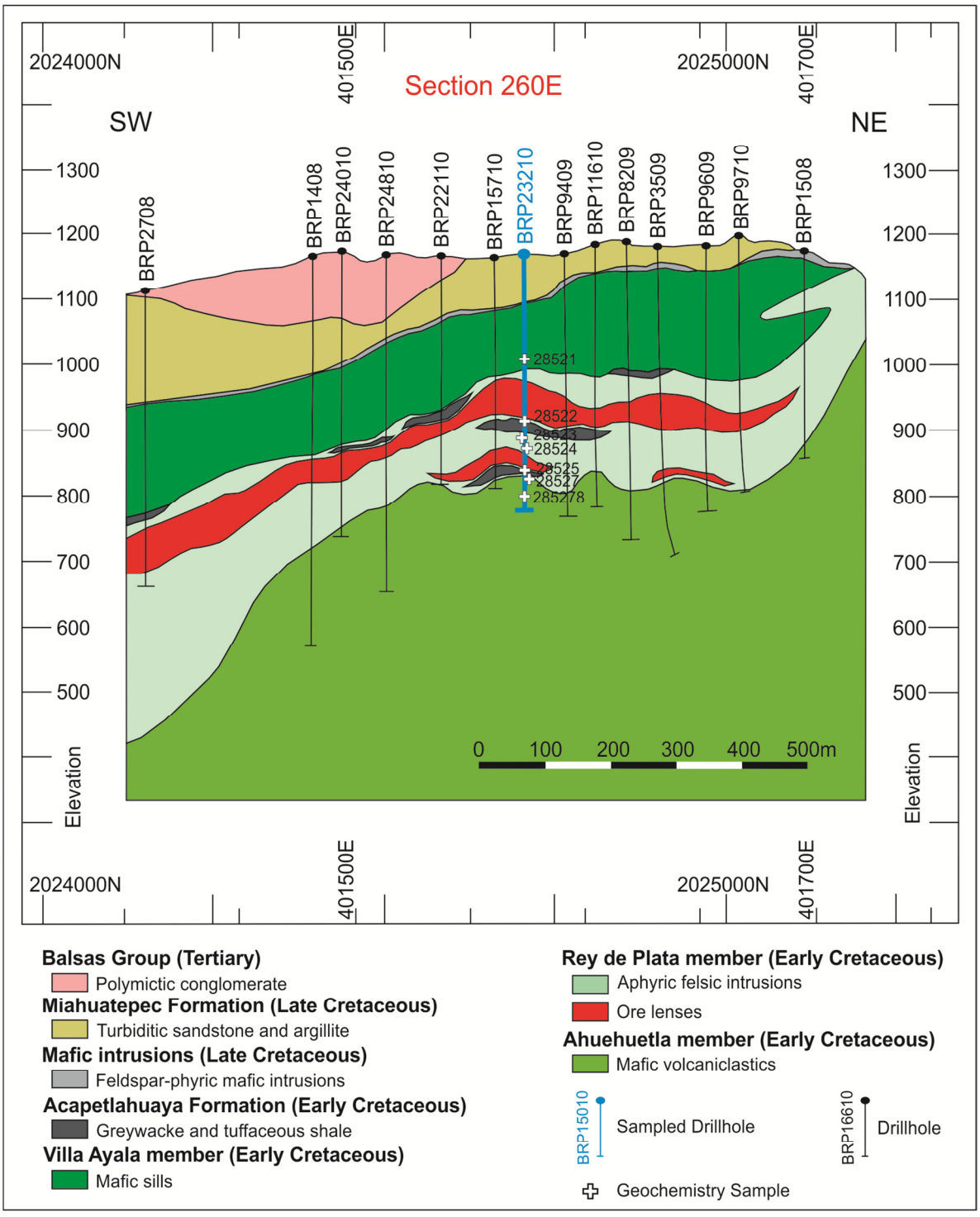

Figure 3.14. Section 260 illustrates an increase in thickness of the Rey de Plata member towards the South.

Figure 3.15. Felsic flow with epithermal veins containing quartz + pyrite ± sphalerite ± galena.

3.3.2.3 Felsic Volcaniclastic Deposits

The felsic volcaniclastic rocks are commonly heterolithic and contain subangular fragments (2mm to 7cm) of rhyolite, graphitic argillite, pumice, quartz and massive sulphide in a fine vitric matrix. Normal grading is common and the fragments are often elongated due to deformation, which is best developed within areas of intense quartz + sericite ± pyrite ± chlorite alteration (Figure 3.17).

Figure 3.16. Massive, quartz porphyritic felsic sills.

3.3.2.4 Felsic Lapilli Tuffs

The lapilli tuffs are monolithic volcaniclastic deposits that contain pumice and angular lithic felsic fragments (less than 5cm in size), in a vitric, ash-sized matrix; fragments are flattened parallel to the penetrative foliation. Contacts with other volcaniclastic lithofacies are commonly transitional, except contacts with felsic sills that are typically sharp. Intense to moderate quartz + sericite ± pyrite and sometimes weak chloritic alteration are characteristic of this lithofacies (Figure 3.18).

Figure 3.17. Felsic volcaniclastic deposits containing massive sulphide lenses (galena + sphalerite + pyrite).

3.3.2.5 Graphitic Argillites

Thinly bedded to laminated, fine, black, graphitic argillite is characteristic of the Rey de Plata unit (Figure 3.19). The argillite occurs intercalated with felsic volcaniclastic lithofacies, as in the central and southern part of the area where thicknesses range from 10cm up to 60m, and at the top and locally, at the base of the Rey de Plata formation. In the central and southern part of the map area, the argillite commonly occurs in direct contact with, or in proximity to, the massive sulphide lenses (Figures 3.13, 3.14). The argillites differ from those in the Ahuehuetla member (Figure 3.11), by the absence of intercalated beds of mafic lapilli tuff and a higher content of quartz and/or calcite veins; the latter were emplaced during at least two stages (evidence for this is the cross cutting relationships between vein sets). However, layers (up to 8cm width) of massive sulphide and fragments of massive sulphides (sphalerite ± pyrite ± galena) occur within argillite. Contacts with other lithofacies are sharp and are always sheared.

Figure 3.18. Felsic lapilli tuff with flattened sericitic, vitric fragments that are elongate parallel to the penetrative foliation.

Figure 3.19. Typical, thinly bedded and calcite-quartz veined black, graphitic argillite of the Rey de Plata member in the central and southern part of the map area.

3.3.3 Villa Ayala Member

This mafic member comprises amygdaloidal sills and volcaniclastic deposits. The contact with the underlying Rey de Plata member is conformable, but locally is sheared; argillite and massive sulfide lenses usually occur in the Rey de Plata member immediately below the contact. The upper contact of the Villa Ayala member is unconformably overlain by the Miahuatepec formation in the western and southern area of the map when it is not obscured by feldspar-phyric mafic intrusions, but the contact is tectonic with the Balsas conglomerate in the northwestern and southeastern portions of the map area. The Villa Ayala member is well exposed in the eastern part of the map area (Figure 3.1) and its absence to the north where argillaceous sediments of the Acapetlahuaya Formation directly overlie the Rey de Plata member is consistent with an unconformable, erosive contact. Based on drillhole intersections the thickness of the Villa Ayala member ranges up to 250m.

3.3.3.1 Mafic Sills

This lithofacies comprises plagioclase porphyritic or aphyric mafic intrusions, containing amygdules, which are filled by quartz, calcite or epidote and pyrite. The amygdules are often elongate parallel to the penetrative foliation, which affects the entire sequence. Thicknesses range from few centimeters up to 35 meters and occasionally, the sills are intruded by other sills with well-defined sharp contacts that range in thickness from centimeters up to 3 meters. Weak to intense chlorite + epidote alteration is common and characteristic of this lithofacies. However, a moderate to weak argillic alteration occurs in sills located near the contact with the Rey de Plata member, where intense epithermal quartz + euhedral pyrite veining is concentrated. Contacts with volcaniclastic lithofacies are typically sharp, but are transitional where peperite occurs at the contact (Figure 3.20).

3.3.3.2 Volcaniclastic Deposits

The volcaniclastic deposits are typically heterolithic and contain subangular to rounded fragments of mafic volcanic rocks, argillite, scoria and fragments of plagioclase phenocrysts within a finer (<2mm), mafic, tuff-sized matrix. Clast size ranges from 0.2cm to 20cm, and the beds commonly show normal grading. Lithological variations include tuff breccia, lapillistone and volcanic sandstone/tuff lithofacies. The tuff breccia contains rounded to subangular, elongate fragments (due to flattening) of amygdular mafic volcanic rocks with sporadic quartz fragments in a fine, aphyric tuff-sized matrix. The lapillistone is monolithic, poorly bedded and contains clasts up to 15cm in size. Volcanic sandstones/tuffs are poorly bedded and show grain sizes that range from 0.5mm to 5mm, with no ash-sized material. Moderate to intense chlorite ± epidote alteration is the most common alteration type, although there are intervals that display weak argillic alteration. Contacts with other volcaniclastic lithofacies are transitional, but sharp with sills. Veinlets of quartz, calcite and ankerite are common (Figure 3.21). This lithofacies displays a tectonic foliation due to regional deformation.

Figure 3.20. Porphyritic mafic sill with plagioclase phenocrysts.

Figure 3.21. Mafic volcaniclastic lithofacies containing sparse blocks and clasts of argillite.

3.4 Feldspar-phyric mafic Intrusions

Massive, feldspar-phyric mafic intrusions are exposed in outcrop within the western and southern parts of the map area (Figure 3.1) where they were emplaced between the Miahuatepec Formation and the Villa Ayala member. The intrusions are massive, feldspar porphyritic, have a microcrystalline groundmass, and display a penetrative foliation. Their thickness ranges from 1m to 25m and they constitute about 3% of the map area. Contacts with the underlying Villa Ayala member are sharp, but are peperitic with overlying turbiditic sediments of the Miahuatepec Formation whose beds dip shallowly towards the southwest at less than 20 degrees. The peperites are a mixture of fluidal to blocky clasts of the intrusion within a matrix of argillite and sandstone (Figure 3.22). The peperite indicates that the intrusion was emplaced into the Miahuatepec Formation when the sediments were unconsolidated and wet; they are syn-sedimentary intrusions.

Figure 3.22. Peperite at the contact between the feldspar-phyric mafic intrusion and turbiditic sedimentary lithofacies of the Miahuatepec Formation (upper right corner).

3.5 Acapetlahuaya Formation

This Aptian to Early Cenomanian (Talavera-Mendoza et al. 1995) lithofacies consists of thinly bedded greywacke and tuffaceous shale intercalated with volcaniclastic beds less than 10cm thick and is cut by basaltic dikes with widths of up to 1.5m. It generally plunges towards the southwest at less than 20° and crops out in the northern part of the map area, where it has thicknesses that range from few meters to 260m (Figure 3.1). Its contact with the Villa Ayala member and the Rey de Plata member has been inferred as an unconformity is overlies both the Villa Ayala and the Rey de Plata members (Figure 3.23). Sample (RP-13-8)

collected from this formation yielded detrital zircons that range in age from 115 ± 4 Ma to 152 ± 4 Ma.

Figure 3.23. Acapetlahuaya Formation consisting of thinly bedded greywacke, tuffaceous shale and volcaniclastic layers with widths cut by basaltic dikes.

3.6 Miahuatepec Formation

The Cenomanian Miahuatepec Formation (Talavera-Mendoza et al. 1995) is a turbiditic succession composed of intercalated graphitic argillite with calcareous sandstone and polymictic conglomerates; bed thicknesses range from 1cm to 1m and dip shallowly towards the southwest. Extensive outcrops of this formation are located in the southwestern part of the map area where overturned folds and penetrative foliation are described (Figure 3.1). Based on drillhole intersections, the Miahuatepec Formation ranges from few meters to about 200m in thickness. Its lower contact with the Villa Ayala member is an angular unconformity and commonly sheared, whereas the contact with the overlying Balsas conglomerate is

tectonic. The absence of the Aptian-Cenomanian Amatepec Formation (Campa and Ramirez 1979) and the Aptian-Albian reefal limestone of the Teloloapan Formation (Guerrero-Suastegui et al. 1991), which regionally overlies the Villa Ayala member, is also evidence for an unconformity between the Villa Ayala and the post-early Cenomanian Miahuatepec Formation at Rey de Plata. The Miahuatepec Formation contains two different generations of quartz ± calcite veinlets with widths of 0.5cm to 5cm that cross cut bedding and foliation planes (Figure 3.24). Sample (RP-13-47) collected from this formation yielded detrital zircons that range in age from 200 Ma to 1200 Ma.

3.7 Balsas Group

The Balsas Group consists of polymictic conglomerate intercalated with sandstone, siltstone, and intervals of silicic ignimbrite. Conglomeratic beds include clasts of limestone, sandstone, siltstone, mafic and felsic volcanic rocks and quartz. The ignimbrites are welded, and contain crystals of plagioclases and biotite, along with lithic fragments in a vitric matrix. The lower contact of the Balsas Group is tectonic where it overlies the Villa Ayala member and the Miahuatepec Formation. Extensive outcrops occur in the northwestern and southwestern parts of the map area where the Group has thicknesses up to 150m (Figure 3.1). The Balsas conglomerate is not foliated, but the succession is moderately (20° to 40°) tilted to the northwest to southwest due to normal faulting (Figure 3.25). K-Ar dating of biotite within ignimbritic intervals in the Amacuzac area yielded an age of 38.51 ± 1 Ma (Monter-Ramírez 2004).

Figure 3.24. Miahuatepec Formation consisting of turbiditic sediments composed of intercalated conglomerate, sandstone and argillite.

Figure 3.25. Balsas Group with intercalated polymictic conglomerate, sandstone siltstone and ignimbrite.

3.8 Geochemistry

Forty-five representative samples were collected from the Villa Ayala Formation, of these. 9 samples are of the Villa Ayala member, 24 samples are of the Rey de Plata member, 6 samples are of the Ahuehuetla member, 3 samples are of the feldspar-phyric mafic intrusions (but only two samples are plotted) and 3 samples are of the Miahuatepec Formation. The samples were collected from surface outcrops (22), from drill hole BRP15010 (18) and from drill hole BRP23210 (5); the location of surface samples and the sampled drill holes are shown in Figure 3.1. Table A1 in Appendix 1 shows the lithofacies and member for each sample. The samples were sent to ALS Chemex in Vancouver, Canada to obtain a complete geochemical characterization through combining methods that included the use of XRF (fused pellet) and ICP-AES, to determine major elements, plus carbon and sulfur. Trace elements, including the full rare earth element suite, were analyzed using a lithium borate fusion of the sample prior to acid dissolution and ICP-MS analysis. Details of the analytical techniques, precision and accuracy can be found in the ALS Chemex schedule of services and fees (http://www.alsglobal.com/). Geochemical analyses for each sample are contained in Table A2 of Appendix 2.

3.8.1 Element mobility

Hydrothermal alteration may result in the mobility of major, trace and REE elements such that the resulting compositional changes do not reflect the original composition of the samples. In VMS hydrothermal systems the major elements, particularly SiO_2, CaO, Na_2O, K_2O, MgO and Fe_2O_3, are commonly mobile and are not used in the discussion that follows (Franklin et al. 2005). However, most high field strength elements (HFSE) and rare earth elements (REE) are generally immobile during hydrothermal alteration, and are highly useful for chemo-stratigraphic correlation, and for plotting discrimination diagrams (Hocker 2005; Franklin et al. 2005). Certain key elements such as Al, Ti, the high field strength trace elements Zr, Nb, Y and the REE have been shown to remain relatively

immobile during physical and chemical alteration processes (MacLean 1990; MacLean and Barrett 1993).

In the discussion that follows the oxides Al_2O_3 and TiO_2 and Y, Zr, Nb plus the REE are used to classify the volcanic rocks, determine their magmatic affinity, and to infer their geodynamic setting. The relative immobility of these elements is illustrated in Appendix 3 where binary plots and correlation coefficients are used to assess the relative immobility/mobility of element pairs as per the method of Mclean and Barrett (1993) and Cann (1970), respectively.

3.8.2 Results

3.8.2.1 Mafic Rocks

In a plot of Zr/TiO_2 vs Nb/Y (Pearce 1996), the majority of the mafic samples from the Ahuehuetla member plot in the basalt field, and one sample of the Feldspar-phyric mafic intrusions plots just into the andesite field. Most samples have a subalkaline affinity, but four samples of the Villa Ayala member plot just into the alkaline basalt field, indicating slight mobility of Nb or Y, and or a weakly alkaline affinity (Figure 3.26).

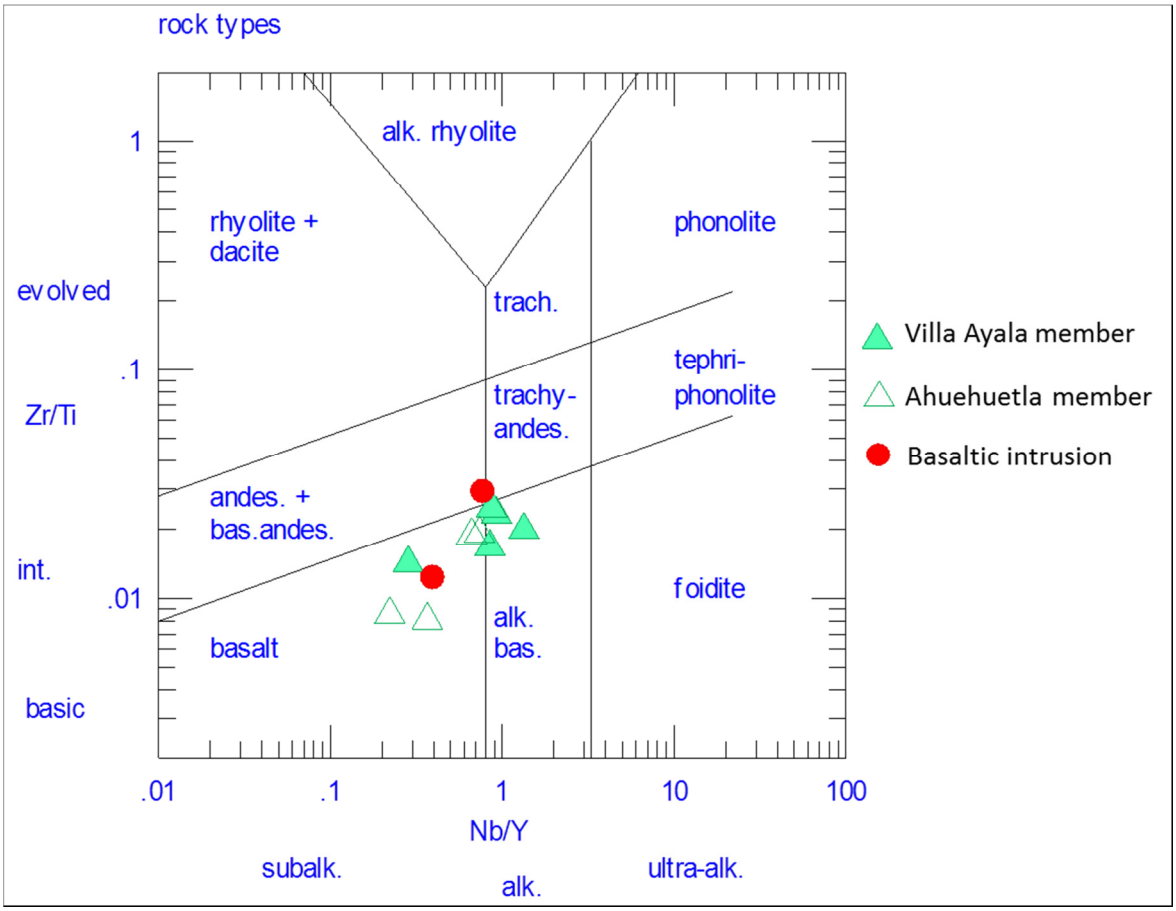

Figure 3.26. Zr/TiO_2 vs Nb/Y composition diagram of Pearce (1996) for mafic rocks.

Most of the basaltic samples from the Villa Ayala and Ahuehuetla members and the Feldspar-phyric mafic intrusions plot in the mid ocean ridge (MORB) and back-arc basin (BAB) field on the V vs Ti/1000 diagram of Shervais (1982) (Figure 3.27). Two samples from the Ahuehuetla member plot in the island arc tholeiite field.

To further refine interpretations regarding the magmatic affinity and geodynamic setting, the basaltic samples were plotted on a primitive mantle normalized spider diagram shown in Figure 3.28 (after Sun and McDonough 1989). All the basaltic samples show minimal to slight enrichment in the light rare earth elements (LREE), near flat patterns with respect to the heavy rare earth elements (HREE), negative Nb anomalies with respect to Th and La (except one sample from the Villa Ayala member), negative Ti with respect to Eu and Gd and negative to positive Zr and Hf with respect to Sm and Eu. The LREE enrichment, negative Nb and relatively flat

HREE are features consistent with primitive island arc tholeiitic basalts (Pearce 1996). The LREE enrichment, negative Nb and positive Zr and Hf anomalies could also reflect contamination by more evolved arc crust (continental crust?) (Pearce 1996).

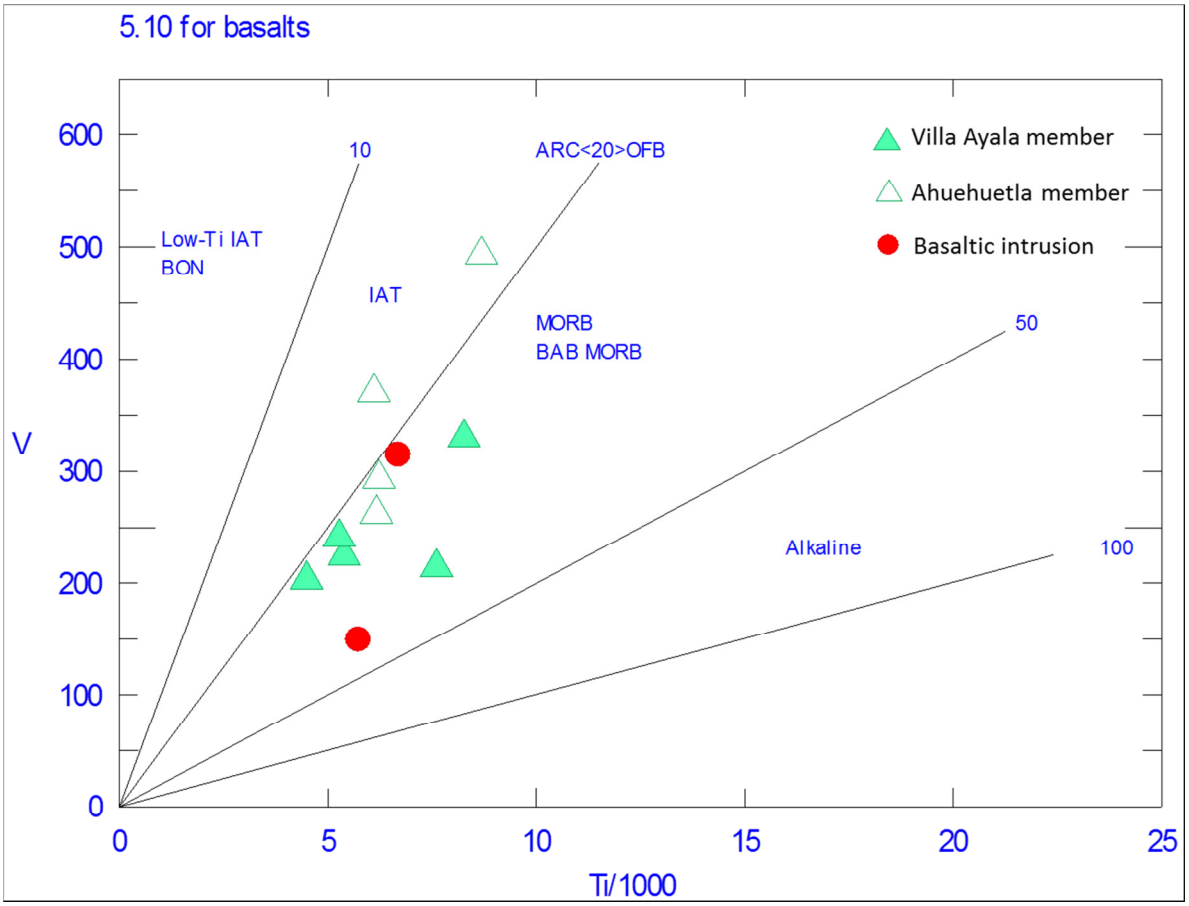

Figure 3.27. V vs Ti tectonic discrimination diagram for basalts (modified from Shervais 1982).

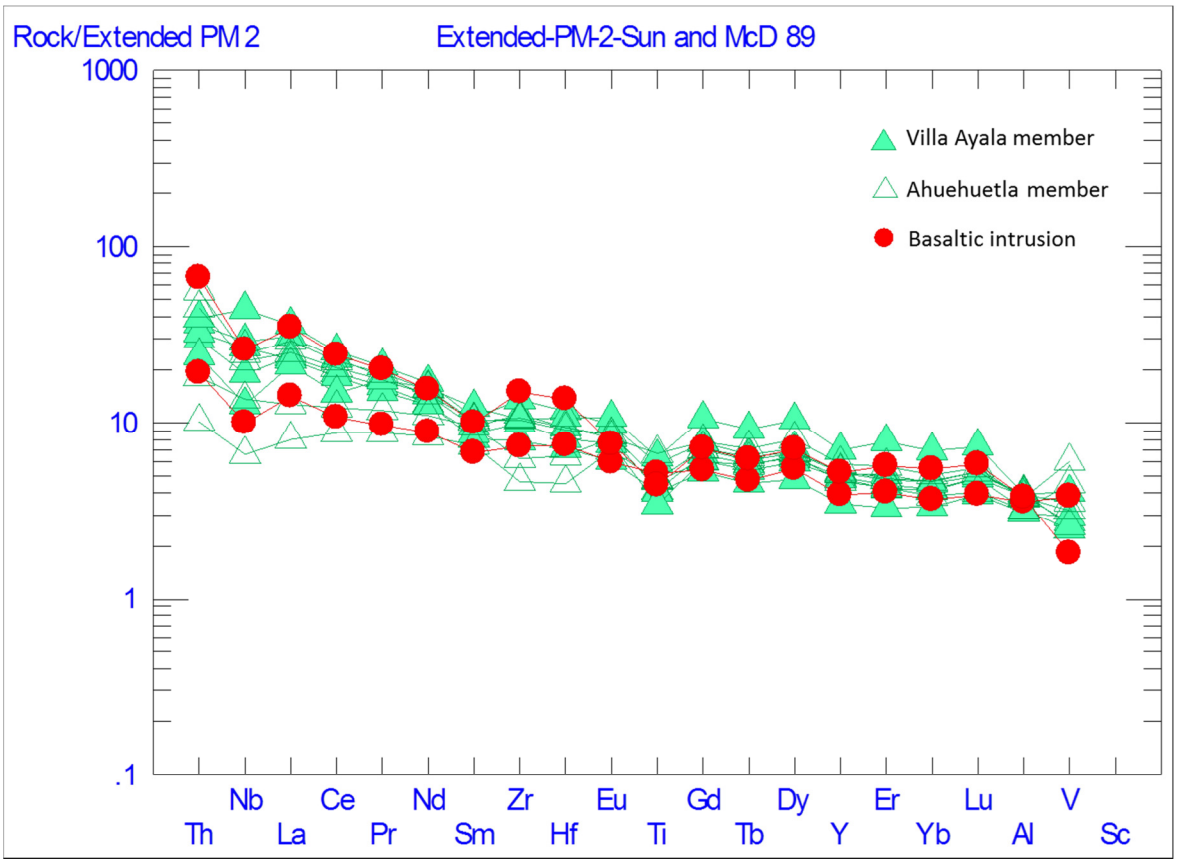

Figure 3.28. Primitive mantle normalized multi-element (spider) diagram for basaltic lithologies (normalization after sun and McDonough 1989).

3.8.2.2 Felsic rocks

The suite of least altered samples from the Rey de Plata member plotted on a Zr/TiO_2 vs Nb/Y (Winchester and Floyd 1977) diagram define a tight cluster within the rhyodacite/dacite field (Figure 3.29) and fall within the volcanic-arc granite (VAG) field of a Ta versus Yb diagram (Pearce et al. 1984, Figure 3.30) supporting an arc geodynamic setting, similar to that interpreted for the basalts.

On a primitive mantle normalized spider diagram (Figure 3.31) the felsic volcanic rocks show LREE slight enrichment, a flat HREE pattern and pronounced negative Nb (relative to Th and La), Sm (relative to Nd and Zr) and Eu and Ti anomalies (relative to Hf and Gd). These features are consistent with FII rhyolites of Hart et al. (2004). The positive Zr and Hf anomalies with respect to Sm and Eu along with

negative Nb anomalies are also consistent with contamination by younger (continental) crust (Pearce 1984).

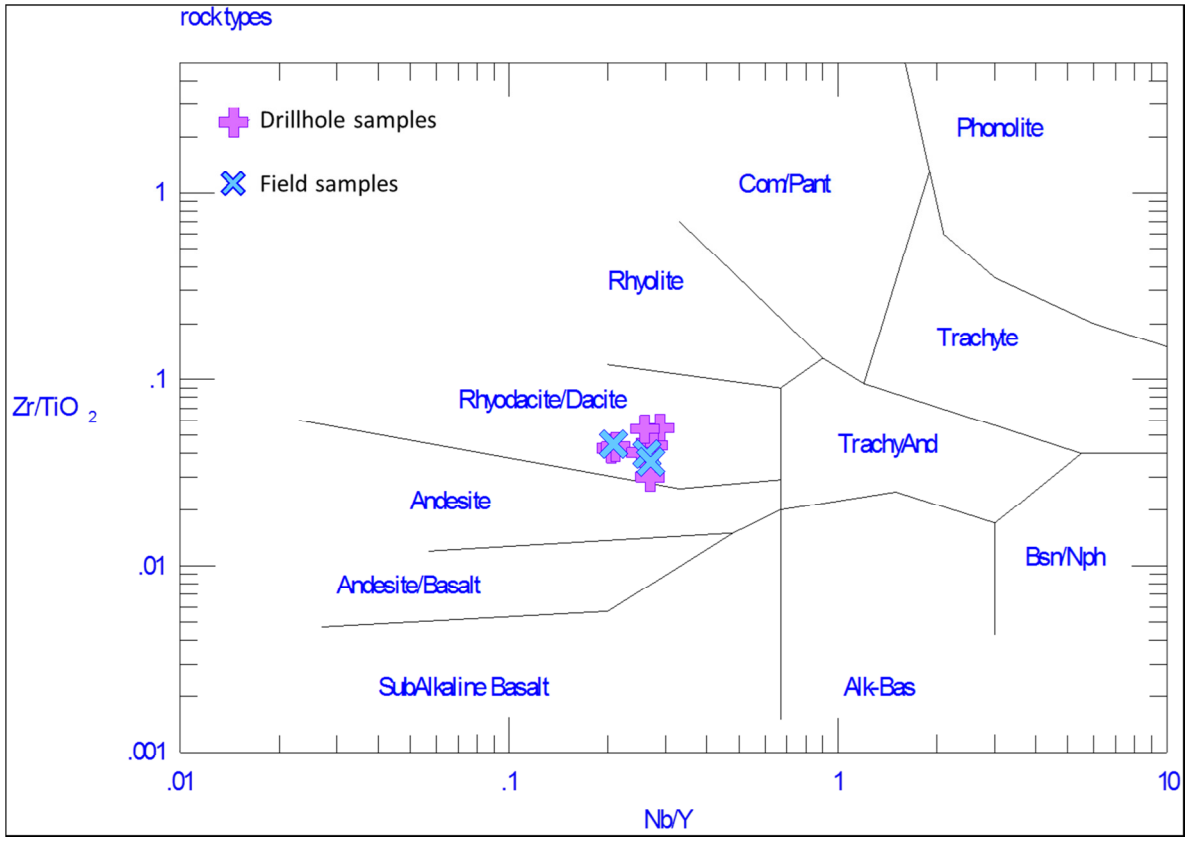

Figure 3.29. Zr/TiO_2 vs Nb/Y composition diagram of Winchester and Floyd (1977). Rey de Plata samples fall in the rhyodacite/dacite field.

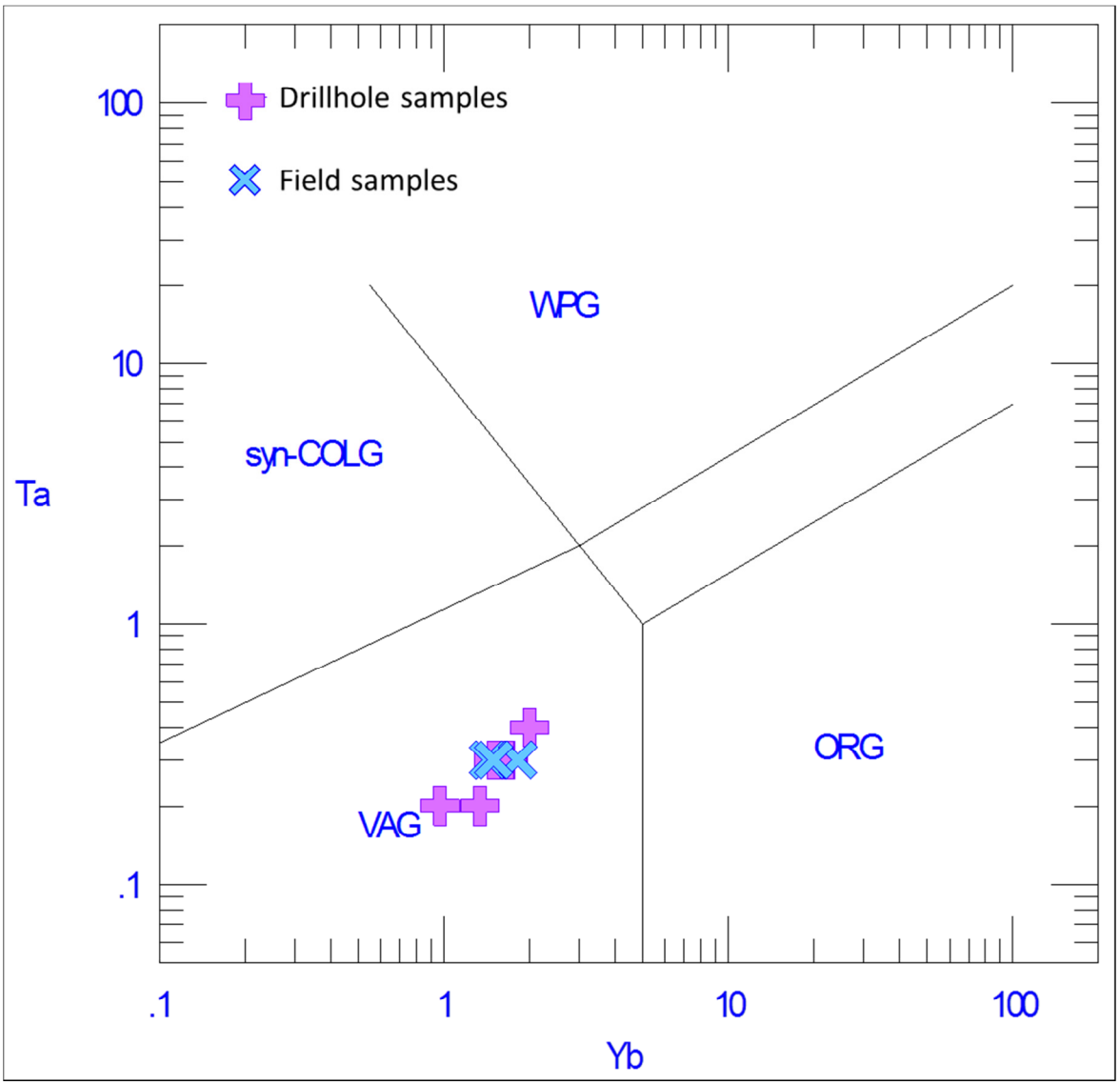

Figure 3.30. Ta-Yb tectonic discrimination diagram for felsic rocks (after Pearce et al. 1984). All the suite of samples is in the volcanic-arc granites field (VAG).

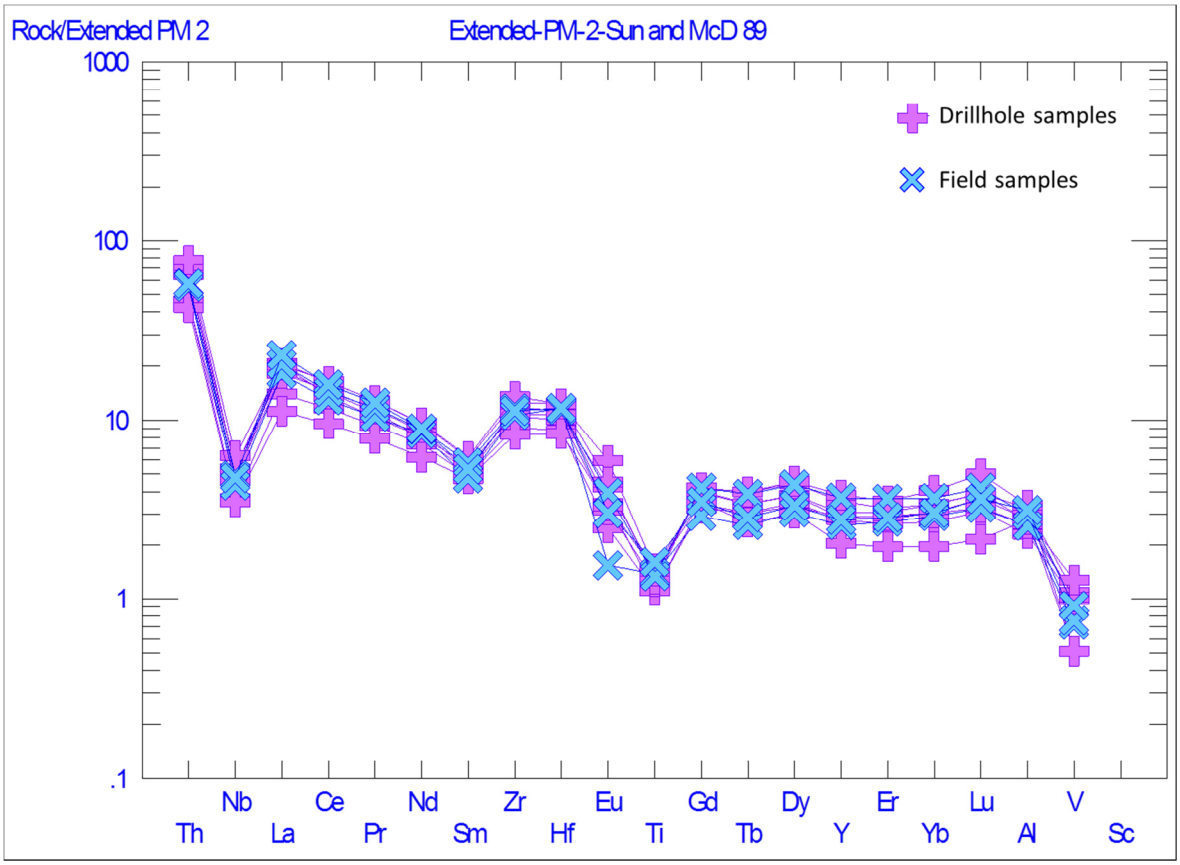

Figure 3.31. Primitive mantle normalized multi-element (spider) diagram for Rey de Plata felsic volcanic rocks (normalization after Sun and McDonough 1989).

3.8.2.3 Sedimentary Rocks

Post-Archean Australian Shale (PAAS) and Primitive Mantle normalized multi-element diagrams (spider diagram) constructed for samples from sedimentary rocks of the Miahuatepec and Acapetlahuaya Formations are shown in Figures 3.32 and 3.33. The profiles for samples from both sedimentary formations are similar on the PAAS normalized diagram (Fig. 3.32), the main difference being that the Acapetlahuaya shales are slightly less depleted in LREE and have a weak positive Eu anomaly relative to the PAAS, but both formations are not as depleted in the LREE, or in the HREE as is graphitic argillite of the Rey De Plata member (H. Gibson, personal communication, 2014). The Acapetlahuaya shale profile is similar to that of coherent Rey De Plata rhyolite, although the latter shows progressive HREE enrichment from Tb to Lu, relative to PAAS.

On a primitive mantle normalized diagram (Figure 3.33) sedimentary rocks of the Miahuatepec and Acapetlahuaya Formations and Rey De Plata rhyolite have identical LREE enriched and flat HREE profiles, which are characterized by negative Nb (relative to Th and La), Sm (relative to Nd and Zr), Ti (relative to Eu and Tb), and V anomalies, and positive Zr and Hf anomalies (relative to Nd and Eu). The Rey De Plata graphitic argillite lacks the negative Sm and positive Zr and Hf anomalies, and has an overall lower abundance and slightly less enriched LREE pattern relative to the Miahuatepec and Acapetlahuaya Formations.

Thus, sedimentary rocks of the Cenomanian Miahuatepec and Aptian Acapetlahuaya Formations have REE abundances that are slightly depleted in the LREEs relative to PAAS, but otherwise are similar to continental derived sediments and differ from older graphitic argillite of the Lower Cretaceous (Valanginian) Rey de Plata member.

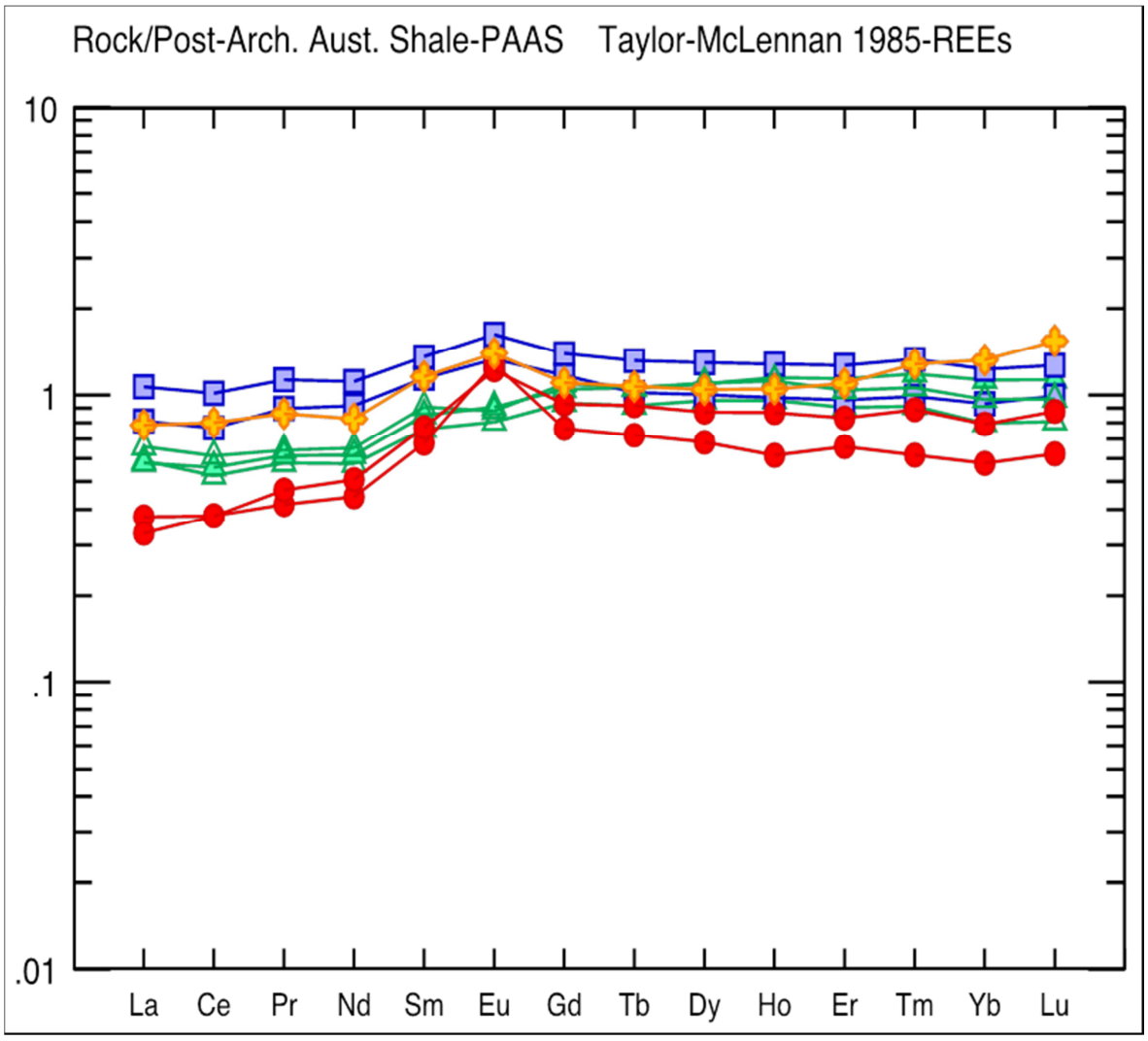

Figure 3.32. Post-Archean Australian Shale (PAAS) normalized multi-element (spider) diagram for Miahuatepec (sandstone- open green triangle; shale - green triangle) and Acapetlahuaya (tuffaceous shale - blue box) sedimentary rocks, intra Rey de Plata graphitic argillite (red circles) and a representative Rey De Plata coherent rhyolite flow (yellow cross) (normalization after Taylor and Mclennan 1985).

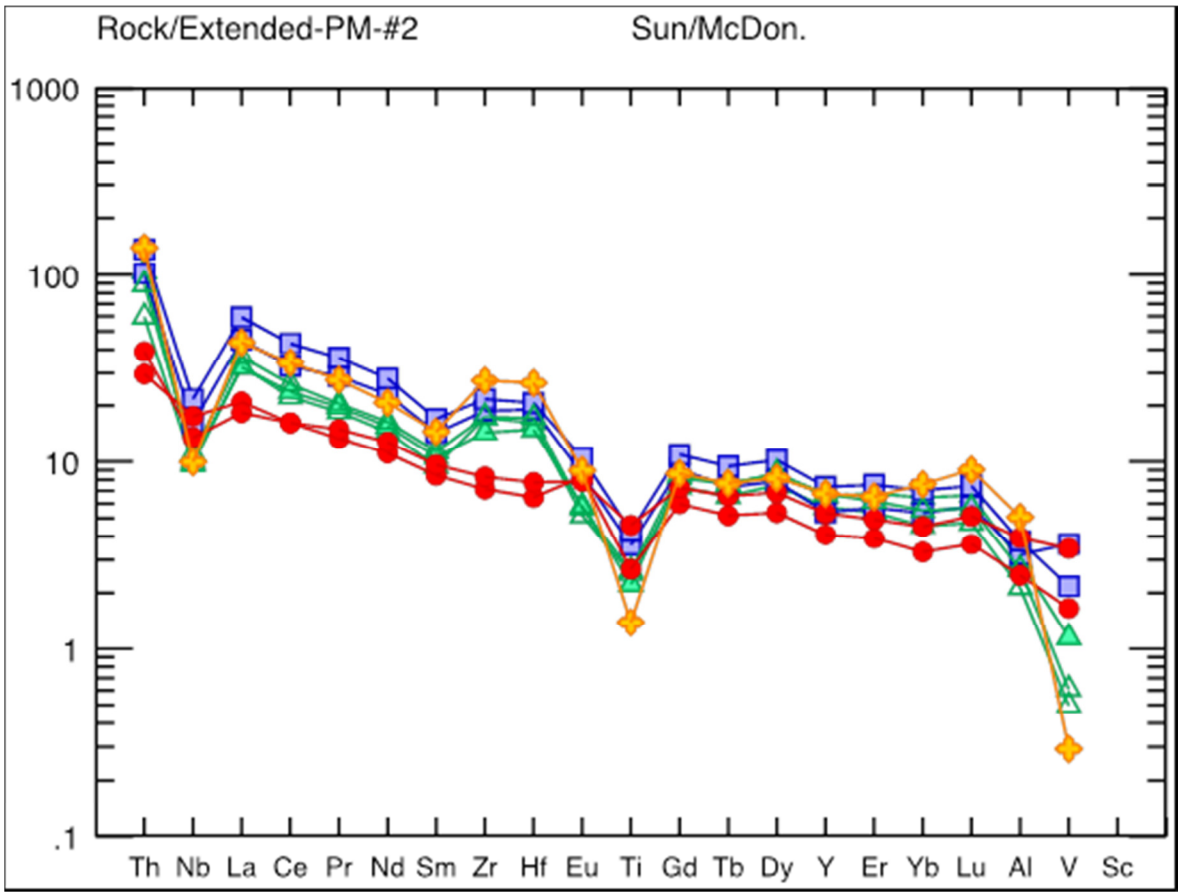

Figure 3.33. Primitive mantle normalized multi-element (spider) diagram for Miahuatepec (sandstone - open green triangle; shale - green triangle) and Acapetlahuaya (tuffaceous shale - blue box) sedimentary rocks, intra Rey De Plata graphitic argillite (red circles) and a representative Rey De Plata coherent rhyolite flow (yellow cross) (normalization after Sun and McDonough 1989).

3.8.2.4 Tectonic setting

The island arc tholeiitic to MORB-BAB affinity for the Villa Ayala Formation basalts is consistent with a supra subduction zone geodynamic setting within an arc or nascent back-arc environment (negative Nb anomalies consistent with slab influence, Pearce 1996). The LREE enriched and flat HREE profiles for the felsic volcanic rocks are consistent with shallow, lower pressure partial melting of older hydrated arc crust (hence the negative Nb anomaly) during extension and arc rifting (FII rhyolite of Hart et al. 2004). The positive Zr and Hf anomalies and negative Nb anomaly for both basaltic and felsic volcanic rocks suggests

interaction with older arc crust (continental crustal sliver?) within a juvenile oceanic or evolved arc setting, an interpretation that is consistent with the occurrence of significantly older xenocrystic zircons within the Villa Ayala Formation as reported by Mortensen et al. (2008). The profiles and abundance of the REEs for sedimentary rocks of the Miahuatepec and Acapetlahuaya Formations are consistent with their derivation from continental and arc crust during accretion and post accretion sedimentary events.

Chapter 4: Structural Geology

4.1 Structures in the Rey de Plata VMS camp

The structural history of the Rey de Plata district began with tilting of the volcanic rocks followed by the deposition of sedimentary rocks as unconformable successions overlying the volcanic rocks. Thereafter, the district underwent four deformational events: i) D_1, which is characterized by the formation of a shallowly-dipping S_1 cleavage, L_1 stretching lineation, and E-verging F_1 folds; ii) D_2, which is characterized by the development of an extensional, spaced, shear band cleavage; iii) D_3 which is characterized by brittle normal faults, associated transfer faults, and SW-verging F_3 drag folds; and iv) D_4 which is characterized by late upright F_4 folds.

Structural data collected from outcrops and from drill cores are tabulated in Appendices A4.1 and A4.2.

4.1.1 Early unconformities

Two unconformities are recognized in the Rey de Plata VMS camp. One of them is along the contact between the Villa Ayala Formation volcanic rocks and overlying interlayered greywacke, tuffaceous shale and volcaniclastic rocks of the Acapetlahuaya Formation (Figure 4.1). On regional scale, the Acapetlahuaya Formation is interpreted to have a transitional contact with the Villa Ayala Formation (Talavera-Mendoza et al. 1995). At Rey de Plata, the Acapetlahuaya Formation overlies both the Villa Ayala and Rey de Plata members. Its basal contact with the volcanic rocks is at an angle with the contact between the two volcanic members. This angular discordance and the absence of the Villa Ayala member where volcanic sediments of the Acapetlahuaya Formation directly overlie the Rey De Plata member (Figure 4.1) suggests that the volcanic rocks were tilted and eroded prior to the deposition of the Acapetlahuaya Formation.

The second unconformity occurs along the contact between the Villa Ayala Formation and overlying turbiditic sandstone of the Miahuatepec Formation. An angular unconformity is observed between these two formations along the creek next to the existing head frame and ramp (Figure 4.1). Bedding in the turbiditic sandstone is parallel to the contact with underlying volcaniclastic rocks of the Villa Ayala member. Bedding in the volcanic rocks is oblique to the unconformity, suggesting that the volcanic rocks were tilted during an early deformation event prior to the deposition of the turbiditic sandstone (Figure 4.2a).

Elsewhere in the Rey de Plata camp, the presence of an unconformity is obscured by deformation and by the emplacement of feldspar-phyric mafic intrusions. Peperitic textures along the upper margin of the intrusions suggest that the turbiditic sandstone was not lithified at the time of emplacement of the intrusions. This relationship is observed at different locations across the map area such as locations A (Fig. 4.2b) and B (Fig. 4.3) in the West domain. Thus, the emplacement of the intrusions was coeval with deposition of the Miahuatepec turbiditic sandstones. This contact is usually modified by faulting and the turbiditic sandstones above the contact are locally strongly folded (Figure 4.4).

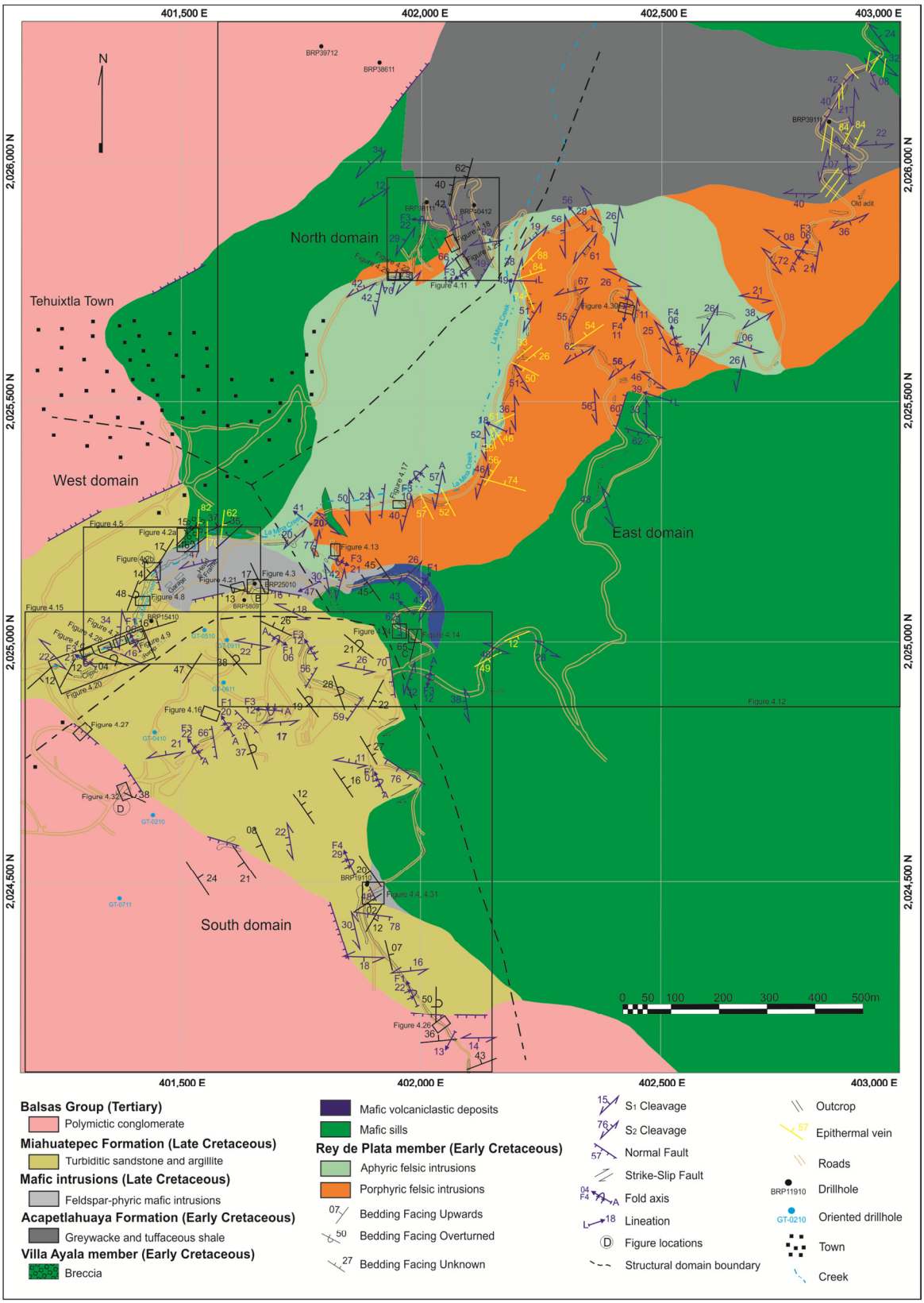

Figure 4.1. Geological map of the Rey de Plata deposit area showing structural domains and location of figures (from this study).

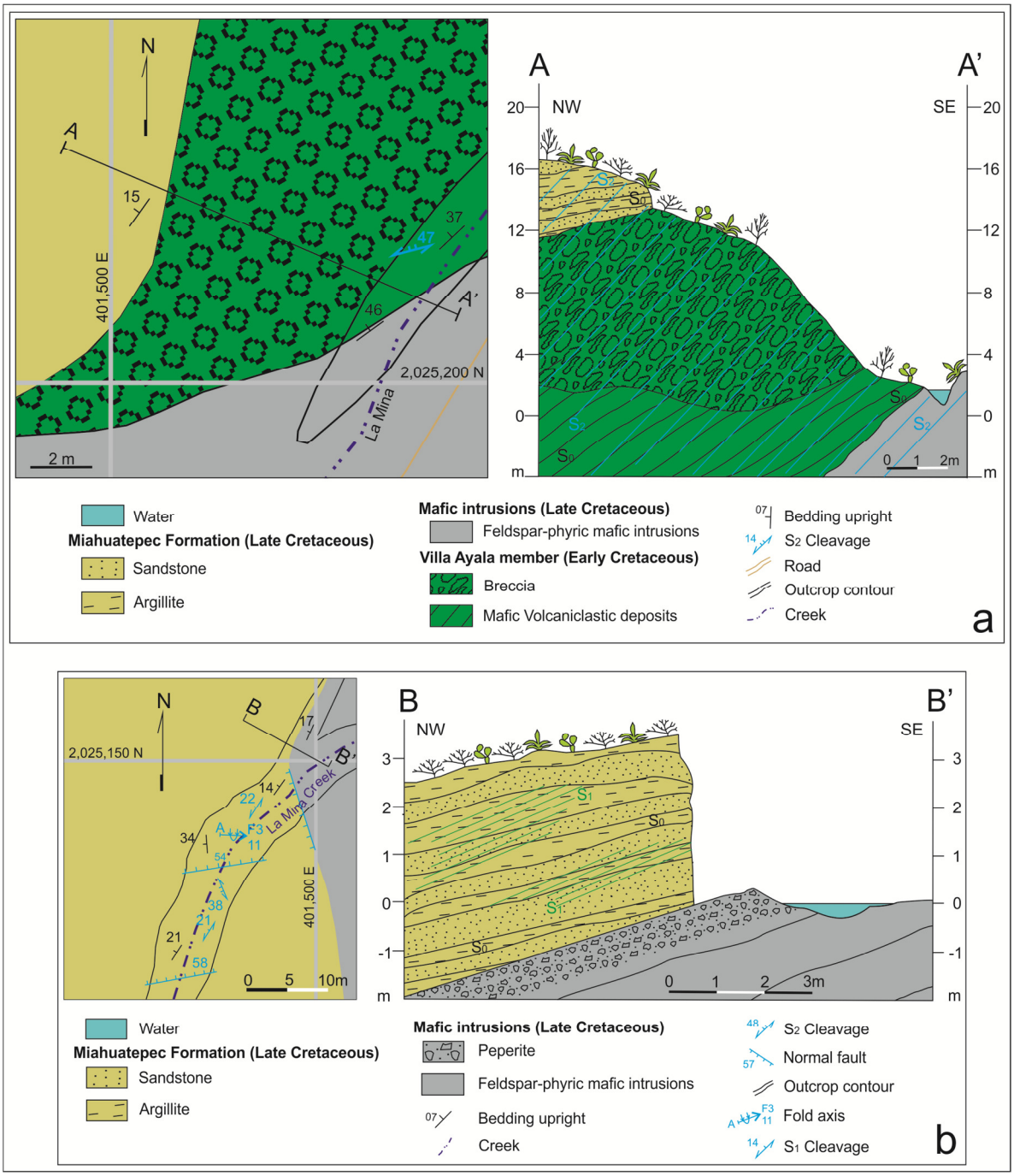

Figure 4.2. Angular unconformity between the Miahuatepec Formation and the Villa Ayala member of the Villa Ayala Formation (a); Peperite at the contact between sediments of the Miahuatepec Formation and underlying feldspar-phyric mafic intrusion (b). Location of diagrams is shown in Figures 4.1, 4.5.

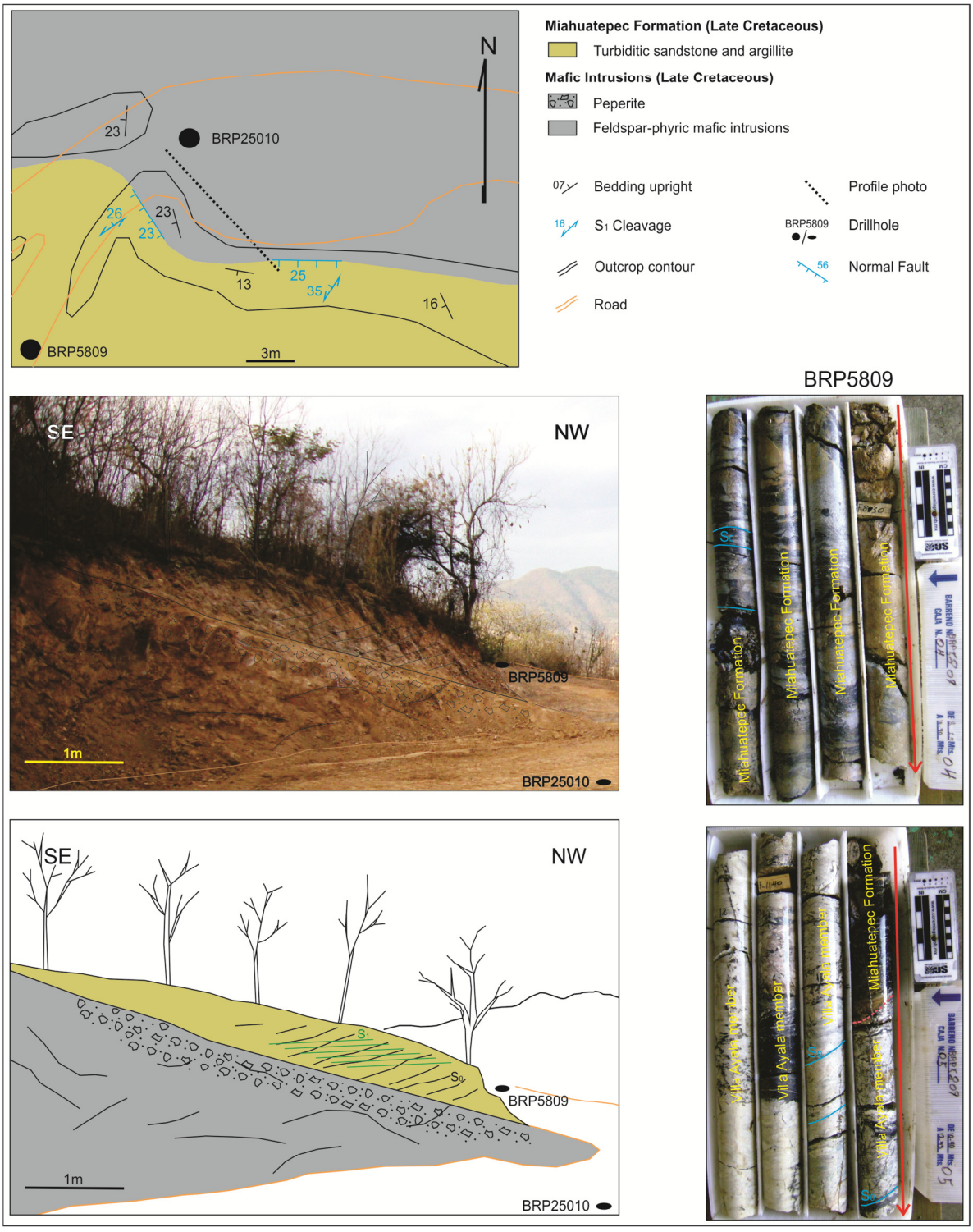

Figure 4.3. Peperite at the contact between the Miahuatepec Formation and the Feldspar-phyric mafic intrusion. Red arrows show the down-hole direction. Location of diagram is shown in Figures 4.1, 4.5.

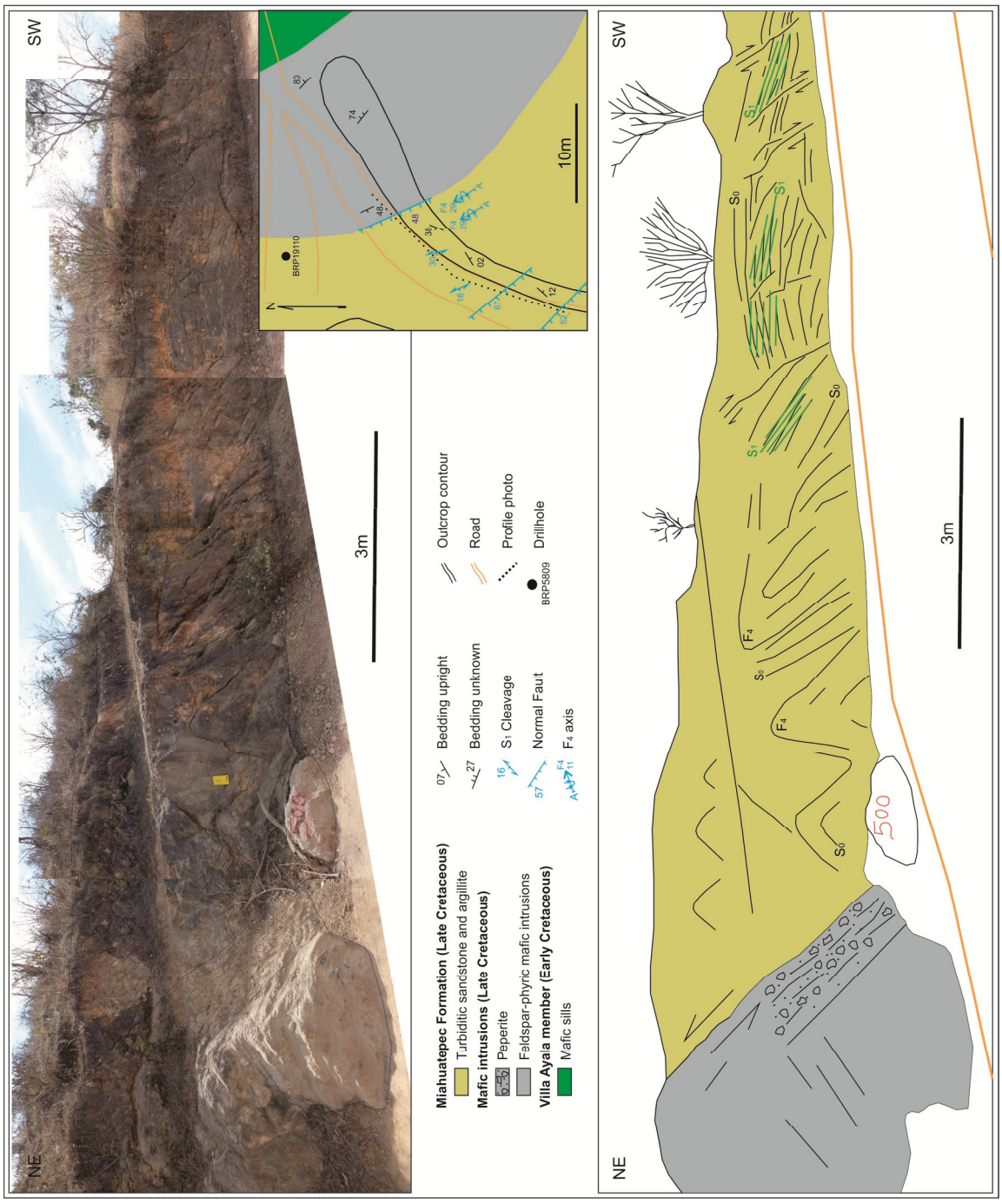

Figure 4.4. The Miahuatepec Formation sedimentary rocks are resting against a reverse fault surface and show northeast-verging F_4 folds. Location of photo is shown in Figures 4.1, 4.5.

4.1.2 D_1 deformation event

D_1 is characterized by a penetrative S_1 cleavage and L_1 lineation. For ease of interpretation, the map area has been divided into four structural domains, based on the consistency of S_0 and S_1 orientation patterns within each domain. For instance, in the West and South domains, sandstones and argillites of the Miahuatepec Formations show S_0 and S_1 better than in the North and East domains, as well as the average orientation of S_0 and/or S_1 between the four domains is different (Figure 4.1 and the map in Appendix 6). Stereoplots of S_0 and S_1 are contained in figure A5.1 of Appendix 5.

4.1.2.1 West domain

Excellent D_1 structures are observed in turbiditic sandstone of the Miahuatepec Formation along La Mina creek in the West domain (Figure 4.5). S_1 is expressed as an E-verging, continuous, slaty cleavage defined by sericite and chlorite in mudstone beds and by a disjunctive pressure solution cleavage in sandstone beds (Figure 4.6). S_1 usually strikes SSE and locally dips more steeply (up to 20°) to the W than bedding, which is near horizontal in orientation (Figure 4.6). S_1 is axial planar to inclined to recumbent, E to NE-verging, F_1 folds (Figures 4.7 to 4.9). F_1 folds trend and plunge shallowly (<20°) to the N to NW. The vergence direction is defined as the vector perpendicular to F_1 fold axes and perpendicular to the intersection lineation between S_1 and bedding on the long limb of F_1 folds. It is opposite in direction to the dip direction of S_1 and F_1 axial plane. The poles to S_1 and the poles to the short limb and long limb of F_1 folds are plotted in Figure 4.10a. Because the long limb of F_1 folds is near horizontal, the intersection lineation between bedding and S_1 is also near horizontal. Therefore, the vergence direction can be represented as a horizontal NE-directed vector (open arrow in Fig. 4.10a), which is opposite in trend to the dip direction of the great circle representing the mean S_1 orientation. Because the vergence directions are near horizontal, they can be represented on rose diagrams (Figure 4.10b) where they plot in the northeast

quadrant with maxima oriented northeast and east-northeast.

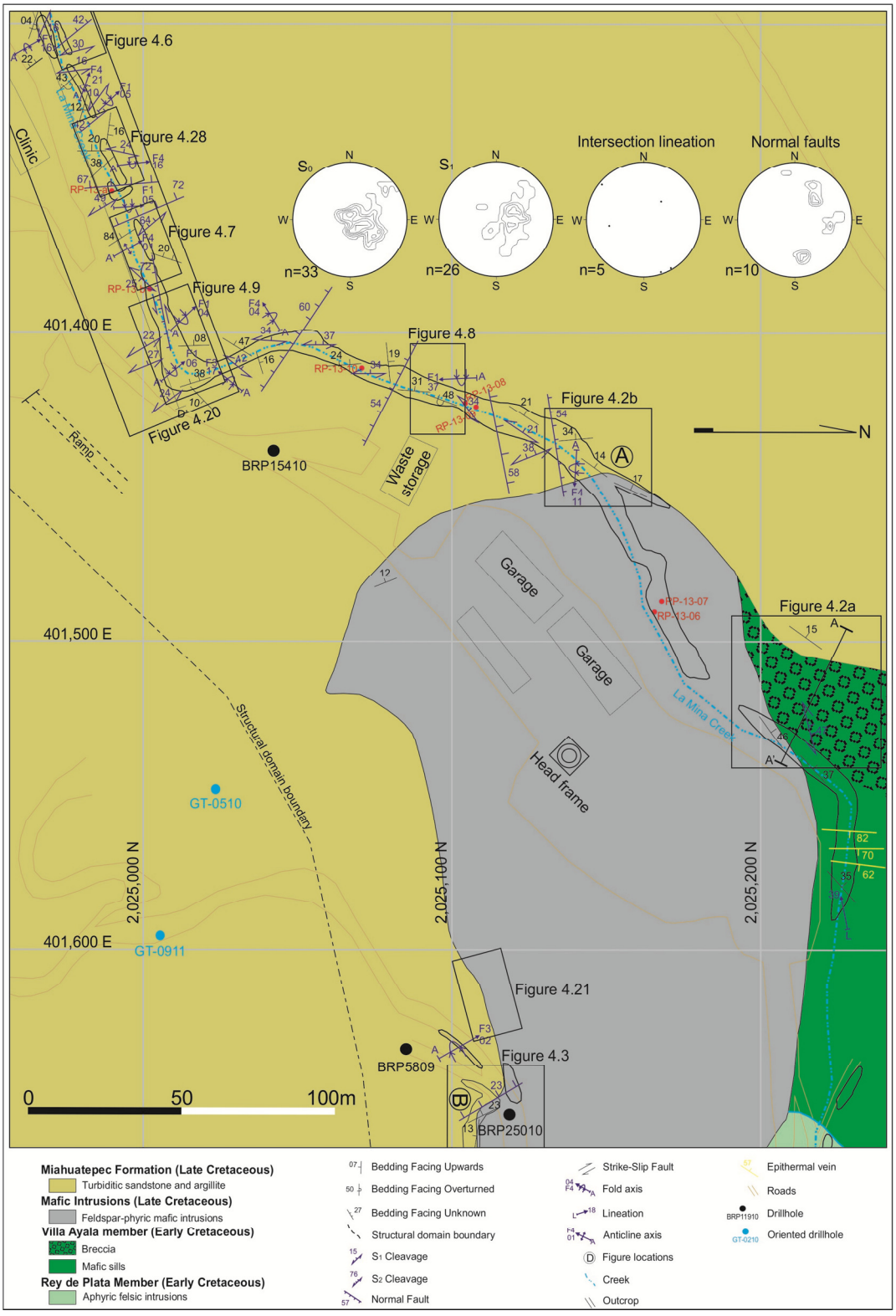

Figure 4.5. Geological map of the West domain.

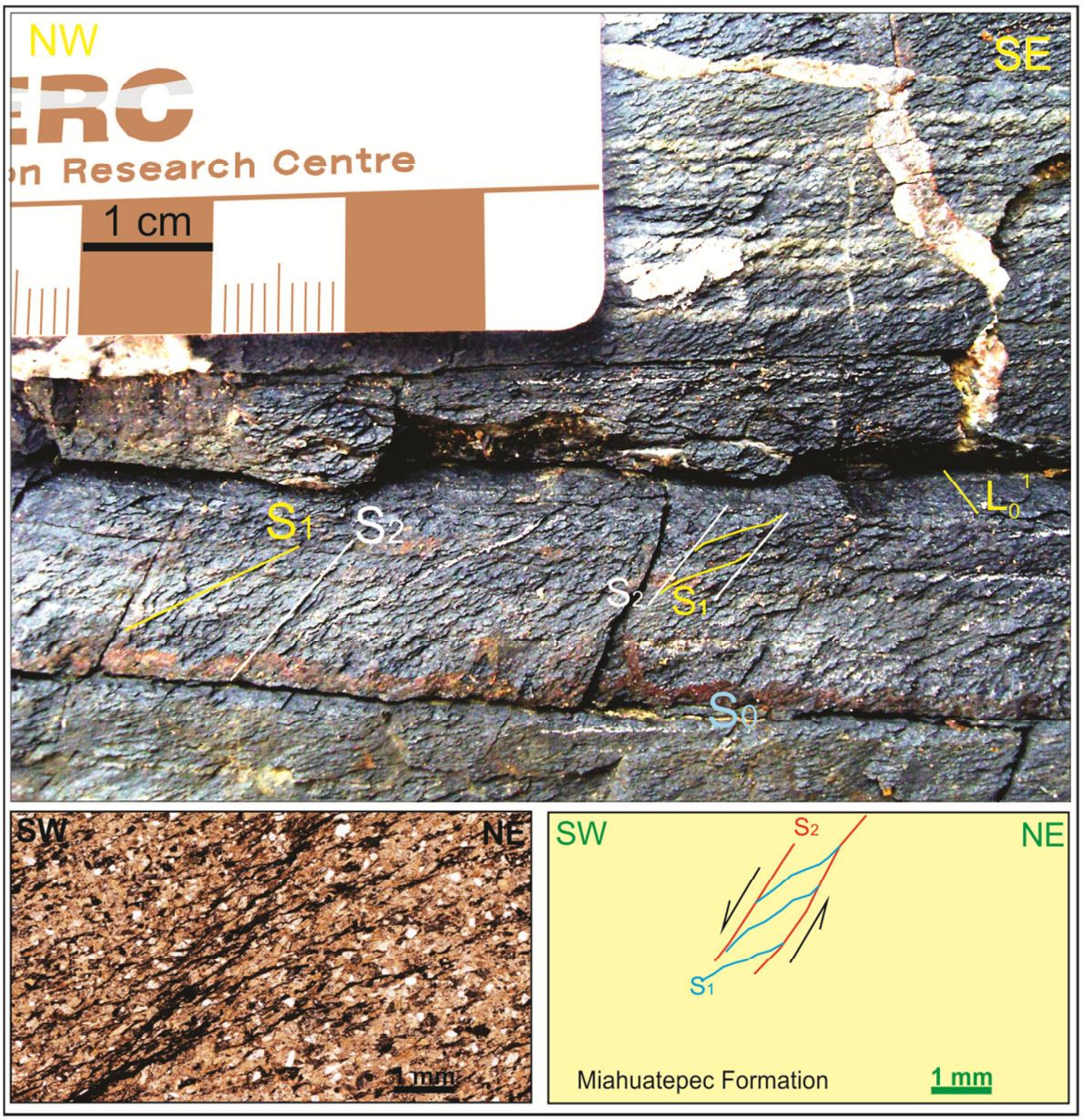

Figure 4.6. East-verging S_1 slaty cleavage with west-verging normal-slip S_2 cleavage and L_0^1 intersection lineation in outcrop and thin section of the Miahuatepec Formation. Location of photo is shown in Figures 4.1, 4.5.

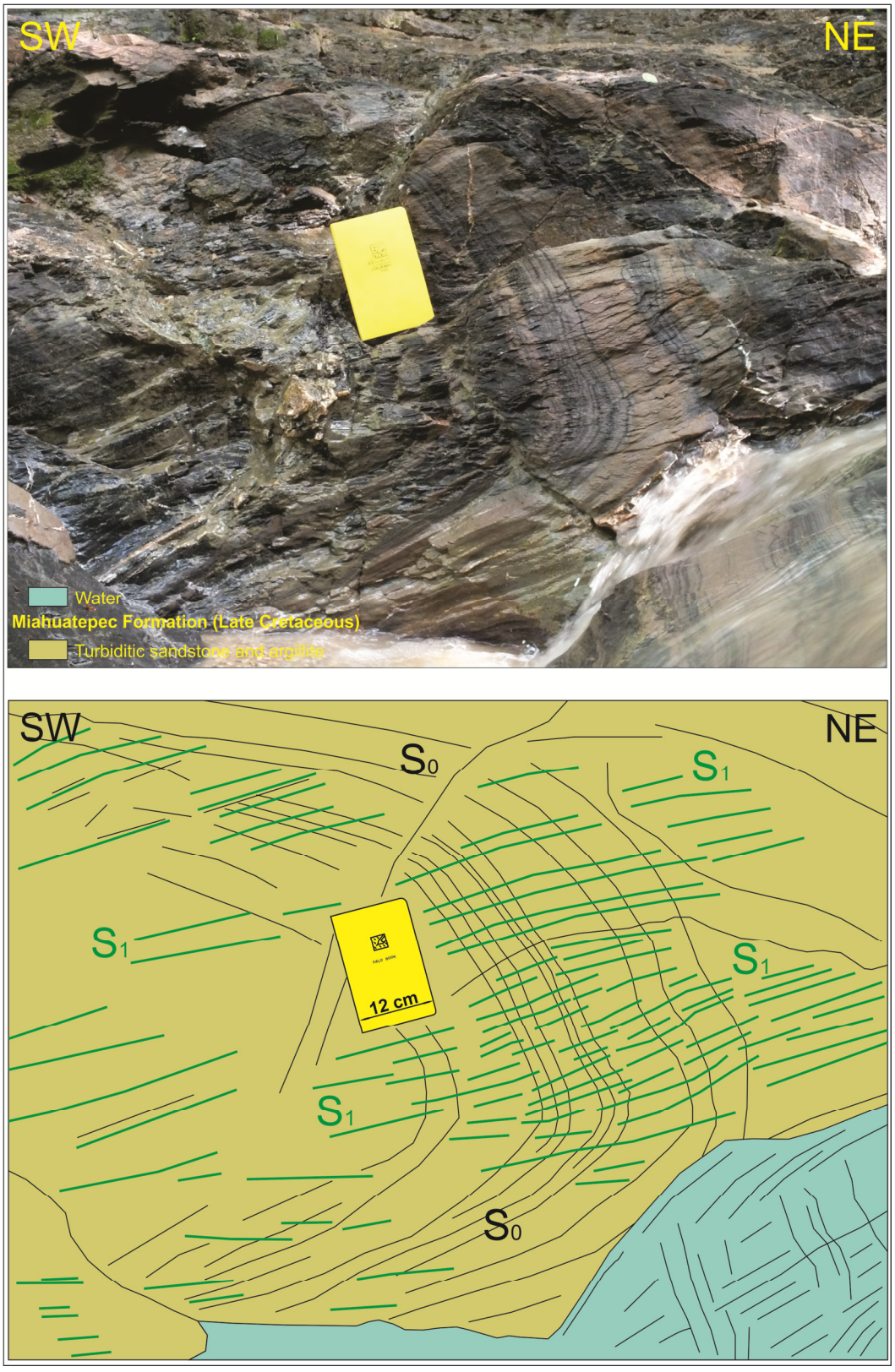

Figure 4.7. Northeast-verging, tight, F_1 fold with axial planar S_1 cleavage. Location of photo is shown in Figures 4.1, 4.5.

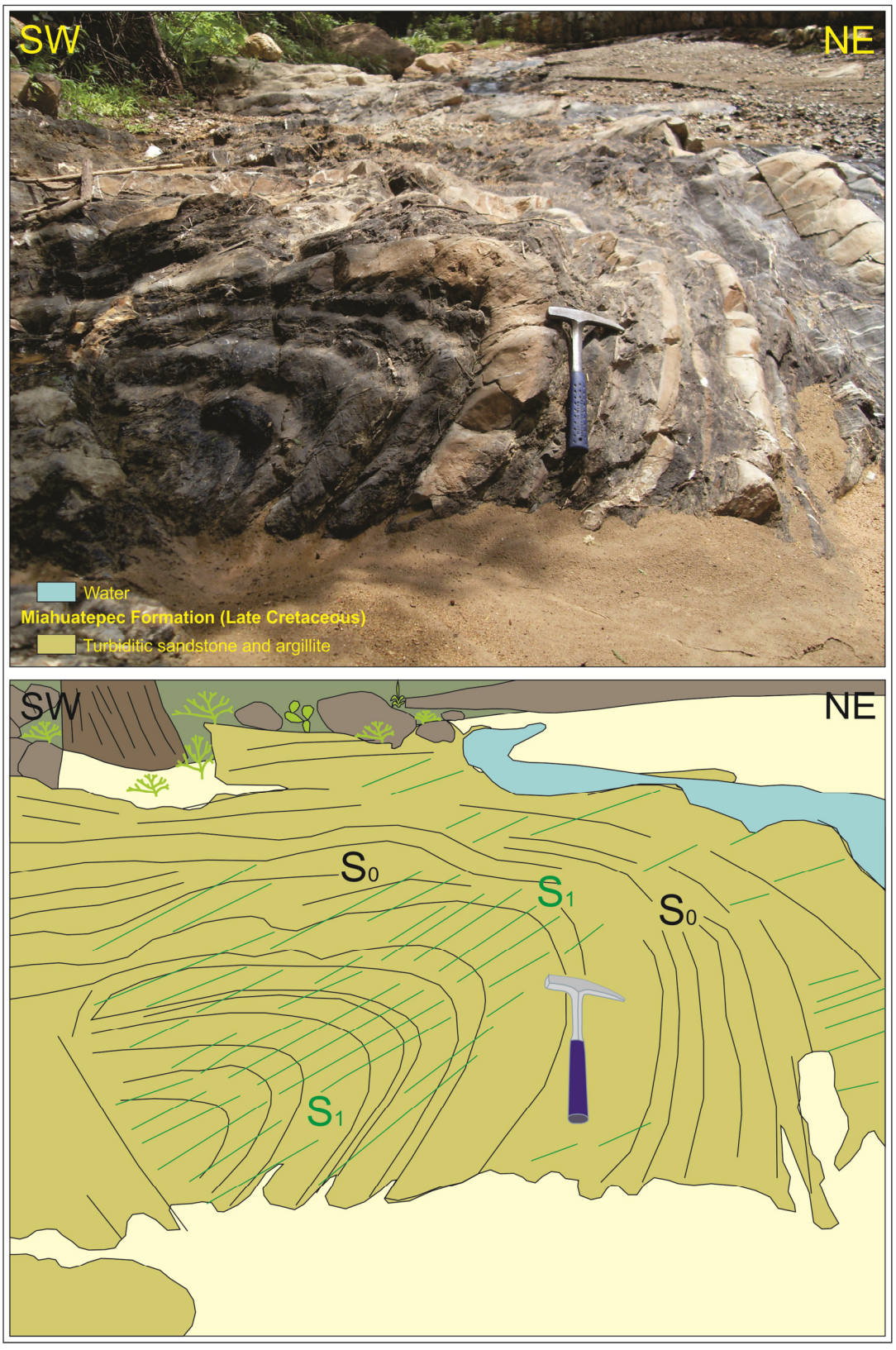

Figure 4.8. Northeast-verging, tight F_1 fold with axial planar S_1 cleavage. Location of photo is shown in Figures 4.1, 4.5.

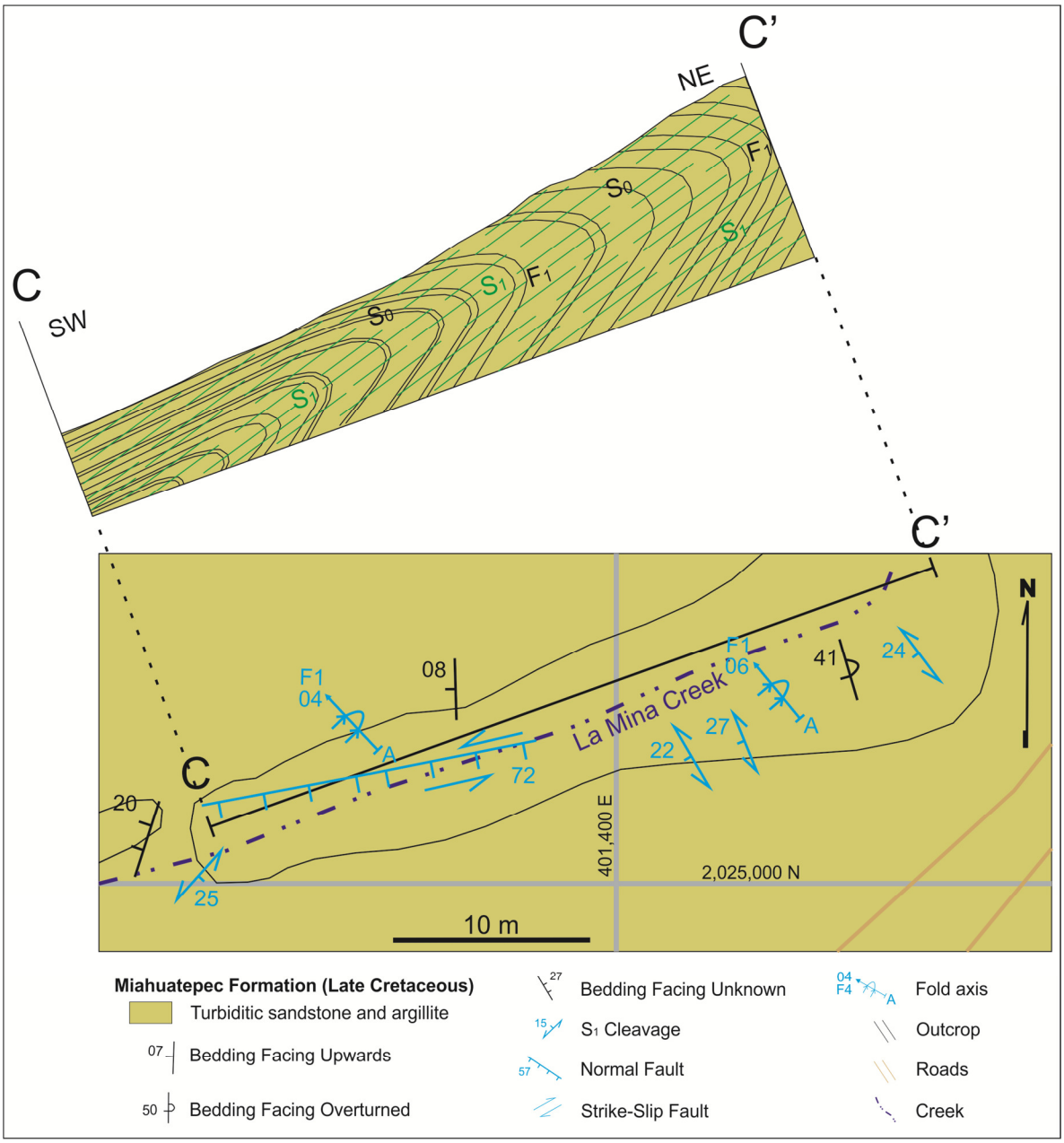

Figure 4.9. Northeast-verging, tight, F_1 folds in the Miahuatepec Formation. S_1 is steeper than bedding. Location of diagram is shown in Figures 4.1, 4.5.

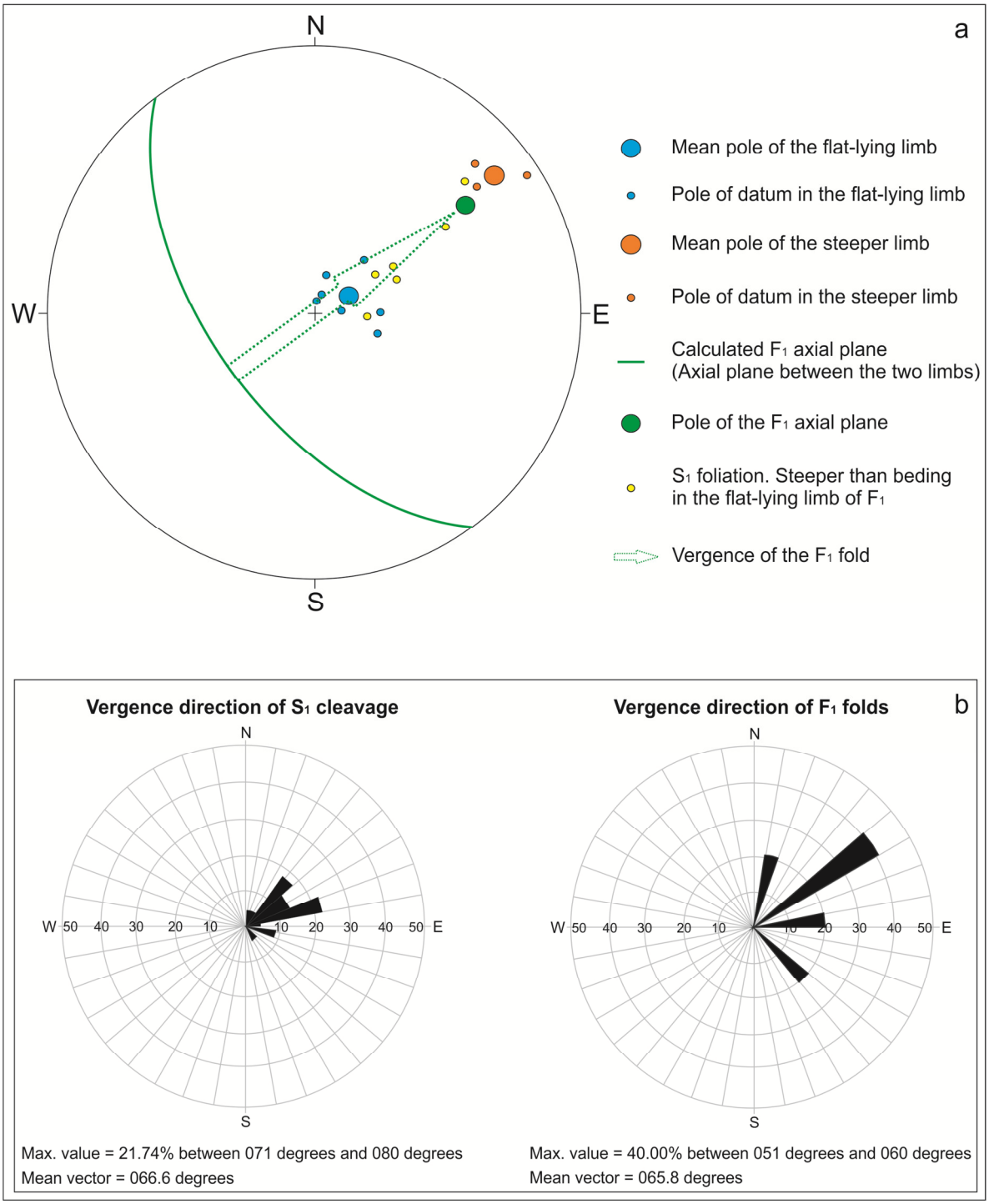

Figure 4.10. Vergence of F_1 folds determined from the attitude of their limbs and S_1 (a), and rose diagrams showing the vergence direction of S_1 and F_1 folds (b).

4.1.2.2 North domain

In the North domain (Figure 4.11), S_1 is expressed as a continuous cleavage defined by recrystallized quartz micro-lenses and by either sericite in the Rey de Plata member or chlorite in the Villa Ayala member. S_1 is SSW striking and WNW dipping. A W-plunging, down-dip, mineral stretching lineation (L_1) is present on S_1 planes. It is defined by elongated quartz-feldspar ridges alternating with white mica-rich grooves in the Rey de Plata rhyolite and by elongate mafic fragments and amygdules in Villa Ayala mafic volcaniclastic rocks and flows. Only one F_1 fold is present. The fold plunges to the NW and is overturned towards the NE.

4.1.2.3 East domain

In the East domain, S_1 strikes SSW and dips 20° to 70° to the WNW (Figure 4.12). L_1 has an average plunge ranging between 41° and 56° towards the WNW (Figure 4.13). At location C (Figure 4.12), S-C fabrics suggest top-to-the-southeast movement, which is consistent with the general ESE-vergence of the S_1 foliation (Figure 4.14).

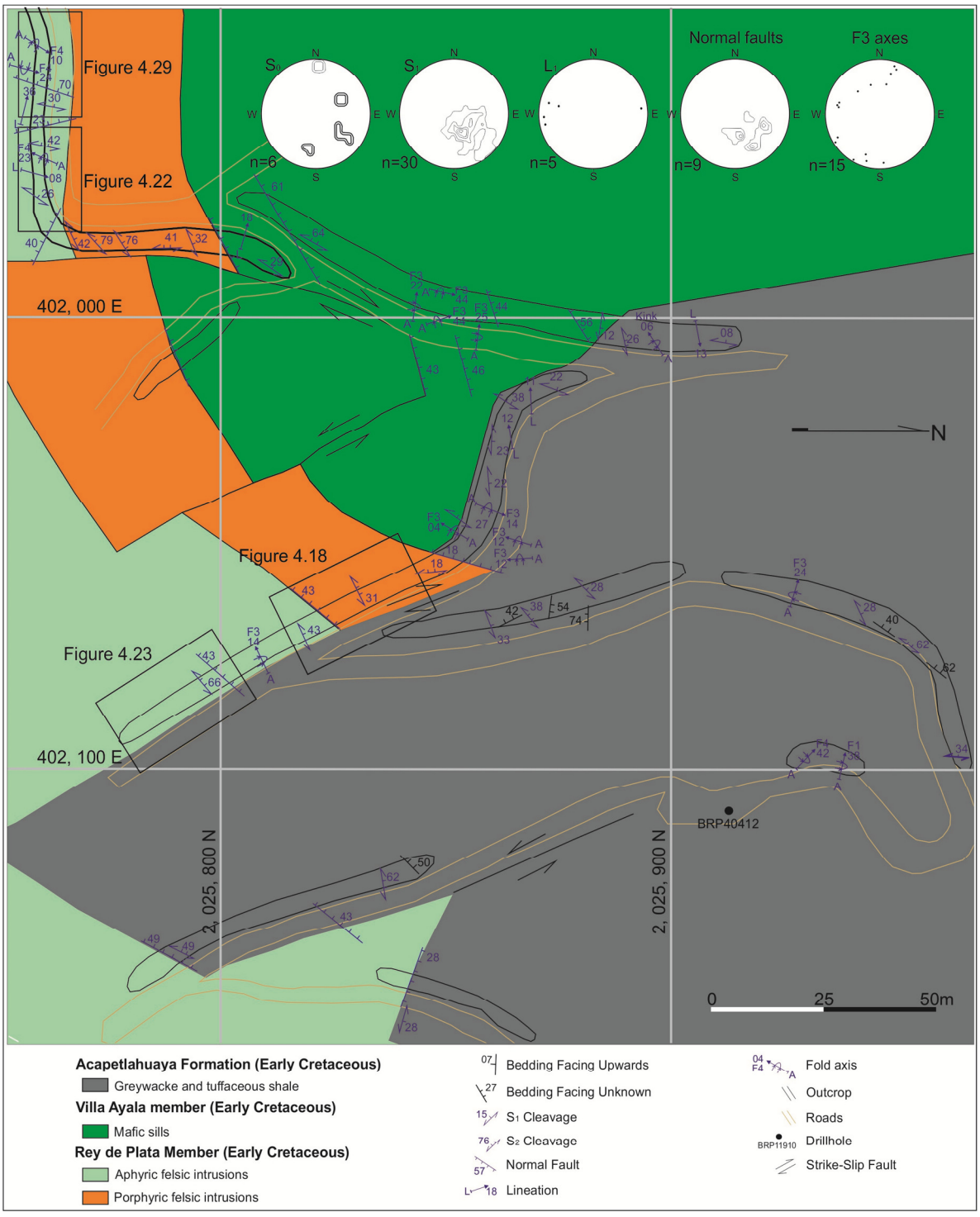

Figure 4.11. Geological map of the North domain.

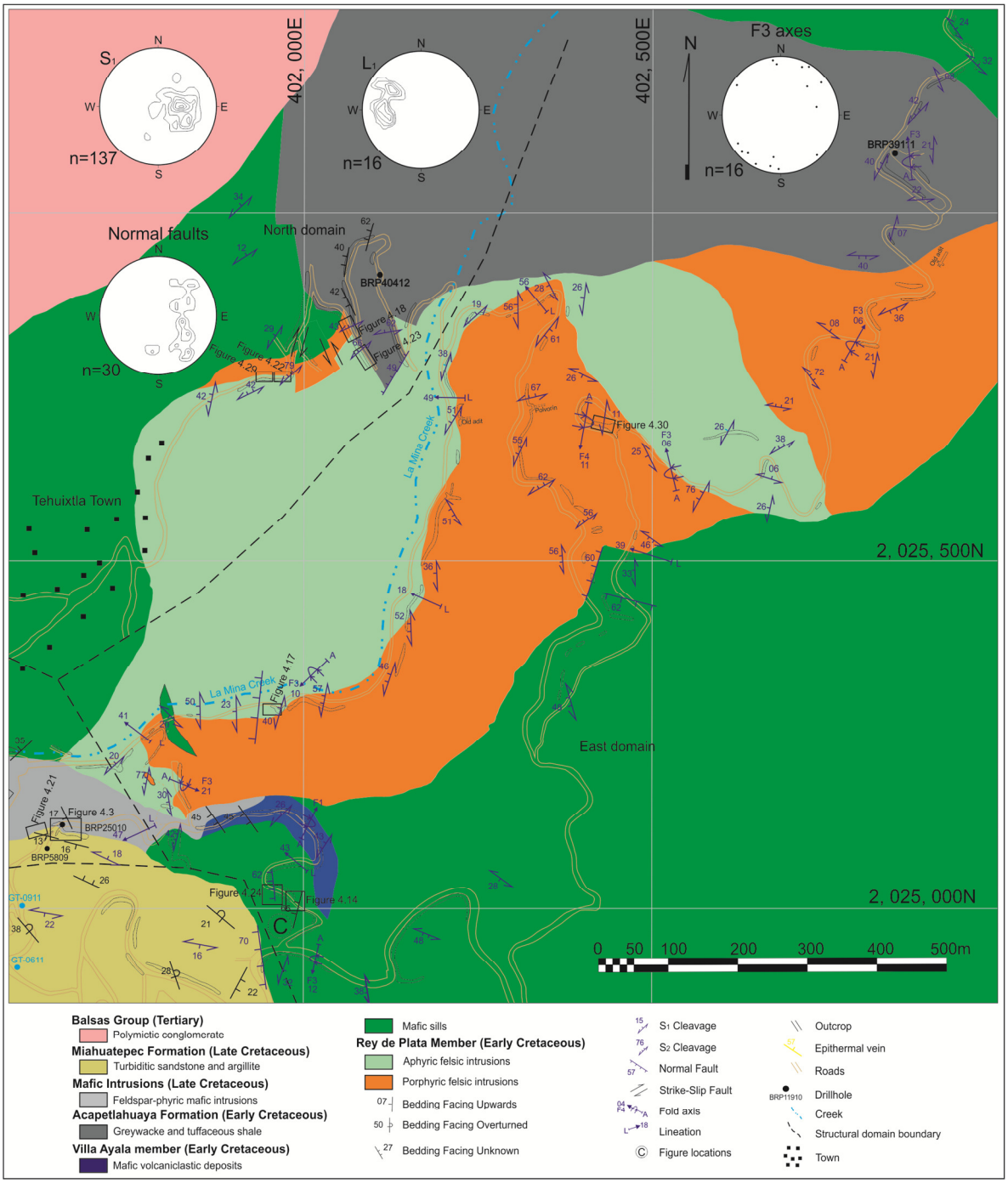

Figure 4.12. Geological map of the East domain.

Figure 4.13. L_1 lineation along shallowly-dipping, S_1 foliation in rhyolite of the Rey de Plata member. Location of photo is shown in Figures 4.1, 4.12.

4.1.2.4 South domain

In the South domain, S_1 has the same SE strike as bedding, but it dips more steeply to the SW (Figure 4.15). It is axial planar cleavage to NE-verging, F_1 folds plunging NW (Figure 4.16). The intersection between bedding and S_1 defines a shallowly, SE-plunging, L_0^1 intersection lineation which is well expressed in the southeastern area of this structural domain. Structural measurements from 6 oriented drillholes yielded a mean, E-verging, S_1 cleavage, striking S and dipping W, as well as a shallowly, WSW-plunging, L_1 stretching lineation. The location of the drill holes is shown in Figure 4.15.

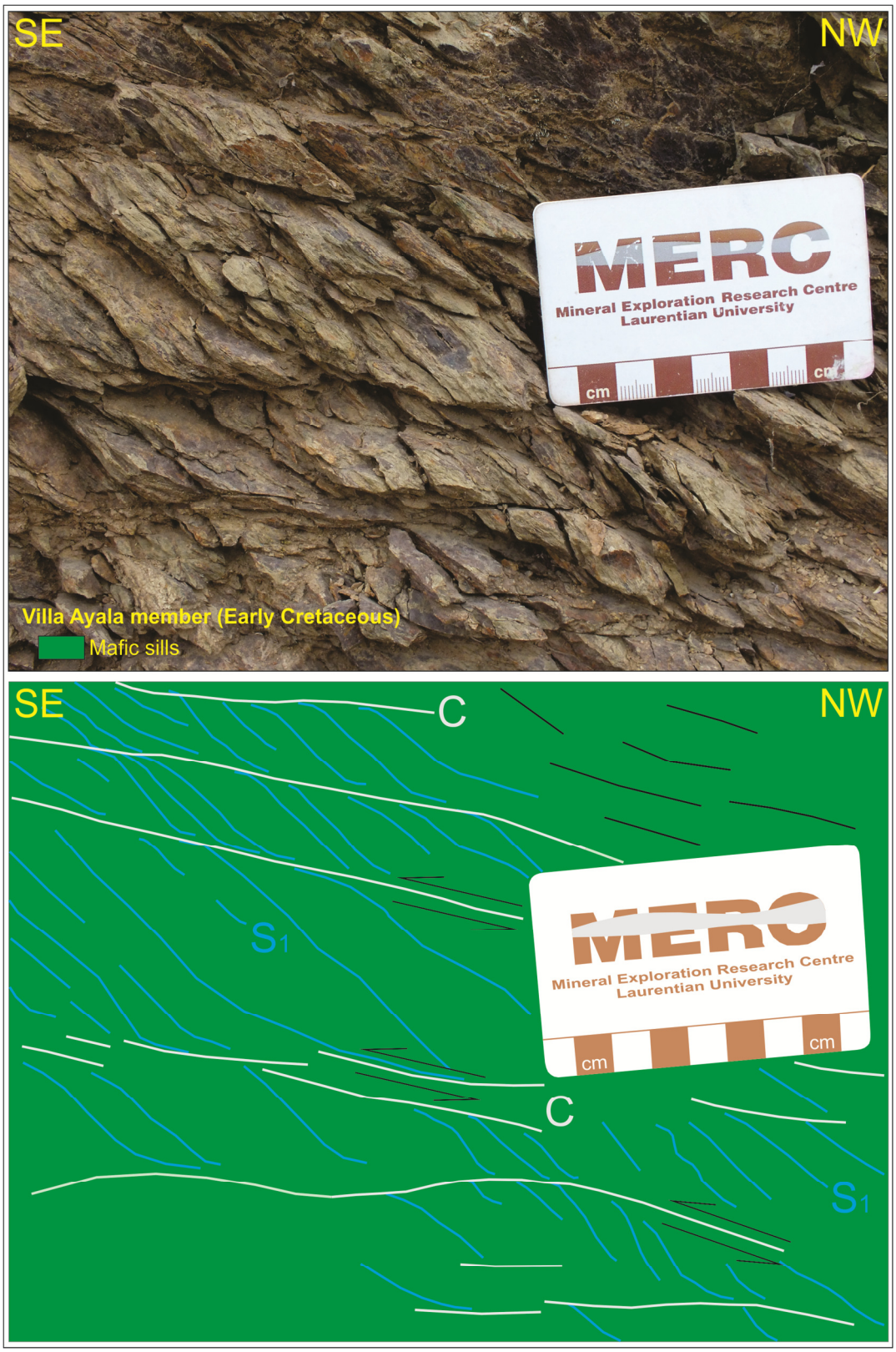

Figure 4.14. S-C fabrics defining an upwards top-to-the-southeast movement. S_1 is dragged by C fabrics. Location of photo is shown in Figures 4.1, 4.12.

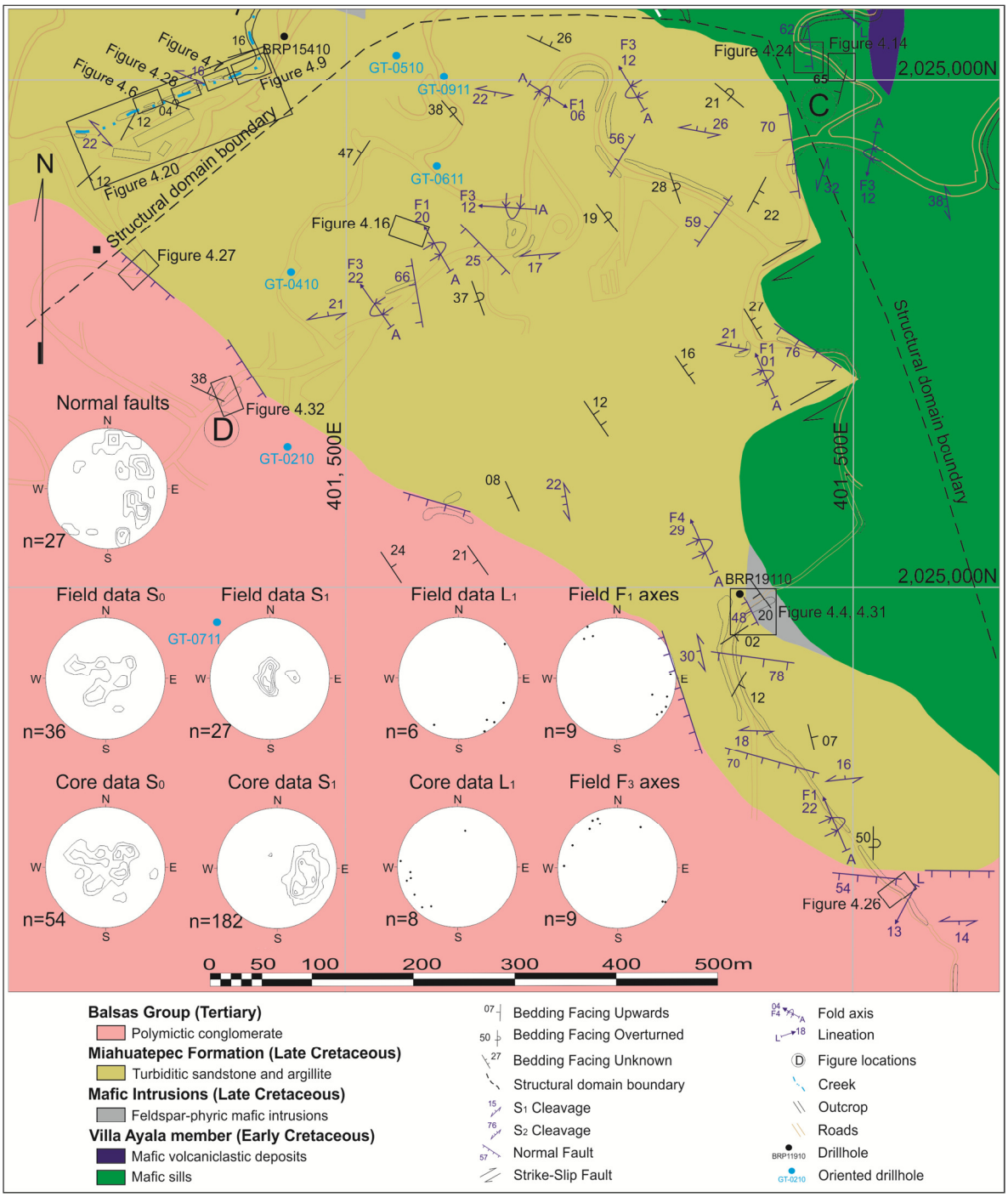

Figure 4.15. Geological map of the South domain.

Figure 4.16. Northeast-verging, F_1 fold in the Miahuatepec Formation. Location of photo is shown in Figures 4.1, 4.15.

4.1.3 D_2 deformation event

The most prominent D_2 structure is a spaced cleavage (S_2) with a spacing of a few centimeters. Overprinting of S_1 by S_2 is observed in volcanic rocks of the Villa Ayala and Rey de Plata members and in turbiditic sandstone of the Miahuatepec Formation. The two cleavages are not present in the conglomerates of the younger Balsas Group, suggesting that D_2 predates the deposition of the conglomerate.

4.1.3.1 West domain

In the West domain (Figure 4.5), S_2 is defined by chlorite in turbiditic sandstone. S_2 usually has the same S to SE strike as S_1 but it dips to the WSW more steeply (40°-70°) than S_1 (<40°). S_1 is dragged in normal fashion along S_2, suggesting top-to-the-west normal movement (Figure 4.6). In the East domain, altered Rey de Plata rhyolite has the same strong S_1 and S_2 foliations. S_2 has similar strike and dip

as measured in the West domain. S_1 is rotated in normal fashion along S_2, which is consistent with the asymmetry of drag folds overprinting S_1 (Figure 4.17).

4.1.3.2 North and East domains

In the North Domain, within altered Rey de Plata rhyolite, the same S_1 and S_2 overprinting relationships are observed as in the East and West domains, but S_2 differs slightly in strike (SSW) and dip (42°-79° to WNW) (Figure 4.18).

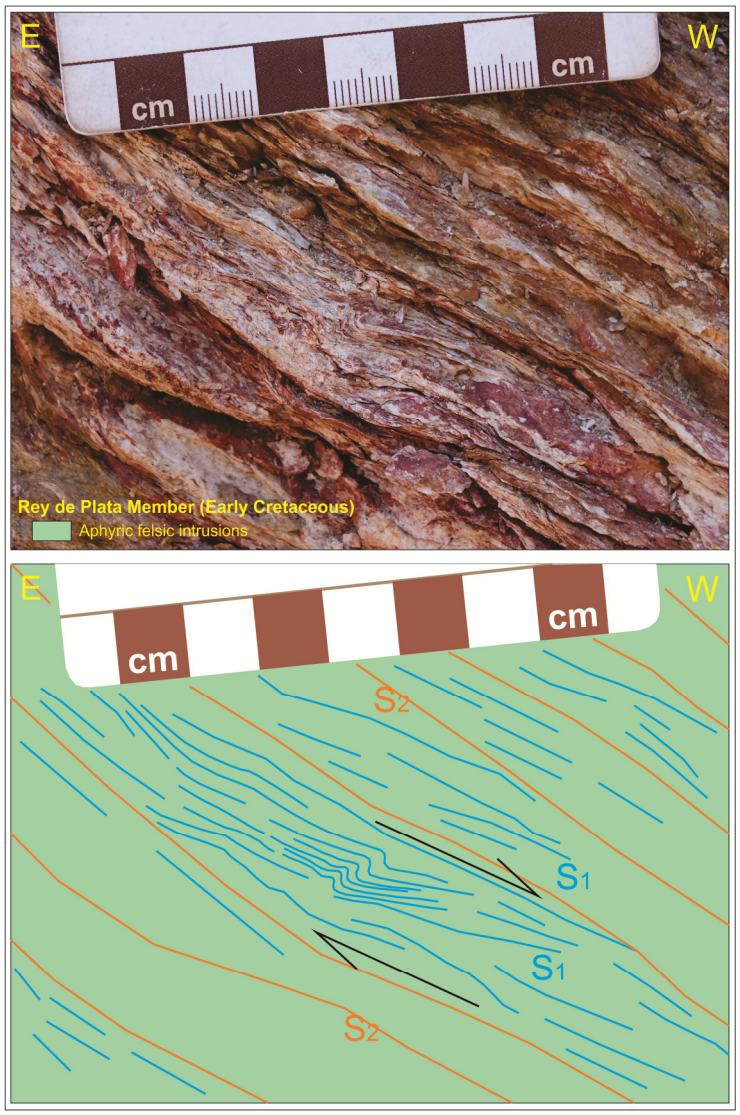

Figure 4.17. West-directed normal movement suggested by the dragging of S_1 along S_2 and by asymmetrical folding of S_1. Location of photo is shown in Figures 4.1, 4.12.

Figure 4.18. East-verging S_1 slaty cleavage with west-verging normal-slip S_2 cleavage. Location of photo is shown in Figures 4.1 and 4.11.

4.1.3.3 South domain

In the South domain (Figure 4.15), S_2 is expressed as a normal-slip spaced cleavage in turbiditic sandstone of the Miahuatepec Formation. S_2 strikes WNW and dips between 21° and 26° to the NNE. The dip of S_2 is opposite to that in the other structural domains, likely due to either superimposed F_4 folding or D_3 normal faulting. In oriented drill cores through volcanic rocks of the Villa Ayala member, the overprinting of S_1 by S_2 suggests top-to-the-southwest normal movement, similar to that observed in the other structural domains (Figure 4.19).

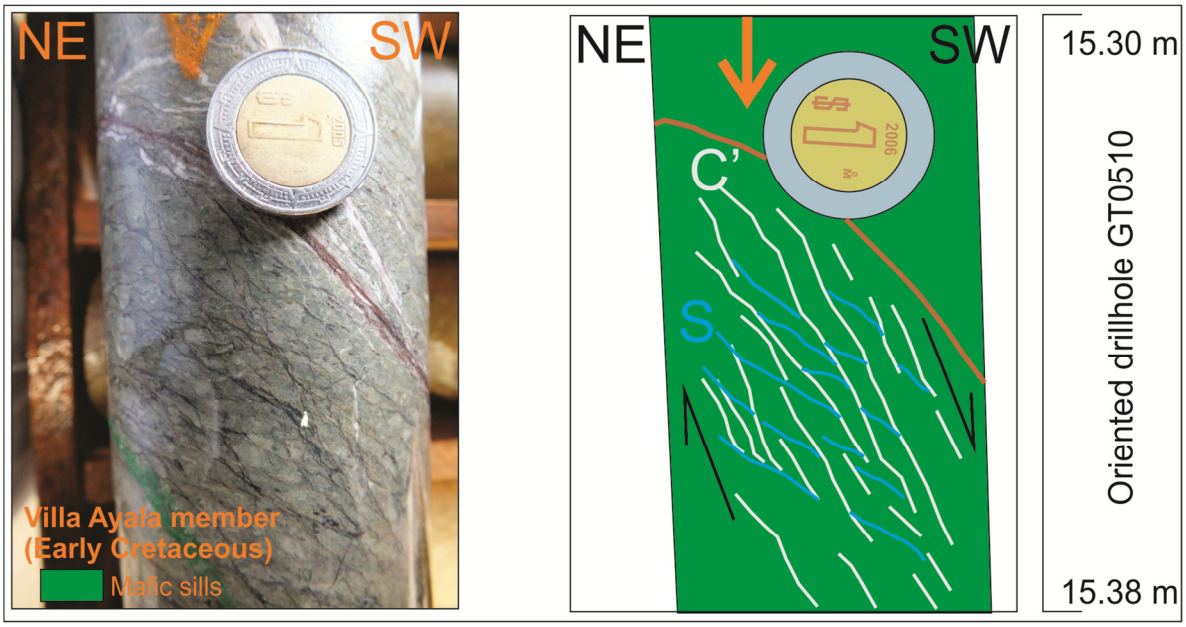

Figure 4.19. S-C' fabrics in drillhole cores defining a SW normal movement. The S_1 foliation, which represents the S fabric, is dragged by the S_2 cleavage, which represents the C' fabric.

4.1.4 D_3 deformation event: Normal and transfer faulting

D_3 is a west-directed extensional event similar in transport direction to D_2. D_3 differs from D_2 in that it produced discrete brittle fault zones that cut across S_1 and S_2.

4.1.4.1 West domain

In the West domain (Figure 4.5), shallowly to steeply-dipping, D_3 brittle faults cut across S_1 and F_1 folds in turbiditic sandstones of the Miahuatepec Formation. The faults generally strike SE and dip 40°-70° to the SW but a few strike WSW and dip 50°-60° to the NNW (Figure 4.20). F_3 drag folds are associated with the faults. This can be seen at location B in Figure 4.1, where a F_3 drag fold in the hanging wall above a fault is folding both S_1 and S_2 cleavages (Figure 4.21a). The fault is at the contact between turbiditic sandstone of the Miahuatepec Formation and underlying volcanic rocks of the Villa Ayala member. S_1 and S_2 are dragged in

normal fashion along the fault (Figure 4.21b), which is consistent with normal slip along the fault as indicated by the west vergence of the F_3 drag fold.

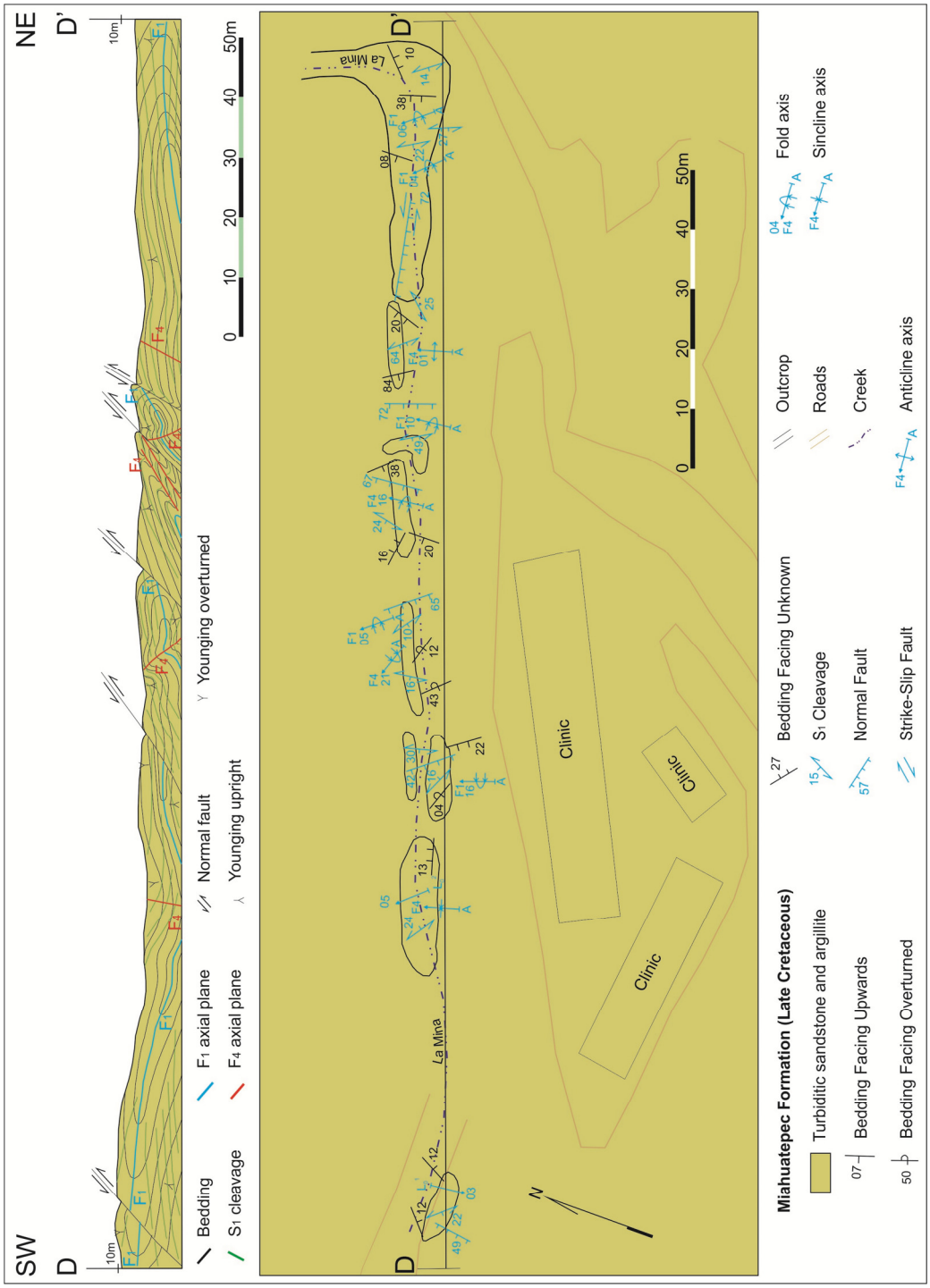

Figure 4.20. Open to tight, NE- and SW-verging F_4 folds overprinting large recumbent F_1 folds, which are transected by D_3 normal faults. The section is along La Mina creek in the West domain. Location of photo is shown in Figures 4.1, 4.5.

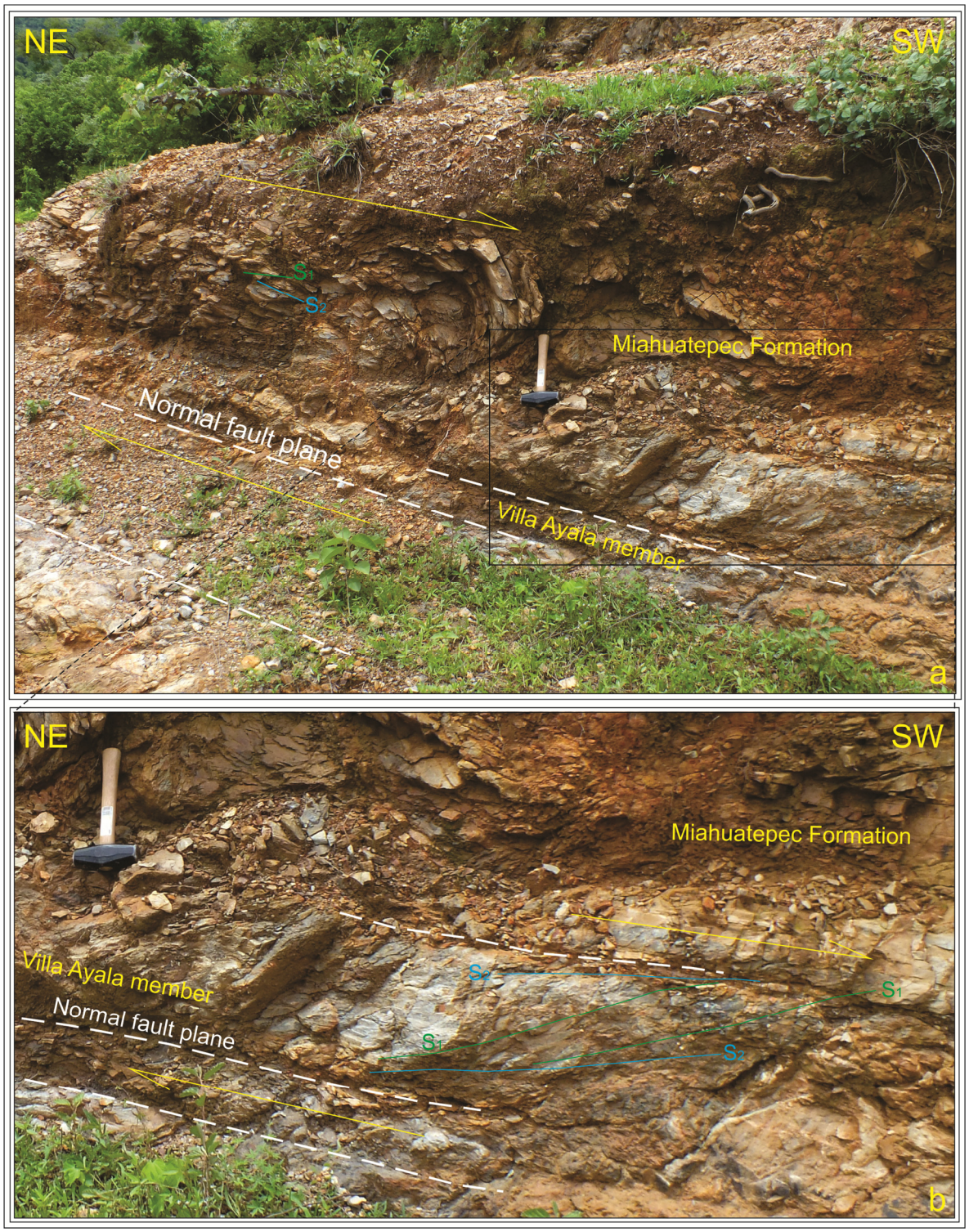

Figure 4.21. Southwest-verging F_3 fold over a D_3 normal fault plane (a); inset of the fault showing a sliver of volcanic rocks of the Villa Ayala member between two normal fault planes. S_1 and S_2 are dragged in normal fashion along the faults, consistent with normal slip movement along the faults (b). Location of photos is shown in Figures 4.1, 4.5.

4.1.4.2 North domain

In the North domain (Figure 4.11), WSW striking and NNW-dipping normal faults (Figure 4.22) are linked by NNW-striking transfer faults which are not exposed but have been inferred by the offset of units. F_3 folds adjacent to the normal faults are generally NW-verging and NNE-SSW-plunging, suggesting normal dip-slip movement along the fault (Figure 4.23).

Figure 4.22. D_3 normal faults in North domain. Location of photo is shown in Figures 4.1, 4.11.

Figure 4.23. Northwest-verging F_3 folds in the Rey de Plata member. Location of photo is shown in Figures 4.1, 4.11.

4.1.4.3 East domain

Normal faults are well exposed on road cuts across volcanic rocks of the Villa Ayala member in the East domain (Figure 4.12). The faults are SSE-striking and moderately WSW-dipping. SW-verging and NW-verging F_3 folds, folding both S_1 and S_2, formed during faulting (Figure 4.24).

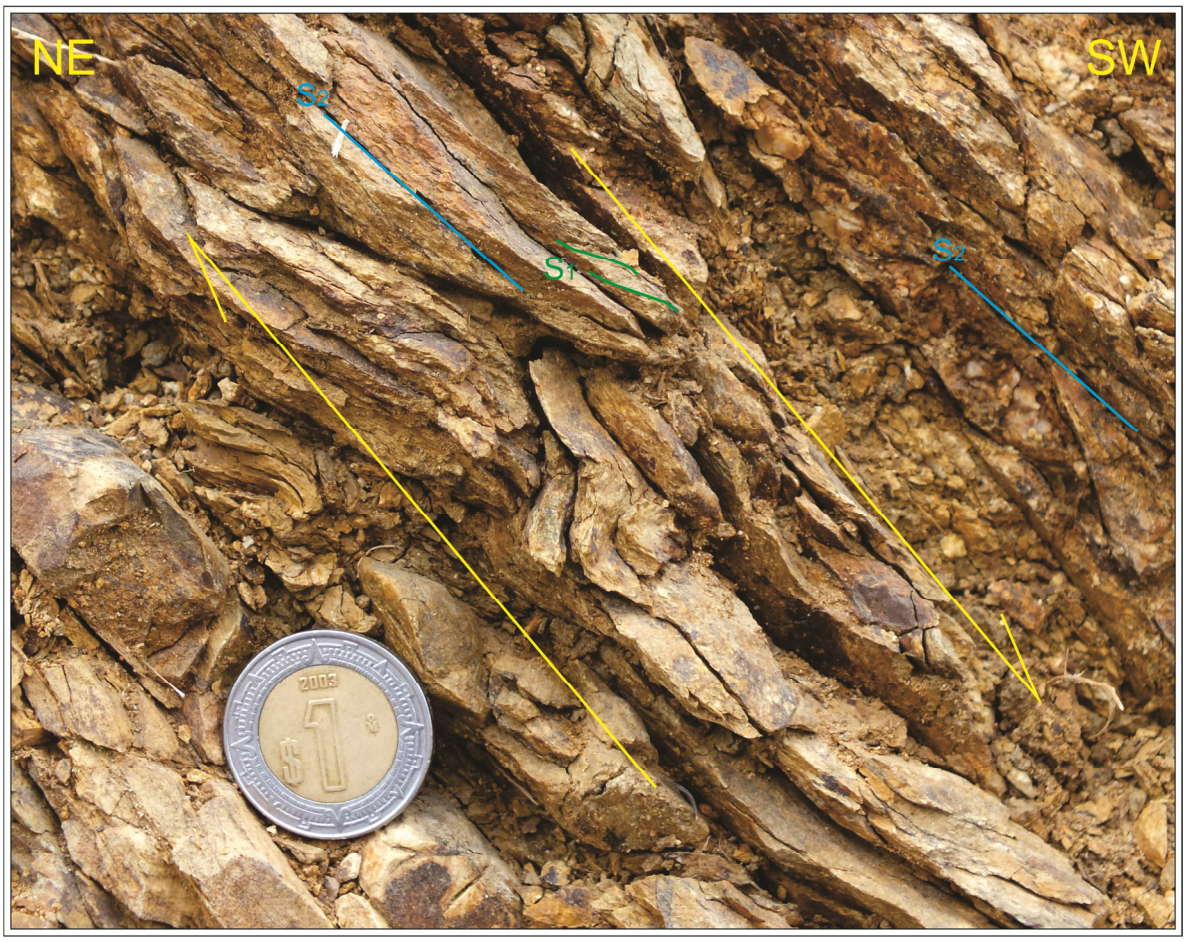

Figure 4.24. S_1 and S_2 folded by southwestwards normal faulting. Location of photo is shown in Figures 4.1, 4.12.

4.1.4.4 South domain

In the South domain (Figure 4.15), normal faults generally strike S to SE and dip 25º to 70º to the W to SW. They occur at the contact between the Miahuatepec Formation and Villa Ayala member both in drill core (Figure 4.25) and in outcrop. They are linked on the map by dextral SW-striking transfer faults (Figure 4.15). SW-verging F_3 folds with SE- and NW-plunging folds axes fold S_1 and S_2 in Miahuatepec sandstone within the southern part of the domain. Similar fold orientations and overprinting relationships are observed in oriented drill core that intersects the Rey de Plata member below the exposed Miahuatepec sandstone.

The contact between the younger Balsas conglomerate and underlying Miahuatepec sandstone can be traced across the South domain (Figure 4.15). Where exposed, this contact was reactivated as an ESE- to SE-striking, SW-dipping, fault. The rotation of an oblique shape fabric into a shear fabric parallel to the contact between the two units (Figure 4.26), and dragging of bedding along the faults (Figure 4.27), suggest top-to-the southwest normal movement parallel to the dip of the faults.

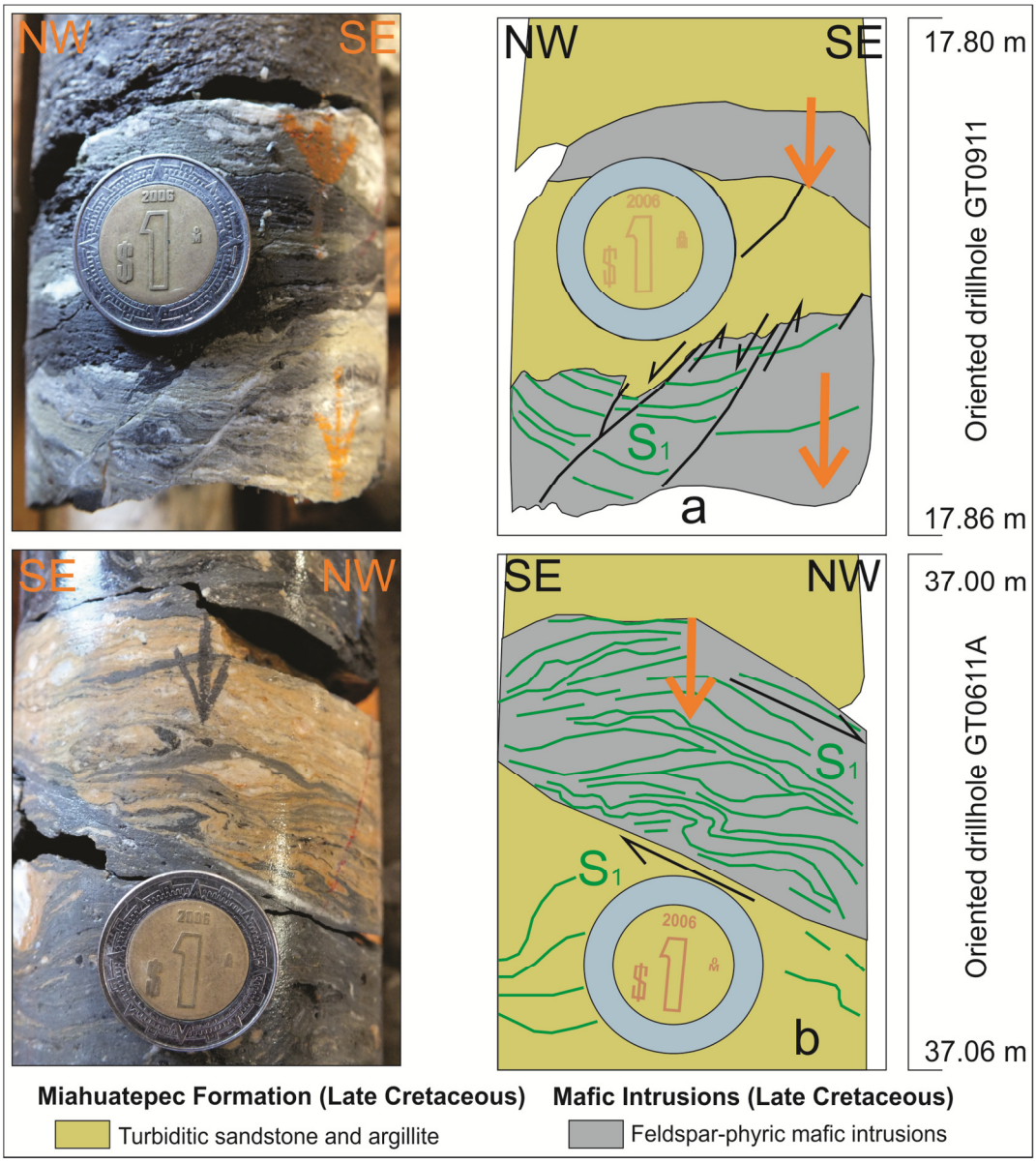

Figure 4.25. Normal movement along the contact between the Miahuatepec Formation and the Feldspar-phyric mafic intrusion (a and b). Orange arrows indicate down-hole direction.

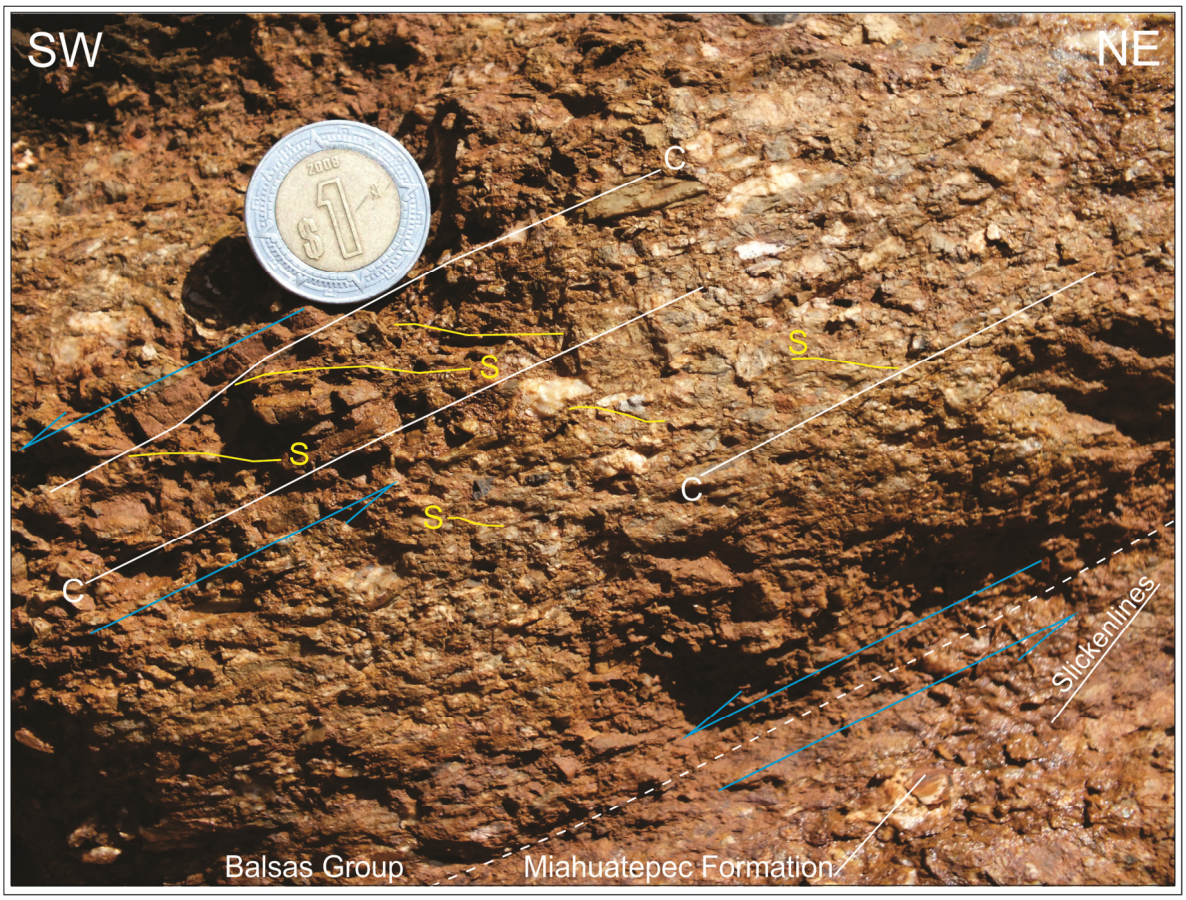

Figure 4.26. Normal fault at the contact between the Balsas Group and the Miahuatepec Formation. S fabric is rotated into a C fabric which is parallel to the contact between the Balsas conglomerate and Miahuatepec sandstone. Location of photo is shown in Figures 4.1, 4.15.

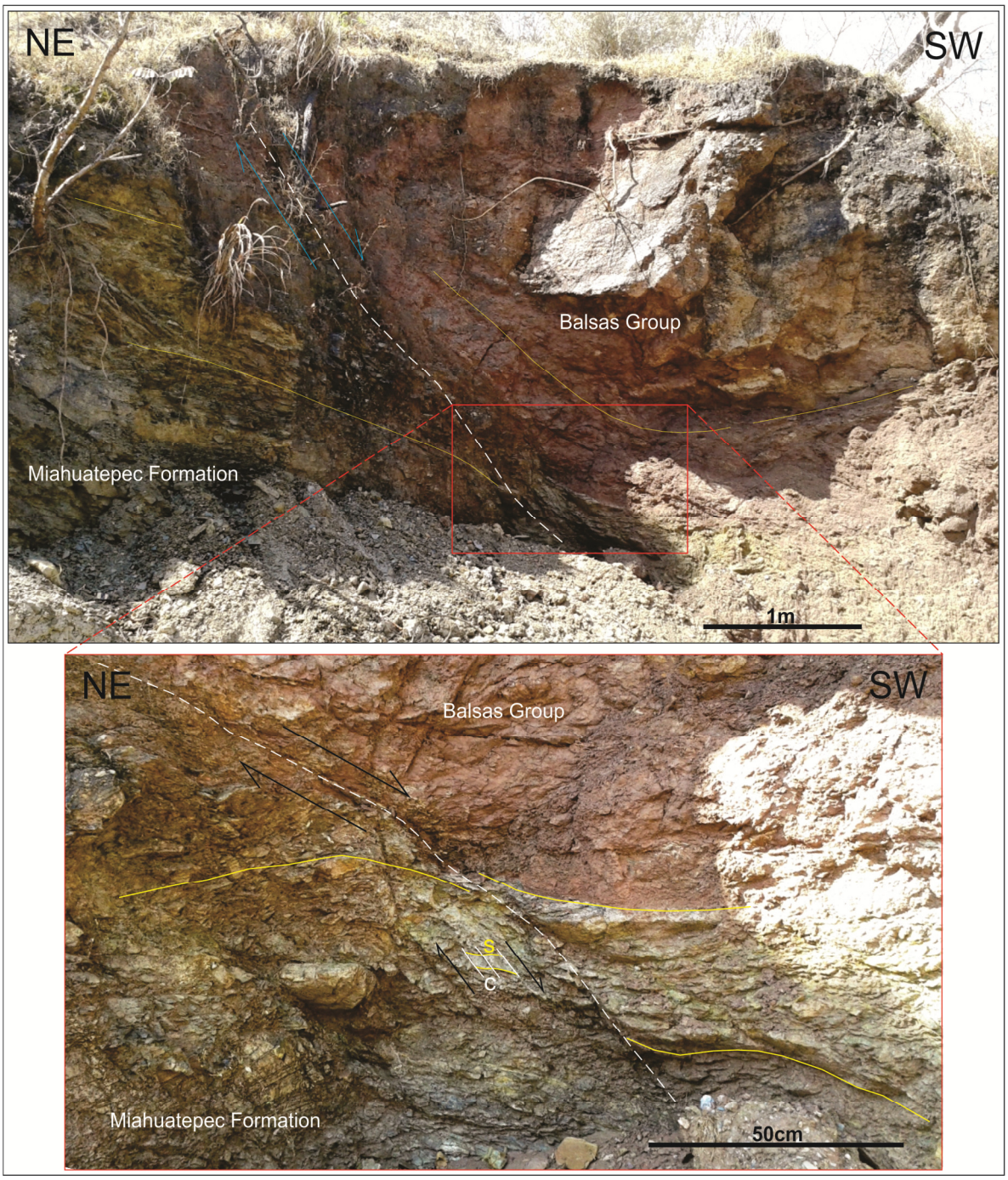

Figure 4.27. Dragging of bedding along a normal fault between the hanging wall Balsas conglomerate and footwall Miahuatepec sandstone. Location of photo is shown in Figures 4.1, 4.15.

At the intersection between the roads that lead to the towns of Tehuixtla and Ahuehuetla, where sample D is placed in the map (Figure 4.15), tilted beds of Balsas conglomerate overlie Miahuatepec turbiditic sandstone which is exposed

below this outcrop at lower elevation. The contact between the two units is not exposed but the tilting of the beds likely occurred during rotational movement along a normal fault at the contact between the two rock units (Figure 4.28).

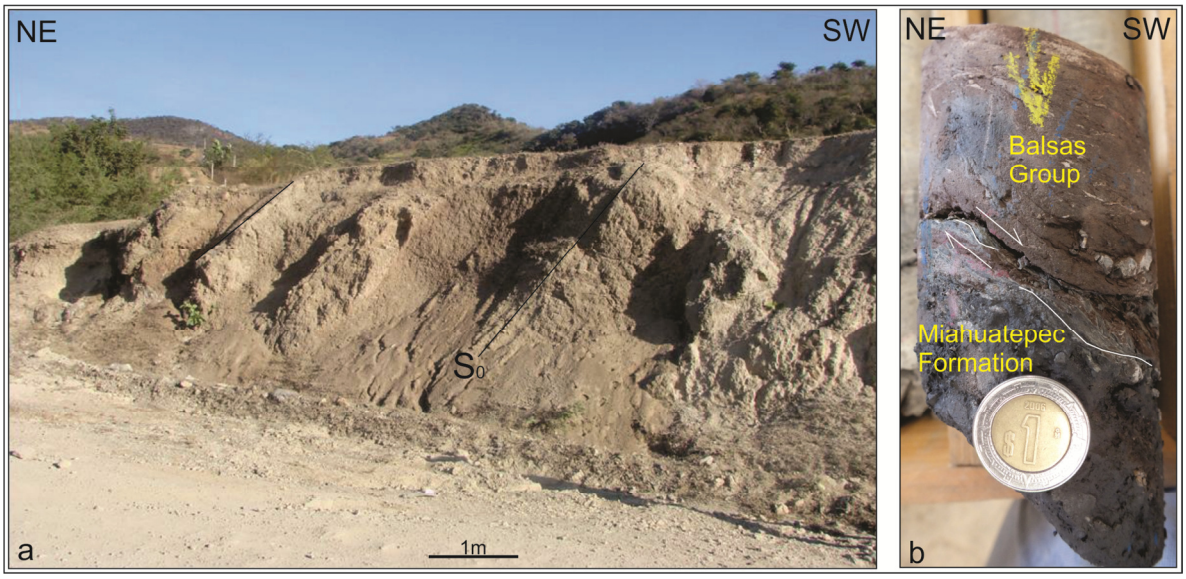

Figure 4. 28. Northeastwards tilting of the Balsas Group (a), core sample showing the contact between the Balsas Group and the Miahuatepec Formation due to normal faulting (b). Location of photo is shown in Figures 4.1, 4.15.

4.1.5 D_4 deformation event

D_4 is the last deformation event to affect the Rey de Plata VMS camp.

4.1.5.1 West and North domains

D_4 produced generally upright, open to tight, F_4 folds. The folds are well exposed in the section of turbiditic sandstone of the Miahuatepec Formation along La Mina creek (Figure 4.20) in the West domain (Figure 4.5). The folds vary in style from open folds, which gently bend large recumbent isoclinal F_1 folds, to tight, inclined, NE- and SW-verging folds, plunging shallowly (1° to 21°) to the NNW (Figure 4.20). The recumbent F_1 folds are offset by D_3 normal faults and the F_4 folds becomes tighter against the faults, which were locally reactivated as reverse faults during the

formation of the F_4 folds (Figure 4.29). Similar tightening of F_4 folds against reactivated normal faults is also observed in the North domain (Figure 4.30).

4.1.5.2 East and South domains

F_4 folds are defined by folded bedding and S_1 in turbiditic sandstone and by folded S_1 and S_2 in altered volcanic rocks. For example, an open, NE-plunging, F_4 fold at the old Rey Viejo mine in the East domain folds S_1 and S_2 in altered Rey de Plata rhyolite (Figure 4.31). Good examples of F_4 folds, folding S_1, S_2 as well as bedding, are also present in the South domain. The folds have NE-vergence and plunge 30° towards 310°. They occur in Miahuatepec turbiditic sandstone in normal fault contact with a feldspar-phyric mafic intrusion, which was emplaced along the contact between the turbiditic Miahuatepec Formation and the Villa Ayala member (Figures 4.4, 4.32).

Figure 4.29. Tight, NE-verging F_4 folds against a D_3 normal fault in the Miahuatepec Formation along La Mina creek in the West domain. Location of photo is shown in Figures 4.1, 4.5.

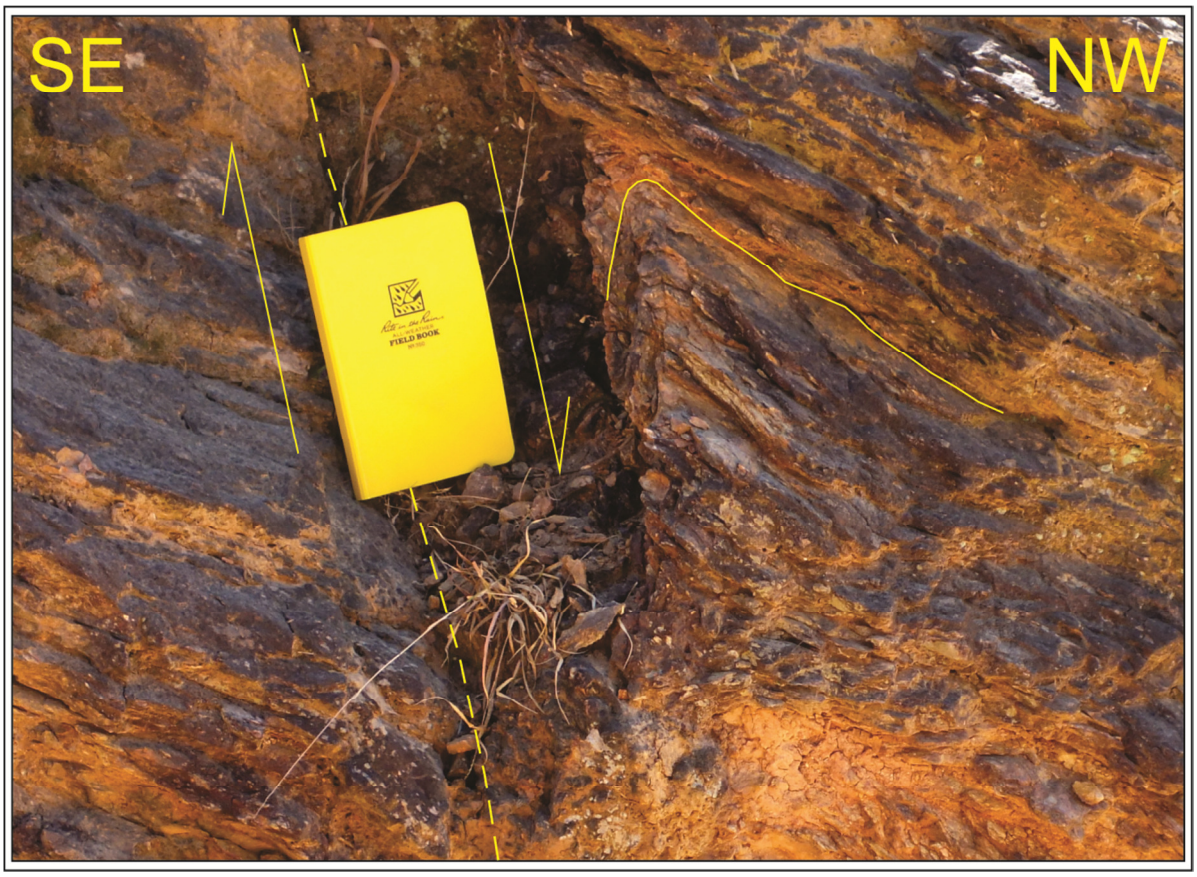

Figure 4.30. Tightening of SE-verging F_4 folds against reactivated normal faults in the North domain. Location of photo is shown in Figures 4.1, 4.11.

Figure 4.31. SE-verging F_4 folds defined by folded S_1 and S_2 in altered Rey de Plata rhyolite at the old Rey Viejo mine in the East domain. Location of photo is shown in Figures 4.1, 4.12.

Figure 4.32. Northeast-verging F_4 folds in turbiditic sandstone in normal fault contact with underlying feldspar-phyric mafic intrusion. Location of photo is shown in Figures 4.1, 4.15.

Northwest-verging kinkband folds were also identified in the area and are folding the S_1 and S_2 cleavages. They could have been generated either during D_3 or D_4.

4.2 Epithermal veins

Two types of veins are present at Rey de Plata. Both types fill fractures, strike SW-NE striking and are most abundant in volcanic rocks of the Villa Ayala and Rey de Plata members in the East domain (Figure 4.1). The first type is characterized by cryptocrystalline quartz bands oriented parallel to vein walls which, according with the classification of quartz veins as proposed by Dong et al. (1995), are defined as crustiform epithermal veins based on the geometrical relationships between individual crystals or crystal aggregates. Vein bands are intercalated with

brecciated wall rocks and by bands of either sphalerite ± pyrite ± galena (Figure 4.33a) or quartz ± pyrite (Figure 4.33b). Samples from drill core yielded gold values of up to 102 g/ton Au. The veins range up to 60 cm in thickness, typically strike SSE and dip WSW, and were emplaced parallel to S_1 and S_2. The second vein type commonly have a homogeneous appearance and often are not banded, which, according to the classification of quartz veins as proposed by Dong et al. (1995) are classified as massive epithermal veins, but are sometimes crustiform and composed of cryptocrystalline quartz, alternating with coarse pyrite bands with euhedral pyrite crystals up to 1 cm in size. The veins range up to 45cm in thickness. They cross-cut the first vein type as well as S_1 and S_2, but are also folded, boudinaged and offset parallel to S_2, suggesting that they were emplaced during D_2 (Figures 4.33c, d). The two vein types are offset by D_3 normal faults and by D_4 reverse reactivation of the normal faults.

Both epithermal vein sets formed post VMS mineralization as both cross-cut S_1. Therefore, the age of epithermal veins at Rey de Plata deposit is constrained between early Cretaceous to pre-Aptian.

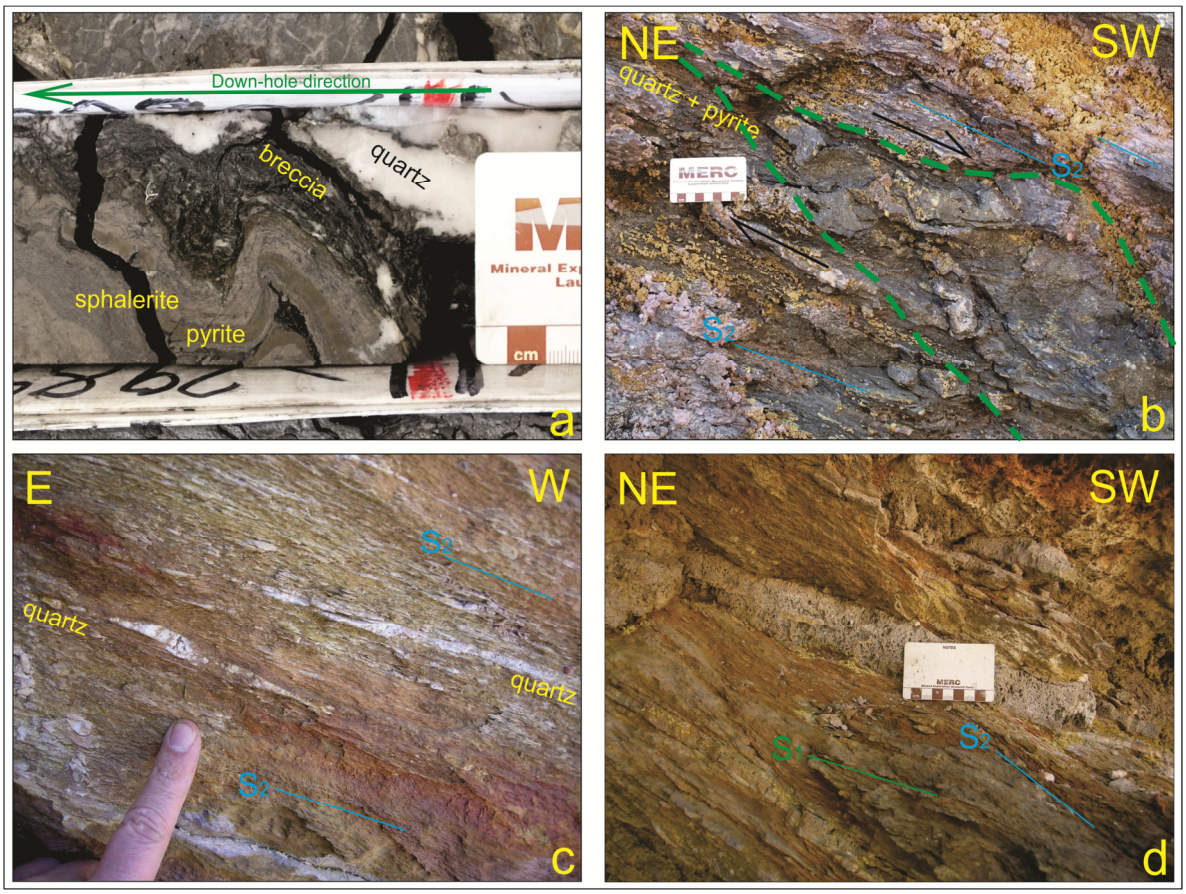

Figure 4.33. Quartz + sphalerite ± pyrite ± galena crustiform epithermal vein (a); cryptocrystalline quartz ± pyrite epithermal vein (delimited by the green dashed line, b); second vein type is offset parallel to S_2, suggesting that they were emplaced during D_2 (c); and cut across the first vein type as well as S_1 and S_2 and are commonly boudinaged (d).

4.3 Summary

(1) Interlayered greywacke, tuffaceous shale and volcaniclastics of the Acapetlahuaya Formation are in unconformable contact with volcanic rocks of the Rey de Plata and Villa Ayala members.

(2) The Miahuatepec Formation is in angular unconformable contact with older volcanic rocks of the Villa Ayala member. Feldspar-phyric mafic intrusions with peperitic margins were emplaced along this contact before complete lithification of the turbiditic sandstone of the Miahuatepec Formation.

(3) The first deformation event D_1 produced large, NE-verging, inclined to recumbent, tight to isoclinal, F_1 folds in turbiditic sandstone of the Miahuatepec Formation. A shallowly-dipping S_1 cleavage is axial planar to the folds. S_1 is expressed as a strong continuous cleavage with a down-dip, W-plunging, mineral stretching lineation in altered rhyolite of the Rey de Plata member.

(4) The second deformation event D_2 is characterized by a S_2 shear band cleavage that formed during southwest- to west-directed normal slip roughly parallel to the dominant planar anisotropy, i.e. bedding or S_1, in the rock.

(5) Epithermal veins cut across S_1 and S_2, are folded, and are offset parallel to S_2, suggesting that they were emplaced during D_2.

(6) Normal brittle faults linked by transfer faults formed during D_3. W-verging F_3 drag folds occur along the faults. Normal faults propagated along the contact between Miahuatepec turbiditic sandstone and Balsas conglomerate. S_1 and S_2 do not overprint the conglomerate, suggesting that D_1 and D_2 predate the deposition of the Balsas Formation.

(7) Upright to inclined, NE- and SW-verging F_4 folds overprint S_1 and S_2 and formed late during D_4 compression across the Rey de Plata area. D_3 normal faults were reactivated as reverse faults during D_4.

Chapter 5: Rey de Plata Deposit.

The Rey de Plata VMS deposit consists of four Zn-Cu-Pb ore lenses with high Ag-Au grades. They are named the Manto Tehuixtla, Manto Superior, Manto Medio, and Manto Inferior lenses (mantos in Figure 5.1). The lenses have a flat lenticular shape and range in thickness from 3m to 60m, in length from 300m to 1500m, and in width from 100m to 500m. The lenses are hosted by felsic volcanic rocks of the Rey de Plata member and occur within the Rey de Plata member, at its lower contact with the Ahuehuetla member, or at its upper contact with the Villa Ayala member. Graphitic argillite units up to 40m in thickness typically occur at the top and bottom contacts of the ore lenses.

The lenses consist of massive, semi-massive, and disseminated pyrite ± sphalerite ± galena ± chalcopyrite ± gold ± silver sulphosalts, together with gangue minerals of barite ± quartz. Extensive alteration defined by the assemblage quartz + sericite + pyrite surrounds the ore lenses.

5.1 Manto Tehuixtla Lens

The Manto Tehuixtla lens is about 300m long, 50m thick and 250m wide. It consists of two distinctive mineralogical zones: a lower zone defined by pyrite-chalcopyrite and an upper zone defined by pyrite-sphalerite-galena-barite-silver sulphosalts. The two zones are internally folded and display a strong tectonic foliation. Textures range from disseminated to completely massive, and they are locally overprinted by epithermal veins composed of quartz ± barite ± galena ± chalcopyrite.

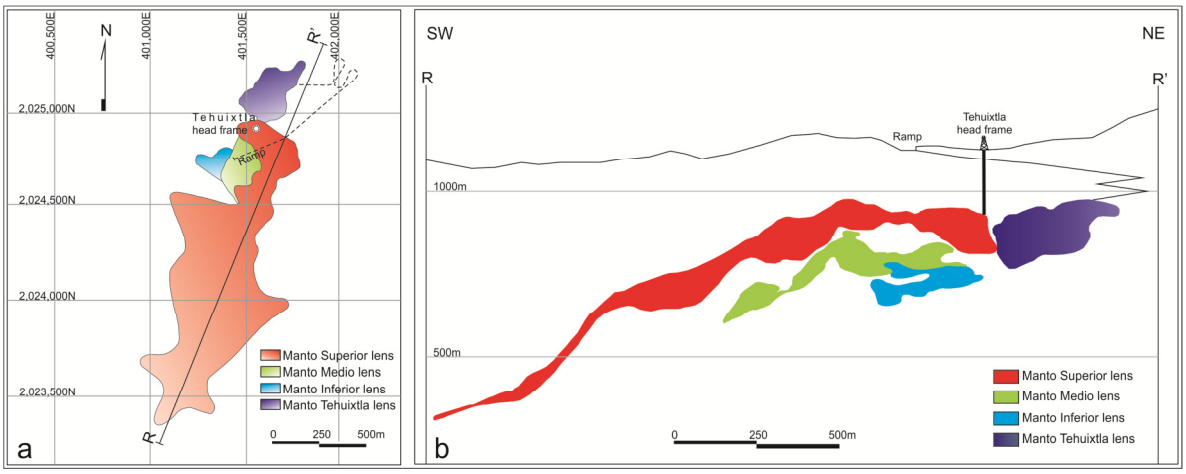

Figure 5.1. Ore lenses (mantos) of the Rey de Plata deposit. Surface plan projection (a), and cross section (b).

5.2 Manto Superior Lens

The Manto Superior lens is enclosed by felsic volcanic rocks of the Rey de Plata member immediately below its contact with the overlying Villa Ayala member. In plan view, it has a maximum length of 1500m, a maximum width of 700m, and a maximum thickness of 60m. It consists of massive to semi massive pyrite-chalcopyrite and it contains minor bornite and covelite along its lower margin and layers of sphalerite and galena ± silver sulphosalts along its upper margin. Graphitic argillite occurs at both the lower and upper margins of the ore body. In the center of the lens, auriferous epithermal veins composed of quartz-barite-pyrite-chalcopyrite cut across the orebody and are associated with gold enriched ore zones up to 20m in thickness and with ore grades of up to 8 g/ton Au and 3.8 % Cu (Figure 5.2).

5.3 Manto Medio Lens

The Manto Medio lens occurs mid-way within the Rey de Plata member. It is approximately 650m in length, 400m in width, and 30m in thickness. It consists of massive to semi-massive pyrite-chalcopyrite with lesser galena-sphalerite-barite and silver sulphosalts. Graphitic argillites are not common but where present occur

at the upper and lower contacts of the lens. The lens contains a mineralized zone that is very rich in gold, silver and zinc with grades ranging up to 102 g/ton Au, 6.4 kg/ton Ag, 14.7% Zn, 6.4% Pb, and just <1% Cu over a thickness up to 15m. The lens is strongly deformed and is locally characterized by a folded tectonic foliation defined by bands of quartz + barite intercalated with bands of sphalerite + galena + pyrite (Figure 5.3).

Figure 5.2. Manto Superior lens composed of pyrite and chalcopyrite.

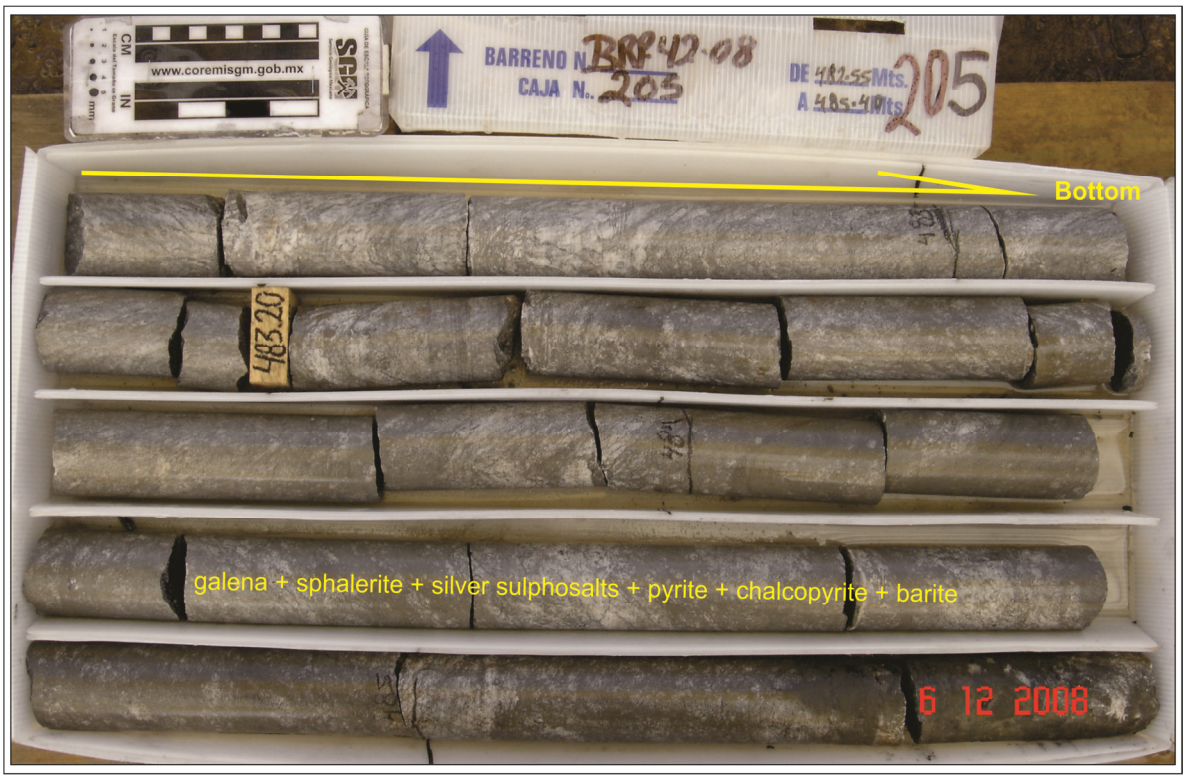

Figure 5.3. Manto Medio lens composed of quartz-barite-pyrite-sphalerite-galena-silver sulphosalts.

5.4 Manto Inferior Lens

The Manto Inferior lens is located within the Re de Plata member or at the contact with the underlying basalts of the Ahuehuetla member. It is about 300m in length, up to 200m in width, and about 10m in thickness. It consists of massive to semi-massive to disseminated galena-sphalerite-silver sulphosalts±pyrite±chalcopyrite, associated with barite and quartz. Graphitic argillite typically occurs along the upper and lower margins of the ore lens and is deformed by the same strong penetrative foliation and folds present in the ore lens. The lens contains several high-grade intervals of up to 10m in thickness with grades up to 6.2 g/ton Au, 1000 g/ton Ag, 2.2% Pb, 8.6% Zn, and 1.8% Cu (Figure 5.4).

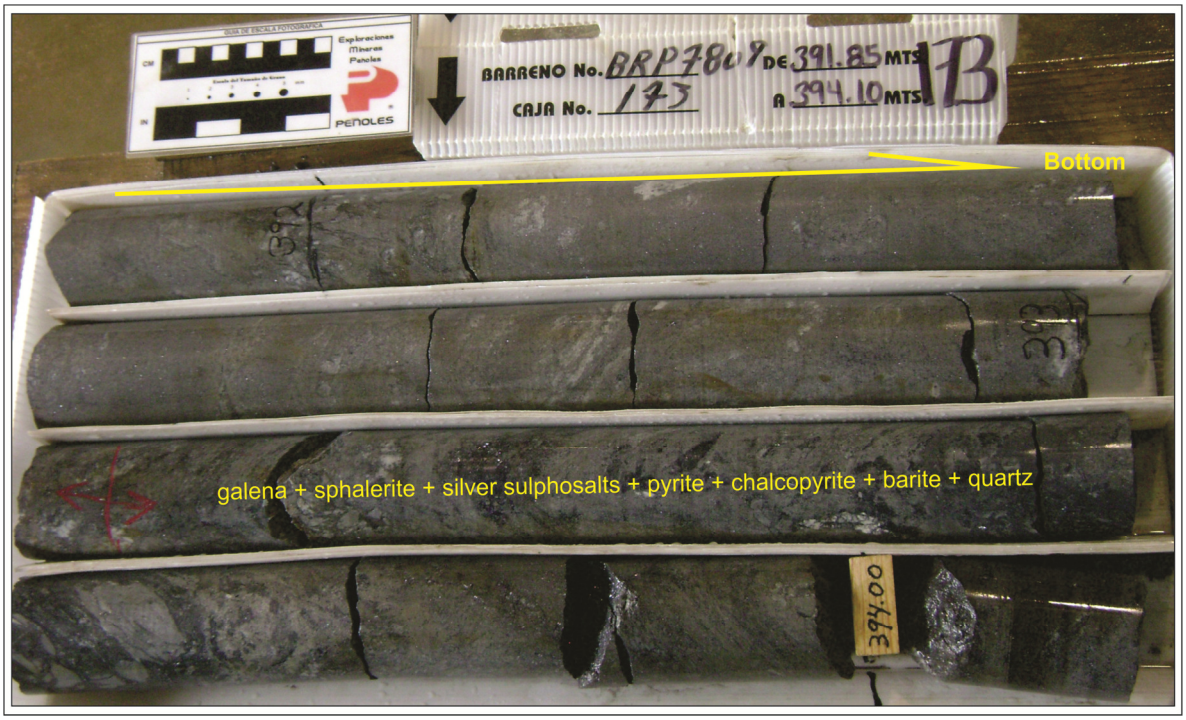

Figure 5.4. Manto Inferior lens consisting of sphalerite-galena-pyrite-barite-silver sulphosalts-chalcopyrite.

5.5 Base Metal zonation in the Rey De Plata Deposit

Base metal zonation, essentially zonation of copper and zinc (lead distribution parallels that of zinc), is a product of zone refining during the thermal evolution of sulfide lenses (Lydon 1984) and is best illustrated using the Cu/(Cu+Zn) ratio developed by Knuckey et al. (1982). Areas with high Cu/(Cu+Zn) ratio are copper rich and define primary hydrothermal vent areas within a massive sulphide lens (Knuckey et al. 1982, Gibson and Watkinson 1990, Gibson 2005). To illustrate the base metal zonation at Rey de Plata, block models (constructed with mine data and based in the total sulfide content of the lenses), were contoured using the Cu/(Cu+Zn) ratio and projected onto sections and plans. The zonation pattern was then examined to determine if the ore lenses are part of the same hydrothermal system and if the sulphide lenses are stratigraphically stacked or fold/fault repeated.

In plan view two areas with high Cu/(Cu+Zn) ratio can be defined for both the Manto Superior and the Manto Medio lenses (Figure 5.5). The Cu-rich areas do not line up as would be expected if the Manto Superior lens formed directly above the Manto Medio lens (Figure 5.5C). However, if the Manto Medio lens is shifted 200m to the southwest relative to the Manto Superior lens the two Cu-rich hydrothermal vents for each lens are juxtaposed. This implies that the two sulfide lenses represent primary, stratigraphically stacked VMS lenses that were offset during deformation. The Manto Inferior orebody has lower Cu/(Cu+Zn) ratio and may represent the fringe of the Manto Superior orebody.

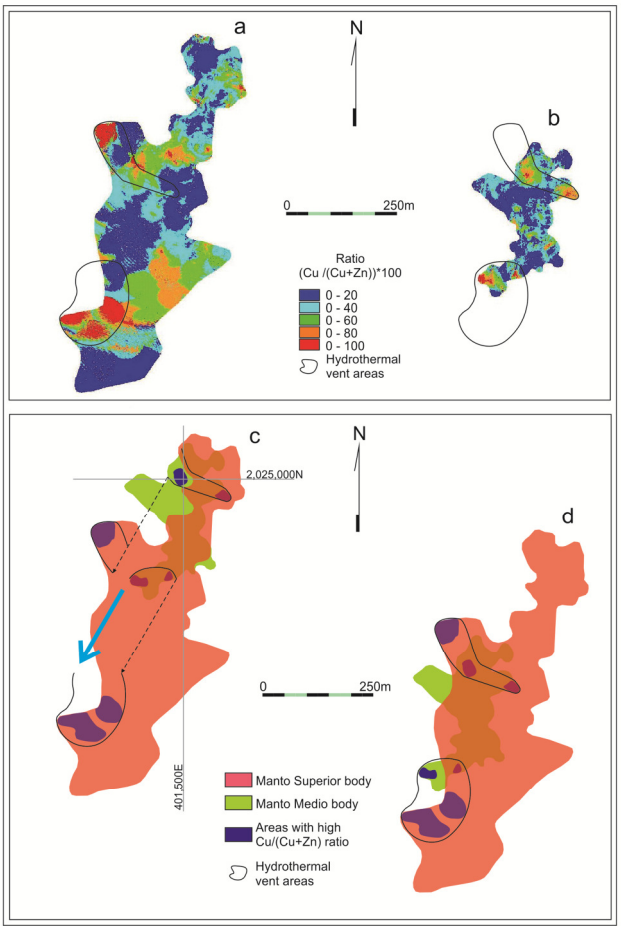

Figure 5.5. Plan projection of ore lenses showing Cu and Zn zonation using the Cu/(Cu+Zn) ratio. Areas with high Cu/Cu +Zn ratio (red and orange) outlined by irregular circles define hydrothermal vent areas during lens formation; Manto Superior lens (a); Manto Medio lens (b). The offset of vent areas within the Manto Superior from those in the underlying Manto Medio as shown in (c) can be corrected (re-aligned) by shifting the Manto Medio lens by roughly 200m to the southwest to juxtapose areas with high Cu/(Cu+Zn) ratios as shown in (d).

5.6 Deformation History of the Rey de Plata VMS deposit

The Rey de Plata ore lenses formed as stratigraphically stacked lenses above two main hydrothermal vents as defined by the Cu/(Cu+Zn) ratio. They were tilted westward prior to the deposition of the Acapetlahuaya and Miahuatepec formations, which formed unconformable sequences overlying the volcanic rocks. During D_1, the orebody was internally sheared and deformed, as evidenced by the strong tectonic S_1 foliation in the ore lenses and the elongation of the ore lenses parallel to the stretching L_1 lineation (Figure 5.6). Shearing during D_1 may also have caused the internal southwestward rotation and flattening of the Manto Superior lens (Figures 5.7, 5.8). During D_2 and D_3, the ore lenses were displaced southwestward along normal faults (deduced from interpretation; Figure 5.7) and/or shear planes constructed during D_1 (Figure 5.8) and then folded by open, upright F_4 folds and northeast-verging F_4 folds, which resulted in their final curviplanar shape (Figures 5.7, 5.8).

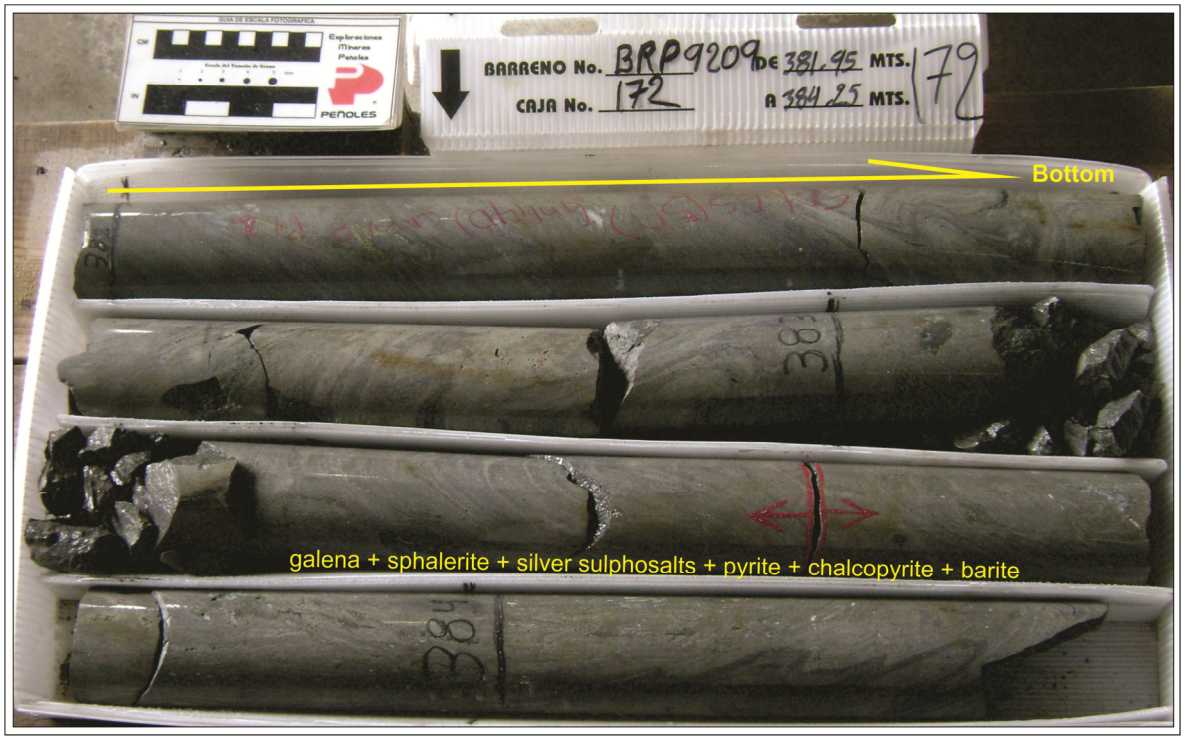

Figure 5.6. S_1 foliation into the orebodies.

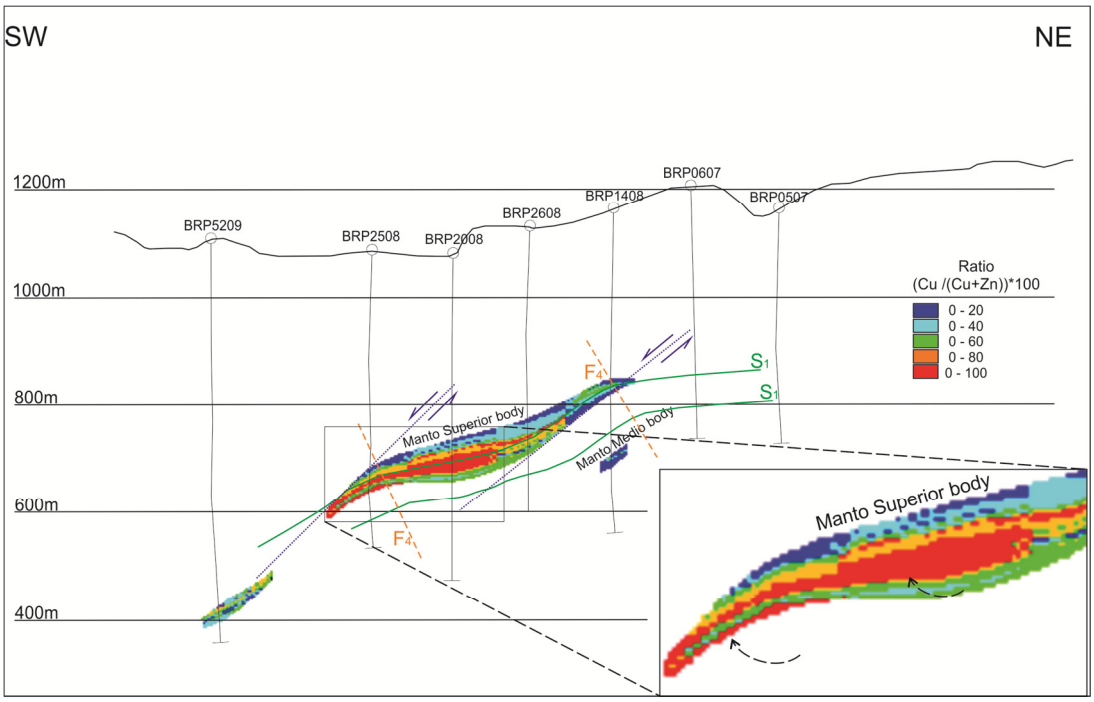

Figure 5.7. Manto Superior body showing the flattening of the lenses parallel to S_1, the southwestward internal rotation of the vent during D_1 (see inset), normal-slip westward translation of the orebodies during or D_3, and open folding of the orebodies during D_4.

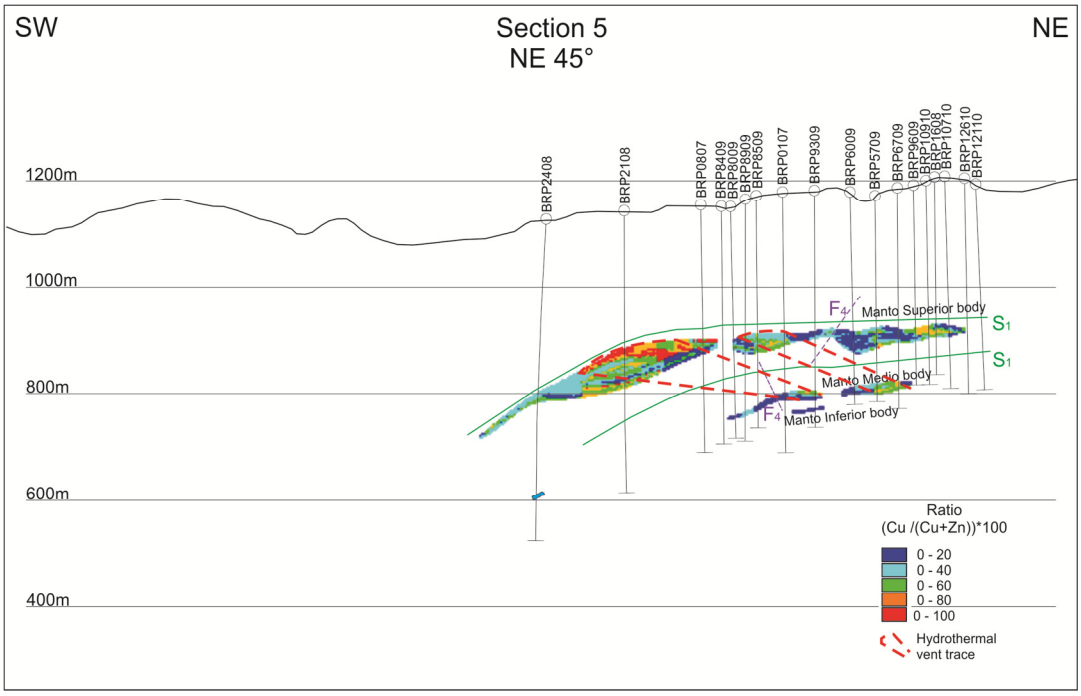

Figure 5.8. Westward normal-slip translation of the Manto Superior orebody relative to the Manto Medio orebody.

Chapter 6: Discussion and Conclusions

6.1 Pre-Cretaceous tectonic evolution of the Guerrero Composite Terrane

The Guerrero Composite Terrane is divided into five subterranes: Tahue, Zihuatanejo, Guanajuato, Arcelia and Teloloapan. It consists of Late Paleozoic to Middle-Late Cretaceous arc volcanic rocks overlying basement rocks, which are exposed in the Tahue and Zihuatanejo subterranes. Basement rocks in the Tahue subterrane are represented by the Ordovician El Fuerte Complex, which consists of subaqueous rhyolitic-andesitic flows, epiclastic rocks and calcareous rocks (Centeno-García 2005, Centeno-García et al. 2008). In the Zihuatanejo subterrane, the basement rocks are represented by the Late Triassic to Early Jurassic Arteaga Complex and Zacatecas Formation. The latter consists of siliciclastic rocks with abundant late Paleozoic detrital zircons, interlayered with mafic arc volcanic rocks (Centeno-García 1994, Centeno-García et al. 2008). These rocks were first sheared, tightly folded and foliated within an Upper Triassic accretionary prism that formed above a subduction zone that was either dipping toward the west under an oceanic arc or toward the east under continental rocks of the Oaxaquia Terrane in northern Mexico (Centeno-García et al. 1993, Talavera-Mendoza 2000, Centeno-García et al. 2008, Martini et al. 2010). In southern Mexico, the Teloloapan subterrane is in thrust contact over metamorphosed sedimentary and arc-related volcanic and volcaniclastic rocks of the Lower Paleozoic to Middle Jurassic Mixteca Terrane (de Cserna and Fries 1981, Ortega-Gutiérrez 1981, Ruíz et al. 1988, Yañez et al. 1991, Talavera-Mendoza 1993, Campa and Iriondo 2004).

6.2 Late Jurassic to Late Cretaceous tectonic evolution of the Teloloapan subterrane and the VMS Rey de Plata deposit

The Teloloapan subterrane contains several polymetallic VMS deposits, including the Campo Morado, Tizapa and Rey de Plata deposits. The Rey de Plata deposit

is in the western half of the subterrane, where it is hosted by the Villa Ayala Formation. The latter was emplaced in a deep marine environment and consists of basaltic, andesitic and rhyolitic flows and volcaniclastic rocks. These rocks are subdivided in this study into three informal members: the Ahuehuetla, Rey de Plata and Villa Ayala members.

Basalts of the Ahuehuetla member have island arc tholeiitic to MORB-BAB affinity, whereas the basalts of the Villa Ayala member have MORB-BAB affinity only. This is consistent with their formation in an arc and nascent back-arc environment above a subduction zone (Pearce 1996). The LREE enriched and flat-HREE profiles of the felsic rocks of the Rey de Plata member, as well as their negative Nb anomaly, are indicative of shallow, low pressure partial melting of an older, hydrated arc crust during arc extension and rifting i.e. FII rhyolite of Hart et al. (2004). Negative Nb and positive Zr and Hf anomalies could also indicate contamination by older, more evolved arc crust that possibly contained slivers of older continental crust (Pearce 1984). This is consistent with the occurrence of older xenocrystic zircons in felsic rocks of the Campo Morado VMS deposit (Mortensen et al. 2008). This interpretation differs from that of Talavera-Mendoza et al. (1995), who interpreted the Teloloapan subterrane as an evolved, intra-oceanic island arc without crustal roots and/or contamination.

VMS deposits typically form during punctuated periods of rifting during an otherwise collisional environment (Franklin et al. 2005, Belkabir et al. 2008, Gibson et al. 1999, Hart et al. 2004, Marcoux et al. 2008). Rifting results in depressurized partial melting of the mantle, underplating and partial melting of hydrated mafic crust producing hot rhyolitic magmas, and the formation of a long-lived fault system along which melts and hydrothermal fluids migrated and precipitated metals at the seafloor or sub seafloor (Franklin et al. 2005). The Rey de Plata deposit formed in such environment at 139.1 ± 0.4 Ma to 129.4 ± 0.7 Ma, which brackets in age the emplacement of an aphyric rhyolitic flow immediately below one of the massive sulphide lens. Rhyolites of the Campo Morado deposit yielded similar Late Jurassic

to Early Cretaceous (Oxfordian-Valanginian) U/Pb zircon ages of 139.7 ± 2.5 Ma to 157.4 ± 4.1 Ma (Mortensen et al. 2008). According to the lithotectonic classification of VMS deposits by Franklin et al. (2005), most of the VMS deposits in Mexico, including the Campo Morado deposit, are classified as siliciclastic-felsic. However, at Rey de Plata, the abundance of felsic and mafic volcanic rocks relative to sedimentary rocks at the district scale is consistent with bimodal-felsic type deposits. Bimodal-felsic deposits are typically found in mature arcs settings (e.g. Kuroko deposits) whereas siliciclastic-felsic deposits typically occur in mature epicontinental back arc settings (e.g the Paleozoic Iberian Pyrite Belt and the Bathurst deposits as well as the Mesozoic Campo Morado deposit).

Block faulting of the Villa Ayala and Rey de Plata members occurred either during rifting or intraoceanic accretion. This tilted the volcanic rocks prior to the deposition of a thick sequence of argillite/siltstone, which unconformably overlie the volcanic rocks. The argillite and siltstone contain detrital zircons that are derived from the surrounding volcanic rocks. The absence of older zircons suggests that a large backarc basin existed at that time between the Teloloapan arc and continental Mexico. The youngest population of zircons provides a maximum age of 115 ± 4 Ma for the deposition of these rocks. This unit correlates with volcaniclastic rocks at the top of the Villa Ayala Formation in the western region of the Teloloapan subterrane. These volcaniclastic rocks contain Early Cretaceous gastropods and bivalves, ranging in age from Hauterivian to Aptian (Guerrero-Suastegui et al. 1991, Ramírez-Espinoza et al. 1991, Talavera-Mendoza et al. 1995). It also correlates with the late Early Cretaceous (Aptian) argillaceous Acapetlahuaya Formation, which overlies the Villa Ayala Formation in the western half of the Teloloapan subterrane (Talavera et al. 1995), and with argillite containing Aptian-age ammonoids and radiolarians in other parts of the Teloloapan Terrane (Campa et al. 1974). In the eastern half of the Teloloapan subterrane, the Villa Ayala Formation, grades upward into Early Cretaceous (Aptian-Albian) calcareous rocks of the Teloloapan Formation, which are intercalated with volcaniclastic rocks at the base of the formation.

Sedimentation continued in the western half of the Teloloapan subterrane with the deposition of the Early to Late Cretaceous (Albian-Cenomanian) Amatepec Formation. The latter consist of thin-bedded, detrital, black limestone that was deposited in a deep marine environment. It lacks a volcanic detrital component and it unconformably overlies the Acapetlahuaya Formation (Talavera-Mendoza et al. 1995).

6.3 Late Cretaceous to Paleogene tectonic evolution of the Teloloapan subterrane and the VMS Rey de Plata deposit

The deposition of the regionally extensive turbiditic sandstone and mudstone of the Late Cretaceous (Cenomanian) Miahuatepec Formation marks the closure of the backarc basin and the amalgamation of the Zihuatanejo, Arcelia and Teloloapan subterranes (Talavera-Mendoza et al. 1995, Mendoza and Suastegui 2000). The Miahuatepec Formation is exposed in the western half of the Teloloapan subterrane and it correlates with similar rocks of the early Late Cretaceous (Turonian) Pachivia Formation in the eastern half of the subterrane (Talavera-Mendoza et al. 1995, Mendoza and Suastegui 2000). Two main populations of detrital zircons were derived from the sample of Miahuatepec sandstone analysed in this study. The oldest population spans an age interval between 800 to 1200 Ma, which is consistent with their derivation from Proterozoic rocks of the Oaxaquia Terrane. The second population consists of zircons ranging in age between 200 Ma and 300 Ma, which suggests a derivation from the erosion of Lower Paleozoic to Middle Jurassic metamorphosed sedimentary and arc-related volcanic and volcaniclastic rocks of the nearby Mixteca Terrane (Elías-Herrera and Ortega-Gutierrez 2002, Keppie et al. 2006, Centeno-García et al. 2011). No younger zircon was retrieved, suggesting that the Villa Ayala Formation was not deeply excised and did not have a pronounced topography when the Miahuatepec Formation was deposited. Feldspar-phyric basaltic intrusions located between the Villa Ayala and Miahuatepec formations were emplaced during the deposition of the lower section of the Miahuatepec Formation.

Deposition of the Miahuatepec Formation likely occurred in response to the Late Cretaceous to Early Paleocene Sevier-Laramide Orogeny, which uplifted the Oaxaquia Terrane and other terranes along the western continental Mexico. These two overlapping orogenies occurred throughout the western margin of North America from Canada to Mexico. This new interpretation explains the provenance of detrital zircons from continental Mexico in the Miahuatepec Formation, but contradicts the previous interpretation of the Miahuatepec Formation as sediments in a thrust-related basin that formed during the amalgamation of the Zihuatanejo, Arcelia and Teloloapan subterranes prior to the accretion of the Guerrero Composite Terrane to continental Mexico (Guerrero-Suastegui et al. 1991, Ramírez-Espinoza et al. 1991, Talavera-Mendoza et al. 1995, Mendoza and Suastegui 2000, Guerrero-Suastegui 2004, Centeno-García et al. 2008).

As the orogenic front migrated eastward, the Guerrero Composite Terrane was thrusted over the calcareous platformal rocks of the Oaxaquia Terrane and metamorphosed rocks of the Mixteca Terrane. Cretaceous rocks in the southern region of the Zihuatanejo subterrane were folded by open east-verging folds associated with minor east-directed thrust faults (Mendoza and Suastegui 2000, Guerrero-Suastegui 2004, Centeno-García 2005, Centeno-García et al. 2008). This orogenic event is expressed by the formation of the northeast verging S_1 cleavage and F_1 folds at Rey de Plata. D_1, at Rey de Plata, therefore corresponds with the Sevier/Laramide Orogeny.

At Campo Morado, and in other parts of the Teloloapan subterrane, the east-verging F_1 folds and S_1 cleavage are overprinted by west-verging folds with an axial planar crenulation cleavage. The latter overprinting structures have been attributed to west-directed back-thrusting during the Sevier-Laramide Orogeny (Salinas-Prieto et al. 2000; Rhys et al. 2000, Lewis and Rhys 2000). At Rey de Plata, D_2 structures are also west-verging and expressed by a west-side-down slip cleavage (S_2) and asymmetrical folds defined by folded S_1. S_2 is interpreted as a shear band cleavage (C') that formed during normal west-directed slip down the

dip of the S_1 foliation. Thus, although these structures may have formed during west-directed backthrusting as interpreted above, the normal-slip movement associated with these structures is better explained by extensional orogenic collapse either during or shortly after D_1. Extensional orogenic collapse following thickening of the crust during mountain building has been documented in many orogens (Dewey 1988, Andersen 1991, Fossen 1992). The gold- and silver-rich epithermal veins, which show mutually overprinting relationships with respect to S_2, were emplaced during D_2 extensional collapse and exhumation of the Teloloapan subterrane. These veins may have contributed to the high grade gold and silver zones at Rey de Plata. Because D_2 occurred shortly after or during the D_1 Sevier-Laramide Orogeny, the timing of these veins differs significantly from that of the well-known Tertiary epithermal silver deposits in Mexico.

Major NNW-SSE extension during the Eocene and NE-SW extension during the Oligocene, both possibly associated with strike-slip reactivation of major, terrane-bounding, Sevier-Laramide thrust faults, produced sedimentary basins that were filled by ignimbrites and fluvial sedimentary rocks, such as the Balsas conglomerate (Alaniz-Álvarez et al. 2002, Cerca-Martinez 2004). At Rey de Plata, WSW-striking and SSE-striking D_3 normal faults linked by strike-slip transfer faults formed during these two extensional events. Thus, the Balsas conglomerate was deposited in basins bounded by normal faults, which follow its contact with underlying older rocks.

Late D_4 compression produced upright to inclined, NE- and SW-verging F_4 folds that overprint S_1 and S_2. The folds are usually tighter in the hanging wall of D_3 normal faults, suggesting that the faults acted as strong planar structures that facilitated the nucleation of folds in their layered and/or foliated wall rocks. Structures related to this late deformation event have yet to be found in other parts of the Teloloapan subterrane.

6.4 Effect of the deformation events on the Rey de Plata deposit

Zone refining during the thermal evolution of a sulfide lens results in a pronounced base and precious metal zonation (Lydon 1984). Copper-rich areas, those with a high Cu/(Cu+Zn) ratio, define primary, higher temperature hydrothermal vent areas within massive sulphide lenses (Knuckey et al. 1982). The spatial correspondence of areas with high Cu/(Cu+Zn) ratio between the Manto Superior and Manto Medio sulphide lenses indicates that the Rey de Plata deposit originally consisted of stratigraphically stacked lenses that were subsequently displaced relative to each other by only 200 meters. This is remarkable given that shearing during D_1 resulted in strong elongation of the lenses parallel to the L_1 stretching lineation and may have caused internal clockwise rotation (looking NW) of the sulfide lenses. During D_2 and/or D_3, the ore lenses were displaced southwestward along normal faults and/or shears and then folded during D_4 into their present and final curviplanar geometry.

6.5 Conclusions

1) The Villa Ayala Formation is divided into three members, consisting from bottom to top of: 1) basaltic volcaniclastic rocks, flows, and sills of the Ahuehuetla member; 2) rhyodacitic to dacitic volcaniclastic rocks, domes/flows, and sills intercalated with intervals of black graphitic argillite of the Rey de Plata member; and 3) basaltic amygdaloidal sills and volcaniclastic rocks of the Villa Ayala member.

2) The slight LREE enrichment, and negative Nb and weakly positive Zr anomalies that are characteristic of the basaltic rocks are indicative of a primitive to slightly evolved arc to back-arc setting and minor contamination by older arc (or continental) crust. The felsic volcanic rocks show slight LREE enrichment, a flat HREE pattern and pronounced negative Nb, Sm, Eu and Ti anomalies, indicative of partial melting of hydrated arc basaltic

rocks during extension and rifting (Hart et al. 2004). They plot in the field of volcanic-arc granite (VAG) on a Ta versus Yb diagram of Pierce et al. (1984).

3) The Rey de Plata VMS deposit is hosted by felsic rocks of the Rey de Plata member and one of its lenses sits immediately above an aphyric rhyolite flow that yielded U/Pb zircon ages of 139.1 ± 0.4 Ma to 129.4 ± 0.7 Ma. The Rey de Plata can be described as a bimodal-felsic deposit using the classification of Franklin et al. (2005); however, at a larger scale, VMS deposits of the Teloloapan subterrane were interpreted as siliciclastic–felsic (Mortensen, et al., 2008).

4) Block faulting of the Villa Ayala Formation at Rey de Plata either during rifting or intraoceanic accretion tilted the volcanic rocks prior to the deposition of the younger sedimentary Acapetlahuaya and Miahuatepec formations.

5) Argillaceous sedimentary rocks of the Acapetlahuaya Formation unconformably overly volcanic rocks of the Villa Ayala Formation. They were deposited in a large backarc basin that separated the Teloloapan arc from continental Mexico. These argillites contain detrital zircons that are derived from the surrounding volcanic rocks and provide a maximum age of 115 ± 4 Ma for the deposition of these rocks.

6) The Miahuatepec Formation yielded two detrital zircon populations. The oldest population spans an age interval between 800 to 1200 Ma, which is consistent with their derivation from Proterozoic rocks of the Oaxaquia Terrane. The second population consists of zircons ranging in age between 200 Ma and 300 Ma. They were likely derived from the erosion of Lower Paleozoic to Middle Jurassic metamorphosed sedimentary and arc-related volcanic and volcaniclastic rocks of the nearby Mixteca Terrane. The absence of zircons from the Villa Ayala Formation suggests that the Villa

Ayala volcanic rocks were not deeply excised and did not have a pronounced topography at the time of deposition of the Miahuatepec Formation unconformably above the volcanic rocks.

7) D_1 is a northeast directed compressive event related to the Late Cretaceous-Early Paleocene Sevier-Laramide Orogeny. It produced large, NE-verging, inclined to recumbent, tight to isoclinal, F_1 folds in turbiditic sandstone of the Miahuatepec Formation, as well as a shallowly-dipping S_1 continuous cleavage and down-dip, W-plunging L_1 mineral stretching lineation.

8) The second deformation event D_2, is defined by a west-side-down S_2 slip cleavage and asymmetrical folds folding S_1. S_2 is interpreted as C' shear band cleavage that formed during normal west-directed slip down the dip of the S_1 foliation. Thus, D_2 structures record the extensional collapse of the orogeny and exhumation of the Teloloapan subterrane either during or shortly after D_1.

9) The gold- and silver-rich epithermal veins, which show mutually overprinting relationships with respect to S_2, were emplaced during D_2 extensional orogenic collapse and exhumation of the Teloloapan subterrane. They may have contributed to high grade gold and silver zones at Rey de Plata deposit. Because D_2 occurred shortly after or during the D_1 Sevier-Laramide Orogeny, the timing of these veins differs significantly from that of the well-known Tertiary epithermal silver deposits in Mexico.

10) D_3 is interpreted as a Eocene-Oligocene brittle extensional event. The Balsas conglomerate was emplaced in extensional basins during this event and is itself bounded and overprinted by west-directed normal faults. During D_2 and/or D_3, the ore lenses were displaced southwestward along normal faults and/or shears.

11) D_4 is a late NE-directed compressional event responsible for the formation of upright to inclined, NE- and SW-verging, F_4 folds, which overprint S_1 and S_2. These structures have not yet been found elsewhere in the Teloloapan subterrane.

12) After horizontal deposition and stacking on oceanic floor, the ore lenses and their vents were tilted prior to the deposition of the Acapetlahuaya and Miahuatepec Formations. During D_1, the sulfide lenses were clockwise rotated and the lenses were flattened parallel to the L_1 stretching lineation. During D_2 and D_3, the ore lenses were displaced southwestward along normal faults and/or shears and then, during D_4 were folded by F_4 folds.

References

Alaniz-Álvarez, S. A., Nieto-Samaniego, A. F., Morán-Zenteno, D. J., and Alva-Aldave, L. 2002. Rhyolitic volcanism in extension zone associated with strike-slip tectonics in the Taxco region, southern México. Journal of Volcanology and Geothermal Research, v. 118, p. 1 – 14.

Andersen, T. B., Jamtveit, B., Dewey, J. F. and Swensson, E. 1991. Subduction and eduction of continental crust: major mechanisms during continent-continent collision and orogenic extensional collapse, a model based on the south Norwegian Caledonides: Terra Nova, v. 3, p. 303–310.

Belkabir, A., Gibson, H.L., Marcoux, E., Lentz, D., Rziki S. 2008. Geology and wall rock alteration at the Hercynian Draa Sfar Zn–Pb–Cu massive sulphide deposit, Morocco Original Research Article: Ore Geology Reviews, v. 33, p. 280-306.

Bissig, T., Mortensen, J.K., and Hall, B. 2003. The volcano-sedimentary setting of the Kuroko type Vhms District of Cuale, Jalisco, Mexico: Geological Society of America Abstracts with Programs, v. 35, no. 4, p. 61.

Campa, M.F., Campos, M., Flores, R., Oviedo, R. 1974. La secuencia Mesozoica volcánico-sedimentaria metamorfizada de Ixtapan de la Sal, Mex.-Teloloapan, Gro. Boletín de la Sociedad Geológica Mexicana, v. 35, p. 7-28.

Campa, M.F., and Ramirez, J. 1979. La Evolución Geológica y la Metalogénesis de Guerrero: Universidad Autónoma de Guerrero, Ser. Técnico-Científica, v. 1, 84 p.

Campa, M.F., and Iriondo, A. 2004. Significado de dataciones Cretácicas de los arcos volcánicos de Taxco, Taxco Viejo y Chapolapa, en la evolución de la

plataforma Guerrero-Morelos: Unión Geofísica Mexicana: Reunión Nacional de Ciencias de la Tierra, GEOS, v. 24, p. 173.

Cann, J. R. 1970. Rb, Sr, Y, Zr, and Nb in some ocean floor basaltic rocks; Earth and Planetary Science Letters, v.10, p.7-11.

Centeno-García, E., Ruíz, J., Coney, P.J., Patchett, P.J., and Ortega-Gutiérrez, F. 1993. Geology of the Guerrero Terrane and its role in the tectonic evolution of the southern North America Cordillera from new geochemical data: Geology, v. 21, p. 419–422.

Centeno-García, E. 1994. Tectonic evolution of the Guerrero Terrane, western Mexico [Ph.D. thesis]: Tucson, University of Arizona, 220 p.

Centeno-García, E., Corona-Chavez, P., Talavera-Mendoza, O., and Iriondo, A. 2003. Geology and tectonic evolution of the Western Guerrero terrane—A transect from Puerto Vallarta to Zihuatanejo, México, *in* Alcayde, M., and Gómez-Caballero, A., eds., Geologic Transects across Cordilleran México: Guidebook for Field Trips of the 99th GSA Cordilleran Section Meeting: Universidad Nacional Autónoma de México, Instituto de Geología Publicación Especial 1, p. 201–228.

Centeno-García, E. 2005. Review of Upper Paleozoic and Lower Mesozoic stratigraphy and depositional environments of central and west Mexico: Constraints on terrane analysis and paleogeography, *in* Anderson, T.H., et al., eds., The Mojave-Sonora Megashear Hypothesis: Development, Assessment, and Alternatives: Geological Society of America Special Paper 393, p. 233–58.

Centeno-García, Elena, Guerrero-Suastegui, Martín, Talavera-Mendoza, Oscar. 2008. The Guerrero Composite Terrane of Western Mexico: Collision and

subsequent rifting in a supra-subduction zone: The Geological Society of America, Special Paper 436.

Centeno-García, Elena, Busby C., Busby, M., and Gehrels, G. 2011. Evolution of the Guerrero composite terrane along the Mexican margin, from extensional fringing arc to contractional continental arc; Geological Society of America Bulletin, September 2011, v. 123, no. 9-10, p. 1776-1797.

Cerca, M., 2004, Deformación y magmatismo cretácico tardío - Terciario temprano en la zona de la Plataforma Guerrero Morelos: Universidad Nacional Autónoma de México, Centro de Geociencias, Posgrado en Ciencias de la Tierra, tesis doctoral, 175 p., 1 mapa.

Danielson, T.J. 2000. Age, paleotectonic setting, and common Pb isotope signature of the volcanogenic massive sulfide deposit, southeastern Zacatecas State, central Mexico [M.S. thesis]: Vancouver, University of British Columbia, 120 p.

De Cserna, Z., and Fries, C. Jr. 1981. Hoja Taxco 14Q-h(7), and Resumen de la Geología de la Hoja Taxco, Estados de Guerrero, México y Morelos: Universidad Nacional Autónoma de México, Insituto de Geología, Carta Geologica de Mexico: Map Ser., scale 1:100,000, and 47 p. text.

Dewey, J. F. 1988. Extensional collapse of orogens: Tectonics, v. 7(6), p. 1123–1139.

Dong, G., Morrison, G., and Subhash, J. 1995. Quartz textures in epithermal veins, Queensland-clasiffication, origin and implication: Economic Geology, v. 90., p. 1841-1856.

Elías-Herrera, M., and Sánchez-Zavala, J.L. 1992. Tectonic implications of a mylonitic granite in the lower structural levels of the Tierra Caliente Complex (Guerrero Terrane), Southern México: Universidad Nacional Autónoma de México, Instituto de Geología: Revista Mexicana de Ciencias Geológicas, v. 9, p. 113–125.

Elías-Herrera, M., Sánchez-Zavala, J.L., and Macias-Roma, C. 2000. Geologic and geochronologic data from the Guerrero terrane in the Tejupilco area, southern Mexico: New constraints on its tectonic interpretation: Journal of South American Earth Sciences, v. 13, p. 355–375.

Elías-Herrera, M., and Ortega-Gutiérrez, F. 2002. Caltepec fault zone: An Early Permian dextral transpressional boundary between the Proterozoic Oaxacan and Paleozoic Acatlan Complexes, southern Mexico, and regional tectonic implications. Tectonics, v. 21 (3), p. 1-18.

Fisher, R. V. 1961. Proposed classification of volcaniclastic sediments and rocks; Geological Society of America Bulletin, v. 72, p.1395–1408.

Fossen, H., and Rykkelid, E. 1992. Post-collisional extension of the Caledonide orogen in Scandinavia: structural expressions and tectonic significance. Geology, v. 20, p. 737-740.

Franklin, J. M. Gibson, H. L. Jonasson, I. R. and Galley, A. G. 2005. Volcanogenic Massive Sulfide Deposits, *in* Economic Geology 100th Anniversary Volume, J.W. Hedenquist, J.F.H. Thompson, R.J. Goldfarb, and J.P. Richards eds. p. 523-560.

Fries, C. Jr. 1960. Geología del Estado de Morelos y de partes adyacentes de México y Guerrero, región central meridional de México: Universidad Nacional Autónoma de México, Instituto de Geología, Boletín no. 60, 236 p.

García-Fons, Javier, Pérez, Juan M., Novelo, Luis Felipe. 1981. Geología del Yacimiento Rey de Plata, Teloloapan, Mexico. Technical Proceedings, AIMMGM Convention.

Gibson, H.L., and Watkinson, D.H. 1990. Volcanogenic massive sulfide deposits of the Noranda cauldron and shield volcano, Quebec: Canadian Institute of Mining and Metallurgy Special Volume 43, p. 119–132.

Gibson, H. L., Morton, R. L., and Hudak, G. J. 1999. Submarine volcanic processes, deposits, and environments favourable for the location of volcanic associated massive sulfide deposits; *in* Volcanic associated massive sulfide deposits: processes and examples in modern and ancient settings, Barrie, C. T., and Hannington, M. D., eds.: Reviews in Economic Geology, 8, 13-49.

Gibson, H.L. 2005. Volcanic-hosted ore deposits, *in* Marti, J., and Ernst, G., eds., Volcanoes in the environment: New York, NY, Cambridge University Press, p. 944-1952.

Giles, David A., and García-Fons, Javier. 2000. Volcanogenic Deposits in Mexico: The Producing Mines in VMS Deposits of Latin America, Geological Association of Canada, Mineral Deposits Division, p. 135-140.

Guerrero-Suastegui, M., Ramírez-Espinosa, J., Talavera-Mendoza, O., and Campa-Uranga, M.F. 1991. El desarrollo carbonatado del Cretácico Inferior asociado al arco de Teloloapan, Noroccidente del Estado de Guerrero: Convención sobre la evolución Geológica Mexicana, 1er Congreso Mexicano de Mineralogía, Pachuca, Memoir, p. 67–70.

Guerrero-Suastegui, M. 2004. Depositional and tectonic history of the Guerrero Terrane, Sierra Madre de Sur; with emphasis on sedimentary successions of

the Teloloapan area, southwestern Mexico [Ph.D. thesis]: St. John's, Newfoundland, Memorial University, 600 p.

Hart, T., Gibson, H.L., and Lesher, C.M. 2004. Trace Element Geochemistry and Petrogenesis of Felsic Volcanic Rocks Associated with Volcanogenic Cu-Zn-Pb Massive Sulfide Deposits. Economic Geology, v.99, p.1003-1013.

Hocker, S. M. 2005. Volcanic Stratigraphy, Synvolcanic Intrusions and Controls on Mineralization at the Archean Genex Mine, Kamiskotia Area, Timmins, Ontario [M.Sc. thesis]: Sudbury, Laurentian University, 215 p.

Keppie, J.D., Nance, R.D., Fernández-Suárez, J., Storey, C.D., Jeffries, T.E., and Murphy, J.B. 2006. Detrital zircon data from the Eastern Mixteca terrane, southern Mexico: Evidence for an Ordovician–Mississippian continental rise and a Permo-Triassic clastic wedge adjacent to Oaxaquia: International Geology Review, v. 48, p. 97–111.

Knuckey, M. J., Comba, C. D. A., and Riverin, G. 1982. Structure, metal zoning and alteration at the Millenbach deposit, Noranda, Quebec: Geological Association of Canada Special paper 25, p. 255–295.

Lapierre, H., Brouxel, M., Albarède, F., Coulon, C., Lecuyer, C., Martin, P., Mascle, G., and Rouer, O. 1987. Paleozoic and Lower Mesozoic magmas from the eastern Klamath Mountains (North California) and the geodynamic evolution of northwestern America: Tectonophysics, v. 140, p. 155–177.

Lewis, P.D., and Rhys, D.A. 2000. Geological setting of the Tizapa volcanogenic massive sulfide deposit, Mexico State, Mexico: Geological Association of Canada, Mineral Deposits Division Special Publication 2, p. 87–112.

Lydon, J. W. 1984. Ore deposit model: Volcanogenic massive sulfide deposits. Part 1: A descriptive model: Geoscience Canada, v. 11, p. 195–202.

MacLean, W.H. 1990. Mass Change calculations in altered rock series. Mineralium Deposita, vol. 25, p. 44-49.

MacLean, W.H., and Barret, T.J. 1993. Lithogeochemical techniques using immobile elements; Journal of Geochemical Exploration, v. 48, no. 2, p. 109-133.

Marcoux, E., Belkabir, A., Gibson, H. L., Lentz, D., Ruffet, D. 2008. Draa Sfar, Morocco: A Visean (331 Ma) pyrrhotite-rich, polymetallic volcanogenic massive sulphide deposit in a Hercynian sediment-dominant terrane: Ore Geology Reviews, v. 33, p. 307-328.

Martini, M., Ferrari, L., López-Martínez, M., and Valencia, V. 2010. Stratigraphic redefinition of the Zihuatanejo area, southwestern Mexico. Revista Mexicana de Ciencias Geológicas, v. 27, num. 3, 2010, p.412-430.

Mendoza, O.T., and Suastegui, M.G. 2000. Geochemistry and isotopic composition of the Guerrero terrane (western México): Implications for the tectonomagmatic evolution of southwestern North America during the late Mesozoic: Journal of South American Earth Sciences, v. 13, no. 4, p. 297–324.

Monter-Ramírez, A. 2004. Estratigrafía, sedimentología y relaciones tectónicas de la Formación Balsas en la región de Amacuzac, Morelos: Universidad Nacional Autónoma de México, Facultad de Ingeniería, tesis de licenciatura, 55 p., unpublished.

Mortensen, J. K., Hall, B. V., Bissing, T., Friedman, R. M, Danielson, T., Oliver, J., Rhys, D. A., and Ross, K. V. 2003. U-Pb zircon age and Pb isotopic constraints

on the age and origin of volcanogenic massive sulfide deposits in the Guerrero Terrane of central Mexico: Geological Society of America Abstracts with Programs, v. 35, no. 4, p. 61.

Mortensen, J.K., Hall, B.V., Bissig, T., Friedman, R.M., Danielson, T., Oliver, J., Rhys, D.A., Ross, K.V., and Gabites, J.E. 2008. Age and paleotectonic setting of volcanogenic massive sulfi de deposits in the Guerrero terrane of central Mexico: Constraints from U-Pb age and Pb isotope studies: Economic Geology and the Bulletin of the Society of Economic Geologists, v. 103, p. 117–140.

Ortega-Gutiérrez, F. 1981. Metamorphic belts of southern Mexico and their tectonic significance: Geofísica Internacional, v. 20, p. 177–202.

Ortega-Gutiérrez, F., Ruíz, J., and Centeno-García, E. 1995. Oaxaquia—A Proterozoic microcontinent accreted to North America during the Late Paleozoic: Geology, v. 23, p. 1127–1130.

Ortiz-Hernandez, E.L., Yta, M., Talavera, O., Lapierre, H., Monod, O., and Tardy, M. 1991. Origine intra-océanique des formations volcano-plutoniques d'arc du Jurassique supérieur–Crétacé inférieur du Mexique centro-méridional: Comptes Rendus de l'Académie des Sciences (Paris) (Ser. 2), v. 305, p. 1093–1098.

Ortiz-Hernandez, E.L. 1992. L'arc intra-océanique allocthone Jurassique supérieur–Crétacé inférieur du domaine Cordillerain Mexicain (Guerrero Terrane): Pétrographie, géochimie et mineralisations associées des segments de Guanajuato et de Palmar Chico–Arcelia consequences paleogéographiques [thesis]: Université Joseph Fourier-Grenoble, France, 109 p.

Ortiz-Hernandez, E.L., Acevedo-Sandoval, O.A., and Flores-Castro, K. 2003. Early Cretaceous intraplate seamounts from Guanajuato, central México, geochemical and mineralogical data: Universidad Nacional Autónoma de

México, Instituto de Geología: Revista Mexicana de Ciencias Geológicas, v. 20, p. 27–40.

Pearce, J.A., Harris, B.W., and Tindle, A.G. 1984. Trace element discrimination diagrams for the tectonic interpretation of granitic rocks. J. Petrol., v. 25, p. 956-983.

Pearce, J.A. 1996. A user's guide to basalt discrimination diagrams; *in* Trace element geochemistry of volcanic rocks: applications for massive sulphide exploration, Geological Association of Canada, Short Course Notes, v.12, p.79-113.

Petrus, J.A. & Kamber, B.S. 2012. VizualAge: A Novel Approach to Laser Ablation ICP-MS U-Pb Geochronology Data Reduction. Geostandards and Geoanalytical Research, vol. 36(3), p.247–270.

Poole, F.G., Perry, W.J. Jr., Madrid, R.J., Amaya-Martínez, R. 2005. Tectonic synthesis of the Ouachita-Marathon-Sonora orogenic margin of southern Laurentia: Stratigraphic and structural implications for timing of deformational events and platetectonic model, *in* Anderson, T.H., Nourse, J.A., McKee, J.W., Steiner, M.B. (eds.), The Mojave-Sonora Megashear Hypothesis: Development, Assessment, and Alternatives: Boulder, Colorado, Geological Society of America, Special Paper 393, p. 543-596.

Ramírez-Espinosa, J., Campa, M.F., Talavera, O., and Guerrero, M. 1991. Caracterización de los arcos insulares de la Sierra Madre del Sur y sus implicaciones tectónicas: Convención sobre la evolución Geológica Mexicana, 1er Congreso Mexicano de Mineralogía, Pachuca, Memoir, p. 163–166.

Rhys, D.A., Enns, S.G., and Ross, K.V. 2000. Geological setting of deformed VMS-type mineralization in the Azulaquez-Tlanilpa area, northern Guerrero State,

Mexico: Geological Association of Canada, Mineral Deposits Division. Special Publication 2, p. 113–133.

Ruíz, J., Patchett, P.J., and Ortega-Gutiérrez, F. 1988. Proterozoic and Phanerozoic basement terranes of México from Nd isotopic studies: Geological Society of America Bulletin, v. 100, p. 274–281.

Salinas-Prieto, J.C., Monod, O., and Faure, M. 2000. Ductile deformations of opposite vergence in the eastern part of the Guerrero Terrane (SW Mexico): Journal of South American Earth Sciences, v. 13, p. 389–402.

Shervais, J.W. 1982. Ti-V plots and the petrogenesis of modern and ophiolitic lavas, Earth and Planetary Science Letters, v. 59 (1), p. 101-118.

Sun, S-s., and McDonough, W.F. 1989. Chemical and isotopic systematics of oceanic basalts: implications for mantle composition and processes; *in* Magmatism in the ocean basins, Geological Society of London, Special Publication No.42, p. 313-345.

Talavera-Mendoza, O. 1993. Les formations orogéniques mésozoïques du Guerrero (Mexique méridional): Contribution à la connaissance de l'évolution géodynamique des cordillères mexicaines [Ph.D. thesis]: Université Joseph Fourier-Grenoble I, France, 462 p.

Talavera-Mendoza, O., Ramírez, E. J., and Guerrero-Suastegui, M. 1995. Petrology and Geochemistry of the Teloloapan Subterrene, a Lower Cretaceous evolved intra-oceanic island-arc: Geofísica Internacional, v. 34, p. 3-22.

Talavera-Mendoza, M.O. 2000. Mélanges in southern México: Geochemistry and metamorphism of Las Ollas complex (Guerrero Terrane): Canadian Journal of Earth Sciences, v. 37, p. 1309–1320.

Tardy, M., Lapierre, H., Freydier, C., Coulon, C., Gill, J.B., Mercier de Lepinay, B., Beck, C., Martinez, J., Talavera, M., Ortiz, E., Stein, G., Bourdier, J.L., and Yta, M. 1994. The Guerrero suspect terrane (western Mexico) and coeval arc terranes (the Greater Antilles and the Western Cordillera of Colombia): A late Mesozoic intra-oceanic arc accreted to cratonal America during the Cretaceous: Tectonophysics, v. 234, p. 49–73.

Taylor, S. R., and McLennan, S. M. 1985. The Continental Crust: Its Composition and Evolution. xvi + 312 pp. Oxford, London, Edinburgh, Boston, Palo Alto, Melbourne: Blackwell Scientific.

White, J.D.L. and Houghton, B.F. 2006. Primary volcaniclastic rocks: Geology, v. 34, p. 677-680.

Winchester, J. A., and Floyd, P. A. 1977. Geochemical discrimination of different magma series and their differentiation products using immobile elements: Chemical Geology, v. 20 (4), p. 325-343.

Yañez, P., Ruiz, J., Patchett, P.J., Ortega-Gutiérrez, F., and Gehrels, G. 1991. Isotopic studies of the Acatlan Complex, southern Mexico: Implications for Paleozoic North American tectonics: Geological Society of America Bulletin, v. 103, p. 817–828.

Appendix 1: Distribution of collected samples of the Rey de Plata deposit

Table A1. Distribution of samples.

Sample	Source	Description	Member/Formation
28504	DDH 15010	Monolithic felsic breccia	Rey de Plata
28505	DDH 15010	Felsic clast	Rey de Plata
28506	DDH 15010	Felsic hyaloclastite	Rey de Plata
28507	DDH 15010	Felsic lapilli tuff	Rey de Plata
28508	DDH 15010	Massive QP Felsic	Rey de Plata
28509	DDH 15010	Massive Felsic	Rey de Plata
28510	DDH 15010	Felsic tuff-wispy	Rey de Plata
28514	DDH 15010	Massive QP Felsic	Rey de Plata
28515	DDH 15010	Felsic quartz crystal tuff	Rey de Plata
28516	DDH 15010	Felsic quartz crystal tuff	Rey de Plata
28519	DDH 15010	Felsic quartz crystal tuff	Rey de Plata
28502	DDH 15010	Mafic sill	Villa Ayala
28503	DDH 15010	Mafic sill	Villa Ayala
28512	DDH 15010	Mafic sill	Ahuehuetla
28513	DDH 15010	Mafic sill	Ahuehuetla
28517	DDH 15010	Mafic sill	Ahuehuetla
28518	DDH 15010	Mafic sill	Ahuehuetla
28520	DDH 15010	Mafic volcaniclastic	Ahuehuetla
28523	DDH 23210	Massive Felsic	Rey de Plata
28524	DDH 23210	Massive Felsic	Rey de Plata
28527	DDH 23210	Felsic quartz crystal tuff	Rey de Plata
28521	DDH 23210	Mafic sill	Villa Ayala
28528	DDH 23210	Mafic sill	Ahuehuetla
RP-13-1	Field	Rhyolitic intrusion	Rey de Plata
RP-13-2	Field	Rhyolitic intrusion	Rey de Plata
RP-13-11	Field	Rhyolitic intrusion	Rey de Plata
RP-13-13	Field	Rhyolitic intrusion	Rey de Plata
RP-13-20	Field	Rhyolitic intrusion	Rey de Plata
RP-13-24	Field	Rhyolitic intrusion	Rey de Plata
RP-13-40	Field	Rhyolitic intrusion	Rey de Plata
RP-13-41	Field	Rhyolitic intrusion	Rey de Plata
RP-13-14	Field	Mafic volcaniclastic	Villa Ayala
RP-13-17	Field	Mafic volcaniclastic	Villa Ayala
RP-13-22	Field	Mafic sill	Villa Ayala
RP-13-23	Field	Mafic sill	Villa Ayala
RP-13-39	Field	Mafic sill	Villa Ayala
RP-13-44	Field	Mafic volcaniclastic	Villa Ayala
RP-13-6	Field	Feldspar-phyric mafic intrusion	Intrusion
RP-13-31	Field	Feldspar-phyric mafic intrusion	Intrusion
RP-13-42	Field	Feldspar-phyric mafic intrusion	Intrusion
RP-13-9	Field	Sandstone	Miahuatepec
RP-13-10	Field	Argillite	Miahuatepec
RP-13-15	Field	Volcanic mafic sandstone	Acapetlahuaya
RP-13-26	Field	Volcanic mafic sandstone	Acapetlahuaya
RP-13-33	Field	Sandstone	Miahuatepec

Appendix 2: Listing of geochemical data from the Rey de Plata deposit

The samples were sent to ALS Chemex in Vancouver, Canada to obtain complete geochemical characterization through combining methods that included the use of XRF (fused pellet) and ICP-AES, to determine major elements, plus carbon and sulfur. Trace elements, including the full rare earth element suite, were analyzed using a lithium borate fusion of the sample prior to acid dissolution and ICP-MS analysis. Details of the analytical techniques, precision and accuracy can be found in the ALS Chemex schedule of services and fees (http://www.alsglobal.com/).

Table A2. Listing of geochemical data from the Rey de Plata deposit.

Sample	Source	Description	Member	SiO_2	Al_2O_3	Fe_2O_3	CaO
				%	%	%	%
28504	DDH 15010	Monolithic felsic breccia	Rey de Plata	63.3	18.8	1.9	0.94
28505	DDH 15010	Felsic clast	Rey de Plata	69.4	13.05	2.71	2.03
28506	DDH 15010	Felsic hyaloclastite	Rey de Plata	73.3	10.15	4.47	0.37
28507	DDH 15010	Felsic lapilli tuff	Rey de Plata	72.1	10.7	5.49	0.06
28508	DDH 15010	Massive QP Felsic	Rey de Plata	69.2	12.8	3.99	0.06
28509	DDH 15010	Massive Felsic	Rey de Plata	65.7	14.95	4.06	0.13
28510	DDH 15010	Felsic tuff-wispy	Rey de Plata	68.6	12.2	4.37	0.34
28514	DDH 15010	Massive QP Felsic	Rey de Plata	68	15.6	2.25	1.66
28515	DDH 15010	Felsic quartz crystal tuff	Rey de Plata	56.4	12.9	4.36	6.03
28516	DDH 15010	Felsic quartz crystal tuff	Rey de Plata	68.2	12.8	4.46	0.3
28519	DDH 15010	Felsic quartz crystal tuff	Rey de Plata	72.3	12.9	4.68	0.26
28502	DDH 15010	Mafic sill	Villa Ayala	44.5	17.8	7.67	9.82
28503	DDH 15010	Mafic sill	Villa Ayala	59.2	14.35	4.69	4.07
28512	DDH 15010	Mafic sill	Ahuehuetla	50.2	19.85	9.87	4.13
28513	DDH 15010	Mafic sill	Ahuehuetla	41.4	17.2	10.9	9.25
28517	DDH 15010	Mafic sill	Ahuehuetla	45.2	17.4	9.82	5.49
28518	DDH 15010	Mafic sill	Ahuehuetla	42.7	14.85	10.75	4.89
28520	DDH 15010	Mafic volcaniclastic	Ahuehuetla	51.7	17.5	7.18	6.37
28523	DDH 23210	Massive Felsic	Rey de Plata	30	22.2	4.09	9.08
28524	DDH 23210	Massive Felsic	Rey de Plata	34.1	23.5	3.86	6.92
28527	DDH 23210	Felsic quartz crystal tuff	Rey de Plata	64.3	14.3	4.32	0.9
28521	DDH 23210	Mafic sill	Villa Ayala	42.6	15	6.96	8.89
28528	DDH 23210	Mafic sill	Ahuehuetla	50.2	18.1	6.49	4.02
RP-13-1	Field	Rhyolitic intrusion	Rey de Plata	80.1	11.9	0.86	0.02
RP-13-2	Field	Rhyolitic intrusion	Rey de Plata	74.8	15.65	0.38	0.02
RP-13-11	Field	Rhyolitic intrusion	Rey de Plata	65.5	13.7	3.62	5.51
RP-13-13	Field	Rhyolitic intrusion	Rey de Plata	61.4	23	5.16	0.22
RP-13-20	Field	Rhyolitic intrusion	Rey de Plata	75.6	14.6	1.84	0.03
RP-13-24	Field	Rhyolitic intrusion	Rey de Plata	86.5	7.26	1.82	0.06
RP-13-40	Field	Rhyolitic intrusion	Rey de Plata	71.3	14.05	5.73	0.05
RP-13-41	Field	Rhyolitic intrusion	Rey de Plata	66.9	16.55	5.42	0.03
RP-13-14	Field	Mafic volcaniclastic	Villa Ayala	59	16.45	8.27	0.34
RP-13-17	Field	Mafic volcaniclastic	Villa Ayala	53.9	17.95	7.9	0.35
RP-13-22	Field	Mafic sill	Villa Ayala	50.1	18.6	8.18	7.87
RP-13-23	Field	Mafic sill	Villa Ayala	53.9	18.45	9.91	1.88
RP-13-39	Field	Mafic sill	Villa Ayala	47.8	14.7	9.01	10.3
RP-13-44	Field	Mafic volcaniclastic	Villa Ayala	47.7	18.15	7.52	9.68
RP-13-6	Field	Feldspar-phyric mafic intrusion	Intrusion	36.5	16.5	9.31	8.73
RP-13-31	Field	Feldspar-phyric mafic intrusion	Intrusion	68.1	17.55	4.5	0.61
RP-13-42	Field	Feldspar-phyric mafic intrusion	Intrusion	47.4	15.7	8.56	8.96
RP-13-9	Field	Sandstone	Miahuatepec	43.3	9.84	2.16	20.8
RP-13-10	Field	Argillite	Miahuatepec	62.5	13.6	5.15	4.03
RP-13-15	Field	Volcanic mafic sandstone	Villa Ayala	73.2	14.8	1.58	0.38
RP-13-26	Field	Volcanic mafic sandstone	Villa Ayala	63.9	17.55	7.21	0.04
RP-13-33	Field	Sandstone	Miahuatepec	47.7	12.35	2.33	18.3

Table A2. Listing of geochemical data from the Rey de Plata deposit. Continued.

Sample	MgO	Na_2O	K_2O	Cr_2O_3	TiO_2	MnO	P_2O_5	SrO	BaO	LOI	Total
	%	%	%	%	%	%	%	%	%	%	%
28504	2.03	0.1	4.44	0	0.26	0.02	0	0.02	0.19	6.52	98.52
28505	1.81	0.3	3.39	0	0.24	0.08	0.06	0.01	0.24	5.8	99.12
28506	0.7	0.12	2.75	0.01	0.26	0.01	0.02	0	0.5	4.48	97.14
28507	0.55	0.11	3.12	0.01	0.24	0.01	0	0	0.15	4.61	97.15
28508	0.77	0.13	3.66	0.01	0.27	0.01	0.06	0	0.13	4.66	95.75
28509	0.86	0.13	4.44	0	0.32	0.01	0.09	0	0.14	5.03	95.86
28510	0.82	0.13	3.44	0.01	0.3	0.02	0.08	0	0.11	5.08	95.5
28514	0.58	1.86	2.05	0	0.28	0.02	0.07	0.02	0.08	4.76	97.23
28515	1.96	0.76	1.63	0	0.31	0.05	0.06	0.02	0.16	12	96.64
28516	2.28	0.12	3.46	0	0.45	0.03	0.06	0	0.17	5.19	97.52
28519	0.73	0.14	3.7	0	0.39	0.01	0	0	0.24	5.28	100.63
28502	4.87	3.23	0.97	0.01	0.9	0.16	0.35	0.05	0.04	7.98	98.35
28503	1.82	0.01	1.32	0.04	0.88	0.1	0.18	0.02	0.03	11.55	98.26
28512	2.69	3.37	1.57	0.02	1.69	0.09	0.67	0.01	0.08	5.8	100.04
28513	4.2	1.54	1.45	0.01	1.43	0.19	0.51	0.02	0.25	11.7	100.05
28517	6.58	4.83	0.37	0.01	1.45	0.18	0.24	0.03	0.04	8.07	99.71
28518	13.4	0.9	0.01	0.08	1.02	0.11	0.16	0.03	0	8.41	97.31
28520	4.57	2.59	2.23	0.01	1.03	0.07	0.3	0.04	0.07	5.35	99.01
28523	6.68	0.52	4.4	0	0.28	0.09	0.02	0.01	0.18	17.4	94.95
28524	8.25	0.19	3.23	0	0.3	0.07	0.02	0.01	0.1	16.3	96.85
28527	1.1	0.24	3.36	0	0.43	0.02	0.09	0	0.18	6.05	95.29
28521	3.46	0.23	1.31	0.01	0.75	0.14	0.36	0.04	0.04	16.85	96.64
28528	3.38	4.91	1.73	0.01	1.04	0.13	0.35	0.02	0.09	6.3	96.77
RP-13-1	0.25	0.18	3.11	0.01	0.3	0.01	0.03	0.01	0.1	2.57	99.45
RP-13-2	0.37	0.18	3.36	0.01	0.54	0.01	0.03	0.01	0.07	3.42	98.85
RP-13-11	0.25	2.86	1.66	0.01	0.29	0.05	0.06	0.01	0.04	7.33	100.89
RP-13-13	0.19	1.8	1.81	0.01	1.05	0.03	0.12	0.01	0.04	6.52	101.36
RP-13-20	0.39	0.29	3.92	0.01	0.35	0.01	0.03	0.01	0.08	3.7	100.86
RP-13-24	0.34	0.09	2.02	0.01	0.16	0.01	0.01	0.01	0.05	1.79	100.13
RP-13-40	0.57	0.09	3.22	0.01	0.29	0.03	0.05	0.01	0.09	4.03	99.52
RP-13-41	0.56	0.09	3.56	0.01	0.64	0.02	0.08	0.01	0.15	4.8	98.82
RP-13-14	4.67	3.77	0.14	0.01	1.03	0.04	0.12	0.01	0.01	5.96	99.82
RP-13-17	10.7	0.19	1.77	0.02	0.77	0.08	0.11	0.01	0.04	6.83	100.62
RP-13-22	4.75	5.07	0.89	0.01	1.27	0.16	0.42	0.05	0.04	3.59	101
RP-13-23	3.36	4.52	1.57	0.01	1.38	0.14	0.33	0.06	0.09	5.7	101.3
RP-13-39	5.49	2.43	0.77	0.03	0.87	0.16	0.2	0.08	0.02	9.33	101.19
RP-13-44	5.26	3	0.89	0.01	0.99	0.09	0.24	0.05	0.03	8.2	101.81
RP-13-6	4.83	0.08	0.65	0.03	1.12	0.2	0.18	0.02	0.01	21.7	99.86
RP-13-31	0.24	0.05	0.47	0.01	0.96	0.06	0.14	0.03	0.02	7.74	100.48
RP-13-42	2.18	0.04	0.82	0.04	0.95	0.14	0.21	0.01	0.02	16.05	101.08
RP-13-9	0.87	2.1	1.7	0.01	0.55	0.17	0.08	0.03	0.05	18.55	100.21
RP-13-10	1.67	0.06	3.15	0.01	0.48	0.04	0.09	0.01	0.08	9.41	100.28
RP-13-15	0.27	0.68	2.87	0.02	0.78	0.02	0.2	0.01	0.09	3.37	98.27
RP-13-26	0.41	0.27	4.08	0.02	0.93	0.06	0.14	0.01	0.09	4.73	99.44
RP-13-33	0.49	0.1	2.33	0.01	0.57	0.09	0.08	0.02	0.04	17.6	101.96

Table A2. Listing of geochemical data from the Rey de Plata deposit. Continued.

Sample	Ag	Ba	Ce	Co	Cr	Cs	Cu	Dy	Er	Eu	Ga	Gd	Hf
	ppm	ppm	ppm	ppm	ppm	ppm	ppm	ppm	ppm	ppm	ppm	ppm	ppm
28504	0	1845	49.1	3.3	5	5.69	1	3.62	2.46	0.84	23.8	3.37	6.4
28505	0	2070	26.9	5	10	3.77	12	1.97	1.34	0.58	15.9	1.93	3.5
28506	10	4680	17.3	12.2	60	2.5	382	1.38	0.92	0.51	16.6	1.28	2.3
28507	1	1435	21.8	15.5	50	2.14	39	2.07	1.26	0.42	15.3	2.03	2.7
28508	1	1345	27.3	9.3	30	3.37	17	2.65	1.55	0.53	17	2.49	3.1
28509	1	1435	30.5	11.6	30	3.83	21	2.28	1.48	1	18.3	2.34	3.8
28510	1	996	25.4	10.5	70	2.64	32	2.26	1.41	0.71	16.3	2.4	3.3
28514	0	820	30.7	1.8	5	3.81	2	2.72	1.71	0.76	19.8	2.5	3.8
28515	0	1405	17.8	3.8	5	3.18	7	1.8	0.94	0.56	16.2	2.09	2.6
28516	0	1625	24.8	10.8	20	6.85	17	2.64	1.65	0.43	17	2.64	3.2
28519	15	1960	20.9	11.2	20	5.93	50	2.02	1.43	0.34	14.6	1.93	2.6
28502	0	365	43.4	28	90	7.93	39	3.76	2.14	1.37	18.3	3.91	2.9
28503	0	327	35.9	34	330	2.62	66	2.85	1.59	1.02	17.3	3.13	2.2
28512	0	725	58.3	21.4	90	1.95	75	4.55	2.46	1.83	22.2	5.15	4.5
28513	0	2170	55.1	16.7	80	2.23	7	4.23	2.3	1.77	17.7	4.73	3.4
28517	0	404	22.7	32.5	120	3.04	53	4.78	2.71	1.37	20.1	4.63	2
28518	0	70.4	16.3	50.2	620	4.43	85	3.86	2.06	1.17	15.7	3.6	1.4
28520	1	642	38.4	24.2	60	3.22	26	4.05	2.32	1.43	17.6	4.22	2.8
28523	0	1655	37.4	2.6	5	6.17	5	3.56	2.2	0.65	27	3.14	6.9
28524	0	956	63.7	2.6	10	4.51	9	4.89	3.13	1.51	27.9	5.15	8.2
28527	0	1720	12.5	16.8	20	5.16	25	2.3	1.5	0.57	18.4	2.3	2.9
28521	0	386	34.2	17.5	80	2.83	24	3.56	2.04	1.27	16.1	3.63	2.5
28528	0	805	42	18.6	40	2.32	1	4.01	2.28	1.42	18.2	4.18	2.9
RP-13-1	1.3	841	24.2	1	30	1.72	9	1.82	1.3	0.26	16.5	1.74	3.6
RP-13-2	0.9	539	25.9	1	40	1.54	2	2.69	1.85	0.37	19.1	2.44	3.6
RP-13-11	0.5	301	26.9	4	20	2.82	4	2.61	1.75	0.66	14.2	2.5	3.5
RP-13-13	0.5	326	36.1	11	40	3.45	14	7.03	4.34	1.63	25.3	6.49	5.3
RP-13-20	2.2	606	29.4	1	90	4.48	4	1.99	1.38	0.51	16.8	2.09	3.6
RP-13-24	5.2	418	30	1	20	3.57	12	3.57	2.27	0.59	9.9	3.37	4.4
RP-13-40	0.7	757	39.6	3	40	2.07	419	5.23	3.56	1.24	17.1	4.56	7.1
RP-13-41	0.5	1190	19.8	3	60	1.68	192	2.24	1.7	0.42	17.7	1.8	4.5
RP-13-14	0.5	83.2	24.9	13	70	0.36	14	5.37	3.24	1.41	19.1	5.46	4.2
RP-13-17	0.5	322	28	16	120	3.1	48	3.63	2.31	1.1	19.1	3.64	4
RP-13-22	0.5	288	47.6	22	90	1.86	45	4.24	2.45	1.63	18.7	4.57	3.6
RP-13-23	0.5	725	27.5	21	10	6.64	51	6.16	3.73	1.79	20.2	6.28	3.3
RP-13-39	0.5	191	31	24	210	0.83	95	3.81	2.11	1.28	14.5	4.17	2.4
RP-13-44	0.5	242	26.7	26	110	0.68	63	3.95	2.51	1.22	17	4.02	2.6
RP-13-6	114	20	34	250	5.36	78	3.27	1.94	1	16	3.21	2.3	0.7
RP-13-31	128.5	45.5	15	90	2.89	28	4.22	2.73	1.27	17.6	4.25	4.2	0.93
RP-13-42	181	29.3	28	320	1.62	58	4.33	2.43	1.37	14.7	4.6	2.4	0.93
RP-13-9	366	41.7	6	30	6.13	6	4.47	2.58	0.87	9.1	4.37	5	0.95
RP-13-10	643	44.5	5	50	12.7	15	5.12	3.25	0.98	16.9	4.88	4.6	1.14
RP-13-15	703	61	8	150	4.72	32	4.69	2.74	1.44	18.7	5.47	5.9	0.97
RP-13-26	657	80.7	9	120	4.32	61	6.08	3.62	1.76	22.1	6.51	6.4	1.27
RP-13-33	342	48.8	4	30	6.22	5	5.15	2.96	0.95	13.8	5.1	5.3	1.11

Table A2. Listing of geochemical data from the Rey de Plata deposit. Continued.

Sample	Ho	La	Lu	Mo	Nb	Nd	Ni	Pb	Pr	Rb	Sm	Sn	Sr
	ppm	ppm	ppm	ppm	ppm	ppm	ppm	ppm	ppm	ppm	ppm	ppm	ppm
28504	0.81	24.3	0.55	3	6.5	19.1	0	16	5.47	97.2	3.78	2	153.5
28505	0.43	13	0.27	2	3.8	10.8	0	18	3.04	91.4	2.28	1	63.8
28506	0.29	8	0.19	6	2.4	7.2	19	294	1.94	90.2	1.5	18	47.5
28507	0.44	9.6	0.23	2	2.6	9.9	17	22	2.58	95.5	2.18	32	17.8
28508	0.55	12.5	0.29	0	3.4	11.7	10	12	3.18	114	2.3	2	15.1
28509	0.49	14.2	0.29	2	3.8	12.9	12	30	3.54	145.5	2.71	2	14
28510	0.46	14.1	0.24	2	3.3	10.9	35	23	2.86	104	2.49	3	31.9
28514	0.59	13.9	0.37	0	4.5	13	0	0	3.53	66.8	2.77	2	150
28515	0.35	7.7	0.16	0	2.5	8.4	0	0	2.18	47.7	2.1	1	171.5
28516	0.59	11.1	0.3	2	3.7	11.5	0	32	2.97	96.9	2.69	1	27.7
28519	0.48	9	0.26	3	2.9	9.6	6	491	2.51	86.7	2.15	2	29.9
28502	0.77	21.3	0.36	0	20.7	19.3	51	0	5.03	24.4	4.21	1	430
28503	0.59	16.3	0.29	0	13.5	17.3	81	0	4.46	34.6	3.59	1	226
28512	0.86	28.7	0.34	2	47.5	26.8	29	0	6.81	38.8	5.93	1	117
28513	0.79	27.7	0.3	2	40.6	24.7	24	0	6.45	42	5.48	1	193.5
28517	1	8.7	0.41	0	9.7	14.8	40	5	3.23	9.8	4.21	1	325
28518	0.77	5.5	0.3	0	4.7	11.3	289	0	2.41	0.6	3.28	1	307
28520	0.85	17.2	0.39	0	16	19.4	30	6	4.84	60.3	4.6	1	368
28523	0.75	19.3	0.44	13	6.6	11.2	0	10	3.7	118	2.23	6	117.5
28524	1.04	30	0.67	17	7.1	28	25	12	7.6	88.3	6.44	4	63.8
28527	0.53	4.9	0.27	4	3.3	6.7	7	194	1.59	89.2	2	3	58.5
28521	0.75	15.7	0.36	2	19.1	17	36	5	4.15	38.3	3.85	1	390
28528	0.82	20.1	0.39	0	17.5	20.9	21	0	5.26	59.7	4.52	1	160.5
RP-13-1	0.42	12.4	0.24	1	3.1	11.3	1	41	2.88	88.5	2.1	8	43.4
RP-13-2	0.62	14.3	0.3	1	4.1	11	1	7	2.95	95.6	2.43	9	31.7
RP-13-11	0.59	14.1	0.31	1	3.5	12	3	2	3.22	34.3	2.57	1	61.9
RP-13-13	1.53	18.3	0.66	1	6.5	22	2	7	5.31	45.2	5.55	2	92.6
RP-13-20	0.44	15.8	0.27	1	3.4	12.1	1	19	3.45	113.5	2.36	6	37.9
RP-13-24	0.79	14.6	0.35	1	4.2	14.9	1	25	3.8	48.7	3.33	13	10.1
RP-13-40	1.18	19.4	0.56	1	6.8	19.5	1	32	5.04	93.9	4.53	3	78.7
RP-13-41	0.52	10	0.31	1	4.5	8.7	3	19	2.27	92.7	1.78	2	69.2
RP-13-14	1.13	16.8	0.48	1	5.9	19.8	3	4	4.73	4.3	5	2	32.5
RP-13-17	0.81	13.1	0.36	1	4.5	16.1	16	4	3.81	43.8	3.77	1	27
RP-13-22	0.89	24.7	0.37	1	31.3	22.8	34	2	5.76	21.6	4.73	1	389
RP-13-23	1.31	14.6	0.54	1	9	21.2	3	7	4.83	51.3	5.43	1	507
RP-13-39	0.8	14.8	0.3	1	5.2	18.2	64	2	4.26	23.1	4.05	1	637
RP-13-44	0.87	12.5	0.37	1	7.4	15.2	42	2	3.62	19.4	3.71	1	438
RP-13-6	9.7	0.29	1	7.1	11.9	110	2	2.67	17.2	2.99	1	161.5	0.5
RP-13-31	23.9	0.43	2	18.5	20.8	18	7	5.55	15.7	4.41	1	286	1.4
RP-13-42	13.6	0.35	1	6.6	16.8	78	7	3.96	19.2	4.18	1	71.8	0.4
RP-13-9	22.5	0.35	2	6.9	19.5	6	11	5.11	65.7	4.22	2	272	0.5
RP-13-10	22.1	0.49	1	7.2	20.9	6	12	5.43	133.5	4.71	3	91.7	0.6
RP-13-15	31	0.43	7	11.5	31.1	14	18	7.93	100.5	6.35	2	93.6	0.9
RP-13-26	40.8	0.55	1	15.5	37.8	31	4	9.99	155.5	7.55	3	71.5	1.1
RP-13-33	25.2	0.42	13	7.9	22.1	4	9	5.66	89	5.04	2	140	0.7

Table A2. Listing of geochemical data from the Rey de Plata deposit. Continued.

Sample	Ta	Tb	Th	Tl	Tm	U	V	W	Y	Yb	Zn	Zr
	ppm	ppm	ppm	ppm	ppm	ppm	ppm	ppm	ppm	ppm	ppm	ppm
28504	0.5	0.59	10.7	3.4	0.41	4.62	9	2	25	3.01	64	235
28505	0.3	0.33	5.51	2.1	0.22	1.78	42	1	13.2	1.52	27	131
28506	0.2	0.21	3.24	3.3	0.14	1.7	94	2	9.2	1	213	85
28507	0.2	0.33	3.92	2	0.2	1.93	81	2	12.7	1.34	45	102
28508	0.3	0.43	5.44	3.1	0.25	2.25	84	3	16.1	1.68	47	117
28509	0.3	0.37	6.15	2.6	0.24	2.11	89	2	13.8	1.67	106	141
28510	0.3	0.37	3.86	2	0.22	1.42	84	3	13.1	1.5	937	121
28514	0.4	0.43	6.58	0	0.29	1.97	42	1	17.4	2	44	151
28515	0.2	0.29	3.6	0.5	0.14	0.51	105	1	9.3	0.97	42	93
28516	0.3	0.43	4.68	1.1	0.27	1.6	111	4	16.2	1.85	94	119
28519	0.2	0.33	3.9	3	0.22	1.96	111	2	13.6	1.48	938	94
28502	1.2	0.63	3.08	0	0.32	1.18	224	1	22.4	2.08	76	125
28503	0.8	0.49	2.54	0	0.24	0.94	241	5	15.9	1.65	85	88
28512	3.1	0.78	4.33	0.5	0.34	0.69	255	1	23.2	2.25	120	179
28513	2.5	0.76	3.66	1	0.31	0.64	212	1	22.3	2.08	109	145
28517	0.5	0.77	1.55	0	0.4	0.63	493	2	26.5	2.5	139	70
28518	0.3	0.62	0.86	0	0.31	0.28	370	1	21.2	1.9	112	52
28520	1	0.69	3.8	0.5	0.36	1.18	262	1	24.1	2.31	93	116
28523	0.6	0.58	11.3	1.2	0.36	5.59	15	1	22.1	2.53	154	247
28524	0.6	0.83	11.85	0.9	0.52	7.27	24	2	30.8	3.74	57	306
28527	0.2	0.39	3.97	1.1	0.23	1.41	169	2	14.6	1.59	277	108
28521	1.1	0.58	2.76	0.5	0.3	1.23	203	1	22	2.04	83	111
28528	1.1	0.66	4.74	0.6	0.35	1.35	293	1	23.7	2.29	119	119
RP-13-1	0.3	0.28	4.68	1.1	0.2	1.61	59	2	11.8	1.44	9	119
RP-13-2	0.3	0.4	4.2	0.9	0.27	1.41	126	2	17.1	1.82	3	134
RP-13-11	0.3	0.42	4.89	0.5	0.27	1.33	62	1	16.8	1.82	50	130
RP-13-13	0.4	1.08	4.25	0.5	0.64	1.58	224	1	40.7	4.16	73	192
RP-13-20	0.3	0.31	4.86	2	0.22	1.48	75	1	12.6	1.5	8	126
RP-13-24	0.4	0.56	4.73	1.4	0.34	1.7	25	1	20.4	2.24	20	153
RP-13-40	0.6	0.79	7.26	0.6	0.54	2.41	50	2	30.2	3.43	129	246
RP-13-41	0.4	0.32	4.59	1.1	0.28	2.35	165	1	15	1.84	1175	165
RP-13-14	0.4	0.87	3.11	0.5	0.46	1.08	138	1	30.2	3.08	158	160
RP-13-17	0.4	0.58	4.03	0.5	0.34	1.28	218	1	21.5	2.26	114	147
RP-13-22	2.1	0.71	3.34	0.5	0.36	1.07	214	1	23.4	2.24	83	151
RP-13-23	0.6	0.99	2.04	0.7	0.53	0.85	330	1	31.7	3.41	411	117
RP-13-39	0.4	0.64	3.04	0.5	0.31	0.98	264	1	20.7	1.94	84	84
RP-13-44	0.5	0.64	1.96	0.5	0.36	0.69	262	1	22.4	2.26	64	95
RP-13-6	0.51	1.63	0.5	0.28	0.61	314	2	17.8	1.81	68	82	36.5
RP-13-31	0.67	5.6	0.5	0.4	2.41	149	7	23.7	2.69	32	167	68.1
RP-13-42	0.72	3.15	0.5	0.35	1.38	244	1	24.5	2.18	52	87	47.4
RP-13-9	0.71	5.08	1	0.37	1.92	41	1	26.1	2.25	46	193	43.3
RP-13-10	0.82	8.84	1	0.48	2.6	94	2	29.9	3.18	86	161	62.5
RP-13-15	0.79	8.65	0.7	0.4	2.8	299	1	24.5	2.63	163	210	73.2
RP-13-26	1.02	11.6	0.9	0.54	2.75	177	2	33.5	3.47	81	243	63.9
RP-13-33	0.82	7.55	0.7	0.43	2.28	50	4	30.7	2.72	51	195	47.7

Appendix 3: McLean and Cann methods for assessing mobility of elements during hydrothermal alteration

McLean Method

Binary diagrams in Figures A3.1 to A3.11 for Al_2O_3, TiO_2, and selected rare earth and high field strength elements used in the classification/petrogenesis diagrams in Chapter 3 are shown below. Blue lines drawn on the diagrams are hand drawn lines that pass through the origin to define distinct sample populations. Samples that fall on, or near a line, have identical or similar element ratios indicating relative immobility of the plotted elements (oxides) as per MacLean (1990) and MacLean and Barrett, (1993).

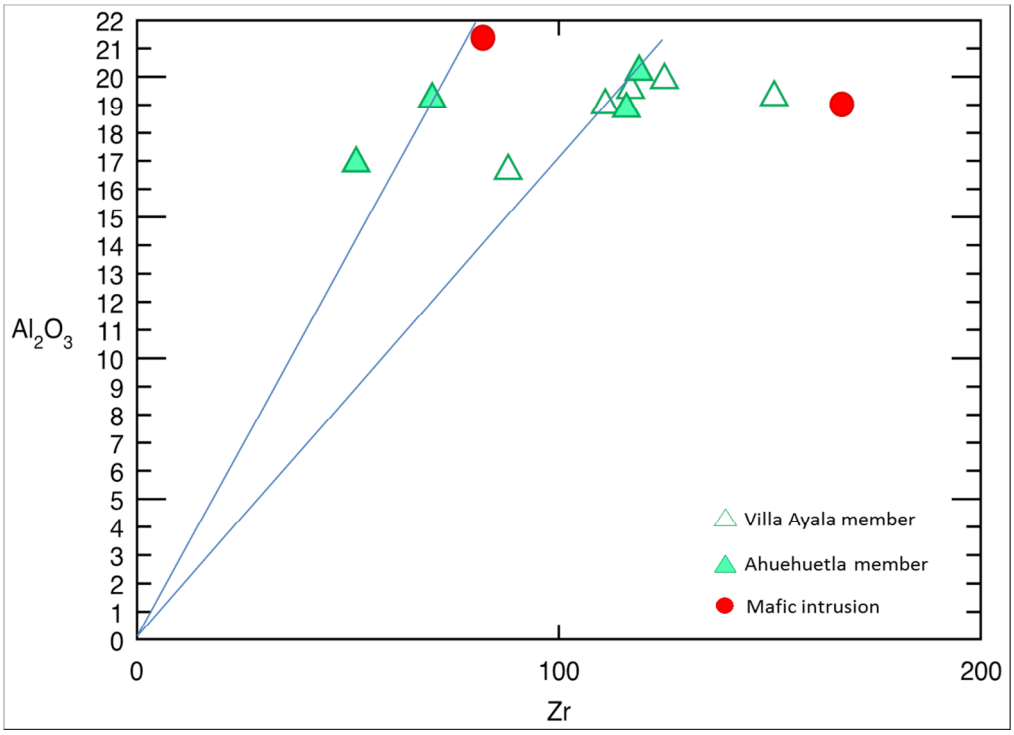

Figure A3.1. Binary diagram for Al_2O_3 versus Zr.

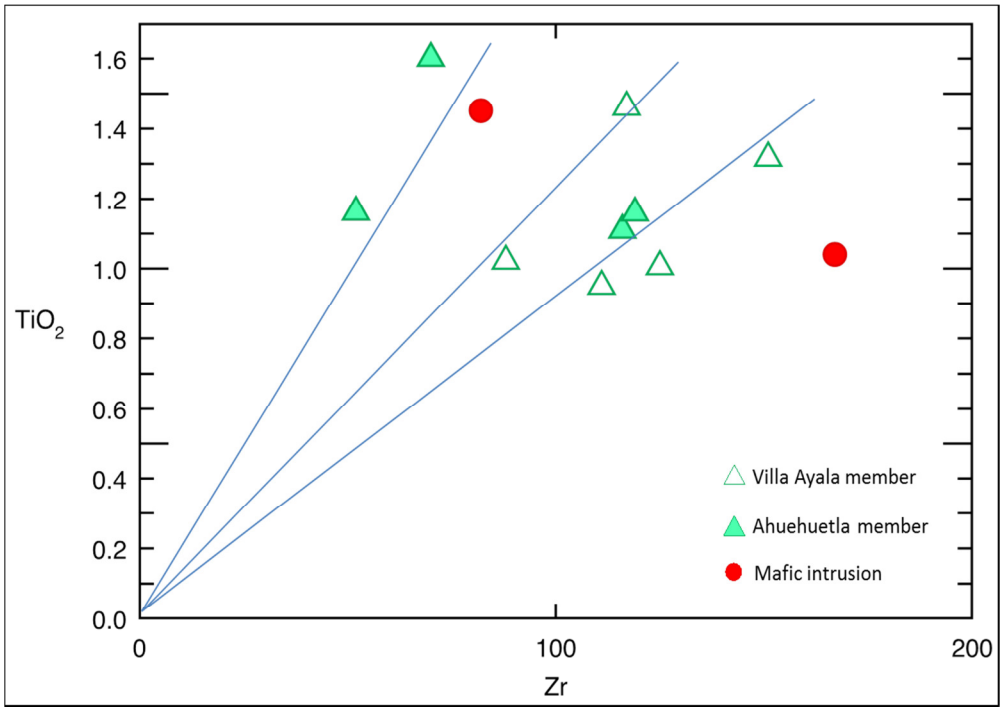

Figure A3.2. Binary diagram for TiO_2 versus Zr.

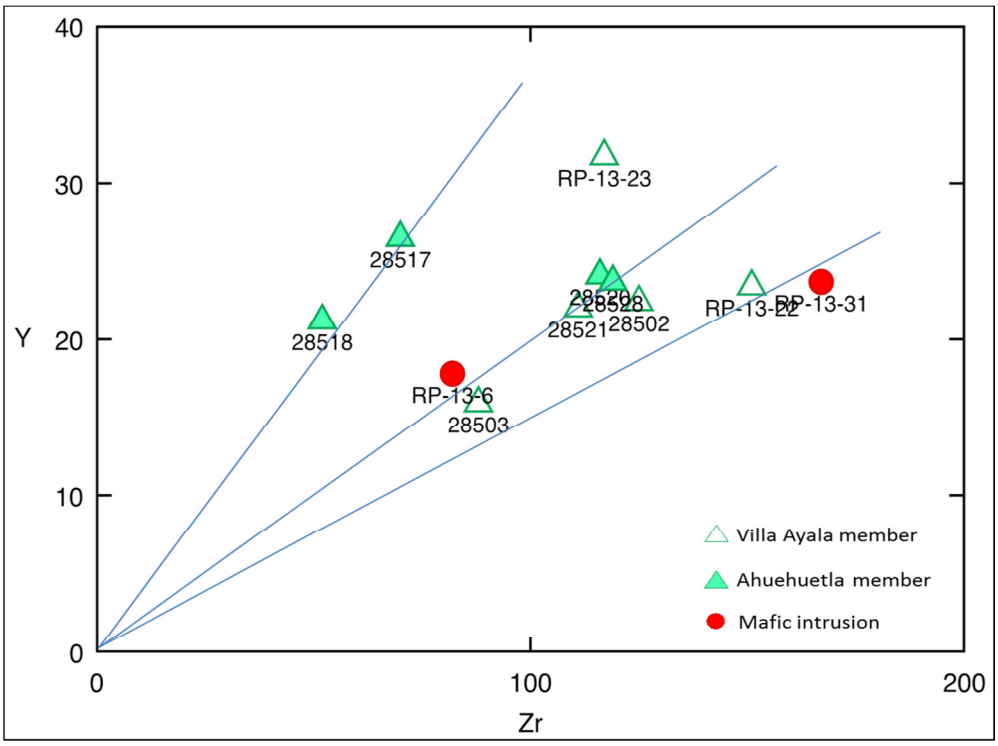

Figure A3.3. Binary diagram for Y versus Zr.

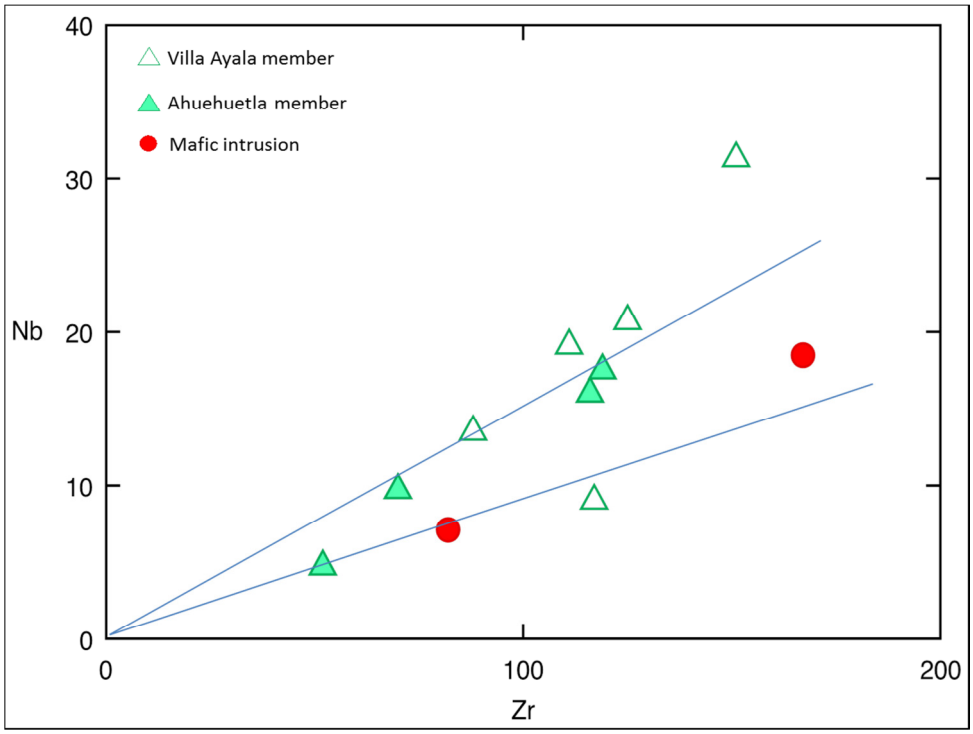

Figure A3.4. Binary diagram for Nb versus Zr.

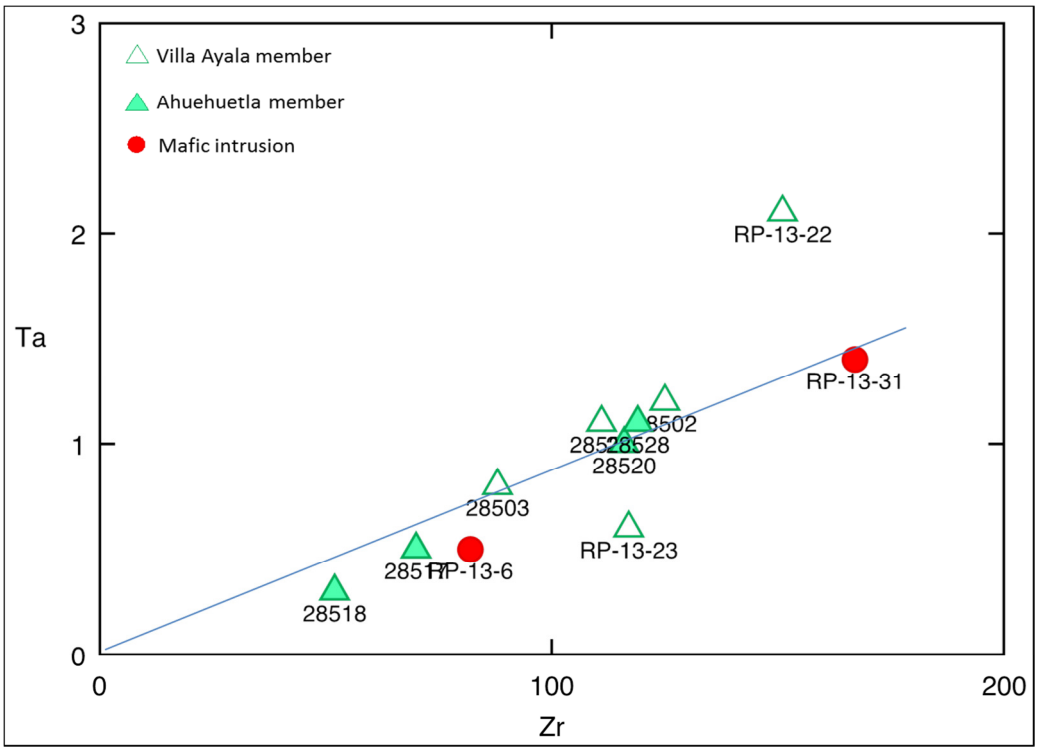

Figure A3.5. Binary diagram for Ta versus Zr.

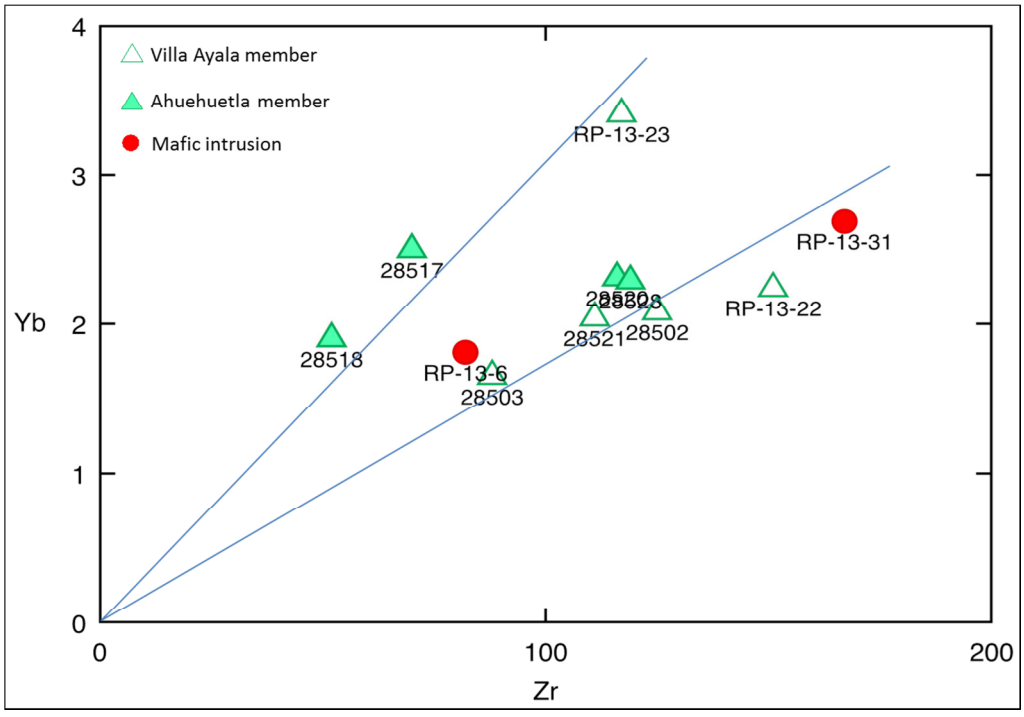

Figure A3.6. Binary diagram for Yb versus Zr.

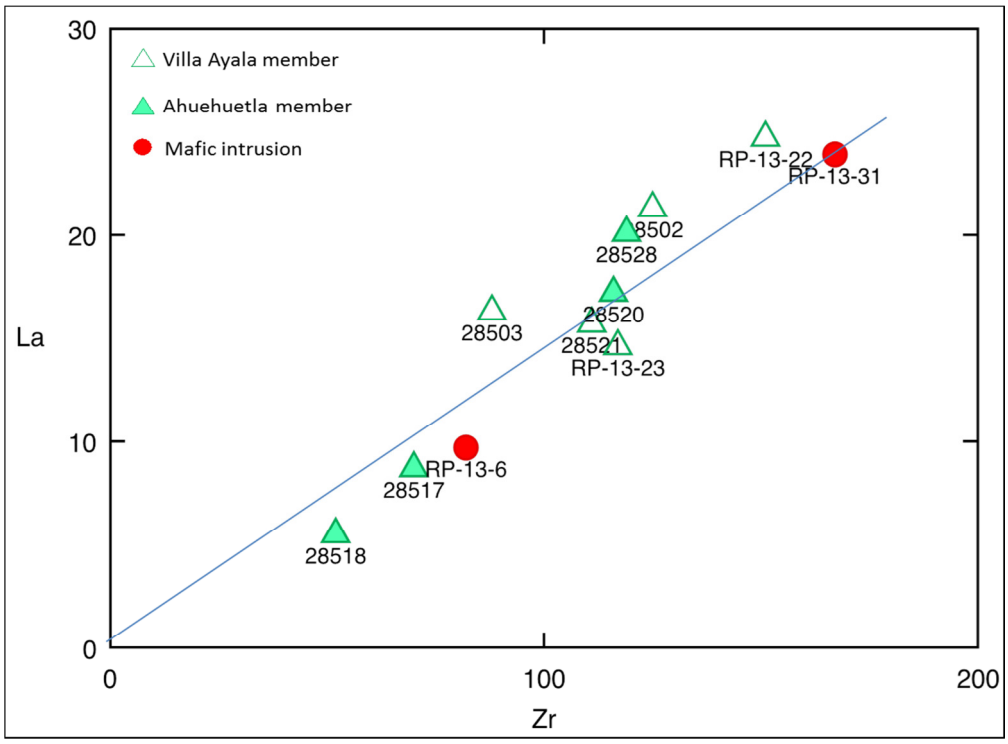

Figure A3.7. Binary diagram for La versus Zr.

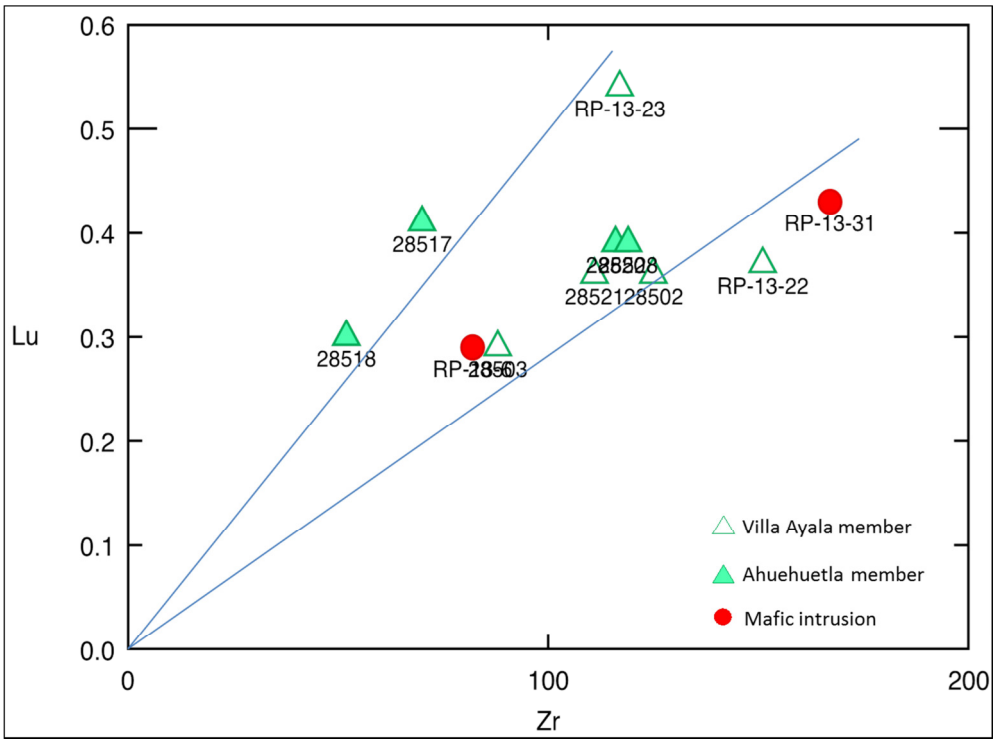

Figure A3.8. Binary diagram for Lu versus Zr.

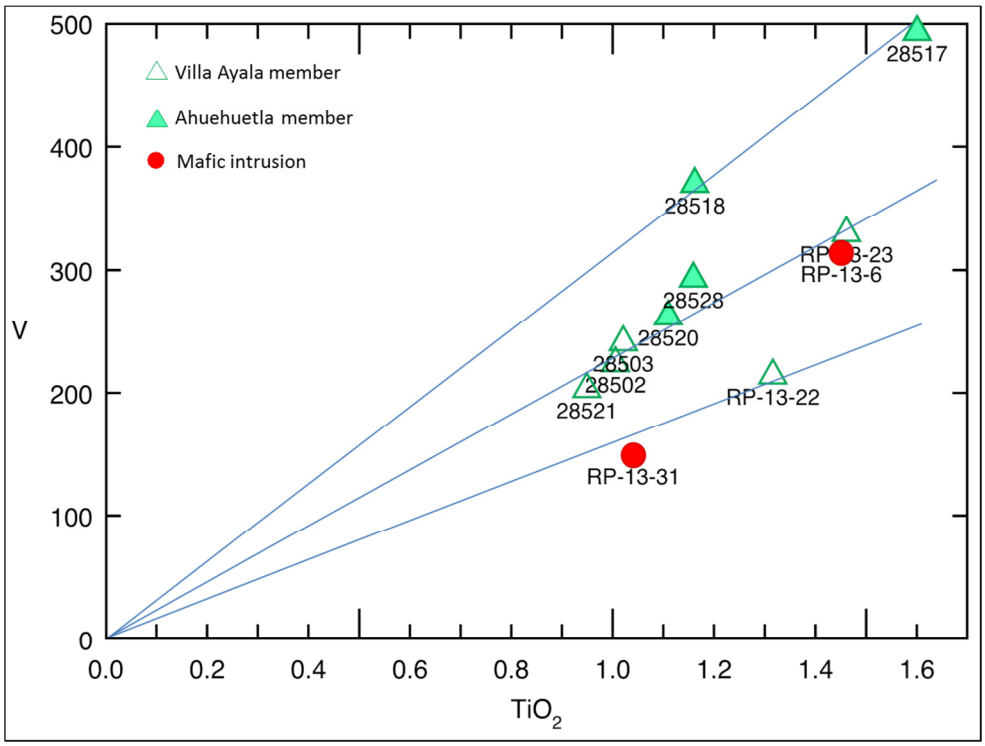

Figure A3.9. Binary diagram for V versus TiO_2.

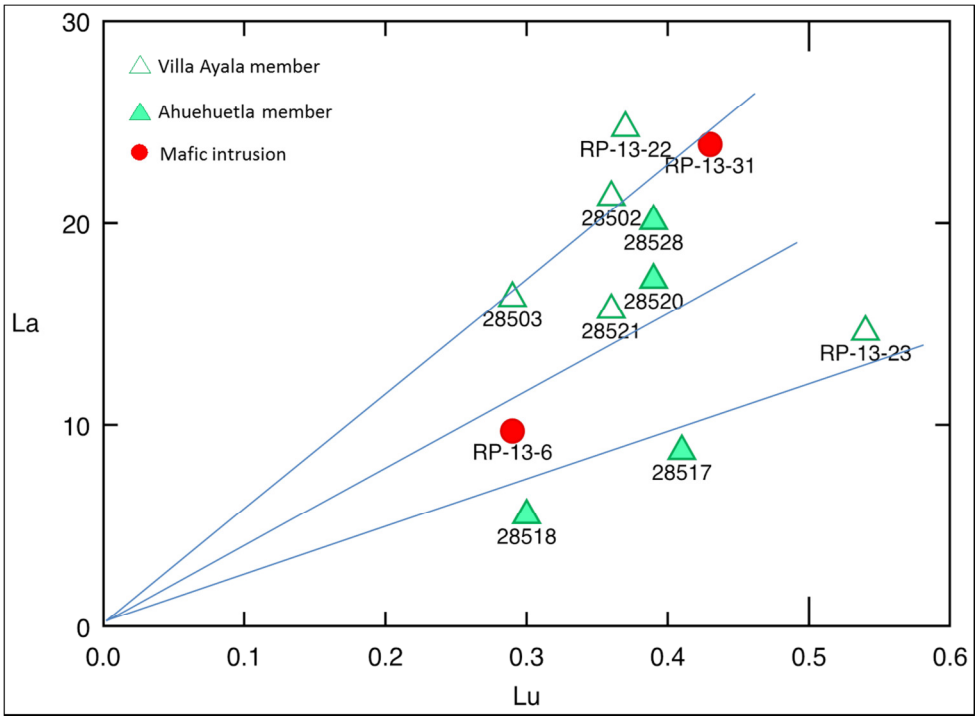

Figure A3.10. Binary diagram for La versus Lu.

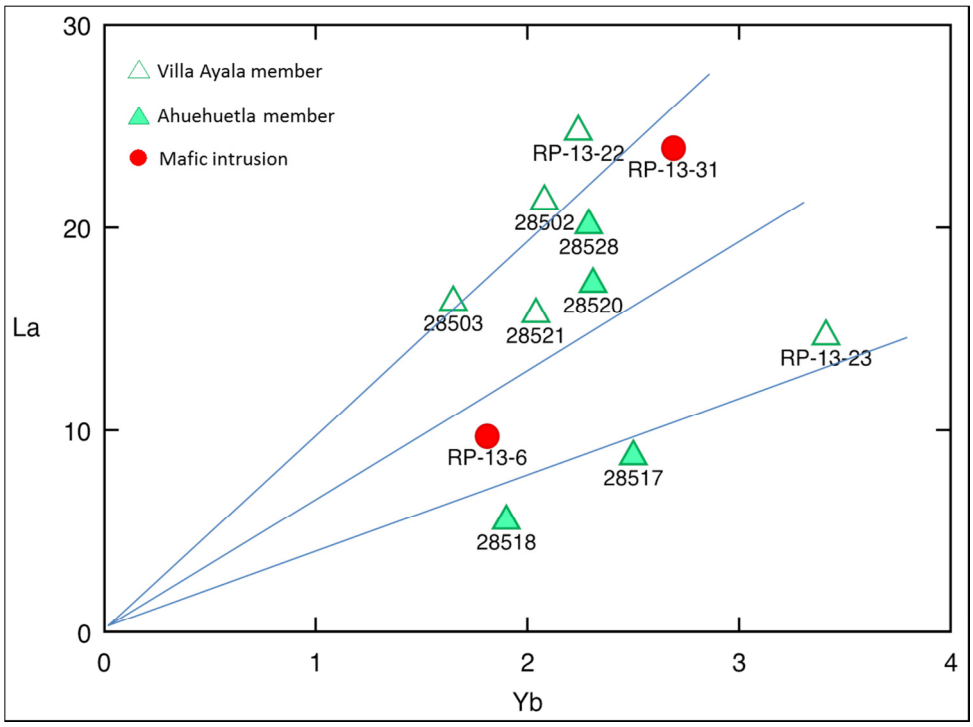

Figure A3.11. Binary diagram for La versus Yb.

Correlation Coefficients (Cann, 1970)

To investigate element mobility during hydrothermal alteration, a methodology developed by Cann (1970) represents one possible procedure. As in the Maclean Method, it involves binary plots of the elements, but element mobility is assessed through examination of correlation coefficients for element (oxide) pairs plotted on of X-Y plots. High correlation coefficient values close to +1 or -1 indicate that both of the plotted elements are immobile, but low correlation coefficient values tending to 0 indicates that at least one of the plotted elements is mobile (Table A3). For example, if Zr-Hf have a high correlation coefficient (close to +1 or -1) then both Hf and Zr can be assumed immobile. However, if a Zr-Y variation diagram has a low correlation coefficient (close to 0) then Y must be a mobile element because Zr has previously determined as immobile (Hocker 2005). Correlation coefficients for the Villa Ayala member, Rey de Plata member, Ahuehuetla member and the feldspar-

phyric mafic intrusion were obtained using Igpet (2008) and are tabulated in Table A3.

Table A3. Correlation coefficients for selected variation diagrams for mafic and felsic rocks of the Rey de Plata deposit.

Plot	Villa Ayala member	Ahuehuetla member	Basaltic intrusion	Rey de Plata member
	r	r	r	r
Zr-TiO_2	0.06	0.54	-0.64	0.08
Zr-Nb	0.25	0.94	1	0.97
Zr-Ta	0.28	0.95	0.99	0.97
Zr-P_2O_5	0.01	0.96	-0.99	-0.2
Zr-Y	0.46	-0.27	-0.11	0.82
Zr-Ga	0.6	0.56	0.03	0.81
Zr-Ce	0.07	0.98	0.91	0.92
Zr-La	0.36	0.98	0.96	0.92
Zr-Yb	0.41	0	0.89	0.88
Zr-Th	0.56	0.85	0.9	0.92
Zr-V	-0.75	-0.82	-0.86	-0.39
Zr-MgO	0.35	-0.82	-0.78	0.79
Zr-Na_2O	0.19	0.06	-0.37	0.01
Zr-K_2O	-0.16	0.73	-0.97	0.38
Zr-Fe_2O_3	0.15	-0.11	-0.96	0.15
Zr-SiO_2	0.05	0.31	0.93	-0.8
Zr-Rb	-0.18	0.66	-1	0.24
Zr-CaO	-0.47	0.17	-1	0.58
Zr-Al_2O_3	0.42	0.86	-0.36	0.83
Nb-Hf	-0.12	0.94	1	0.97
Hf-Ta	-0.06	0.95	1	0.97
Nb-Al_2O_3	0.32	0.77	-0.29	0.84
Hf-Al_2O_3	0.33	0.9	-0.33	0.8
Ta-Al_2O_3	0.33	0.77	-0.24	0.75
Zr-Ni	-0.68	-0.67	-0.9	0.21
Zr-Cs	0.07	-0.88	-0.26	0.35
Zr-Gd	0.26	0.74	-0.21	0.77
Nd-Zr	0.34	0.99	0.76	0.83
Zr-Sm	0.4	0.96	0.33	0.79

The correlation coefficients shown in Table A3 indicate that the trace and REE elements such as the Hf, Zr, Nb, V and Ta are immobile for all the rock types

based on correlation coefficient greater than 0.97. For the Ahuehuetla member, Ce, La and Nd elements are also shown to be immobile, and P_2O_5 is immobile for the Feldspar-phyric mafic intrusion. Y, Ga, Gd, Cs, Sm and Rb are moderately immobile in all rock types, and Yb is immobile in samples from the Rey de Plata member.

References

Cann, J. R. 1970. Rb, Sr, Y, Zr, and Nb in some ocean floor basaltic rocks; Earth and Planetary Science Letters, v.10, p.7-11.

Hocker, S. M. 2005. Volcanic Stratigraphy, Synvolcanic Intrusions and Controls on Mineralization at the Archean Genex Mine, Kamiskotia Area, Timmins, Ontario [M.Sc. thesis]: Sudbury, Laurentian University, 215 p.

MacLean, W.H. 1990. Mass Change calculations in altered rock series. Mineralium Deposita, vol. 25, p. 44-49.

MacLean, W.H., and Barret, T.J. 1993. Lithogeochemical techniques using immobile elements; Journal of Geochemical Exploration, v. 48, no. 2, p. 109-133.

Appendix 4: Structural data collected from fieldwork and core-logging

Field data

Structural data collected from field work along 7 traverses and used in construction of stereoplots, as well as the Rey de Plata map is presented in tables A4.1 to A4.7.

Table A4.1. Field structural data of traverse #1.

		S0		D1					D2	D3		D4					
Traverse #	Location on map	Strike/dip	Younging	S1	Vergence	F1 axis	F1 A. P.	Stretch L.	S2	F3 axis	F3 A. P.	F4 axis	F4 A. P.	Normal Faults	Shear	Veins	Sample
1	0m	040 12	UP	130 38	East				162 03					183 49			
		026 12	UP	136 22	East				151 02								
1	50m	248 13		295 24	West				310 05								
1	70m	100 04	Down	284 16	West	340 16	280 18										
		112 06															
		133 22		154 30	East									132 42			
1	90m	137 43	Down	173 16	East												
		142 66		124 62	East							290 21	286 77				
		137 71															
		108 12	Down	305 10	East												
1	120m	180 20	Up	190 24	West							358 16	191 49	198 52			
		278 16		212 24	West							012 14	194 61				
1	140m	147 84	Up	139 64	East									175 64			RP-13-a
		139 38	Up	147 49	East												
1	200m	198 20		040 25	East	316 04	179 34							078 72			RP-13-b
				184 16													
		176 08	Up	148 22	East	319 06	140 22										
				158 27													
		162 38		149 28	West												
1	230m	250 16	Up	184 34	East							238 04	074 48	124 60			
														132 38			
		045 10		144 14													
		209 47		216 42								220 17					RP-13-10
		176 24		179 37													
1	300m	198 33	Up	178 34	East	176 37	224 38										RP-13-09
		210 28															
		220 17	UP														
		202 48	Down	232 34													
		262 19	Up											118 54			
		185 31	Up														
1	320m	214 21	Up	214 21								097 11	290 68	261 54			
		172 34	Up	156 38													
		216 14	Up											258 58			RP-13-06
1	340m	196 17															RP-13-07
1	450m	232 46		257 47													
1	480m	227 37							260 39								
1	490m	222 35							044 54								

Table A4.2. Field structural data of traverse #2.

		S0		D1					D2	D3		F3 A. P.	D4					
Traverse #	Location on map	Strike/dip	Younging	S1	Vergence	F1 axis	F1 A. P.	Stretch L.	S2	F3 axis			F4 axis	F4 A. P.	Normal Faults	Shear	Veins	Sample
2	80m			228 20					212 45									
2	80m			198 48				322 41	238 38									
2	160m			130 20											135 58			RP-13-17
															149 44			
2	190m			174 43				300 34	179 50									
2	310m			177 23				280 34	184 34				226 10	80 34				
2	310m			197 40					221 50									
2	370m			194 57					220 71									RP-13-18
								259 46	204 72						152 52			
2	520m			198 46											282 74	64 86		
															214 56			
2	570m			176 52				272 32							235 72			RP-13-01
2	620m			158 33				287 37	160 47						160 29			
				156 34					134 61						188 34			
									144 51						330 46			
															302 61			
2	640m			182 38				296 30							68 12			RP-13-02
2	670m			174 36				301 26	160 48						204 28			RP-13-03
								294 18										
2	780m			148 51				294 41	165 56							169 49	040 33	RP-13-19
				165 44													126 50	
				164 44													238 26	
																	170 42	
2	910m			213 56				284 63	271 49									
				214 54														
2	950m			195 38				294 38									040 88	
																	164 74	
																	252 84	
2	980m			216 41				285 38							274 84			
2	1050m			138 19														
2	1090m			179 06											248 47			
2	1120m			184 24				308 18										
2	1190m			252 64				316 56										
				154 28				299 22										
2	1230m			188 26														
2	1290m			232 54														
2	1390m			256 67				272 54					042 34	358 37	046 87	312 60		
													078 38	011 46		112 46		
													051 12	047 66				
2	1440m			198 51				278 47							232 60			RP-13-20
2	1510m								233 71								230 74	
2	1540m			238 62									236 14	234 62	233 71			
2	1610m			232 33				291 23										
2	1640m			176 52				278 58	172 73						140 69			
2	1680m			172 26				271 16										
2	1780m														285 50			RP-13-21
															276 48			RP-13-22
															234 45			
2	1930m			216 45					166 48									

Table A4.3. Field structural data of traverse #3.

		S0		D1					D2	D3		D4					
Traverse #	Location on map	Strike/dip	Younging	S1	Vergence	F1 axis	F1 A. P.	Stretch L.	S2	F3 axis	F3 A. P.	F4 axis	F4 A. P.	Normal Faults	Shear	Veins	Sample
3	100m	326 27		280 11						330 01	348 08						
		325 16							321 04								
3	130m	331 51		302 12													
3	500m													120 76			RP-13-30
																	RP-13-31
3	530m														264 45		RP-13-32
																	RP-13-33
3	550m	310 74		170 30										204 30			RP-13-34
		202 38	UP	287 10										312 80			
		358 12	UP											147 60			
		344 21	UP											154 48			
		018 16	UP					119 15						098 78			
		326 22	UP					141 06	064 06					105 70			
	630m	346 07	UP	261 16				054 06						095 68			
		028 17	UP	090 18				146 17						075 60			
		156 28		059 04				154 01				296 18	284 37	134 52			
		048 02	UP	155 18										140 67			
		039 12	UP	064 15													
3	750m	180 50	Overturne	172 32								338 22	198 18				
3	800m	216 42		220 62								030 24	240 38				
		292 12												093 54			
		280 28															
	840m	178 24		088 14				208 13									RP-13-38
	900m	250 43	UP														
		265 36							268 25								
	1000m	270 21															
		330 20															
	1060m	284 82							071 83					125 31			
		313 44															

Table A4.4. Field structural data of traverse #4.

Traverse #	Location on map	Strike/dip	Younging	S1	Vergence	F1 axis	F1 A. P.	Stretch L.	S2	F3 axis	F3 A. P.	F4 axis	F4 A. P.	Normal Faults	Shear	Veins	Sample
4	20m								173 32						088 47		
	80m								191 56						174 56		
4	130 m	194 65		177 48				310 43	196 76						174 62		RP-13-04
															202 06		RP-13-44
															186 35		
4	220 m							278 38									
								038 22									
4	280 m			214 43										214 43	214 43		
4	330 m			179 47											179 47		
4	340 m					004 34	202 62										RP-13-43
4	450 m	194 45															
		145 45		226 26													
				188 46													
4	500m			198 40										198 40			RP-13-42
4	540m			192 42				254 47									RP-13-39
								284 38									
				158 30				276 26									
								250 35									
4	610 m			207 43				304 41		112 21	320 48			148 25			RP-13-40
								267 34						218 48			RP-13-41
4	620 m			170 30										156 45			
														112 52			
4	655 m							252 42									
4	670 m			102 77				269 34						098 67			
				123 54													
				118 43													
4	710 m			256 70													
				176 27				306 35	154 62						240 80		
4	740 m			222 87												084 74	
				210 47													
4	760 m			186 34										132 65			
				236 62					182 40								

Table A4.5. Field structural data of traverse #5.

		S0		D1					D2	D3		D4					
Traverse #	Location on map	Strike/dip	Younging	S1	Vergence	F1 axis	F1 A. P.	Stretch L.	S2	F3 axis	F3 A. P.	F4 axis	F4 A. P.	Normal Faults	Shear	Veins	Sample
5	120 m			190 23													
	160 m			120 28													
	180 m								101 48								
				171 38						189 27	016 38						
	210 m			113 14													
				087 22												056 49	
5	420 m			190 31													
	445 m									207 07	048 41						
	430 m			156 50													
	450 m									220 15	049 34						
	455 m									192 12	076 26						
5	500 m	024 22		018 32										172 70			
5	700 m	013 07	UP	012 20													
	700 m	328 26		354 09										200 40			
	730 m	028 12												210 53			
		352 31	UP						306 07					212 59			
														222 38			
5	735 m	058 19	UP	268 12										156 60			
	760 m	137 26												035 50			
	770 m			186 36													
	780 m					320 15	248 15										
	820 m	140 19	Down	098 15										252 66			
														184 59			
														208 56			
	825 m			356 16													
	830 m	160 28	Down														
		148 38															
5	840 m	132 21	Down	098 16													
	845 m	248 11															
	850 m													252 63			
														227 65			
	870 m	172 38	UP											252 78			
	890 m	218 31															
	900 m	294 26		296 18													
5	907 m	212 47	UP	224 38								338 13	244 14	292 65			
												332 12	174 18				
5	920 m	304 32															
	950 m	138 38	Down	102 22		115 35	046 37										
				086 11		084 41											
	960 m			110 12		035 24											
	980 m			120 06		286 52											
5	1155 m	244 28	UP	083 17		127 08	084 12					272 12	269 56	134 25			RP-13-36
		324 12							068 06	132 11	081 12						RP-13-37
	1170 m	350 21	UP						065 22			126 02	308 49				
												127 06	304 47				
5	1290 m	158 37	Down			330 20	264 12										
	1300 m	320 24	UP	254 21						324 22	300 52			170 66			
5	1510 m	300 38															RP-13-05
																	RP-13-35

Table A4.6. Field structural data of traverse #6.

		S0		D1					D2	D3		D4					
Traverse #	Location on map	Strike/dip	Younging	S1	Vergence	F1 axis	F1 A. P.	Stretch L.	S2	F3 axis	F3 A. P.	F4 axis	F4 A. P.	Normal Faults	Shear	Veins	Sample
6	790 m								212 26			199 23	040 38				
												017 08	013 60				
6	810 m			191 42				283 36	191 30			015 24	227 70		168 23		
												035 10	252 26				RP-13-13
6	780 m			242 54													RP-13-12
	770 m			225 79					236 76								RP-13-11
6	750 m			245 32													
	740 m			212 29				284 18									
				179 41													RP-13-14
	730 m			209 64											239 61		
	650 m			278 12				083 13	255 26					236 56			
6	680 m									280 25	252 27				250 44		
										012 44	310 38						
										342 44	268 44						
	650 m			190 08						282 22	268 50	238 06	212 34				
6	630 m			274 23				267 11	202 22					250 54			
	610 m			260 22				258 12	208 38								
6	590 m			174 18						196 12	004 16	176 12	046 16	194 18			
												210 04	052 15				
6	600 m								218 27			020 14	320 10				RP-13-15
6	555 m								246 43					255 27			
									244 31					268 34			
									227 66	242 14	240 46			197 43			
6	505 m	154 42							246 32					220 43			
	500 m	280 54							232 38								
	485 m	094 74							225 28								
	400 m								186 34								
	420 m	212 40							244 28								
6	430 m	216 62							216 62								
6	350 m					284 38	178 44			286 24	280 77	316 42	142 76				RP-13-16
	250 m	222 50							259 62					204 49			
	165 m								288 28					288 28			

Table A4.7. Field structural data of traverse #7.

		S0		D1					D2	D3		D4					
Traverse #	Location on map	Strike/dip	Younging	S1	Vergence	F1 axis	F1 A. P.	Stretch L.	S2	F3 axis	F3 A. P.	F4 axis	F4 A. P.	Normal Faults	Shear	Veins	Sample
7	390 m							286 39	125 46					104 62			RP-13-23
	410 m							305 54	168 59								RP-13-24
	380 m			174 33													
7	570 m			152 25								356 14	326 32				
									207 76	306 11	321 12	194 11	192 82				
	600 m			008 11						348 06	310 05	190 11	300 24				
	650 m			124 26													
				091 14								138 08	070 14				
7	645 m			119 15								182 08	032 31				
7	970 m								190 26								
				290 06					241 38								
				206 26													
7	1340 m			307 08				304 24									
									324 72								
	1440 m								017 18								
				188 21					300 12						350 12		
				186 12						030 06	024 36				352 19		
7	1475 m			092 40					125 24	024 11	018 32						
									124 18								
				070 36					084 50								
7	1710 m			012 07													RP-13-08
	1850 m			190 18													RP-13-25
				264 22													RP-13-26
	1920 m								209 40								
7	BRP39111			170 20				299 14				352 06	350 38			200 84	
				183 21								016 02	060 90				
7	2020m								225 42								
	2110m			338 08					182 31								RP-13-29
									220 20								
									312 14								
	2150m			320 32													RP-13-27
	2210m			326 24													RP-13-28

Core data

Structural data collected from cores along 6 drillholes and which were used in the construction of stereoplots is presented in tables A4.8 to A4.13.

Table A4.8. Core structural data of DDH GT07A11.

							S0			D1				D2		D3		D4	
DDH	Depth	Rock Type	Unit	Beta	Alpha	Gamma	Strike	Dip	Younging	S1	F1 axis	F1 A. P.	Stretch	S2	Qtz	Normal	Normal	F4 axis	F4 axial
				angle	angle	angle							lin.		Veins	Faults	sliken lines		plane
GT07A11	10.7	Conglomerate	Cg. Balsas	214	35		345	45	up										
GT07A11	30.6	Conglomerate	Cg. Balsas	128	50		239	34	up										
GT07A11	38.0	Conglomerate	Cg. Balsas	172	55		293	23	up										
GT07A11	46.7	Conglomerate	Cg. Balsas	8	60		131	42	up										
GT07A11	57.5	Conglomerate	Cg. Balsas	235	50		14	34	up										
GT07A11	70.6	Conglomerate	Cg. Balsas	336	50		105	51	up										
GT07A11	70.9	Contact	Contact	334	70	340										108 31	27 to 164		
GT07A11	71.0	Turbidite	Miahuatepec	273	75		75	20	up										
GT07A11	73.7	Turbidite	Miahuatepec	240	55		22	31	up										
GT07A11	73.9	Turbidite	Miahuatepec	221	75	123					03 to198	038 10							
GT07A11	74.8	Turbidite	Miahuatepec	100	70		193	21	down										
GT07A11	80.9	Turbidite	Miahuatepec	40	85		137	16	down										
GT07A11	82.2	Turbidite	Miahuatepec	44	65														
GT07A11	86.4	Turbidite	Miahuatepec	140	35		258	46	up										
GT07A11	100.0	Turbidite	Miahuatepec	255	70		53	20	down										
GT07A11	106.5	Turbidite	Miahuatepec	215	45		349	36	up										
GT07A11	114.0	Turbidite	Miahuatepec	198	65										338 14				
GT07A11	120.3	Turbidite	Miahuatepec	244	45		21	41	up										
GT07A11	132.5	Turbidite	Miahuatepec	24	60		143	41	down										
GT07A11	160.5	Turbidite	Miahuatepec	64	65		171	32	down										
GT07A11	174.1	Turbidite	Miahuatepec	275	73		73	22	up										
GT07A11	174.3	Turbidite	Miahuatepec	30	85		134	17	up										
GT07A11	174.4	Contact	Contact	20	70	130										138 32	23 to 181		
GT07A11	174.5	Mafic	Villa Ayala	186	85	90					01 to 131	121 07							
GT07A11	176.0	Mafic	Villa Ayala	306	46										079 52				
GT07A11	177.0	Mafic	Villa Ayala	348	40											115 62			
GT07A11	177.1	Mafic	Villa Ayala	125	65					223 20									
GT07A11	181.5	Mafic	Villa Ayala	60	50					175 47									
GT07A11	187.0	Mafic	Villa Ayala	236	65					028 21									
GT07A11	193.4	Mafic	Villa Ayala	47	40	290													
GT07A11	193.6	Mafic	Villa Ayala	260	55					042 35									
GT07A11	193.8	Mafic	Villa Ayala	306	55		82	43											
GT07A11	193.8	Mafic	Villa Ayala	80	50									192 43					
GT07A11	194.7	Mafic	Villa Ayala	292	33										063 62				
GT07A11	204.6	Mafic	Villa Ayala	190	60										321 18				
GT07A11	209.0	Mafic	Villa Ayala	72	60									180 35					
GT07A11	220.0	Mafic	Villa Ayala	35	55		153	45									22 to 51		
GT07A11	7 Core boxes are missed. Due to that, the contact between the Villa Ayala and Rey de Plata units was not messured.																		
GT07A11	257.4	Felsic	Rey de Plata	26	40									148 61					
GT07A11	262.4	Felsic	Rey de Plata	80	30									199 63					
GT07A11	262.4	Felsic	Rey de Plata	90	45					203 46									
GT07A11	267.6	Felsic	Rey de Plata	90	35									207 56					
GT07A11	267.6	Felsic	Rey de Plata	104	60					208 29									
GT07A11	271	Felsic	Rey de Plata	80	35									197 58					
GT07A11	271	Felsic	Rey de Plata	72	57					182 38									
GT07A11	278.5	Felsic	Rey de Plata	68	30									187 65					
GT07A11	278.5	Felsic	Rey de Plata	60	65					168 33									
GT07A11	278.5	Felsic	Rey de Plata	340	15											106 86			
GT07A11	278.8	Felsic	Rey de Plata	48	60					161 39									
GT07A11	278.8	Felsic	Rey de Plata	55	35									174 62					
GT07A11	284	Felsic	Rey de Plata	110	43									224 44	224 44				
GT07A11	284	Felsic	Rey de Plata	74	50					187 45									
GT07A11	293	Felsic	Rey de Plata	65	60					175 37									
GT07A11	293	Felsic	Rey de Plata	52	45									169 53					
GT07A11	306	Felsic	Rey de Plata	356	60											122 42			
GT07A11	317	Felsic	Rey de Plata	121	50									232 35	232 35				
GT07A11	317	Felsic	Rey de Plata	132	70					221 15									
GT07A11	330	Felsic	Rey de Plata	42	60					157 40									
GT07A11	330	Felsic	Rey de Plata	32	40									153 60					
GT07A11	341	Felsic	Rey de Plata	44	50					161 49									
GT07A11	341	Felsic	Rey de Plata	65	30									185 66					
GT07A11	349.2	Felsic	Rey de Plata	52	40					170 58									
GT07A11	349.2	Felsic	Rey de Plata	56	25									177 72					

Table A4.9. Core structural data of DDH GT0911.

							S0			D1				D2		D3		D4	
DDH	Depth	Rock Type	Unit	Beta angle	Alpha angle	Gamma angle	Strike	Dip	Younging	S1	F1 axis	F1 A. P.	Stretch lin.	S2	Qtz Veins	Normal Faults	Normal sliken lines	F4 axis	F4 axial plane
GT0911	12	Turbidite	Miahuatepec	87	35		16	56											
GT0911	13.5	Turbidite	Miahuatepec	116	60		32	27	up										
GT0911	14.5	Turbidite	Miahuatepec	291	50		238	45	up										
GT0911	16.5	Turbidite	Miahuatepec	20	65		310	36											
GT0911	17.8	Contact	Contact	234	75		215	12											
GT0911	30	Mafic	Villa Ayala	340	45		279	55	?										
GT0911	38.3	Mafic	Villa Ayala	122	45		47	40	?										
GT0911	41.4	Mafic	Villa Ayala	294	50														
GT0911	47	Mafic	Villa Ayala	215	55					240 45									
GT0911	47	Mafic	Villa Ayala	20	20					163 27						315 80			
GT0911	59	Mafic	Villa Ayala	255	20		195	68	up										
GT0911	68	Mafic	Villa Ayala	118	53														
GT0911	78.2	Mafic	Villa Ayala	192	55		133	24	up										
GT0911	78.2	Mafic	Villa Ayala	240	60														
GT0911	81.9	Mafic	Villa Ayala	190	50		129	29	up	196 26									
GT0911	90.8	Mafic	Villa Ayala	274	53														
GT0911	91	Mafic	Villa Ayala	182	44		119	35	up	224 39									
GT0911	99.6	Mafic	Villa Ayala	266	65														
GT0911	99.6	Mafic	Villa Ayala	250	45					225 26				197 42					
GT0911	115.5	Mafic	Villa Ayala	188	26		125	53	up										
GT0911	126.9	Mafic	Villa Ayala	251	36	132							22 to 214						
GT09111	142.4	Mafic	Villa Ayala	250	45					195 51									
GT0911	154.3	Mafic	Villa Ayala	272	50					197 42									
GT0911	163.4	Mafic	Villa Ayala	251	55	130				221 42			11 to 221						
GT0911	173	Mafic	Villa Ayala	290	37					203 33									
GT0911	180.3	Mafic	Villa Ayala	280	45					233 57									
GT0911	187.8	Mafic	Villa Ayala	54	60		338	37	up	226 48									
GT0911	196.8	Mafic	Villa Ayala	296	45		241	51											
GT0911	206	Mafic	Villa Ayala	266	57														
GT0911	206	Mafic	Villa Ayala	276	25					219 34				217 67					
GT0911	217.3	Mafic	Villa Ayala	260	34														
GT0911	217.3	Mafic	Villa Ayala	280	59					204 55				232 34					
GT0911	221.8	Mafic	Villa Ayala	276	60		230	33											
GT0911	221.8	Contact	Contact	256	35									200 53					
GT0911	223.7	Graphytic Arg	Rey de Plata	280	60									233 34					
GT0911	224.8	Contact	Contact	142	70		48	13											
GT0911	233.7	Felsic	Rey de Plata	250	35					194 52									
GT0911	244.5	Felsic	Rey de Plata	96	45										021 45				
GT0911	245	Felsic	Rey de Plata	269	25									210 65					
GT0911	245	Felsic	Rey de Plata	292	37					235 58									
GT0911	255	Felsic	Rey de Plata	74	43										001 51				
GT0911	255.3	Felsic	Rey de Plata	240	20									180 65					
GT0911	255.3	Felsic	Rey de Plata	251	35					195 52									
GT0911	256.9	Felsic	Rey de Plata	214	30									154 51					
GT0911	256.9	Felsic	Rey de Plata	223	50					170 33									
GT0911	276.4	Felsic	Rey de Plata	245	45					192 41									
GT0911	276.4	Felsic	Rey de Plata	260	30									202 59					
GT0911	277.4	Felsic	Rey de Plata	86	43										012 49				
GT0911	277.7	Felsic	Rey de Plata	68	70													6 to 354	342 26
GT0911	278.25	No core boxes from 278.25 to 304.55m																	
GT0911	310	Felsic	Rey de Plata	260	35					204 54									
GT0911	315.1	Felsic	Rey de Plata	82	60											001 33			
GT0911	318.5	Felsic	Rey de Plata	207	30											147 50			
GT0911	328.2	Felsic	Rey de Plata	221	45									166 37					
GT0911	336.1	Felsic	Rey de Plata	255	55					207 34									
GT0911	336.1	Felsic	Rey de Plata	256	35									200 53					
GT0911	346.1	Felsic	Rey de Plata	240	22					180 63									
GT0911	353	Felsic	Rey de Plata	236	50					185 35									
GT0911	353	Felsic	Rey de Plata	214	30									154 51					
GT0911	392.1	Contact	Contact	44	15		339	83											
GT0911	396	Graphytic Arg	Rey de Plata	228	55					179 29									
GT0911	396.3	Graphytic Arg	Rey de Plata	180	45											116 34			
GT0911	398.6	Contact	Contact	252	36		196	51											
GT0911	411.3	Mafic	Ahuehuetla	250	40					195 47									
GT0911	422.1	Mafic	Ahuehuetla	80	50					004 43									
GT0911	432	Mafic	Ahuehuetla	260	60					215 30									
GT0911	432	Mafic	Ahuehuetla	247	30									189 56					
GT0911	444	Mafic	Ahuehuetla	250	43					196 44									
GT0911	449.8	Mafic	Ahuehuetla	184	50										121 29				

Table A4.10. Core structural data of DDH GT0510.

							S0			D1				D2		D3		D4	
DDH	Depth	Rock Type	Unit	Beta angle	Alpha angle	Gamma angle	Strike	Dip	Younging	S1	F1 axis	F1 A. P.	Stretch lin.	S2	Qtz Veins	Normal Faults	Normal sliken lines	F4 axis	F4 axial plane
GT0510	4.1	Turbidite	Miahuatepec	296	74		229	22	down										
GT0510	7.3	Turbidite	Miahuatepec	30	80		285	19	up										
GT0510	8.6	Turbidite	Miahuatepec	28	70		289	29	up										
GT0510	10.3	Contact	Contact	114	65		2	23											
GT0510	10.7	Mafic	Villa Ayala	169	57					075 23									
GT0510	15.3	Mafic	Villa Ayala	165	67					064 14									
GT0510	15.7	Mafic	Villa Ayala	144	33									049 49					
GT0510	23.1	Mafic	Villa Ayala	280	60					206 33									
GT0510	23.2	Mafic	Villa Ayala	276	65	327							16 to 238			206 28			
GT0510	23.2	Mafic	Villa Ayala	276	65	338										206 28	20 to 248		
GT0510	33.2	Mafic	Villa Ayala	310	50					228 47									
GT0510	33.2	Mafic	Villa Ayala	326	43									240 56					
GT0510	42.9	Mafic	Villa Ayala	315	55	312				233 43			21 to 257						
GT0510	49.5	Mafic	Villa Ayala	315	55					233 43									
GT0510	49.5	Mafic	Villa Ayala	294	30									209 64					
GT0510	52.5	Mafic	Villa Ayala	58	50	320				319 46			39 to 012						
GT0510	62.5	Mafic	Villa Ayala	316	60					235 38									
GT0510	62.5	Mafic	Villa Ayala	313	35									227 62					
GT0510	73	Mafic	Villa Ayala	292	52					213 43									
GT0510	76.4	Mafic	Villa Ayala	86	60										340 32				
GT0510	84.4	Mafic	Villa Ayala	162	60					064 21									
GT0510	84.4	Mafic	Villa Ayala	125	40									027 45					
GT0510	94.7	Mafic	Villa Ayala	270	43					189 48									
GT0510	107.7	Mafic	Villa Ayala	286	40					203 53									
GT0510	116.3	Mafic	Villa Ayala	224	35					140 48									
GT0510	126	Mafic	Villa Ayala	252	45	270												10 to 342	172 43
GT0510	133.7	Mafic	Villa Ayala	12	20											281 80			
GT0510	148.5	Mafic	Villa Ayala	292	50					212 45									
GT0510	159.5	Mafic	Villa Ayala	193	50					107 30									
GT0510	169.5	Mafic	Villa Ayala	232	25										146 59				
GT0510	181.6	Mafic	Villa Ayala	279	60					205 33									
GT0510	187.8	Contact	Contact	72	35		336	59											
GT0510	197.7	Graphytic Arg	Rey de Plata	232	50											153 35			
GT0510	197.7	Graphytic Arg	Rey de Plata	232	55														
GT0510	209.7	Graphytic Arg	Rey de Plata	350	40		261	60	up										
GT0510	219.7	Contact	Contact	298	55		219	41											
GT0510	220	Felsic	Rey de Plata	4	57					273 43									
GT0510	220	Felsic	Rey de Plata	356	25									266 75					
GT0510	231	Felsic	Rey de Plata	300	45					218 51									
GT0510	231	Felsic	Rey de Plata	320	27									233 71					
GT0510	240.9	Felsic	Rey de Plata	304	55					224 41									
GT0510	240.9	Felsic	Rey de Plata	310	30									224 67					
GT0510	252	Felsic	Rey de Plata	235	55										159 30				
GT0510	261.5	Felsic	Rey de Plata	275	45											195 47			
GT0510	266	Felsic	Rey de Plata	43	30											310 68			
GT0510	276	Felsic	Rey de Plata	257	43					176 46									
GT0510	286	Felsic	Rey de Plata	232	60					159 25									
GT0510	Core missing, so the contact was not watched																		
GT0510	408	Mafic	Ahuehuetla	292	65					219 30									
GT0510	408.3	Mafic	Ahuehuetla	332	20										243 79				
GT0510	418	Mafic	Ahuehuetla	302	60					224 36									
GT0510	418	Mafic	Ahuehuetla	307	27									220 69					
GT0510	428.6	Mafic	Ahuehuetla	310	55					229 42									
GT0510	428.6	Mafic	Ahuehuetla	262	38									180 51					
GT0510	439.1	Mafic	Ahuehuetla	276	40					194 52									
GT0510	450.3	Mafic	Ahuehuetla	270	65					200 27									

Table A4.11. Core structural data of DDH GT0611A.

							S0			D1				D2		D3		D4	
DDH	Depth	Rock Type	Unit	Beta angle	Alpha angle	Gamma angle	Strike	Dip	Younging	S1	F1 axis	F1 A. P.	Stretch lin.	S2	Qtz Veins	Normal Faults	Normal sliken lines	F4 axis	F4 axial plane
GT0611A	16.5	Turbidite	Miahuatepec	356	75		262	33	up										
GT0611A	20.7	Turbidite	Miahuatepec	66	65		305	36	up										
GT0611A	25	Turbidite	Miahuatepec	89	65		320	31	up										
GT0611A	30.6	Turbidite	Miahuatepec	95	80		295	20	up										
GT0611A	36.9	Contact	Contact	299	75		236	28											
GT0611A	37	Mafic	Villa Ayala	3	65											266 43			
GT0611A	38.5	Mafic	Villa Ayala	255	37					173 50									
GT0611A	49.5	Mafic	Villa Ayala	317	70					240 35									
GT0611A	58	Mafic	Villa Ayala	272	70		215	27	down										
GT0611A	67.9	Mafic	Villa Ayala	224	52		151	28	up										
GT0611A	79.8	Mafic	Villa Ayala	147	33									042 43					
GT0611A	90.3	Mafic	Villa Ayala	331	57	298				244 49			13 to 255						
GT0611A	100	Mafic	Villa Ayala	306	56					226 47									
GT0611A	110.2	Mafic	Villa Ayala	307	52					224 51									
GT0611A	110.25	Mafic	Villa Ayala	350	45														
GT0611A	119.8	Mafic	Villa Ayala	341	50	123				250 57			22 to 264						
GT0611A	130.1	Mafic	Villa Ayala	297	45					214 55									
GT0611A	130.1	Mafic	Villa Ayala	283	20									193 75					
GT0611A	140	Mafic	Villa Ayala	357	45					262 63									
GT0611A	140	Mafic	Villa Ayala	345	23									250 84					
GT0611A	150	Mafic	Villa Ayala	304	45					219 57									
GT0611A	150	Mafic	Villa Ayala	295	20									204 78					
GT0611A	160.8	Mafic	Villa Ayala	302	55					222 47									
GT0611A	168.9	Mafic	Villa Ayala	293	50					213 49									
GT0611A	179.9	Mafic	Villa Ayala	240	65					186 22									
GT0611A	185.3	Mafic	Villa Ayala	255	35										172 52				
GT0611A	192.6	Contact	Contact	330	65		245	42											
GT0611A	195	Graphytic Arg	Rey de Plata	269	41									188 51					
GT0611A	202.8	Graphytic Arg	Rey de Plata	245	57					179 30									
GT0611A	202.9	Contact	Contact	292	80														
GT0611A	212	Felsic	Rey de Plata	294	48					213 51									
GT0611A	212	Felsic	Rey de Plata	288	23									198 74					
GT0611A	222	Felsic	Rey de Plata	266	48					190 44									
GT0611A	222	Felsic	Rey de Plata	273	27									186 65					
GT0611A	231.7	Felsic	Rey de Plata	240	55					172 30									
GT0611A	231.7	Felsic	Rey de Plata	256	35									173 53					
GT0611A	243.7	Felsic	Rey de Plata	254	43					176 45									
GT0611A	243.7	Felsic	Rey de Plata	237	27									151 54					
GT0611A	Core boxes are missed																		
GT0611A	295	Felsic	Rey de Plata	6	67					268 41									
GT0611A	295	Felsic	Rey de Plata	342	35									249 72					
GT0611A	307.4	Felsic	Rey de Plata	246	57										180 30				
GT0611A	307.7	Felsic	Rey de Plata	250	40										170 46				
GT0611A	307.9	Felsic	Rey de Plata	295	50					214 50									
GT0611A	In 330.15m the drillhole ends, but there are no more boxes.																		

Table A4.12. Core structural data of DDH GT0410.

							S0			D1					D2		D3		D4	
DDH	Depth	Rock Type	Unit	Beta angle	Alpha angle	Gamma angle	Strike	Dip	Younging	S1	F1 axis	F1 A. P.	Stretch lin.		S2	Qtz Veins	Normal Faults	Normal sliken lines	F4 axis	F4 axial plane
GT0410	30	Turbidite	Miahuatepec	120	60		192	26	up											
GT0410	44.6	Turbidite	Miahuatepec	288	45		27	49	up											
GT0410	51.3	Turbidite	Miahuatepec	278	49		19	43	down											
GT0410	55	Turbidite	Miahuatepec	99	22		185	67	up											
GT0410	71.5	Turbidite	Miahuatepec	118	65		186	22	down											
GT0410	77	Turbidite	Miahuatepec	72	60		148	34	down											
GT0410	85	Turbidite	Miahuatepec	302	45		39	51	down											
GT0410	86	Contact	Contact	70	70		139	25												
GT0410	86.1	Mafic	Villa Ayala	144	73					201 11										
GT0410	98	Mafic	Villa Ayala	42	63												122 35			
GT0410	108	Mafic	Villa Ayala	12	23												101 77			
GT0410	118.8	Mafic	Villa Ayala	24	37					112 62										
GT0410	128	Mafic	Villa Ayala	94	62											166 29				
GT0410	138.8	Mafic	Villa Ayala	180	43	278				270 37			5 to 276							
GT0410	148.6	Mafic	Villa Ayala	93	58					167 33										
GT0410	158.7	Mafic	Villa Ayala	140	26										226 57					
GT0410	168.7	Mafic	Villa Ayala	82	45											163 47				
GT0410	178.6	Mafic	Villa Ayala	255	55					360 34										
GT0410	178.6	Mafic	Villa Ayala	264	34										001 56					
GT0410	194.8	Mafic	Villa Ayala	40	50											124 48				
GT0410	204	Mafic	Villa Ayala	77	52					156 41										
GT0410	204	Mafic	Villa Ayala	82	30										167 62					
GT0410	215	Mafic	Villa Ayala	88	50					166 41										
GT0410	215	Mafic	Villa Ayala	120	25										205 60					
GT0410	226.1	Contact	Contact	96	65		165	26												
GT0410	235	Felsic	Rey de Plata	31	62					114 37										
GT0410	244.9	Felsic	Rey de Plata	65	64					140 31										
GT0410	244.9	Felsic	Rey de Plata	66	30										151 64					
GT0410	254.7	Felsic	Rey de Plata	11	56					099 44										
GT0410	254.7	Felsic	Rey de Plata	9	27										098 73					
GT0410	264.4	Felsic	Rey de Plata	62	57					140 39										
GT0410	264.4	Felsic	Rey de Plata	27	33										115 66					
GT0410	274.6	Felsic	Rey de Plata	247	49												349 38			
GT0410	274.6	Felsic	Rey de Plata	261	55					005 35										
GT0410	274.6	Felsic	Rey de Plata	275	28										010 63					
GT0410	285	Felsic	Rey de Plata	104	50					182 39										
GT0410	285	Felsic	Rey de Plata	90	25										175 65					
GT0410	294.8	Felsic	Rey de Plata	99	38										181 51					
GT0410	295	Felsic	Rey de Plata	159	13											248 68				
GT0410	Missed boxes from 295.3 to 459.85 m																			
GT0410	460.3	Mafic	Ahuehuetla	225	80		22	8												
GT0410	470.7	Mafic	Ahuehuetla	56	54					136 42										
GT0410	End of Drillhole in 471.05m																			

Table A4.13. Core structural data of DDH GT0210.

							S0			D1				D2		D3		D4	
DDH	Depth	Rock Type	Unit	Beta angle	Alpha angle	Gamma angle	Strike	Dip	Younging	S1	F1 axis	F1 A. P.	Stretch lin.	S2	Qtz Veins	Normal Faults	Normal sliken lines	F4 axis	F4 axial plane
GT0210	32.7	Turbidite	Miahuatepec	9	75											133 31			
GT0210	38.3	Turbidite	Miahuatepec	160	65		260	11	down										
GT0210	38.3	Turbidite	Miahuatepec	202	57	320					10 to 017	347 19							
GT0210	40.6	Turbidite	Miahuatepec	178	55		304	19	up										
GT0210	49.2	Turbidite	Miahuatepec	140	70		216	13	down										
GT0210	70.2	Turbidite	Miahuatepec	196	65		348	11	down										
GT0210	80	Turbidite	Miahuatepec	34	65		150	39	up										
GT0210	87.3	Turbidite	Miahuatepec	290	40		69	57	up										
GT0210	101	Contact	Contact	90	47		202	45											
GT0210	113.8	Mafic	Villa Ayala	140	63					235 18									
GT0210	123.7	Mafic	Villa Ayala	145	55					252 24									
GT0210	134.8	Mafic	Villa Ayala	51	65					161 37									
GT0210	144.9	Mafic	Villa Ayala	141	60					241 20									
GT0210	156	Mafic	Villa Ayala	113	55					217 32									
GT0210	169.6	Mafic	Villa Ayala	316	30		89	72	up										
GT0210	178.4	Mafic	Villa Ayala							187 41									
GT0210	178.4	Mafic	Villa Ayala											196 60					
GT0210	189.8	Mafic	Villa Ayala	357	65					126 41									
GT0210	189.8	Mafic	Villa Ayala	14	30									140 76					
GT0210	195.3	Mafic	Villa Ayala	36	55					155 49									
GT0210	199	Mafic	Villa Ayala	354	25										122 81				
GT0210	Missing boxes from 199.65 to 281.5m																		
GT0210	282.9	Felsic	Rey de Plata	30	70					145 35									
GT0210	282.9	Felsic	Rey de Plata	34	47									155 57					
GT0210	282.9	Felsic	Rey de Plata	325	75														
GT0210	Missing boxes from 287.1 to 298.25m																		
GT0210	301.9	Felsic	Rey de Plata	18	70					138 36									
GT0210	313.1	Felsic	Rey de Plata	67	75					161 26									
GT0210	313.1	Felsic	Rey de Plata	54	50									170 51					
GT0210	324.4	Felsic	Rey de Plata	73	70					171 29									
GT0210	324.4	Felsic	Rey de Plata	65	45									181 53					
GT0210	333.6	Felsic	Rey de Plata	74	65					176 33									
GT0210	333.6	Felsic	Rey de Plata	78	44									193 51					
GT0210	242.3	Felsic	Rey de Plata	38	65					153 39									
GT0210	242.3	Felsic	Rey de Plata	45	35									167 67					
GT0210	Missing boxes from 343.25 to 348.75m																		
GT0210	353	Felsic	Rey de Plata	30	60					149 45									

Appendix 5: Stereoplots of S_0 and S_1 in structural domains

Stereoplots showing S0 and S1 from data collected in field and drillholes is presented in Figure A5.1

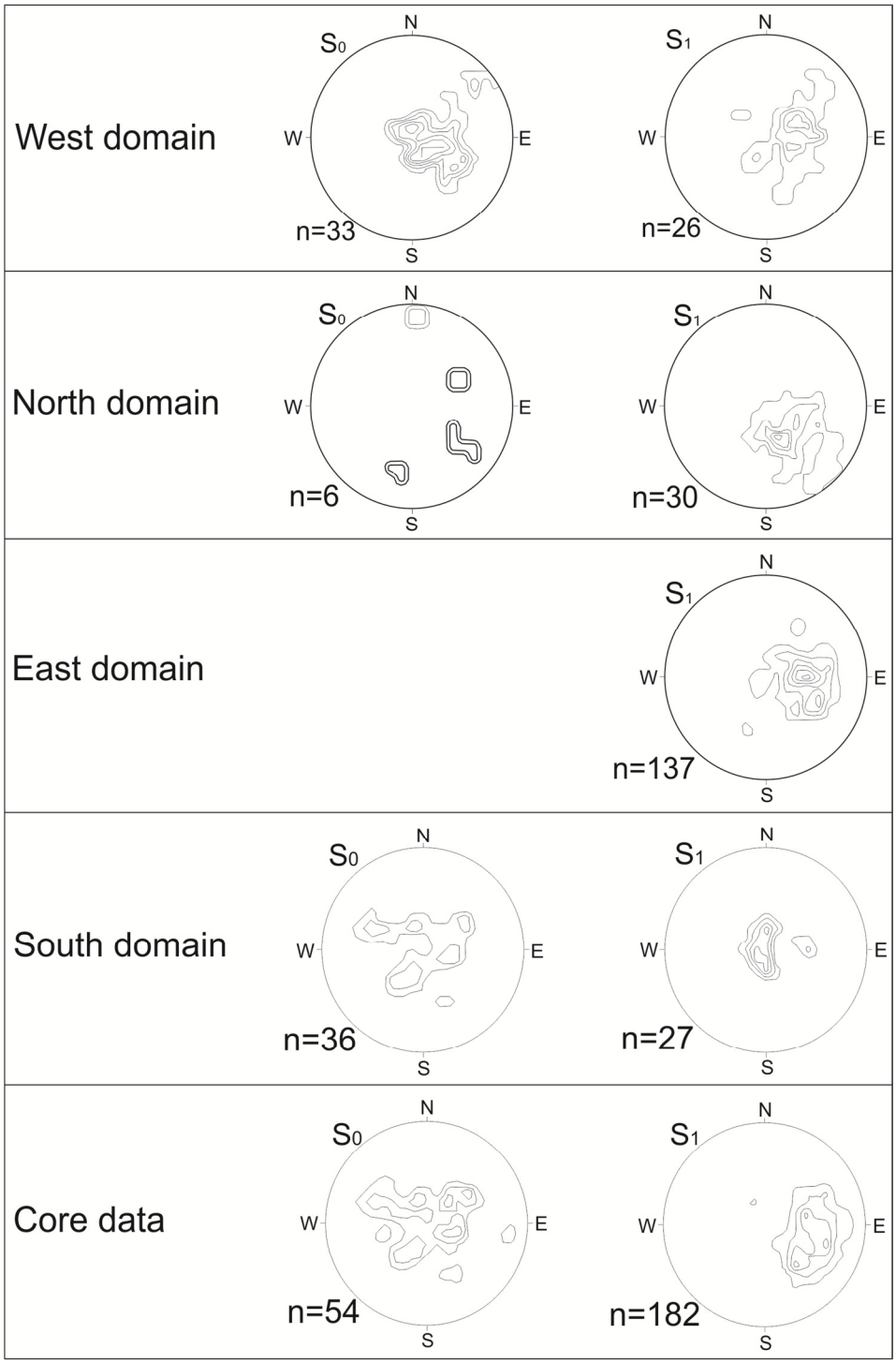

Figure A5.1. Stereoplots showing S_0 and S_1 from structural data collected in field and drill cores.

Appendix 6: Geologic Map of the Rey de Plata Deposit

Figure A6.1 Geologic Map of the Rey de Plata Deposit.